Studies on Porous Soft Materials

Based on Linked Rhodium-Organic Cuboctahedra

WANG ZAOMING

2022

Preface

The whole study in this thesis has been carried out under the supervision of Professor Shuhei Furukawa from October 2018 to March 2022 at the Department of Synthetic Chemistry and Biological Chemistry, Graduate School of Engineering, Kyoto University and at the Institute for Integrated Cell-Material Sciences, Kyoto University.

First of all, the author wishes to sincerely express his gratitude to Professor Shuhei Furukawa for providing me with the opportunity to study in such a wonderful laboratory. The author is particularly grateful for his continuous guidance, unconditional support, valuable discussion and constant encouragement throughout the research work, where the author benefits a lot from his teachings which always broaden the scientific view of the author. The author is grateful to Dr. Gavin A. Craig, Dr. Frederik Haase, Dr. Alexandre Legrand for their valuable discussion, hearty encouragement, selfless help and suggestions in both research and life. The author cannot get used to life in Kyoto so soon without their help.

The author is very thankful to Prof. Susumu Kitagawa, Prof. Satoshi Horike and Prof. Easan Sivaniah for their kind guidance and the fruitful discussions.

The author is very thankful to Prof. Kenji Urayama, Dr. Saori Minami and Mr. Takuma Aoyama for performing rheological measurements and supporting all the research work.

The author sincerely thanks Prof. Yamil J. Colón, Professor Guillaume Maurin, Dr. Rocio Semino, Dr. Aydin Ozcan and Mr. Christian Villa Santos for performing computational simulation and supporting the research work.

The author sincerely thanks Prof. Glen J. Smales and Prof. Brian R. Pauw for performing the small-/wide-angle X-ray scattering and supporting the research work.

The author would like to acknowledge all the past and present secretaries, technicians, undergraduate/graduate students, postdoctoral fellows, visitors and staff of the Furukawa's group. The author wishes to thank Dr. Mingshui Yao, Dr. Yifan Gu for their brother-like help and suggestions, and thank all the Chinese friends. Accompanied by them, the author's life in Kyoto cannot be more colorful.

The author is much indebted to the financial support from the China Scholarship Council (CSC).

Finally, the author would like to offer special thanks to his parents, Jianhui Mei and Bin Wang, and his fiancé, Xiaoxiao Gao for their selfless support and encouragement all the time. I will always forge ahead with their company!

WANG ZAOMING

Department of Synthetic Chemistry and Biological Chemistry
Graduate School of Engineering, Kyoto University

Contents

General introduction

1. Porous soft materials

Porous materials, such as porous carbons, zeolites, metal-organic frameworks (MOFs), covalent organic frameworks (COFs) and porous polymers, are an important class of materials that have witnessed widespread uses in various applications like adsorption, storage and separation, purification as well as catalysis.[1] Among them, the synthesis of MOFs, which are assembled from the ordered coordination of metal clusters with organic linkers,[2] has attracted immense attention due to the possibility to obtain chemically variable architectures with attractive properties underpinned by available design principles surrounding their net topology[3], reticular chemistry[4] and post-synthetic chemistry[5]. However, their highly ordered crystalline structures have made MOFs mechanically rigid and hard, rendering it difficult to process them for practical application. From the perspective of industrial handling, as-synthesized porous materials normally cannot be directly used. Instead, they are typically processed into specific forms, such as pellets, foams and films depending on the demands of various applications.[6] This requirement in processibility has shifted the attention from the chemical structure and property of microcrystalline MOF powders to the creation of MOF systems with shapeable macroscopic structures or processable physical forms.[7]

Intensive efforts have been paid to fabricate the processable MOF materials, and the main achievements are here classified into three aspects depending on their physical states: 1. Amorphization of MOFs into liquids or glasses.[8] 2. Regulation of assembling nucleation and the resulting crystal interactions into MOF gels.[9] 3. Hybridization of MOFs with organic polymers into mixed matrix membranes (MMM).[10] The synthesis of these MOF-derived materials not only provides good processability for industrial use but also affords the possibility to preserve porosity, contributing to the creation of novel porous matter beyond crystallinity. However, due to the limited stability and poor solubility of crystalline MOFs, the development of such processable MOF systems is in its infancy and still remains challenging.

As the building units of MOF architectures, metal-organic polyhedra (MOPs), one type of discrete molecular coordination cages with internal cavities, have recently garnered attention.[11] Containing the similar constituent pieces to MOFs, MOPs also provide the opportunity to control their structures and properties with well-design cavities by the rational combination of versatile metal nodes and organic linkers.[12] In contrast to the insoluble crystalline MOF powders, one of the key features of MOPs is their good solubility in solvents while retaining their molecular integrities and thus cavities, facilitating the solution-based processing of MOPs

for further material synthesis. For example, MOPs are prone to surface functionalization covalently or non-covalently by either monodentate or multidentate organic ligands.[13] The grafting of monodentate ligands on MOP surfaces allows us to tune the surface chemistry of MOPs for subsequent self-assembling control, while the introduction of multi-topic linkers enables the MOPs to be crosslinked by these linkers to form hierarchical porous architectures with higher order.[14] With all these unique advantages, MOPs are expected as promising "building blocks" or "porous synthons" for the construction of novel porous soft materials featuring both porosity and processability.[15-16] For instance, various porous soft materials including porous liquids, gels and films are obtained by utilizing MOPs as "synthons" but in a different way that was applied for MOF systems (Figure 1). In the following section, the development of strategies to form porous liquids, gels and films based on MOFs and MOPs will be described with a special focus on MOPs. Except for the processability and porosity, a further discussion on the possible heterogeneity and gradients which can be afforded by these systems is also given. In particular, different from the common crystalline solids, these porous soft materials (porous liquids, gels and films) can be considered as a hybrid system with either solvents or organic polymer as the continuous phase and MOFs/MOPs as the porous phase. By controlling the spatial arrangement of MOFs/MOPs within the systems, materials with special properties such as directional structural asymmetry can be obtained.

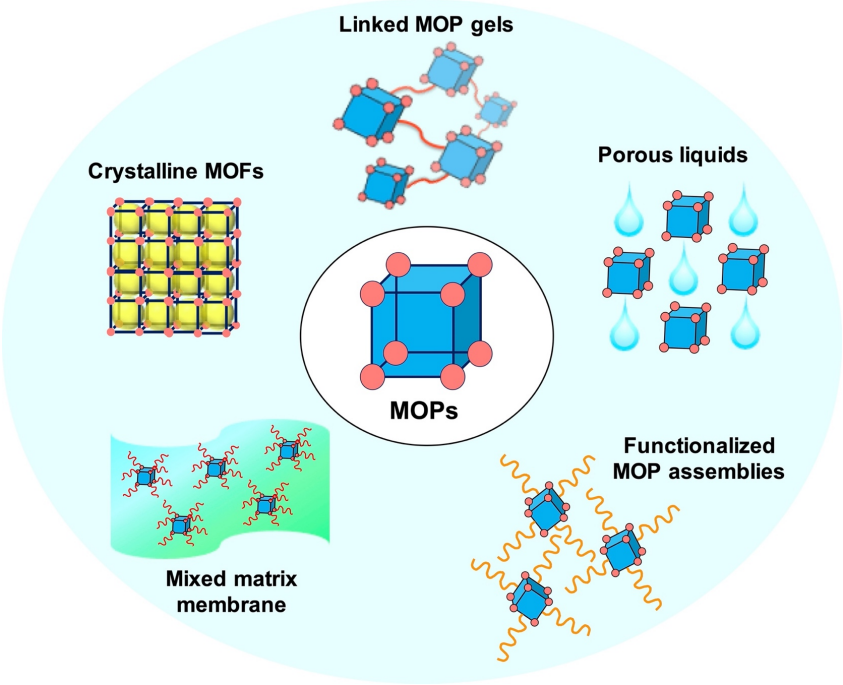

Figure 1. Porous materials based on metal-organic polyhedra (MOPs): Metal-organic frameworks (MOFs), linked MOP gels, porous liquids, functionalized MOP assemblies and mixed matrix membranes (MMMs).

2. Porous liquids

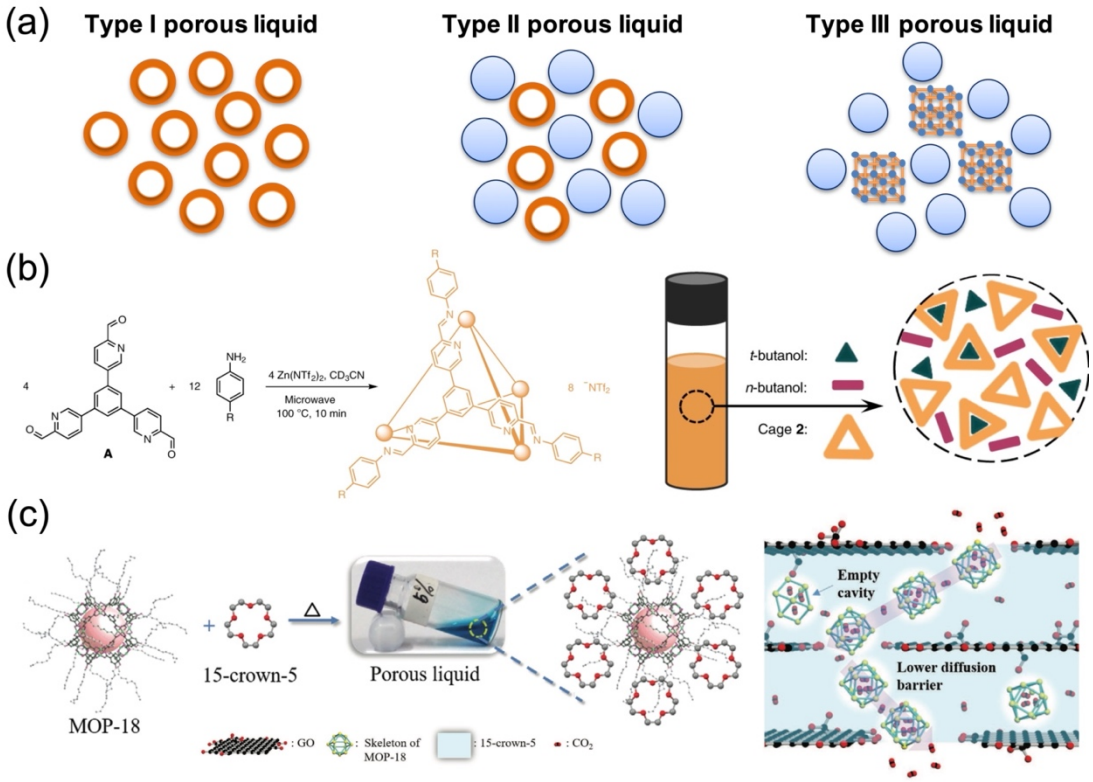

Figure 2. (a) Schematic illustration of the three types of porous liquids proposed by James.[19] (b) Preparation of type I porous liquid by the assembly of $Zn(NTf_2)_2$, a trialdehyde and a PEG-imidazolium-functionalized aniline and its selective encapsulation of *t*-butanol over *n*-butanol.[26] (c) Schematic showing the preparation process of type II porous liquid based on MOP-18 and its corresponding channels in which CO_2 molecules pass through the composite membranes with graphene oxide.[31]

Recent works have shown that persistent cavities can be engineered into liquids to endow the so-called porous liquids with intrinsic permanent porosity.[17] By combining the properties of liquids and porous solids, porous liquids may show promising applications in sorption systems requiring shape- and size-selective behavior, or flowing systems for loading and delivering gaseous guests.[18] Initially proposed by James and co-authors, three different types of porous liquids are recognized: (1) Type I porous liquids are neat molecular liquids containing internal cavities. (2) Type II are solutions of porous molecules dissolved in solvents that are bulkier enough to be sterically hindered from the pores. (3) Type III are suspensions of porous particles which are dispersed in the sterically hindered solvents (Figure 2a).[19] Among them, the type III porous liquids are more straightforward to prepare by dispersing MOF nanocrystals in the bulky solvents that is big enough to be precluded from the MOF pores.[20-21] However, to obtain a highly stable suspension without sediment, additional MOF modification or specialized

solvents are required to further control the MOF particle size or to improve the interactions between MOFs and solvents, which might be difficult and costly to achieve.[22] In contrast, the good solubility of MOPs allows for the formation of type II porous liquids without the issue of precipitation. Featuring a simple molecular identity, MOPs also provide a feasible way to change their physical state into liquid by surface functionalization, facilitating the formation of type I porous liquids. In this section, we present examples of strategies that have been developed for the fabrication of type I and type II porous liquids based on MOPs.

2.1. Type I porous liquids

Type I porous liquids are the most challenging to synthesize due to the requirement of forming pure liquid phases containing permanent and rigid cavities. One possible way is to lower the melting points or to disturb the crystallization of porous cage solids by functionalization with the flexible alkyl chains. An initial trial by James et al. in 2012 reported the external alkylation of a porous organic imine-based cage.[23] The melting point of the functionalized cage was shown to be significantly influenced by the molecular length and branch degree of the attached alkyl chains. Although the existence of long and flexible chains afforded the resulting cages with melting points as low as 40 ºC, the porosity of the liquid-like cage was sacrificed due to the self-filling or penetration of the alkyl chains.

To avoid the loss of cage cavities, another strategy was put forward by Sheng Dai et al. to use the concept of ion liquid, which normally refers to a low-melting salt consisting of a large asymmetric organic cation and an inorganic or organic anion.[18] By replacing the cationic or anionic part of an ionic liquid with the cavity-containing cage and a counterion that is too large to enter the cavity, a porous ionic liquid can be obtained. As the proof-of-statement, they demonstrated the successful fabrication of type I porous ionic liquid by combining an imine-based organic cage as the anionic part and 18-crown-6/potassium ion complex as the cationic part. The resulting cage-based liquid presented enhanced CO_2 sorption capacity compared to the pure 18-crown-6 liquid, indicating its permanent porosity at the liquid state. Based on a similar strategy, the same group reported the transformation of hollow silica nanospheres and carbon spheres into type I porous liquids by incorporating ionic interactions.[24-25]

Despite the wide use of porous organic cages, it is only until recently that MOPs were used to form type I porous liquids, where Nitschke and co-workers reported the first MOP-based liquid by incorporating poly(ethylene glycol) (PEG)-imidazolium chains into the periphery of a Zn_4L_4 tetrahedron (where L is the face-capping tris(pyridylimine) ligand that condenses from the trialdehyde and aniline subcomponents) (Figure 2b).[26] The presence of permanent cavities

in the resulting ionic liquid cages was demonstrated by several techniques, including NMR and positron annihilation lifetime spectroscopy (PALS). Except for the capability to sequester ozone-depleting and climate-warming chlorofluorocarbons (CFCs) including trichlorofluoromethane ($CFCl_3$), dichlorodifluoromethane (CF_2Cl_2) and chlorotrifluoromethane (CF_3Cl), this MOP-based porous liquid was able to bind non-gaseous large guest molecules like butanol and propanol isomers with size and shape selectivity. Different from previously reported examples, the incorporation of MOPs affords the porous liquid system with additional host-guest interaction, together with the extensive library of available MOPs demonstrating the potentials to impart the corresponding porous liquids with more interesting properties for further applications.

2.2. Type II porous liquids

Type II porous liquids avoid the difficulties in forming pure liquid phases by having the porous molecular cages dissolved in a solvent instead of focusing on their neat states. This means that the porous cage must have a very high solubility to provide a high concentration of pores and the selected sterically hindered solvent must be too bulky to fit inside the cage cavities.[27] One of the first and most important examples was reported by James, Cooper and co-workers based on the porous organic cages with tethered crown-ether functionality.[28] The appended crown-ether groups afforded the cages with high solubility in the corresponding 15-crown-5 solvent, which is too large to enter the pores of cages. Only 12 solvent molecules were needed to dissolve one cage, for the first time leading to the formation of a highly concentrated type II porous liquid containing 44 wt% cages at room temperature. Molecular computation and PALS were performed to confirm the presence of empty pores, which were found to contribute to an eightfold increase in the solubility of methane gas even at the liquid state. However, the cage was prepared by a difficult six-step synthesis and the resulting porous liquid was quite viscous due to the high cage concentration, making it hard to scale up for practical applications. Therefore, the same group developed an alternative strategy called " dynamic covalent scrambling" by using a mixture of diamines during the one-step cage synthesis to yield a mixture of so-called "scrambled cages", which exhibit higher solubility in common solvents than the individual cages prepared from a single diamine due to the increasing structural disorder.[29] A high-throughput screening was performed to search for the potential porous liquids by using these scrambled cages in different cavity-excluded solvents. As a result, 29 cage-solvent combinations were identified to possess both high cage-cavity concentrations and acceptable carrier solvents for potential practical use.

Compared to porous organic cages, MOPs might require additional concern on the chemical stability if they are applied in the fabrication of type II porous liquids. However, the ability to control the geometrical topology, window size, porosity as well as surface functionalization of MOPs has made them promising candidates to integrate with the solvent phase. Li and co-workers have reported the synthesis of rhombic dodecahedral nickel-imidazolate cages $Ni_{14}L_{14}$ with a precisely controlled aperture for CO_2 encapsulation either in solid or in solution state (L refers to the imidazole ligands with different substituents).[30] The encapsulation of CO_2 in the solution of MOPs was confirmed by ^{13}C NMR, infrared (IR) spectroscopy and electrospray ionization mass spectrometry (ESI-MS). The results showed that the ultrasmall aperture was required to realize the physical encapsulation of CO_2 into MOPs in the solution. Although the authors did not declare this system as the type II porous liquid, the use of an accessible MOP cavity for selective guest capture in the liquid phase was shown to be possible.

Another example reported by Peng et al. made use of the cuboctahedral cupper-based MOP (MOP-18; $[Cu_2(C_{12}\text{-bdc})_2]_{12}$ with C_{12}-bdc = 5-dodecoxybenzene-1,2-dicarboxylic acid).[31] Due to the existence of 24 alkyl chains on the MOP periphery, MOP-18 showed good solubility in various kinds of organic solvents and can be well-dissolved by 15-crown-5 solvent to form the type II porous liquid (Figure 2c). Both the molecular dynamics simulations and experimental gravimetric CO_2 solubility tests confirmed the preservation of inner MOP cavities, which were unoccupied by the bulkier 15-crown-5 molecules and were thus accessible to CO_2 molecules. Except for the enhanced gas capacity compared to the pure liquid of 15-crown-5, the resulting porous liquid was further infiltrated into graphene oxide (GO) nanoslits to form a GO-supported liquid membrane. Compared with the GO-supported 15-crown-5 sample, this porous liquid membrane showed increased permeability of gas (e.g., H_2, CO_2, and N_2) due to the existence of empty MOP cavities that reduced the gas diffusion barrier.

3. Porous gels

In definition, a gel is defined by IUPAC as a “non-fluid colloidal network or polymer network that is expanded throughout its whole volume by a fluid”.[32] Therefore, gels normally consist of a network of solid structures that trap or immobilize a large amount of solvents. This special feature makes gels very interesting because by weight and volume they are mostly liquid, yet they behave like a solid.[33] Positioned at the boundary between liquids and solids, gels have found uses in many fields, such as drug delivery, catalysis, sensing and optoelectronic devices.[34] Recently, efforts have been made to endow gels with predefined cavities for the purpose of

imbuing these soft materials with additional functionalities.[35] In particular, MOFs and MOPs have been used as inherent porous gelators to fabricate the porous soft materials by combining the gel processability/shapeability and the permanent porosity of these crystalline solids.[36-37] Such soft matter can be prepared from the self-assembly of these porous gelators either by themselves or through crosslinking with multitopic linkers, and the detailed examples are discussed in the following two sections (Figure 3).

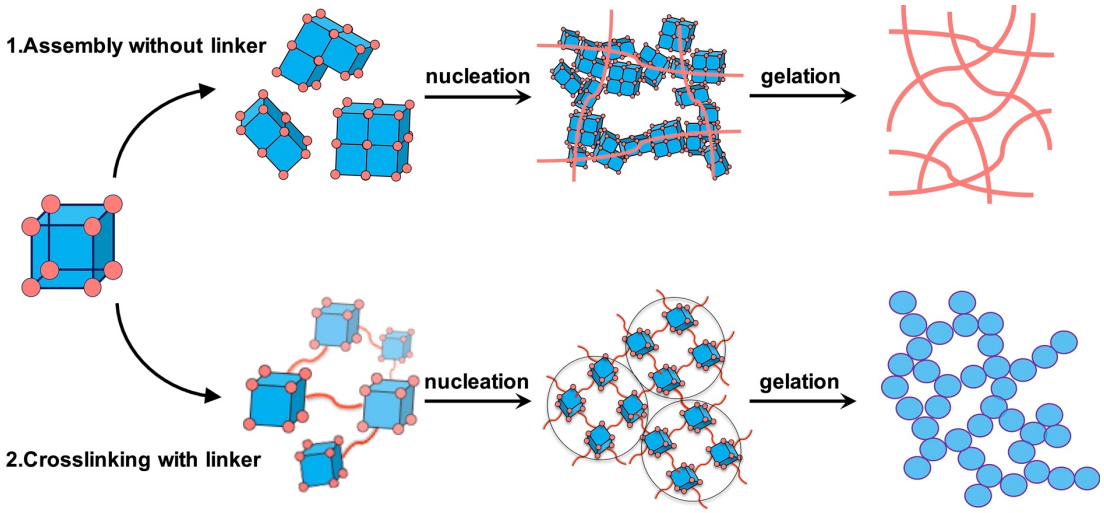

Figure 3. Schematic illustration of the two different approaches for the preparation of porous gels based on MOP or MOFs.

3.1. Gel from the assembly of MOPs without linkers

Gelation of MOF nanocrystals into processable and shapeable monoliths with hierarchical porous structures has attracted intensive interest despite being considered a nightmare for a long time to chemists during the synthesis of MOFs.[38] It was found that gelation can occur between the MOF nanoparticles when their size is small enough to ensure a stable colloidal sol or suspension prior to gelation. Different from the conventional hydrothermal conditions which favor the continuous crystal growth of MOFs towards sedimentation, it is the week non-covalent interactions between MOF nanocrystals that induce the gel formation. Therefore, the MOF gelation strongly relies on the control in both the nucleation and crystal growing process of MOFs.[9] A comprehensive review of the mechanism of MOF gelation has already been given by Bennett and coworkers, [9] therefore further insights will not be discussed here. So far, several examples of MOF gels or their corresponding monoliths have been reported based on ZIF-8,[39] HKUST-1,[40] MIL series[41] and zirconium-based MOFs[36] with particle sizes ranging from 10 nm to 80 nm. On the other hand, MOPs, which are considered as the smallest MOF with the size

of a few nanometers, offer unique advantages in forming porous gels due to their good solubility for solution processing and their larger available surface area than MOF crystals for further functionalization to achieve specific interactions in a more controllable way.

The first example of MOP gels was reported by Su and co-workers by using a discrete O-Pd_2L_4 MOP, which was synthesized by the coordination of palladium ion (Pd^{II}) with a photochromic dithienylethene bispyridine ligand (L = O-PyFDTE).[42] In the presence of suitable solvents like DMSO or MeCN/DMSO, the pre-formed cage molecules were found to aggregate into nanoparticles, which then were further interconnected through supramolecular interactions to yield a three-dimensional gel with reversible stimuli-responsive behaviors. Especially, exposure of such gel to external temperature, light and shear stress resulted in a reversible sol-gel transition, in which a reversible photochromic open-ring/close-ring isomeric conversion of the cages was accompanied upon UV/visible light irradiation. However, although the authors demonstrated the important role of solvents in the gelation of cages, its actual gelation mechanism remained still obscure. Chand and Ganta also reported the solvent-dependent gelation of a Pd-based MOP, $[Pd_2(L)_4](NO_3)_4$ with L refers to N, N′-bis(3-pyridylmethyl)-naphthalenediimide.[43] Except for the reversible sol-gel transformation upon mechanical or chemical stimuli, the corresponding porous gel exhibited the ability to uptake pyrene as a guest and to selectively remove anionic dyes from aqueous solutions. Supported by UV-visible spectroscopy and powder x-ray diffraction (PXRD), the authors inferred the gelation to be driven by intermolecular π-π stacking and hydrogen bonding of L from cages, despite other interactions between cage counterions and solvents were thought to be also responsible for the gel formation.

Specific interaction can be introduced into MOP cages by surface functionalization to assist MOP gelation in a more controlled way. For instance, Cao and co-workers reported the first example of hydrogel which was directly assembled from a copper-based MOP, $[Cu_2(NO_2\text{-}bdc)_2]_{12}$, by a facile ultrasonic procedure (NO_2-bdc = 5-nitroisophthalate).[44] Due to the presence of 24 nitro groups (-NO_2) on the cage surface, this MOP was calculated to have the largest binding energy with H_2O molecules compared with other copper-based MOPs substituted with -Br and -OH groups. Mediated by H_2O molecules as the bridging solvents, the strong hydrogen bonding between MOPs resulted in the formation of hydrogel, which exhibited excellent antibacterial activity towards Gram-negative and Gram-positive bacteria. In a similar strategy, Zhang et al. reported the synthesis of supramolecular MOP gels by the use of van der Waals forces.[45] A Fujita-type cage $Pd^{II}{}_{12}L_{24}$ was synthesized with its periphery attached with 24 cholesteryl groups, which were observed to stack through the cholesteryl-cholesteryl supramolecular interactions to induce cage aggregation and then gelation (L = cholesteryl-

functionalized 3,5-bis(4-pyridyl)benzene). The mechanical properties of the resulting MOP gels were tunable by varying the content of cholesteryl groups on $Pd^{II}_{12}L_{24}$, confirming that the gel was formed by van der Waals interactions between the cholesteryl moieties.

3.2. Gel from the crosslinking of MOPs with linkers

The existence of both the accessible metal sites and the modifiable functional groups on the periphery of MOPs allows them to be crosslinked either covalently or non-covalently with polymers or organic linkers to form polymer networks, which can be transformed into gel state by rational design of MOPs, linkers and the corresponding crosslinking conditions.[35] In general, the linked MOP gels can be synthesized via two basic approaches: (1) Construction of MOPs by the use of bitopic ligands, leading to the construction of crosslinked gel network once MOPs are formed. (2) Post-synthetic crosslinking of pre-formed MOPs with bitopic linkers to form gel network.

In terms of these two strategies, the former is rather simpler and offers a more direct way for gel formation. For instance, Nitschke et al. reported the formation of polymer-linked MOP gels or polyMOP gels by using a multitopic polymer ligand, which was synthesized through condensation of 2-formylpyridyl-end-capped polyethylene glycol (PEG) and 4,4′-diaminobiphenyl-2,2′-disulfonic acid.[46] A direct mixing of these two compounds with $FeSO_4$ under basic conditions yielded a hydrogel immediately after the construction of MOPs which were simultaneously crosslinked by the polymer ligands. Two different spaces were shown to be present in this crosslinked MOP gel with the mesoscopic pores of hydrogel and the inherent cavity of MOP itself, allowing for selected encapsulation and release of guest molecules. In a related effort, Johnson's group reported the synthesis of polyMOP gels with tunable branch functionality *f*, which reflects the average number of flexible polymer crosslinks bridged by MOP junctions.[47] Thermal annealing of a mixture of Pd^{2+} ions and PEG terminated with either para-bispyridyl ligands (L1) or meta-bispyridyl ligands (L2) resulted in two distinct gels through the in situ construction of two interlinked MOPs, $Pd_{12}(L1)_{24}$ and $Pd_2(L2)_4$. In particular, the resulting gels based on $Pd_{12}(L1)_{24}$ with higher *f* were observed to feature not only larger shear moduli, but also a large amount of elastically inactive loop defects that can be further exchanged with other functional ligands without impacting the mechanical properties of gels. Given the vast array of metal-ligand combinations that are known to provide discrete MOP assemblies, the authors demonstrated that the multi-component metal-ligand assembly could offer the controllable way to develop a range of new MOP gels with robust, dynamic and otherwise unprecedented properties.

In the post-synthetic crosslinking approach, the formation of individual MOPs and their subsequent linkage with bitopic linkers were separated into two steps, allowing for better control on both the crosslinking reaction (gelation) and the structures and properties of the resulting gels. As a typical example, Furukawa and co-workers reported the successful fabrication of supramolecular gels with hierarchical porous structures by coordinatively linking rhodium-based cuboctahedral MOPs, $[Rh_2(bdc)_2]_{12}$ (bdc = benzene-1,3-dicarboxylate), with the imidazole-derived bidentate linker, **bix** (1,4-bis(imidazole-1-ylmethyl)benzene).[48] The gelation mechanism of such system was systematically investigated by ^{1}H NMR, scanning electron microscope (SEM), dynamic light scattering (DLS) and UV-visible titration experiments, which revealed the first formation of colloidal nanoparticles followed by their interconnection into a colloidal gel network. Thanks to the use of short and rigid linker **bix**, the resulting MOP gels consist of multiscale porosities as molecular MOP cavities, mesoscale external pores between interlinked MOPs inside the colloids and macropores of the colloidal gel network, affording optimal molecular diffusion through the materials to demonstrate permanent porosity for gas sorption.[49] Furthermore, by attaching functional groups (hydrophobic alkyl chains or hydrophilic hydroxyl groups, for instance) either coordinatively or covalently onto the MOP surface, the same group successfully synthesized a series of Rh-based MOPs with different solubility and surface properties, allowing for the subsequent formation of both organo- and hydrogels with tunable properties for further applications.[50-51]

4. Porous films

Mixed matrix membranes (MMM) are composite membranes made by combining an inorganic or inorganic-organic hybrid in the form of micro- or nanoparticles as fillers and an organic polymer as the continuous matrix phase.[10] The integration between flexible polymers and the porous fillers (MOFs, COFs or MOPs) is concerned as an efficient way to address the processing issue of these crystalline solids while maintaining their well-defined porosities, demonstrating the promising potentials for applications in separation.[52] Compared to other porous candidates like MOFs and COFs, the good solubility of MOPs in various solvents offers a simpler way to integrate with polymer matrix without concerning the influence of crystal size, morphology on the membrane performances.[53] In general, MOP-based MMM can be prepared in two different strategies, either by direct dispersion of isolated MOPs into the polymers or through covalent attachment of MOPs onto the polymer chains as the part of matrix network. Recently, pure MOPs functionalized with polymer chains were reported to be able to self-assemble into processable composites, which is also included here for discussion (Figure 4).

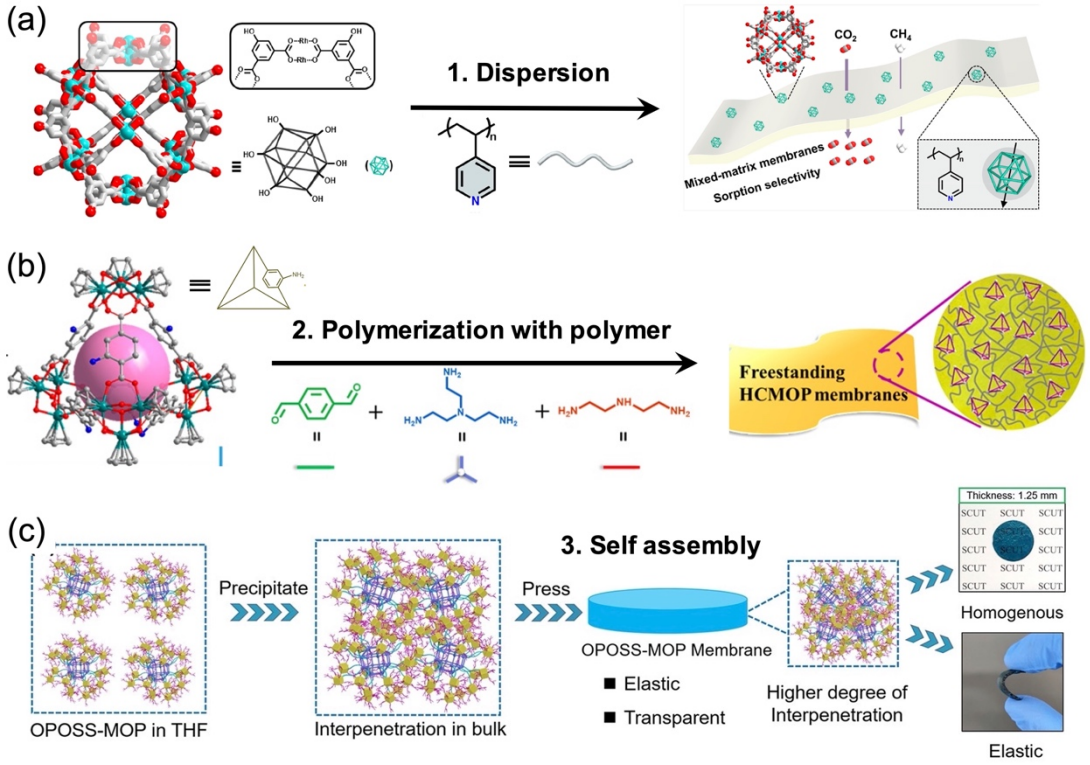

Figure 4. (a) Schematic showing the integration of cuboctahedral **OHRhMOP** with poly(4-vinylpyridine) into MMMs.[56] (b) The process to fabricate hyper-cross-linked membranes by introducing functionalized MOPs as porous comonomers.[57] (c) Schematic illustration of the higher degree of interpenetration between POSS-MOP to afford homogenous and elastic membranes under high pressures.[61]

4.1. MMM based on physically dispersing MOPs within the polymers

The simple mixing of MOPs with organic polymers to obtain MMM was shown efficient. In an early work using MOP-15 ($[Cu_{24}(NH_2\text{-bdc})_{24}]$; NH_2-bdc = 5-aminoisophthalate) as nanofillers in a polyimide 6FDA-DAM, Gascon and co-workers reported a large performance enhancement in gas separation even at a very low MOP loading (1.6 wt%).[54] They attributed this improvement to the molecular size of MOP-15 nanofillers (9 nm in diameter) that provides a much higher external surface to volume ratio than other fillers. Due to the good solubility of MOPs, these nano-sized cages can be encapsulated in between the polymer chains, making them possible to modify the packing structure of the polymer matrix and thus increase the gas permeability, selectivity and aging resistance while maintaining the processability of the polymer phase.

Except for the MOP solubility that matters in film fabrication, the interaction of them with polymers is also important, especially at the high MOP loading where the bad compatibility of MOPs with the polymer matrix often leads to severe aggregation and hide the effect of fillers.

To avoid this issue, modification of MOPs is required to incorporate functional groups that can interact well with the polymers. Kim et al. reported the preparation of CO_2-selective MMM by introducing different amounts of triethylene oxide-modified MOPs (EG_3-MOP) as CO_2-philic nanofillers in the matrix of poly(ethylene glycol)dimethacrylate (PEG_9DMA).[55] Due to the hydrophilic interactions between the triethylene oxide tails of EG_3-MOP and the PEG segments of PEG_9DMA, the nanocages can be homogeneously distributed throughout the polymer matrix with good compatibility at up to 5 wt% MOP loading. The resulting composite showed obvious improvement in the CO_2 permeance and CO_2/N_2 selectivity which was increased by 45% and 50% compared to the pristine PEG_9DMA films, respectively. In a similar effort, Yin and co-workers put forward a feasible approach to synthesize optical gas separation membranes through the combination of MOPs with poly(4-vinylpyridine) (P4VP) via strong supramolecular interactions (Figure 4a).[56] A rhodium-based cuboctahedral MOP $[Rh_2(OH\text{-}bdc)_2]_{12}$ (**OHRhMOP**) was synthesized with its periphery attached with 24 -OH groups, which can form both hydrogen and coordination bonding with the pendent pyridyl groups of P4VP. Such strong interaction not only guaranteed the homogeneous distribution of MOP within the polymer matrix with long-term structural stability, but also slowed down the polymer dynamics and frustrated the packing of rigid P4VP chains, contributing to the intrinsic microporosity of the nanocomposites and the simultaneous enhancement of selectivities.

4.2. MMM based on chemical crosslinking of MOPs with polymers

Chemically crosslinking MOPs with polymers via facile polymerization reactions is considered as a solution to fabricate defect-free membranes with uniform porosity. This approach avoids the potential issues of incompatibility and MOPs leaching, which were often observed in hybrid systems consisting of physically blended MOPs and polymers. Based on the concept of forming hyper-cross-linked MOPs, Zhang and co-workers reported the synthesis of a new class of hybrid membranes by involving MOPs in the polymerization of polymer networks.[57] As the proof-of-concept, they synthesized a zirconium-based cage (MOP-1) substituted with functional amino ($-NH_2$) groups, which can react with the aldehyde group to form the imine band. By adding MOP-1 into the precursor mixtures of terephthaldehyde, diethylene triamine and tris(2-aminoethyl)-amine, a multicomponent condensation was employed to generate a hyper-cross-linked network with diethylene triamine and tris(2-aminoethyl)-amine and MOP-1 serving as 2-, 3-, 6-connected nodes, respectively (Figure 4b). Controlled evaporation of solvents after polymerization gave a macro-scale, defect-free and freestanding membrane possessing multiple functionalities: strong water permeability, self-healing ability,

antimicrobial activity, better separation and mechanical performance than the pristine polyimine membranes.

Following a similar strategy, Zhao and co-workers made use of the same amino-appended MOP-1 as a chemically crosslinked filler in the fabrication of a polyamide selective layer for desalination applications.[58] To verify the possibility of MOPs for crosslinking, a model reaction was performed by reacting the nanocages with benzoyl chloride in hexane, which was confirmed by electrospray ionization time-of-flight mass spectrometry (ESI-TOF-MS) analyses. Further addition of MOPs into the precursor solutions of m-phenylenediamine and trimesoyl chloride prior to interfacial polymerization formed the MOP-linked MMM with enhanced water flux without compromising salt rejection. To expand the use of MOPs, the same groups post-synthetically modified MOP-1 by decorating the cage surface with acrylate groups. The existence of acrylate groups allowed for their following polymerization with poly(ethylene glycol) diacrylate (PEGDA) and poly(ethylene glycol) methyl ether acrylate (PEGMEA) to obtain the so-called "homoporous hybrid membranes" (HHMs) featuring chemically crosslinked MOPs.[59] Compared to the pristine polymeric membrane, these hybrid films displayed an enhanced CO_2 permeability and a comparable CO_2/CH_4 selectivity.

4.3. Pure MOPs functionalized by alkyl chains

Self-assemblies of alkyl-ligand functionalized MOPs were proved viable to form porous films without the addition of other polymers as the matrix. The requirements are: (1) Attachment of functional polymer ligands on the MOP surfaces. (2) The interactions between these substituent chains are strong enough to allow the packing of cages into self-standing materials as desired. As a typical example, Kitagawa and co-workers made use of the paraffinic side chains-substituted MOPs as porous modules, which can self-organize into a body-centered cubic (bcc) ordered structure in the presence of solvent molecules.[60] Moreover, the solution-processability of these MOPs facilitated the fabrication of free-standing films that could be handled with tweezers, offering a new design principle to shape porous materials into films.

Yin and coworkers reported a glassy supra-nanoparticle cluster (SNPC) by convergence of precise giant ligands (GLs) with traditional MOPs.[61] Attaching the groups of isophthalic acid to polyhedral oligomeric silsesquioxane (POSS) afforded the GLs, which were further coordinated with Cu^{2+} to generate the core-shell shaped SNPCs, where one MOP core is surrounded by 24 POSS (Figure 4c). By varying the terminal groups of GLs, the softness of the coronae of the clusters can be regulated to control the ability of SNPCs to intermix or entangle into bulk materials with different mechanical properties. In particular, an unexpected elasticity

was observed for the SNPC assemblies with a high modulus that can be maintained at temperatures far beyond the glass transition temperature. This elastomer can also be reprocessed via solution or pressure processing, which was attributed by authors to the comprehensive results of the inheritance of high mobility from the POSS and the so-facilitated physical interpenetration and inter-locking between the GLs.

5. Porous soft materials presenting directional asymmetry

The above sections have shown the successful fabrication of porous soft materials including porous liquids, gels and films. Despite the different physical states of these three materials, in most cases they can all be considered as hybrid systems consisting of two different components: one is the solvent or organic polymer as the main continuous phase, the other is MOFs/MOPs installed as porous fillers or networks. This means that both the solvent/polymer phase and the porous MOFs/MOPs structures will exert a significant influence on the properties of their corresponding materials, which might allow for the emergence of additional functional properties beyond the porosity and processability. For instance, directional asymmetry can be imparted into these porous soft materials by rational design of MOFs/MOPs structure or their spatial arrangement within the continuous phase.[62] Asymmetry, which is a fundamental concept in nature and science spanning from the molecular level to the cosmic scale, allows for the generation of complexity and new properties from a limited number of building blocks.[63] By combining the asymmetric configurations with porous soft materials, we demonstrate the possibility to create novel systems with functionalities that otherwise cannot be achieved by simple porous crystalline solids.

Considering the largely random thermal motion of the molecules making up the liquids, it is rather difficult for porous liquids to present overall asymmetry at the macroscale. However, creating asymmetry in its porous constituents, MOPs or MOFs, is a viable way to endow the porous liquids with new properties. For MOPs, asymmetry can be demonstrated from the perspective of cage architecture or pore configuration at the nanoscale, relying on mainly two strategies either via (i) the rational design of complementary ligands and metal complexes[64-66] or (ii) the replacement of one of the constituents (metal or ligand) in a preformed cage[67-69] (Figure 5a). For MOFs, on the other hand, asymmetry is more related to the mesoscale MOF crystals and can be achieved via the integration of a MOF crystal with other materials or another MOF with noticeably different properties.[70-72] In such a case, directional asymmetric systems are made through the control over the spatial distribution of MOFs relative to their counterparts (Figure 5b). For example, Maspoch et al. reported the formation of Janus MOF particles by the

partial coating of colloidal MOF particles with metal vapor.[73] With only partial MOF surface coated with metals, the resulting asymmetric MOF crystals not only maintained their porosity but also exhibited additional self-propulsion or self-shaping properties, which might be attractive if they can be inserted into the Type III porous liquids. Especially, the authors also showed that magnetic properties can be incorporated into the MOF crystals by partially coating with cobalt, generating the magnetically guidable porous particles that can be used to form porous liquid with good recyclability.

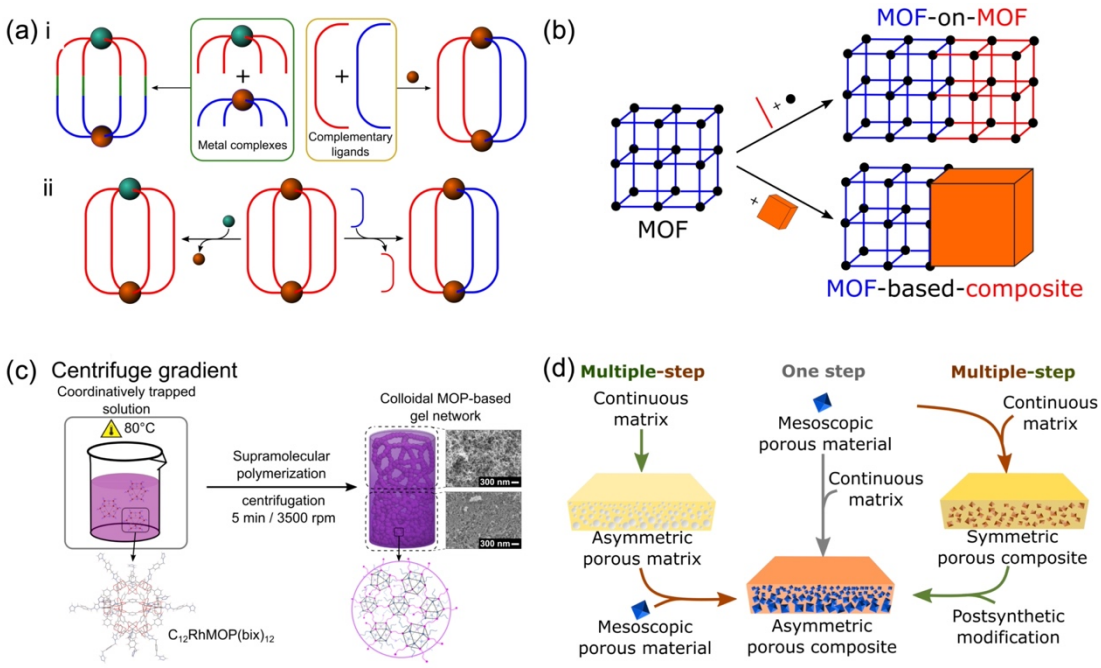

Figure 5. (a) Schematic representation of the different approaches to control the positioning of cage constituents in order to obtain directional asymmetry at the nanoscale.[62] (b) Schematic representation of the integration strategies leading to directional asymmetry at the mesoscale.[62] (c) Creation of a graded MOP gel network by applying centrifugal force at the specific moment of colloidal aggregation, yielding a less dense network of colloidal particles at the top compared to the gel formed at the bottom.[74] (d) Schematic representation showing the different strategies to obtain asymmetric porous composites at the macroscale.[62]

Different from the porous liquids in which MOPs/MOFs are isolated from each other, porous gels are formed by self-assembly of porous cages or MOF nanoparticles with the help of non-covalent or covalent interactions. This unique feature allows for the creation of gel networks with high heterogeneities and gradients by precise control of their hierarchical assembling process during gelation. As a typical example, Furukawa and co-workers reported the synthesis of macroscopic asymmetric MOP-based gels featuring gradients of stiffness and porosity across the whole gel structure (Figure 5c).[74] In this work, a rhodium-based MOP

$[Rh_2(C_{12}\text{-bdc})_2]_{12}$ was crosslinked with a ditopic linker, 1,4-bis(imidazole-1-ylmethyl) benzene (**bix**), by coordination-driven supramolecular polymerization (C_{12}-bdc = 5-dodecoxybenzene-1,3-dicarboxylate). Determined by time-resolved DLS, the gelation process of MOPs was found to involve several stages, including the initial formation of nuclei from the crosslinking of a few MOPs and their subsequent fusion to form colloidal particles, followed by the further interconnection of colloids to give a gel network. By applying centrifugal force at the point of colloidal aggregation, gradients of network density, porosity and mechanical stiffness were created within the resulting MOP gels, demonstrating the potential of MOPs as building blocks for constructing complex porous hierarchical architectures with higher order.

Porous films such as MMM offer a feasible way to create asymmetry by controlling the spatial location of MOPs/MOFs as porous fillers within their macroscopic polymer matrix. So far, several strategies have been developed to form asymmetric porous films, such as the phase inversion method,[75] co-casting of different MOF inks,[76] gravity-assisted solvent evaporation,[77] multiple layering of different MOF composites,[76] chemical post-modification[78] and so on. Depending on the steps required for processing, all these strategies can be divided into two categories: one-step methods, in which the appearance of asymmetry is concomitant with the formation of the macroscopic object, and multi-step methods, in which the porous asymmetric structures are prepared sequentially (Figure 5d). No matter which strategy, the target is to create a hierarchical distribution of the porous fillers or networks within the matrix, thus generating properties that cannot be achieved by homogenous MMM. For example, by using MIL-88A crystals, Maspoch et al. reported the fabrication of humidity responsive composite film actuators by forming a vertical gradient of MOF crystals across the membrane.[79] Later, the same group expanded this approach by patterning the MOF crystals using chemical etching with HCl.[78] This strategy allowed control of the location of MOF crystals in both the vertical and lateral directions, thus leading to novel actuations such as lifting cargo, mechanical gripping, and unidirectional walking.

6. Purpose of this thesis

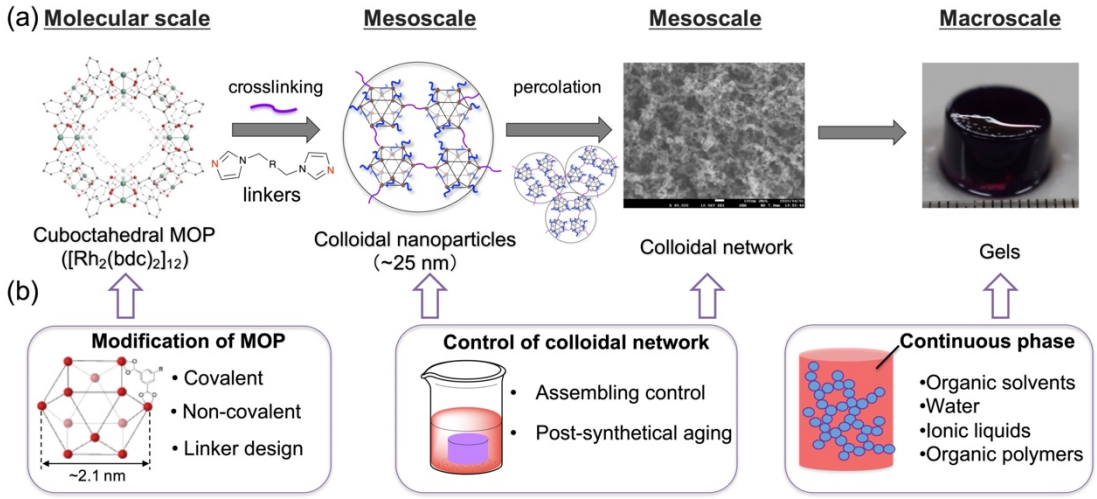

Figure 6. (a) Formation of the linked MOP gels with multiscale hierarchical porous structure by coordination-driven crosslinking of rhodium-based MOPs with bitopic imidazole-derived linkers. (b) Schematic showing the approaches which have been applied in this thesis to control the structures, properties and physical states of the linked MOP gels at different length scales.

As one of the promising porous soft materials, the porous gels stand out with attractive properties because of their ability to combine the advantages of both liquid and solid materials. By using MOPs as porous building blocks, various types of MOP gels have been formed with potential applications in molecular separation, drug delivery, catalysis, electronics, luminescence and so on.[34] However, so far most of the works are focusing on the preparation of MOP gels through the rational design of MOP cages and possible interactions for their subsequent gelation. The effective control of gel structures and properties during and after gelation still remains challenging. This can be attributed to the difficulty in characterizing the resulting gel structure at the amorphous state, limiting the development of these porous soft materials for further applications. Here, by considering the MOP gels as a hybrid system with solvent as the continuous phase and inner MOP networks as the secondary porous phase, the author attempts to put forward a new concept to further control the gel structures and properties from a comprehensive way, ranging from the porous MOP phase to the solvent phase over multiple length scales.

The whole studies are performed based on a linked MOP gel system featuring a colloidal gel network, which was formed by the coordination-driven crosslinking of a rhodium-based cuboctahedral MOP, $[Rh_2(R\text{-}bdc)_2]_{12}$ (RhMOP; R-bdc = benzene-1,3-dicarboxylate with the 5th position of its benzene rings substituted with functional groups), with imidazole-derived bitopic

linkers. The resulting linked MOP gel consists of a hierarchical porous structure over multiple length scales: molecular cavities of MOP cages, mesoscale external pores between interlinked MOPs inside the colloids and macropores of the colloidal gel networks (Figure 6a). Such hierarchical network not only affords optimal molecular diffusion throughout the material to demonstrate permanent porosities, but also allows us to control the gel structures and properties over different length scales.

As shown in Figure 6b, the author is firstly focusing on the structural control of the linked MOP networks through the post-synthetic aging process of gels (chapter 1), modification of MOP surface (chapter 2) and the use of different linkers (chapter 3), which leads to the formation of various linked MOP gels with controllable structures and properties. Then the author demonstrates how the change of continuous solvent phase can be applied to further improve gel properties especially on permanent porosity, mechanical properties and ionic conductivity (chapter 4). By replacing the solvent phase with an organic polymer matrix, the author further shows the successful transformation of the porous MOP gels into porous composite films consisting of hierarchically linked MOP networks (chapter 5). Equipped with all the above achievements to control both the continuous phase and hierarchical porous MOP structures within it, this thesis demonstrates the possibility to construct designable complex porous architectures with multiscale complexity and heterogeneity, offering the possibility to prepare a new generation of porous soft materials with novel properties.

To give more details, a short overview of each chapter was given as follows:

Survey of this thesis

Chapter 1 describes the post-synthetic structural control of the MOP gels by a simple aging process. Coordinatively assembled from organic linkers and cuboctahedral MOPs ($[Rh_2(bdc)_2]_{12}$ (**HRhMOP**; bdc = benzene-1,3-dicarboxylate)), the MOP gels are formed with their hierarchical network trapped at the initial sate with low controllability. Through heating the as-synthesized MOP gels in a fresh solvent, aging process is intentionally performed to direct the coordination equilibrium into a gel network with higher branch functionality, leading to a controllable transition of the whole structure over multiple length scales: (1) Molecular-scale rearrangement of the linked MOPs, which generates more-defined extrinsic microporosity. (2) Further connection of mesoscale colloidal particles, which results in a higher packing density. (3) Macroscale densification of the gel networks, which leads to shrinkage and increased stiffness.

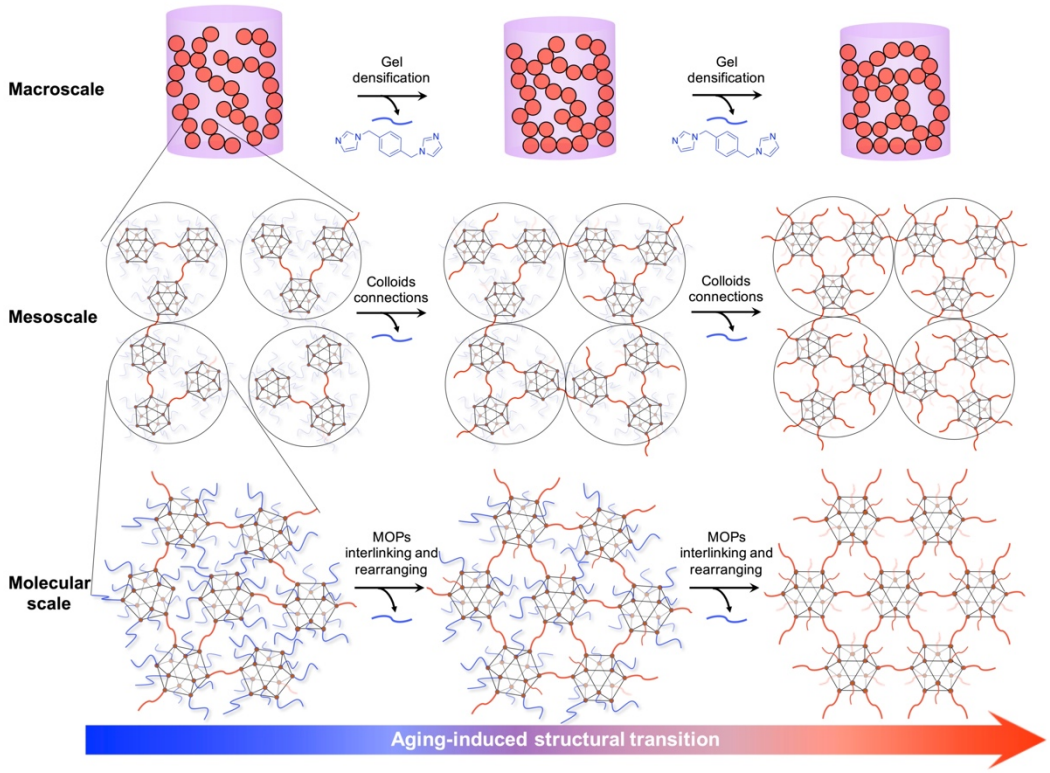

Figure 7. Schematic illustration of the influence of aging on the hierarchical structure of linked MOP gel at multiple length scales.

Chapter 2 describes the formation of porous colloidal hydrogels by using a hydrophilic MOP, $[Rh_2(OH\text{-}bdc)_2]_{12}$ (**OHRhMOP**; OH-bdc = 5-hydroxyl-1,3-benzenedicarboxylate). By deprotonating **OHRhMOP** with the base NaOH, the solubility of MOPs in aqueous solution is greatly increased, allowing for their subsequent supramolecular polymerization with the organic linker to obtain hydrogels with hierarchical networks. We demonstrate that the deprotonation degree, which corresponds to the fraction of deprotonated -OH groups per MOP, plays a key role in the gelation kinetics, mechanical properties and porosities of the resulting hydrogels, the partial decomposition of MOPs. By post-synthetically tuning the deprotonation degree of MOPs inside the hydrogels, a highly charged gel network can be achieved without serious decomposition of the MOPs.

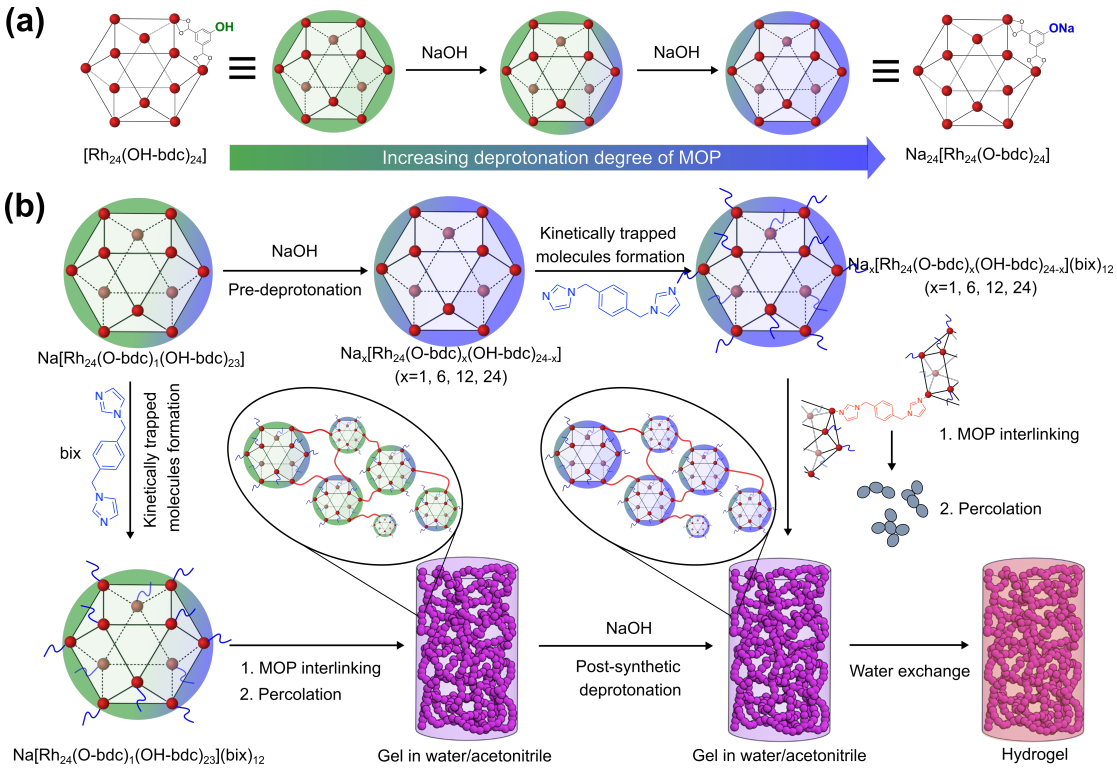

Figure 8. Schematic illustration of (a) MOP with different deprotonation degrees and (c) the two strategies to synthesize MOP-based hydrogel in the aqueous solution

Chapter 3 describes the formation of linked MOP gels with controllable extrinsic porosities by linking organic bidentate ligands with **OHRhMOP** at different deprotonation degrees. Based on chapter 2, deprotonation of **OHRhMOP** by NaOH generated anionic MOP cages with increasing electrostatic repulsion, which is found here to influence their gelation process by competing with the MOP linkage through coordination with bisimidazole linkers. By tuning the electrostatic repulsion between cages, a kinetically trapped state, in which each MOP is coordinated by linkers in a monodentate fashion, can be stabilized after mixing with various types of linkers at a controlled ratio. Further heating the kinetically trapped state leads to the formation of linked MOP gels with similar colloidal gel networks but with different connectivity at the MOP nodes. By N_2 sorption measurement and the pore size distribution analysis, we demonstrate the influence of linker type and ratio on the structure of extrinsic porosity between MOPs.

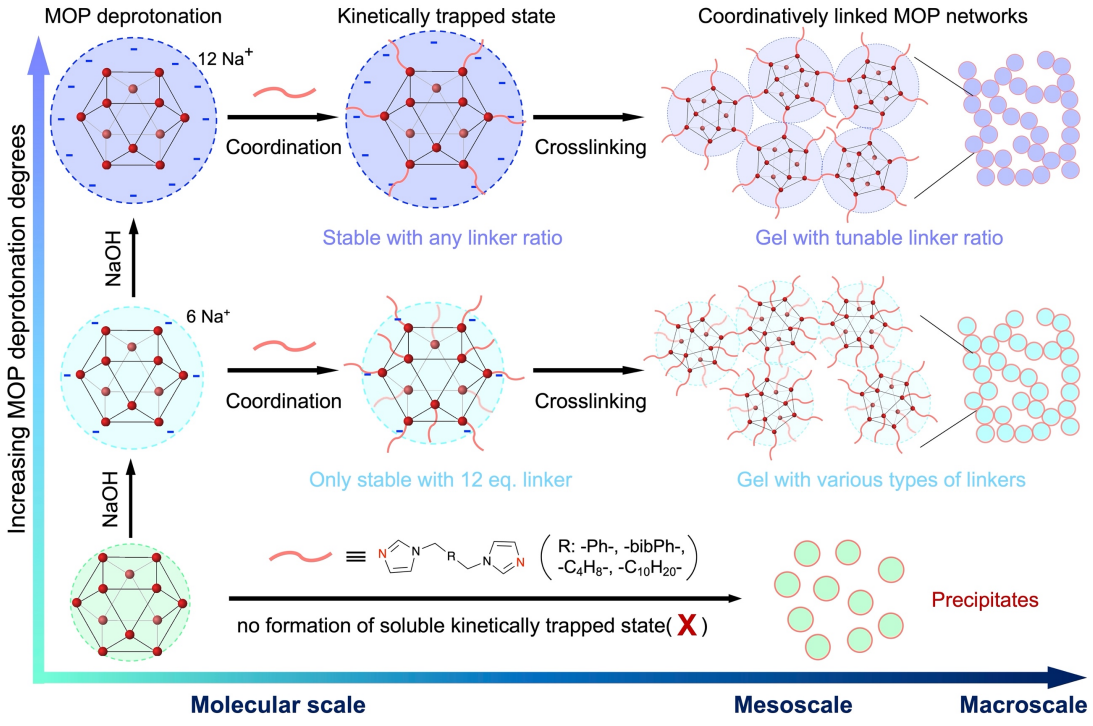

Figure 9. Schematic illustration of the controlled formation of linked MOP gels with tunable linkers types and raito by using MOPs at different deprotonation degrees.

Chapter 4 describes the fabrication of permanently porous MOP gels by simply exchanging the gel solvent with bulkier liquid molecules. Instead of drying the wet gels to obtain common aerogels for the sake of porosity, the as-synthesized MOP gels (**Gel_DMF**) with volatile solvents (DMF) are immersed into other mother liquids for liquid exchange. For proof of concept, Ionic liquid $[BMIM]^+[BF_4]^-$ with bulky molecular structure and zero volatility is selected for exchange to afford a gel (**Gel_IL**) with improved mechanical properties and thermal stability. Thanks to the bulky molecular size of ionic liquid that is too bigger to enter the pore of MOPs, the intrinsic porosity of **Gel_IL** can be maintained without losing the liquids within the gel. Various types of liquid molecules are also introduced into the gel matrix to confirm the versatility of the liquid exchange strategy. Except for the enhanced porosity for gas sorption, new functionalities can be imported into the gels by choosing suitable liquids, such as the high ionic conductivity of **Gel_IL**.

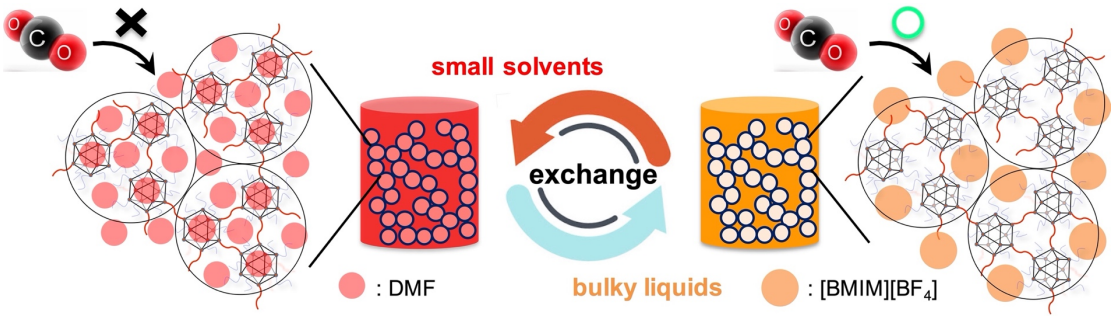

Figure 10. Schematic illustration of the preparation of porous MOP-based gel by liquid exchange.

Chapter 5 describes the fabrication of so-called hierarchical hybrid membranes (HHM) featuring polymers as matrix and hierarchical porous MOP networks as the secondary continuous phase. Instead of gelation in pure solvents to obtain MOP gels, the supramolecular polymerization of MOPs with organic linkers is in situ induced within the solution of polyurethane (PU), allowing for the formation of porous hierarchical MOP networks within PU as the polymer matrix. Unlike the mixed matrix membranes (MMM) in which nanofillers tend to aggregate during synthesis, in situ construction of MOP networks allows these porous cages to be fixed inside the polymer matrix without requiring dispersibility. In addition, the connection of the porous MOPs ensures the molecular diffusion throughout the material, affording the resulting HHM with enhanced gas selectivity and permeability.

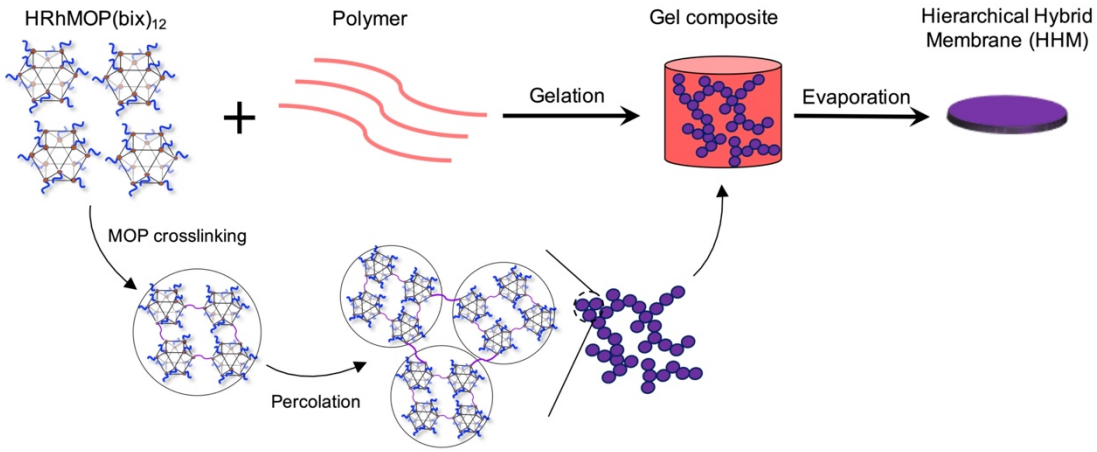

Figure 11. Schematic illustration of the formation of HHM consisting of hierarchical porous MOP networks by sol-gel process.

Reference

1. Slater, A. G.; Cooper, A. I., Function-led design of new porous materials. *Science* **2015,** *348* (6238), aaa8075.

2. Stock, N.; Biswas, S., Synthesis of Metal-Organic Frameworks (MOFs): Routes to Various MOF Topologies, Morphologies, and Composites. *Chem. Rev.* **2012,** *112* (2), 933-969.

3. Robson, R., A net-based approach to coordination polymers. *J. Chem. Soc., Dalton Trans.* **2000,** (21), 3735-3744.

4. Furukawa, H.; Cordova, K. E.; O'Keeffe, M.; Yaghi, O. M., The Chemistry and Applications of Metal-Organic Frameworks. *Science* **2013,** *341* (6149), 1230444.

5. Kalaj, M.; Cohen, S. M., Postsynthetic Modification: An Enabling Technology for the Advancement of Metal-Organic Frameworks. *ACS Cent. Sci.* **2020,** *6* (7), 1046-1057.

6. Hosono, N.; Kitagawa, S., Modular Design of Porous Soft Materials via Self-Organization of Metal-Organic Cages. *Acc. Chem. Res.* **2018,** *51* (10), 2437-2446.

7. Furukawa, S.; Reboul, J.; Diring, S.; Sumida, K.; Kitagawa, S., Structuring of metal-organic frameworks at the mesoscopic/macroscopic scale. *Chem. Soc. Rev.* **2014,** *43* (16), 5700-5734.

8. Horike, S.; Nagarkar, S. S.; Ogawa, T.; Kitagawa, S., A New Dimension for Coordination Polymers and Metal-Organic Frameworks: Towards Functional Glasses and Liquids. *Angew. Chem. Int. Ed.* **2020,** *59* (17), 6652-6664.

9. Hou, J.; Sapnik, A. F.; Bennett, T. D., Metal-organic framework gels and monoliths. *Chem. Sci.* **2020,** *11* (2), 310-323.

10. Dechnik, J.; Gascon, J.; Doonan, C. J.; Janiak, C.; Sumby, C. J., Mixed-Matrix Membranes. *Angew. Chem. Int. Ed.* **2017,** *56* (32), 9292-9310.

11. Gosselin, A. J.; Rowland, C. A.; Bloch, E. D., Permanently Microporous Metal-Organic Polyhedra. *Chem. Rev.* **2020,** *120* (16), 8987-9014.

12. Tranchemontagne, D. J.; Ni, Z.; O'Keeffe, M.; Yaghi, O. M., Reticular Chemistry of Metal-Organic Polyhedra. *Angew. Chem. Int. Ed.* **2008,** *47* (28), 5136-5147.

13. El-Sayed, E.-S. M.; Yuan, D., Metal-Organic Cages (MOCs): From Discrete to Cage-based Extended Architectures. *Chem. Lett.* **2020,** *49* (1), 28-53.

14. Li, B.; He, T.; Fan, Y.; Yuan, X.; Qiu, H.; Yin, S., Recent developments in the construction of metallacycle/metallacage-cored supramolecular polymers via hierarchical self-assembly. *Chem. Commun.* **2019,** *55* (56), 8036-8059.

15. Gong, Y.; Zhang, Y.; Qin, C.; Sun, C.; Wang, X.; Su, Z., Bottom-Up Construction and Reversible Structural Transformation of Supramolecular Isomers based on Large Truncated Tetrahedra. *Angew. Chem. Int. Ed.* **2019,** *58* (3), 780-784.

16. Zhu, W.; Guo, J.; Ju, Y.; Serda, R. E.; Croissant, J. G.; Shang, J.; Coker, E.; Agola, J. O.; Zhong, Q.-Z.; Ping, Y.; Caruso, F.; Brinker, C. J., Modular Metal-Organic Polyhedra Superassembly: From Molecular-Level Design to Targeted Drug Delivery. *Adv. Mater.* **2019,** *31* (12), 1806774.

17. Jie, K.; Zhou, Y.; Ryan, H. P.; Dai, S.; Nitschke, J. R., Engineering Permanent Porosity into Liquids. *Adv. Mater.* **2021,** *33* (18), 2005745.

18. Jie, K.; Onishi, N.; Schott, J. A.; Popovs, I.; Jiang, D.-e.; Mahurin, S.; Dai, S., Transforming Porous Organic Cages into Porous Ionic Liquids via a Supramolecular Complexation Strategy. *Angew. Chem. Int. Ed.* **2020,** *59* (6), 2268-2272.

19. O'Reilly, N.; Giri, N.; James, S. L., Porous Liquids. *Chem. Eur. J.* **2007,** *13* (11), 3020-3025.

20. Cahir, J.; Tsang, M. Y.; Lai, B.; Hughes, D.; Alam, M. A.; Jacquemin, J.; Rooney, D.; James, S. L., Type 3 porous liquids based on non-ionic liquid phases - a broad and tailorable platform of selective, fluid gas sorbents. *Chem. Sci.* **2020,** *11* (8), 2077-2084.

21. Knebel, A.; Bavykina, A.; Datta, S. J.; Sundermann, L.; Garzon-Tovar, L.; Lebedev, Y.; Durini, S.; Ahmad, R.; Kozlov, S. M.; Shterk, G.; Karunakaran, M.; Carja, I. D.; Simic, D.; Weilert, I.; Klüppel, M.; Giese, U.; Cavallo, L.; Rueping, M.; Eddaoudi, M.; Caro, J.; Gascon, J., Solution processable metal-organic frameworks for mixed matrix membranes using porous liquids. *Nat. Mater.* **2020,** *19* (12), 1346-1353.

22. He, S.; Chen, L.; Cui, J.; Yuan, B.; Wang, H.; Wang, F.; Yu, Y.; Lee, Y.; Li, T., General Way to Construct Micro- and Mesoporous Metal-Organic Framework-Based Porous Liquids. *J. Am. Chem. Soc.* **2019,** *141* (50), 19708-19714.

23. Giri, N.; Davidson, C. E.; Melaugh, G.; Del Pópolo, M. G.; Jones, J. T. A.; Hasell, T.; Cooper, A. I.; Horton, P. N.; Hursthouse, M. B.; James, S. L., Alkylated organic cages: from porous crystals to neat liquids. *Chem. Sci.* **2012,** *3* (6), 2153-2157.

24. Zhang, J.; Chai, S.-H.; Qiao, Z.-A.; Mahurin, S. M.; Chen, J.; Fang, Y.; Wan, S.; Nelson, K.; Zhang, P.; Dai, S., Porous Liquids: A Promising Class of Media for Gas Separation. *Angew. Chem. Int. Ed.* **2015,** *54* (3), 932-936.

25. Li, P.; Schott, J. A.; Zhang, J.; Mahurin, S. M.; Sheng, Y.; Qiao, Z.-A.; Hu, X.; Cui, G.; Yao, D.; Brown, S.; Zheng, Y.; Dai, S., Electrostatic-Assisted Liquefaction of Porous Carbons. *Angew. Chem. Int. Ed.* **2017,** *56* (47), 14958-14962.

26. Ma, L.; Haynes, C. J. E.; Grommet, A. B.; Walczak, A.; Parkins, C. C.; Doherty, C. M.; Longley, L.; Tron, A.; Stefankiewicz, A. R.; Bennett, T. D.; Nitschke, J. R., Coordination cages as permanently porous ionic liquids. *Nat. Chem.* **2020,** *12* (3), 270-275.

27. Bennett, T. D.; Coudert, F.-X.; James, S. L.; Cooper, A. I., The changing state of porous materials. *Nat. Mater.* **2021,** *20* (9), 1179-1187.

28. Giri, N.; Del Pópolo, M. G.; Melaugh, G.; Greenaway, R. L.; Rätzke, K.; Koschine, T.; Pison, L.; Gomes, M. F. C.; Cooper, A. I.; James, S. L., Liquids with permanent porosity. *Nature* **2015,** *527* (7577), 216-220.

29. Kearsey, R. J.; Alston, Ben M.; Briggs, M. E.; Greenaway, R. L.; Cooper, A. I., Accelerated robotic discovery of type II porous liquids. *Chem. Sci.* **2019,** *10* (41), 9454-9465.

30. Zhang, X.; Dong, X.; Lu, W.; Luo, D.; Zhu, X.-W.; Li, X.; Zhou, X.-P.; Li, D., Fine-Tuning Apertures of Metal-Organic Cages: Encapsulation of Carbon Dioxide in Solution and Solid State. *J. Am. Chem. Soc.* **2019,** *141* (29), 11621-11627.

31. Deng, Z.; Ying, W.; Gong, K.; Zeng, Y.-J.; Yan, Y.; Peng, X., Facilitate Gas Transport through Metal-Organic Polyhedra Constructed Porous Liquid Membrane. *Small* **2020,** *16* (11), 1907016.

32. Nič, M.; Jirát, J.; Košata, B.; Jenkins, A.; McNaught, A., IUPAC compendium of chemical terminology. *IUPAC, Research Triagle Park, NC* **2009**.

33. Lloyd, G. O.; Steed, J. W., Anion-tuning of supramolecular gel properties. *Nat. Chem.* **2009,** *1* (6), 437-442.

34. Sangeetha, N. M.; Maitra, U., Supramolecular gels: Functions and uses. *Chem. Soc. Rev.* **2005,** *34* (10), 821-836.

35. Jahović, I.; Zou, Y.-Q.; Adorinni, S.; Nitschke, J. R.; Marchesan, S., Cages meet gels: Smart materials with dual porosity. *Matter* **2021,** *4* (7), 2123-2140.

36. Bueken, B.; Van Velthoven, N.; Willhammar, T.; Stassin, T.; Stassen, I.; Keen, D. A.; Baron, G. V.; Denayer, J. F. M.; Ameloot, R.; Bals, S.; De Vos, D.; Bennett, T. D., Gel-based morphological design of zirconium metal-organic frameworks. *Chem. Sci.* **2017,** *8* (5), 3939-3948.

37. Sutar, P.; Maji, T. K., Recent advances in coordination-driven polymeric gel materials: design and applications. *Dalton Trans.* **2020,** *49* (23), 7658-7672.

38. Tian, T.; Zeng, Z.; Vulpe, D.; Casco, M. E.; Divitini, G.; Midgley, P. A.; Silvestre-Albero, J.; Tan, J.-C.; Moghadam, P. Z.; Fairen-Jimenez, D., A sol-gel monolithic metal-organic framework with enhanced methane uptake. *Nat. Mater.* **2018,** *17* (2), 174-179.

39. Tian, T.; Velazquez-Garcia, J.; Bennett, T. D.; Fairen-Jimenez, D., Mechanically and chemically robust ZIF-8 monoliths with high volumetric adsorption capacity. *J. Mater. Chem. A* **2015,** *3* (6), 2999-3005.

40. Chaudhari, A. K.; Han, I.; Tan, J.-C., Multifunctional Supramolecular Hybrid Materials Constructed from Hierarchical Self-Ordering of In Situ Generated Metal-Organic Framework (MOF) Nanoparticles. *Adv. Mater.* **2015,** *27* (30), 4438-4446.

41. Li, L.; Xiang, S.; Cao, S.; Zhang, J.; Ouyang, G.; Chen, L.; Su, C.-Y., A synthetic route to ultralight hierarchically micro/mesoporous Al(III)-carboxylate metal-organic aerogels. *Nat. Commun.* **2013,** *4* (1), 1774.

42. Wei, S.-C.; Pan, M.; Fan, Y.-Z.; Liu, H.; Zhang, J.; Su, C.-Y., Creating Coordination-Based Cavities in a Multiresponsive Supramolecular Gel. *Chem. Eur. J.* **2015,** *21* (20), 7418-7427.

43. Ganta, S.; Chand, D. K., Multi-Stimuli-Responsive Metallogel Molded from a Pd2L4-Type Coordination Cage: Selective Removal of Anionic Dyes. *Inorg. Chem.* **2018,** *57* (7), 3634-3645.

44. Qin, Y.; Chen, L.-L.; Pu, W.; Liu, P.; Liu, S.-X.; Li, Y.; Liu, X.-L.; Lu, Z.-X.; Zheng, L.-Y.; Cao, Q.-E., A hydrogel directly assembled from a copper metal-organic polyhedron for antimicrobial application. *Chem. Commun.* **2019,** *55* (15), 2206-2209.

45. Zeng, L.; Xiao, Y.; Jiang, J.; Fang, H.; Ke, Z.; Chen, L.; Zhang, J., Hierarchical Gelation of a Pd12L24 Metal-Organic Cage Regulated by Cholesteryl Groups. *Inorg. Chem.* **2019,** *58* (15), 10019-10027.

46. Foster, J. A.; Parker, R. M.; Belenguer, A. M.; Kishi, N.; Sutton, S.; Abell, C.; Nitschke, J. R., Differentially Addressable Cavities within Metal-Organic Cage-Cross-Linked Polymeric Hydrogels. *J. Am. Chem. Soc.* **2015,** *137* (30), 9722-9729.

47. Zhukhovitskiy, A. V.; Zhong, M.; Keeler, E. G.; Michaelis, V. K.; Sun, J. E. P.; Hore, M. J. A.; Pochan, D. J.; Griffin, R. G.; Willard, A. P.; Johnson, J. A., Highly branched and loop-rich gels via formation of metal-organic cages linked by polymers. *Nat. Chem.* **2016,** *8* (1), 33-41.

48. Carné-Sánchez, A.; Craig, G. A.; Larpent, P.; Guillerm, V.; Urayama, K.; Maspoch, D.; Furukawa, S., A Coordinative Solubilizer Method to Fabricate Soft Porous Materials from Insoluble Metal-Organic Polyhedra. *Angew. Chem. Int. Ed.* **2019,** *58* (19), 6347-6350.

49. Wang, Z.; Villa Santos, C.; Legrand, A.; Haase, F.; Hara, Y.; Kanamori, K.; Aoyama, T.; Urayama, K.; Doherty, C. M.; Smales, G. J.; Pauw, B. R.; Colón, Y. J.; Furukawa, S., Multiscale structural control of linked metal-organic polyhedra gel by aging-induced linkage-reorganization. *Chem. Sci.* **2021,** *12* (38), 12556-12563.

50. Carné-Sánchez, A.; Craig, G. A.; Larpent, P.; Hirose, T.; Higuchi, M.; Kitagawa, S.; Matsuda, K.; Urayama, K.; Furukawa, S., Self-assembly of metal-organic polyhedra into supramolecular polymers with intrinsic microporosity. *Nat. Commun.* **2018,** *9* (1), 2506.

51. Wang, Z.; Craig, G. A.; Legrand, A.; Haase, F.; Minami, S.; Urayama, K.; Furukawa, S., Porous Colloidal Hydrogels Formed by Coordination-Driven Self-Assembly of Charged Metal-Organic Polyhedra. *Chem. Asian J.***2021,** *16* (9), 1092-1100.

52. Pastore, V. J.; Cook, T. R., Coordination-Driven Self-Assembly in Polymer–Inorganic Hybrid Materials. *Chem. Mater.* **2020,** *32* (9), 3680-3700.

53. Jin, F.; Liu, J.; Chen, Y.; Zhang, Z., Tethering Flexible Polymers to Crystalline Porous Materials: A Win-Win Hybridization Approach. *Angew. Chem. Int. Ed.* **2021,** *60* (26), 14222-14235.

54. Liu, X.; Wang, X.; Bavykina, A. V.; Chu, L.; Shan, M.; Sabetghadam, A.; Miro, H.; Kapteijn, F.; Gascon, J., Molecular-Scale Hybrid Membranes Derived from Metal-Organic Polyhedra for Gas Separation. *ACS Appl. Mater. Interfaces* **2018,** *10* (25), 21381-21389.

55. Sohail, M.; An, H.; Choi, W.; Singh, J.; Yim, K.; Kim, B.-H.; Park, Y. C.; Lee, J. S.; Kim, H., Sorption-enhanced thin film composites with metal-organic polyhedral nanocages for CO_2 separation. *J. Membr. Sci.* **2021,** *620*, 118826.

56. Liu, Y.; Cai, L.; Ma, L.; Li, M.; Yang, J.; Chen, K.; Yin, P., Modulating Polymer Dynamics via Supramolecular Interaction with Ultrasmall Nanocages for Recyclable Gas Separation Membranes with Intrinsic Microporosity. *Nano Lett.* **2021,** *21* (21), 9021-9029.

57. Liu, J.; Duan, W.; Song, J.; Guo, X.; Wang, Z.; Shi, X.; Liang, J.; Wang, J.; Cheng, P.; Chen, Y.; Zaworotko, M. J.; Zhang, Z., Self-Healing Hyper-Cross-Linked Metal-Organic Polyhedra (HCMOPs) Membranes with Antimicrobial Activity and Highly Selective Separation Properties. *J. Am. Chem. Soc.* **2019,** *141* (30), 12064-12070.

58. Liu, G.; Zhang, X.; Di Yuan, Y.; Yuan, H.; Li, N.; Ying, Y.; Peh, S. B.; Wang, Y.; Cheng, Y.; Cai, Y.; Gu, Z.; Cai, H.; Zhao, D., Thin-Film Nanocomposite Membranes Containing Water-Stable Zirconium Metal-Organic Cages for Desalination. *ACS Mater. Lett.* **2021,** *3* (3), 268-274.

59. Yang, Z.; Liu, G.; Yuan, Y. D.; Peh, S. B.; Ying, Y.; Fan, W.; Yu, X.; Yang, H.; Wu, Z.; Zhao, D., Homoporous hybrid membranes containing metal-organic cages for gas separation. *J. Membr. Sci.* **2021,** *636*, 119564.

60. Omoto, K.; Hosono, N.; Gochomori, M.; Kitagawa, S., Paraffinic metal-organic polyhedrons: solution-processable porous modules exhibiting three-dimensional molecular order. *Chem. Commun.* **2018,** *54* (53), 7290-7293.

61. Yin, J.-F.; Zheng, Z.; Yang, J.; Liu, Y.; Cai, L.; Guo, Q.-Y.; Li, M.; Li, X.; Sun, T. L.; Liu, G. X.; Huang, C.; Cheng, S. Z. D.; Russell, T. P.; Yin, P., Unexpected Elasticity in Assemblies of Glassy Supra-Nanoparticle Clusters. *Angew. Chem. Int. Ed.* **2021,** *60* (9), 4894-4900.

62. Legrand, A.; Wang, Z.; Troyano, J.; Furukawa, S., Directional asymmetry over multiple length scales in reticular porous materials. *Chem. Sci.* **2021,** *12* (1), 18-33.

63. Palmer, A. R., From symmetry to asymmetry: Phylogenetic patterns of asymmetry variation in animals and their evolutionary significance. *Proc. Natl. Acad. Sci.* **1996,** *93* (25), 14279.

64. Johnson, A. M.; Hooley, R. J., Steric Effects Control Self-Sorting in Self-Assembled Clusters. *Inorg. Chem.* **2011,** *50* (11), 4671-4673.

65. Li, H.; Yao, Z.-J.; Liu, D.; Jin, G.-X., Multi-component coordination-driven self-assembly toward heterometallic macrocycles and cages. *Coord. Chem. Rev.* **2015,** *293-294*, 139-157.

66. Lisboa, L. S.; Findlay, J. A.; Wright, L. J.; Hartinger, C. G.; Crowley, J. D., A Reduced-Symmetry Heterobimetallic $[PdPtL_4]^{4+}$ Cage: Assembly, Guest Binding, and Stimulus-Induced Switching. *Angew. Chem. Int. Edi.* **2020,** *59* (27), 11101-11107.

67. Yamashina, M.; Yuki, T.; Sei, Y.; Akita, M.; Yoshizawa, M., Anisotropic Expansion of an M2L4 Coordination Capsule: Host Capability and Frame Rearrangement. *Chem. Eur. J.* **2015,** *21* (11), 4200-4204.

68. Preston, D.; Barnsley, J. E.; Gordon, K. C.; Crowley, J. D., Controlled Formation of Heteroleptic $[Pd_2(La)_2(Lb)_2]^{4+}$ Cages. *J. Am. Chem. Soc.* **2016,** *138* (33), 10578-10585.

69. Bloch, W. M.; Abe, Y.; Holstein, J. J.; Wandtke, C. M.; Dittrich, B.; Clever, G. H., Geometric Complementarity in Assembly and Guest Recognition of a Bent Heteroleptic cis-[Pd2LA2LB2] Coordination Cage. *J. Am. Chem. Soc.* **2016,** *138* (41), 13750-13755.

70. Furukawa, S.; Hirai, K.; Takashima, Y.; Nakagawa, K.; Kondo, M.; Tsuruoka, T.; Sakata, O.; Kitagawa, S., A block PCP crystal: anisotropic hybridization of porous coordination polymers by face-selective epitaxial growth. *Chem. Commun.* **2009,** (34), 5097-5099.

71. Tan, T. T. Y.; Cham, J. T. M.; Reithofer, M. R.; Andy Hor, T. S.; Chin, J. M., Motorized Janus metal-organic framework crystals. *Chem Commun.* **2014,** *50* (96), 15175-15178.

72. Feng, L.; Yuan, S.; Li, J.-L.; Wang, K.-Y.; Day, G. S.; Zhang, P.; Wang, Y.; Zhou, H.-C., Uncovering Two Principles of Multivariate Hierarchical Metal-Organic Framework Synthesis via Retrosynthetic Design. *ACS Cent. Sci.* **2018,** *4* (12), 1719-1726.

73. Ayala, A.; Carbonell, C.; Imaz, I.; Maspoch, D., Introducing asymmetric functionality into MOFs via the generation of metallic Janus MOF particles. *Chem. Commun.* **2016,** *52* (29), 5096-5099.

74. Legrand, A.; Craig, G. A.; Bonneau, M.; Minami, S.; Urayama, K.; Furukawa, S., Understanding the multiscale self-assembly of metal-organic polyhedra towards functionally graded porous gels. *Chem. Sci.* **2019,** *10* (47), 10833-10842.

75. Yang, H.; Wu, H.; Yao, Z.; Shi, B.; Xu, Z.; Cheng, X.; Pan, F.; Liu, G.; Jiang, Z.; Cao, X., Functionally graded membranes from nanoporous covalent organic frameworks for highly selective water permeation. *J. Mater. Chem. A* **2018,** *6* (2), 583-591.

76. Denny, M. S.; Kalaj, M.; Bentz, K. C.; Cohen, S. M., Multicomponent metal-organic framework membranes for advanced functional composites. *Chem. Sci.* **2018,** *9* (47), 8842-8849.

77. Peng, S.; Zhang, L.; Zhang, C.; Ding, Y.; Guo, X.; He, G.; Yu, G., Gradient-Distributed Metal-Organic Framework-Based Porous Membranes for Nonaqueous Redox Flow Batteries. *Adv. Energy Mater.* **2018,** *8* (33), 1802533.

78. Troyano, J.; Carné-Sánchez, A.; Maspoch, D., Programmable Self-Assembling 3D Architectures Generated by Patterning of Swellable MOF-Based Composite Films. *Adv. Mater.* **2019,** *31* (21), 1808235.

79. Troyano, J.; Carné-Sánchez, A.; Pérez-Carvajal, J.; León-Reina, L.; Imaz, I.; Cabeza, A.; Maspoch, D., A Self-Folding Polymer Film Based on Swelling Metal-Organic Frameworks. *Angew. Chem. Int. Ed.* **2018,** *57* (47), 15420-15424.

Chapter 1

Multiscale structural control of linked metal-organic polyhedra gel by aging-induced linkage-reorganization

Abstract

Assembly of permanently porous metal-organic polyhedra/cages (MOPs) with bifunctional linkers leads to soft supramolecular networks featuring both porosity and processability. However, the amorphous nature of such soft materials complicates their characterization and thus limits rational structural control. Here we demonstrate that aging is an effective strategy to control the hierarchical network of supramolecular gels, which are assembled from organic ligands as linkers and MOPs as junctions. Normally, the initial gel formation by rapid gelation leads to a kinetically trapped structure with low controllability. Through a controlled post-synthetic aging process, we show that it is possible to tune the network of the linked MOP gel over multiple length scales. This process allows control on the molecular-scale rearrangement of interlinking MOPs, mesoscale fusion of colloidal particles and macroscale densification of the whole colloidal network. In this work we elucidate the relationships between the gel properties, such as porosity and rheology, and their hierarchical structures, which suggest that porosity measurement of the dried gels can be used as a powerful tool to characterize the microscale structural transition of their corresponding gels. This aging strategy can be applied in other supramolecular polymer systems particularly containing kinetically controlled structures and shows an opportunity to engineer the structure and the permanent porosity of amorphous materials for further applications.

Introduction

Nanoporous materials assembled from metal ions and organic ligands have found a wide range of applications in separation, adsorption, catalysis and gas storage.[1-4] Despite the fact that the majority of such porous metal-organic materials studied to date, also known as metal-organic frameworks (MOFs), have a crystalline state, the limitation in processability has shifted the attention to the fabrication of their amorphous counterparts.[5-8] However, unlike the MOFs that can rely on the periodic linkage of metal ions and ligands to create well-defined micropores, amorphous structures consist of disordered networks with less controlled connectivity, which hampers the design of the pore sizes and shapes especially at the molecular scale.[9-11] To tackle this problem, molecular coordination cages with well-defined internal cavities, such as metal-organic polyhedra/cages (MOPs),[12-14] have been integrated as predesigned porous building

blocks into amorphous materials.[15,16] The prerequisite is to introduce connection points (metal ions or functional groups) on the periphery of these cages, allowing their subsequent linkage either by polymers or long alkyl chains.[17-23] The resulting amorphous materials that can be isolated as dried powders,[24] films[25] or wet gels[26] not only retain the rigid cavities of the cages but also possess the mechanical flexibility, processability and functions of the polymers. For example, the introduction of cavity-containing MOPs endows the resulting gels with the ability for selective encapsulation and release of guest molecules.[15] The combination of dynamic coordination bonding of MOPs with the polymer flexibility affords the gel network with photo-switchable topologies and responsiveness.[27,28] Recently we reported the fabrication of wet gels with hierarchical porous structures by coordinatively linking cuboctahedral MOPs, $[Rh_2(bdc)_2]_{12}$ (**HRhMOP**; bdc = benzene-1,3-dicarboxylate), with bidentate linkers, **bix** (1,4-bis(imidazol-1-ylmethyl)benzene).[29,30] The high structural stability of **HRhMOP** with intact cavity results in processable gels that are able to withstand the harsh desolvation process to form the corresponding aerogels with permanent microporosity. Despite these achievements, it is still challenging to further characterize and control the permanent porosity of these linked MOPs inside the resulting dried gel materials. This is because of the lack of fixed directionality and defined topology within the molecular networks, in which the cages are inhomogeneously distributed and thus their crosslinking is hard to control.[31] Besides the isolated cage cavities, the supramolecular arrangement of cages and the connections between them determine the accessible porosity of the materials. When polymer linkers are used to connect cages, the polymers tend to pack densely to minimize the empty spaces (or voids) in the dried state and inhibit the molecular diffusion throughout the materials.[32] Therefore, the development of methods is required to not only incorporate but also further characterize and engineer the permanent microporosity of the linked MOPs in these amorphous materials.

Efforts to manipulate the porous networks of crystalline MOF materials have been intensively made based on the strategy of post-synthetic modification (PSM).[33,34] Thanks to the reversibility of the coordination bonds that dominate the connectivity of metal ions and organic ligands, even after their formation the porous structures and properties of MOFs can be precisely tailored by functionalizing,[35] swapping,[36] eliminating or newly introducing building blocks.[37] When looking at the metal-organic soft materials, in particular gels, the PSM would give a new opportunity to tune their structures. This is because gels contain solvents therein, which ensure the dynamics of reversible coordination bond formation/dissociation for further PSM. Indeed, gels are often prepared in metastable states, which are trapped at the local energy minima.[38-41] By post-synthetically importing external stimuli (like heat, pH and photo-

irradiation), structural transitions can be induced from one trapped state to another metastable state, allowing further structural control.[42-45]

One typical example is the aging treatment of gels.[46] In most cases the gelation process is not performed under thermodynamic control so that the obtained gels inevitably show certain aging behaviours with time-dependent changes in the chemical or physical structure of materials.[47] Despite being mostly recognized as an uncontrollable spontaneous process in polymer materials,[48] aging has been utilized as a tool in the sol-gel chemistry to improve the performance of gels by intentionally intervening the aging process.[49,50] For example, by aging as-synthesized silica gels under controlled temperature, solvent or pH conditions, further chemical reactions involving the remaining unbound oligomers or monomers can be triggered, leading to mesoscale structural rearrangements with increased size of colloidal particles and density of silica gels.[50,51] For the supramolecular gel systems including metal-organic gels, however, the exploration of aging on their structural control is quite rare. Although there are some reports about their gel-to-gel or gel-to-crystal transitions over time,[52,53] most studies only focused on the gel morphology at the mesoscale, where the influence of the structural changes on the macroscale properties like transparency and stiffness are readily apparent.[54] It is still challenging to understand the effect of aging on the relationship between structures and properties at the molecular scale because of the difficulty in characterizing structural transitions of the amorphous materials/gels.

Here we demonstrate that the aging process can effectively control the hierarchical structures of the linked **HRhMOP** gels by inducing gradual structural transitions. By heating the as-synthesized gels in fresh solvent, aging process was performed to induce further crosslinking of MOPs inside the network, leading to a controllable transition of the whole structure over multiple length scales (Fig. 2-1). This transition is characterized by: (1) Molecular scale rearrangement of the crosslinked MOPs generated more-defined extrinsic microporosity. (2) Further connection of mesoscale colloidal particles resulted in a higher packing density. (3) Macroscale densification of the gel networks led to a shrinkage and increased stiffness. By repeating the aging process, we show that the corresponding gel structures and properties can be tailored. Combined with simulation and sorption measurements, we demonstrate a way to characterize the effect of aging on the molecular scale network rearrangements and thus the permanent microporosity.

Results and discussion

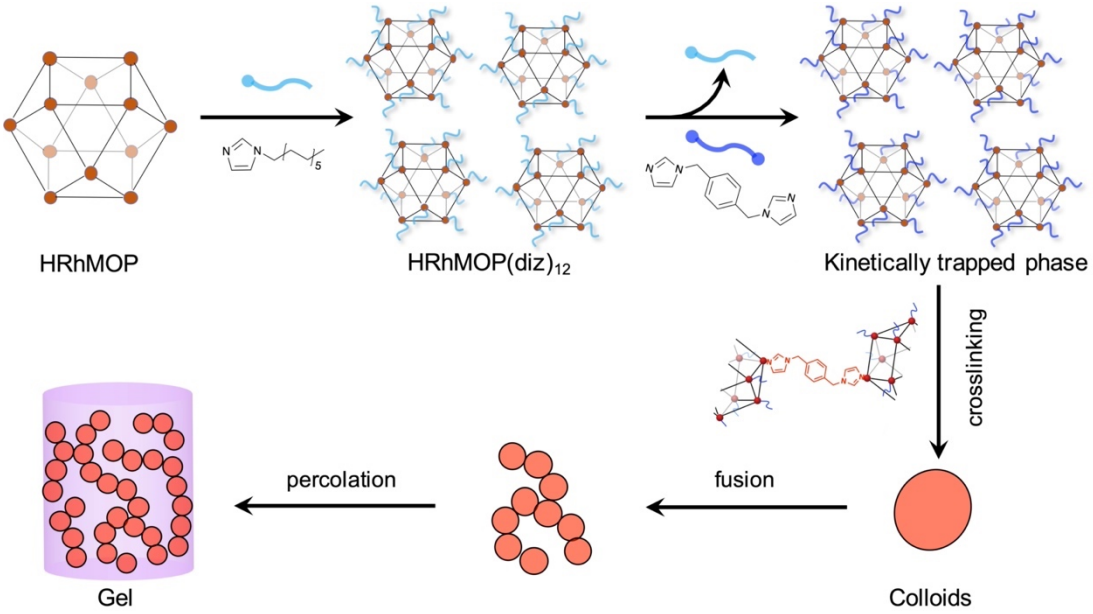

Figure 1-1. Schematic illustration of the synthesis of linked MOP gels by coordination with linkers.

The gels made from **HRhMOP** are attractive targets because the thermal stability of the MOPs allow their internal cavities to be maintained after desolvation process.[30] In contrast to other MOP/MOC gels which incorporate polymers as linkers, the use of the short linker **bix** affords a well-defined hierarchical structure over multiple length scales: isolated MOP cages are crosslinked by **bix** at the molecular scale, leading to the formation of mesoscale colloidal particles (around 25 nm), followed by their further fusion and percolation to give a colloidal gel network (Figure 1-1).[30,52] The resulting linked MOP network consists of multiscale porosities as molecular MOP cavities, mesoscale external pores between linked MOPs inside the colloids and macropores of the colloidal network. Such hierarchical structure affords optimal molecular diffusion throughout the material to demonstrate permanent porosity for gas sorption.

The gel samples were synthesized through previously reported coordinative solubilizer method.[30] Through reversibly attaching a coordinatively monodentate ligand, **diz** (1-dodecyl-1H-imidazole), to the exohedral Rh sites of **HRhMOP**, solubility of the resulting **HRhMOP(diz)$_{12}$** in DMF was greatly increased. Then these monodentate **diz** were replaced with nominally bidentate linker **bix** in DMF through ligand-exchange reaction, forming the so-called kinetically trapped molecules as **HRhMOP(bix)$_{10}$(diz)$_2$** with **bix** coordinating in a monodentate fashion (Figure 1-2). Heating the solution of the kinetically trapped molecules at 80 °C drove the assembly of MOPs into porous gels by the dissociation of excessive imidazole ligands and the subsequent crosslinking of MOPs with remaining **bix**.[55] In a typical reaction here, 1.4 mM kinetically trapped molecules were used to lead to the formation of gels within a

few minutes (Figure 1-3). To characterize the materials, the corresponding aerogel was prepared by solvent exchange from DMF to acetone, followed by supercritical CO_2 drying. Based on the ^{1}H NMR analysis of the digested aerogel, the composition of as-synthesized gel was estimated to be **HRhMOP(bix)$_{9.4}$(diz)$_{1.1}$** (Figure 1-2f). Assuming that all 12 exohedral Rh sites of MOPs in the gel network were coordinated by the imidazole ligands (**bix** or **diz**), the network branch functionality of the gel, *f*, which is the average number of exohedral Rh sites per MOP used as bridges to crosslink with neighbouring MOPs,[16] is calculated to be as low as 3.0 (Table 1, see details of calculation in Experimental Section). This low *f* value indicates that a large amount of monodentate **bix** and a small amount of **diz** remained in the whole network. It is thus hypothesized that the crosslinking reaction of MOPs was trapped at the initial stage.

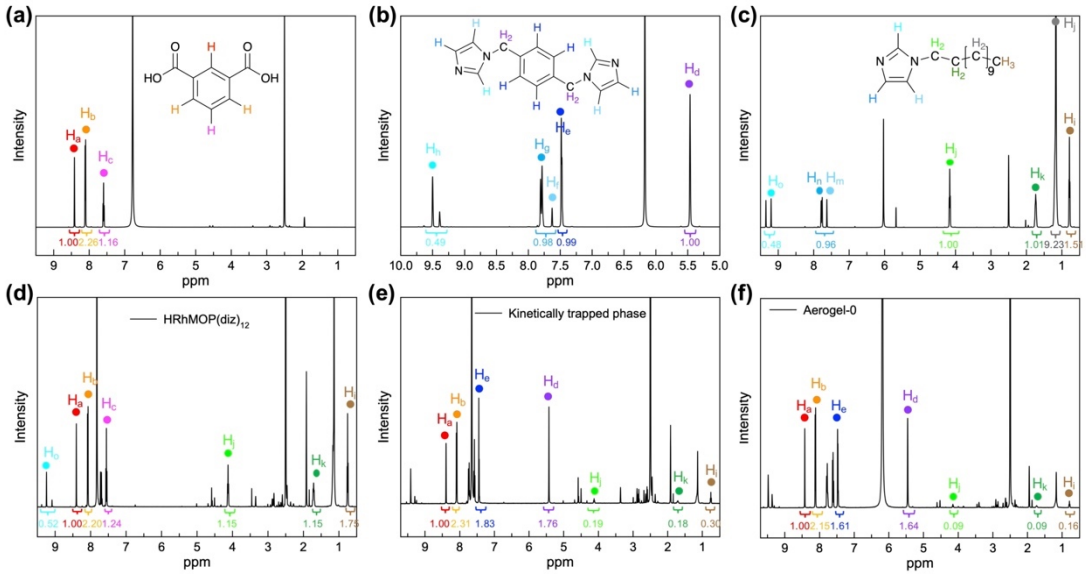

Figure 1-2. ^{1}H NMR spectrum of (a) **bdc**, (b) **bix** and (c) **diz** treated with the same conditions used to digest **Aerogel-*n***. ^{1}H NMR spectrum of the acid digestion of (d) **HRhMOP(diz)$_{12}$**, (e) kinetically trapped phase obtained immediately after adding 12 mol eq. of bix to **HRhMOP(diz)$_{12}$** and (f) the as-synthesized aerogel (**Aerogel-0**). The distinctive protons H_a and H_b for **HRhMOP**, H_d and H_e for **bix**, H_i, H_j and H_k for **diz** were used to calculate the molecular formula of the resulting sample for integration. Several protons were used for each compound and their integrations were averaged for accuracy.

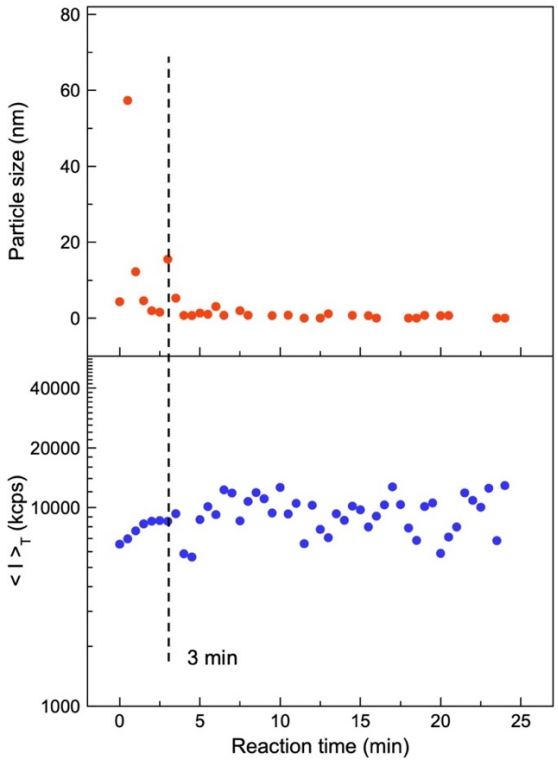

Figure 1-3. Time-resolved dynamic light scattering (TRDLS) experiments during the supramolecular polymerization of MOPs at 80 ºC at a concentration of 1.4 mM, showing the particle size evolution (upper) and the time-averaged scattering intensity (bottom) as a function of time. Once the polymerization begins, the trapped MOP molecules are hierarchically assembled into colloidal particles, leading to a steep increase in particle size. By further forming colloidal networks, the general mobility of the particles is frozen and the diffusion is stopped, rendering reliable measurement of the particle size impossible. As shown in the top figure, the gelation occurring here is too fast to observe the gradual increase in size, making it difficult to estimate the sol-gel transition point. To determine this gelation point, change in the time-averaged scattering intensity, $\langle I \rangle_T$, were plotted as a function of time, where the time at which random fluctuations appear corresponds to the gelation point. The result shows that the kinetically trapped phase used here gelated in 3 mins.

Table 1. Composition and corresponding *f* of gels after treatment of different aging cycles.

Sample	Composition	*f*
Gel-0	HRhMOP(bix)$_{9.4}$(diz)$_{1.1}$	3.0
Gel-1	HRhMOP(bix)$_{8.8}$(diz)$_{1.0}$	4.4
Gel-2	HRhMOP(bix)$_{8.6}$(diz)$_{0.9}$	5.0
Gel-3	HRhMOP(bix)$_{8.3}$(diz)$_{0.8}$	5.8
Gel-4	HRhMOP(bix)$_{8.1}$(diz)$_{0.7}$	6.4
Gel-5	HRhMOP(bix)$_{8.0}$(diz)$_{0.7}$	6.6

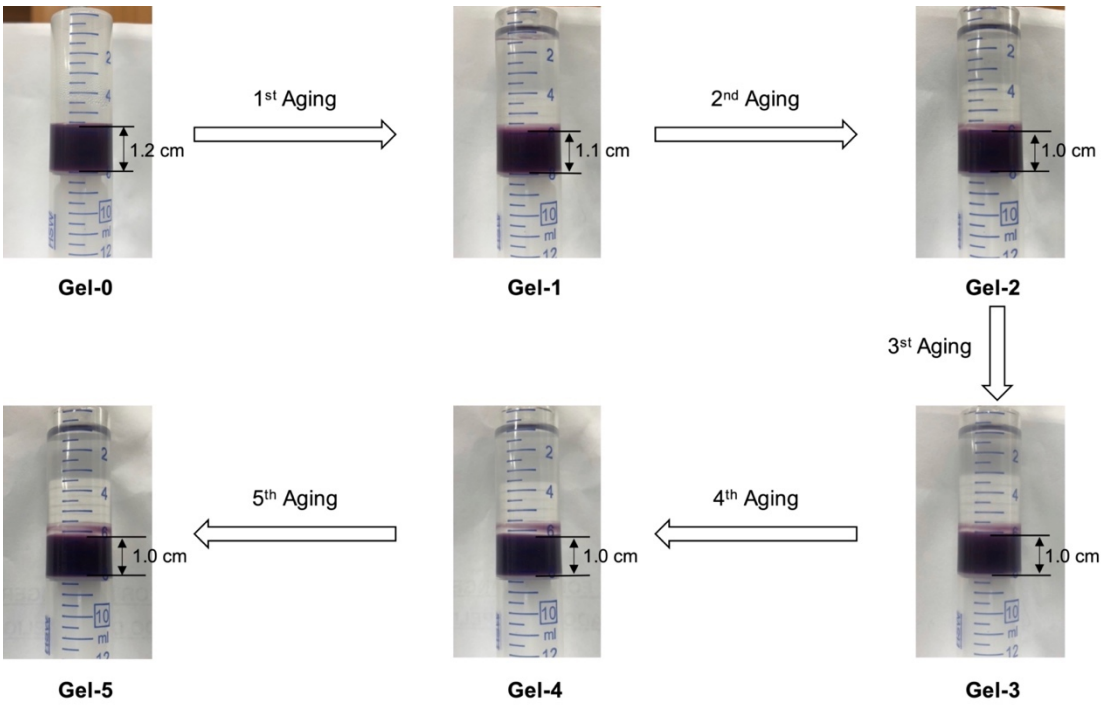

Figure 1-4. Pictures of a gel sample treated with repeated aging process, during which a shrinkage of the gel in volume was observed. For each aging cycle, ~5 mL fresh DMF was added prior to the heating treatment and then removed after 8 h of heating at 80 ºC.

For a typical aging cycle, fresh solvent (DMF) was added to the gels, followed by heating at 80 °C for 8 h (Figure 1-4). By cycling this aging process, gels with different aging degrees were obtained and referred henceforth as **Gel-*n*** (n indicates the number of aging cycles). These gels were then dried by supercritical CO_2 to obtain their corresponding aerogels (named as **Aerogel-*n***). The effect of the aging process on the composition of each aged sample was determined by the ^{1}H NMR experiments of the digested aerogels (Figure 1-5). From the results of ^{1}H NMR it is apparent that during each aging cycle, the number of imidazole ligands (**bix** and **diz**) per MOP inside the gel network is reduced (Table 1). The continuous removal or dissociation of these ligands from MOP exposed free Rh sites which could be subsequently linked by remaining **bix** from neighbouring MOPs for further crosslinking. Assuming that all exohedral Rh sites of MOPs were coordinated by the ligands, the value of *f* was calculated to present a significant increase from 3.0 for **Gel-0** to 6.6 for **Gel-5** (Table 1). In addition, the continuous removal of bix during repeated aging cycles was also confirmed by infrared spectroscopy (IR) (Figure 1-6); the related ratio of the characteristic peaks for **bix** and **HRhMOP** displayed the similar trend as observed from ^{1}H NMR. To demonstrate the reproducibility of the aging process, different batches of gel samples were synthesized and the ^{1}H NMR analysis was performed to estimate the composition along with aging cycles. The

average composition of each **Gel-*n*** was summarized in Table 2, which showed the same composition and the *f* evolution during aging as discussed above. In the next sections, the influences of the change of *f* on the gel structures and properties over multiple length scales are discussed in detail.

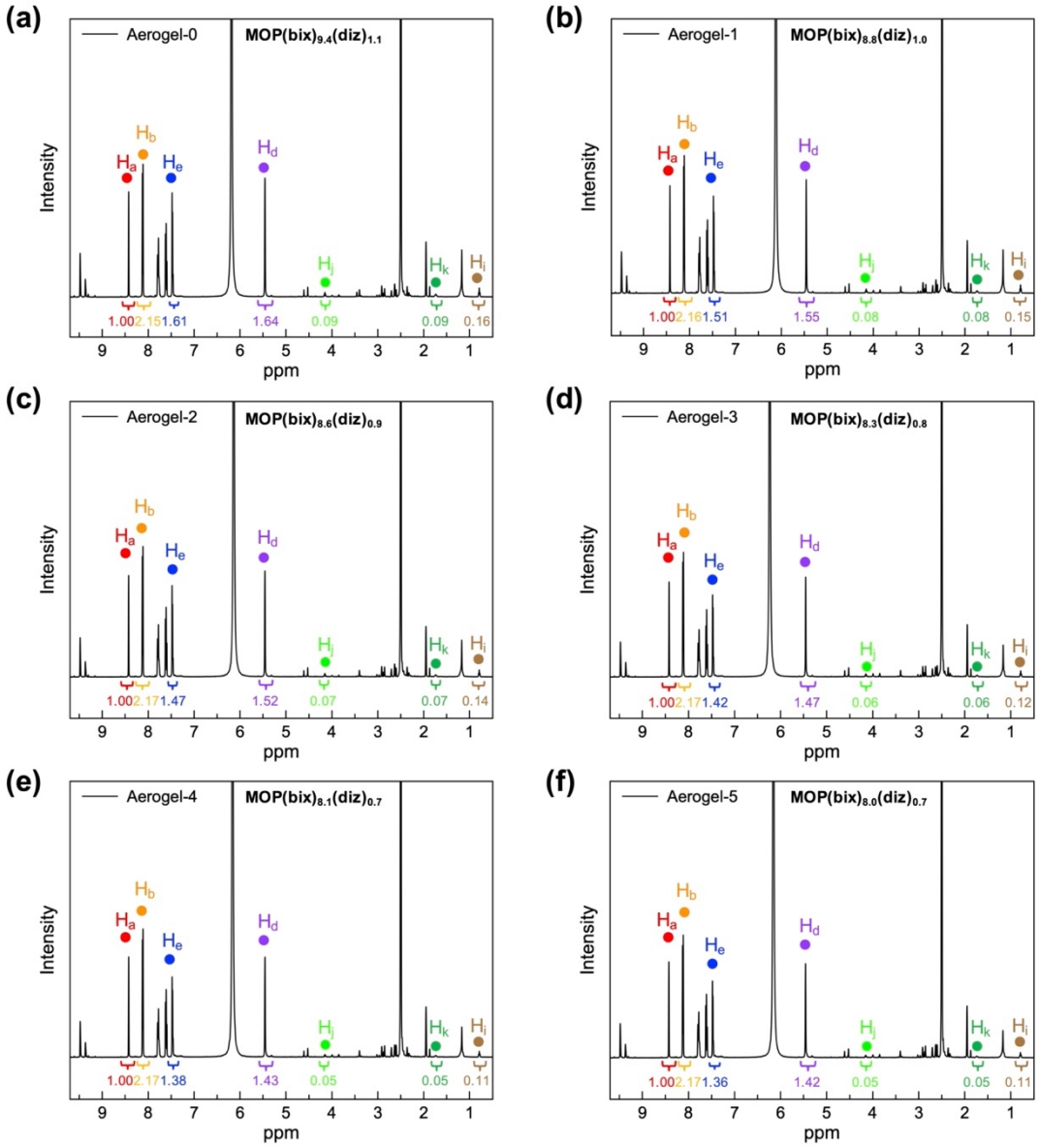

Figure 1-5. ^{1}H NMR spectrum of the acid digested **Aerogel-*n***. The peaks chosen for integration of each component (**HRhMOP**, **bix** and **diz**) are marked by different colors and corresponded to the proton of compound in Figure S3. The distinctive protons H_a and H_b for **HRhMOP**, H_d and H_e for **bix**, H_i, H_j and H_k for **diz** were used to calculate the molecular formula of the resulting aerogels for integration. Several protons were used for each compound and their integrations were averaged for accuracy. Following this methodology, the compositions of each aerogel samples were estimated as shown in Table 1.

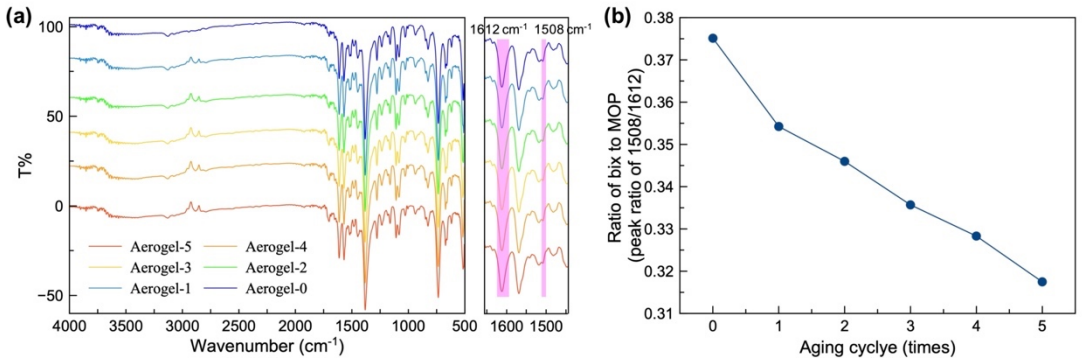

Figure 1-6. (a) IR spectra of **Aerogel-*n***; (b) Evolution of the intensity ratio of peaks at 1508 cm^{-1} and 1612 cm^{-1} in **Aerogel-*n*** as a function of the aging cycles. The peaks at 1508 cm^{-1} and 1612 cm^{-1} correspond to the characteristic vibrational bonds of C=N in **bix** and C=O in **HRhMOP**, respectively. The decreased value of the ratio as increasing aging cycles indicates that the number of **bix** molecules inside the gel networks is effectively reduced by repeated aging cycles.

Table 2. Average number of **diz** and **bix** per MOP and the resulting *f* of the aerogel at different aging cycles (each result was obtained by three replicates of ^{1}H NMR experiment of the corresponding aerogel samples).

Sample	Number of diz per MOP	Number of bix per MOP	*f*
Gel-0	1.3 ± 0.1	9.6 ± 0.5	2.2 ± 1.0
Gel-1	1.3 ± 0.2	9.2 ± 0.4	3.1 ± 1.0
Gel-2	1.3 ± 0.2	8.7 ± 0.4	4.0 ± 0.9
Gel-3	1.2 ± 0.3	8.4 ± 0.2	4.7 ± 0.7
Gel-4	1.1 ± 0.3	8.2 ± 0.2	5.5 ± 0.6
Gel-5	0.8 ± 0.1	7.9 ± 0.3	6.6 ± 0.7

Visual inspection of the gel after aging treatment revealed a shrinkage with the height of as-synthesized gel decreasing from 1.2 cm for **Gel-0** to 1.0 cm for **Gel-2** after two aging cycles (Figure1-4). Further aging processes showed only negligible change in size with the height of **Gel-5** to be 1.0 cm. Scanning electron microscopy (SEM) reveals that in the colloidal network of **Aerogel-2** the colloidal particles were more densely packed than those in the **Aerogel-0** network (Figure 1-7a and c). Consistent with the shrinkage behavior, aerogels treated with increased numbers of aging cycles presented similar colloidal packing density to **Aerogel-2** (Figure 1-7). This result indicated that the gel shrinkage or densification after aging was attributed to the increasing connection between colloidal nanoparticles, which could be triggered through the further crosslinking of MOPs by **bix** at their interface. To confirm the hypothesis, rheology measurements in a compression mode were performed by considering that

the mechanical property of the gels is dominated by the fusion or interaction of colloidal particles.[56-58] As shown in Figure 1-8, the gel samples were observed to show an increased mechanical stiffness upon aging especially at the first two aging cycles; **Gel-2** has a higher storage Young's modulus *E'* (~3.3 kPa) than the as-synthesized **Gel-0** (~1.9 kPa). However, this increase seems to saturate when continuing the aging process above 2 cycles (*E*' = ~3.4 kPa for **Gel-5**), which in accordance with above results confirms the close relationship between colloidal connection and the resulting gel stiffness.

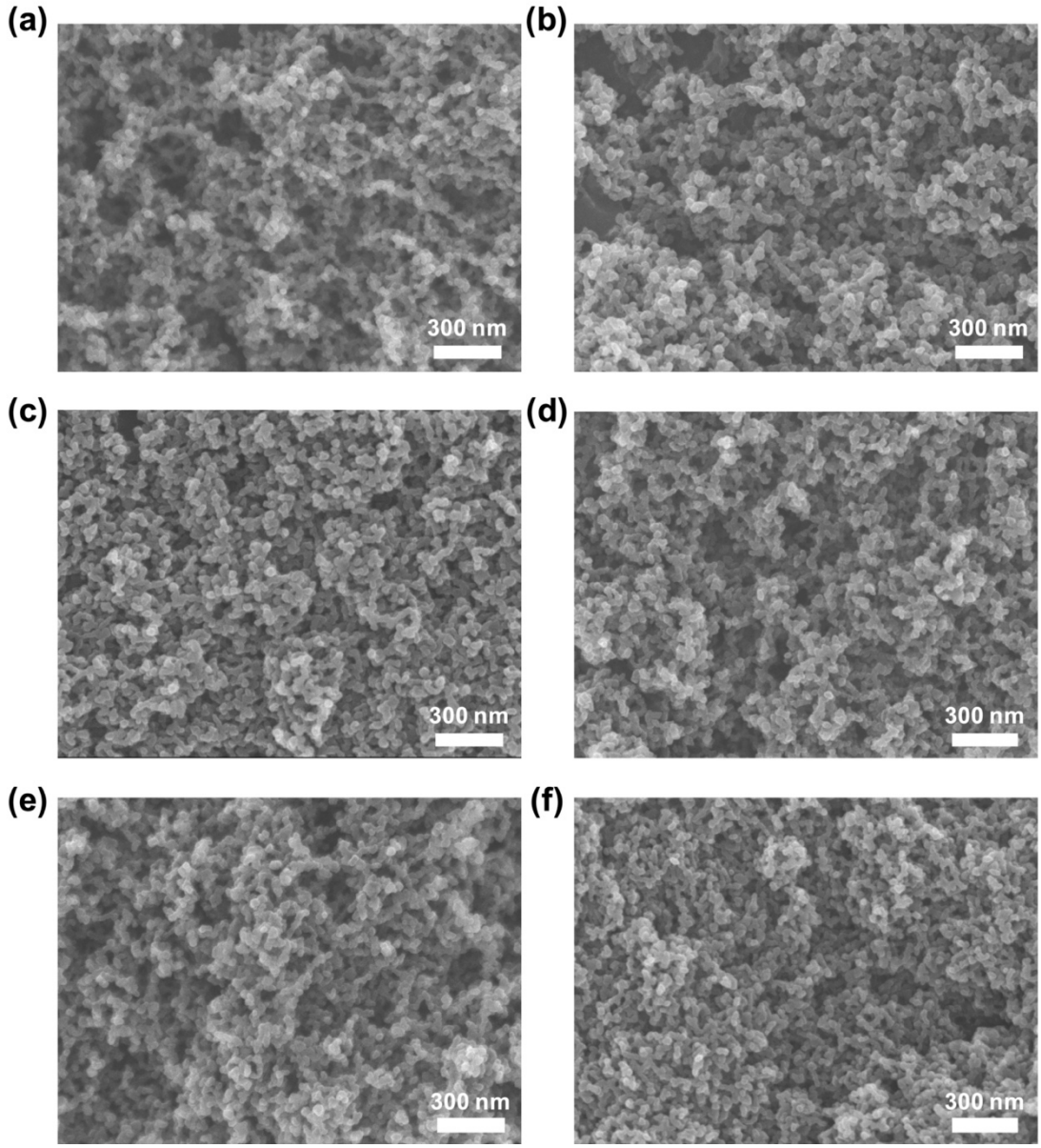

Figure 1-7. SEM images of (a) **Aerogel-0**, (b) **Aerogel-1**, (c) **Aerogel-2**, (d) **Aerogel-3**, (e) **Aerogel-4** and (f) **Aerogel-5**.

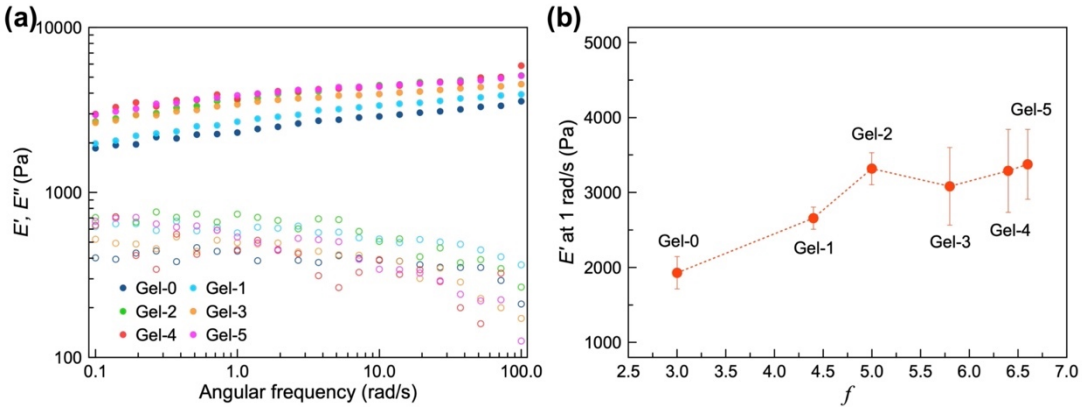

Figure 1-8. (a) Storage Young's modulus (E') (filled circles) and loss Young's modulus (E'') (hollow circles) of aged gels versus scanning frequency (ω). (b) Evolution of storage Young's modulus (E' at 1 rad/s) of **Gel-*n*** as a function of f during repeated aging process.

The major change in gel size and stiffness was only observed at the first two aging cycles, despite the continuous increase of f for gels with higher aging degrees (Fig 1-8b). Considering the hierarchical structures of the gels, aging should induce crosslinking of MOPs not only at the interface of colloidal particles but also within them. The MOP crosslinking at the colloidal interfaces resulted in the mesoscale connection of colloidal particles, giving a macroscopic denser gel structure with higher stiffness. However, this relinkage is restricted by the flexibility of the whole gel network. With the increase of f, the gel became denser and the colloidal particles in the network were fixed with each other through increasing connections, restricting their further packings. In contrast, the MOP crosslinking inside the colloidal particles could continuously occur without having a major impact on their flexibility. Instead of changing the gel properties at the meso- and macroscale, the rearrangement of interlinked MOPs inside each colloid would rather exert the influences at the molecular scale, the studies of which are discussed in the following sections.

To further understand the molecular scale structural rearrangement during the aging process, small-/wide-angle X-ray scattering (SAXS/WAXS) of all aerogels was performed as shown in Figure 1-8a. Fitting of the SAXS data by power-law approximation was applied to obtain information on the fractal structures of the linked MOP gels (Figure 1-8b).[59] Especially, the approximation of the low-q data (0.012 - 0.1 nm^{-1}) reveals a mass fractal dimension (the negative slope) between 1.45 - 1.85 for all aerogel samples (Table 3), implying that the gelation of MOPs follows the diffusion-limited cluster aggregation (DLCA).[60] In the high-q region (0.2 - 2 nm^{-1}), a noticeable change of the slope was observed from the neat **HRhMOP** ($q^{-3.2}$) to the aerogel samples ($q^{-3.78}$ for **Aerogel-0**), indicating a smoother surface of MOP-linked particles than the physical MOP aggregates.[61] After aging, a slight increase of slope was observed from

-3.78 for **Aerogel-0** to -3.83 for **Aerogel-5**, which suggests a further decreased surface roughness of the colloidal particles (Table 3). This change in roughness was attributed to the increasing branch functionality by aging process, together with the above results confirming the structural transition of the gel systems.

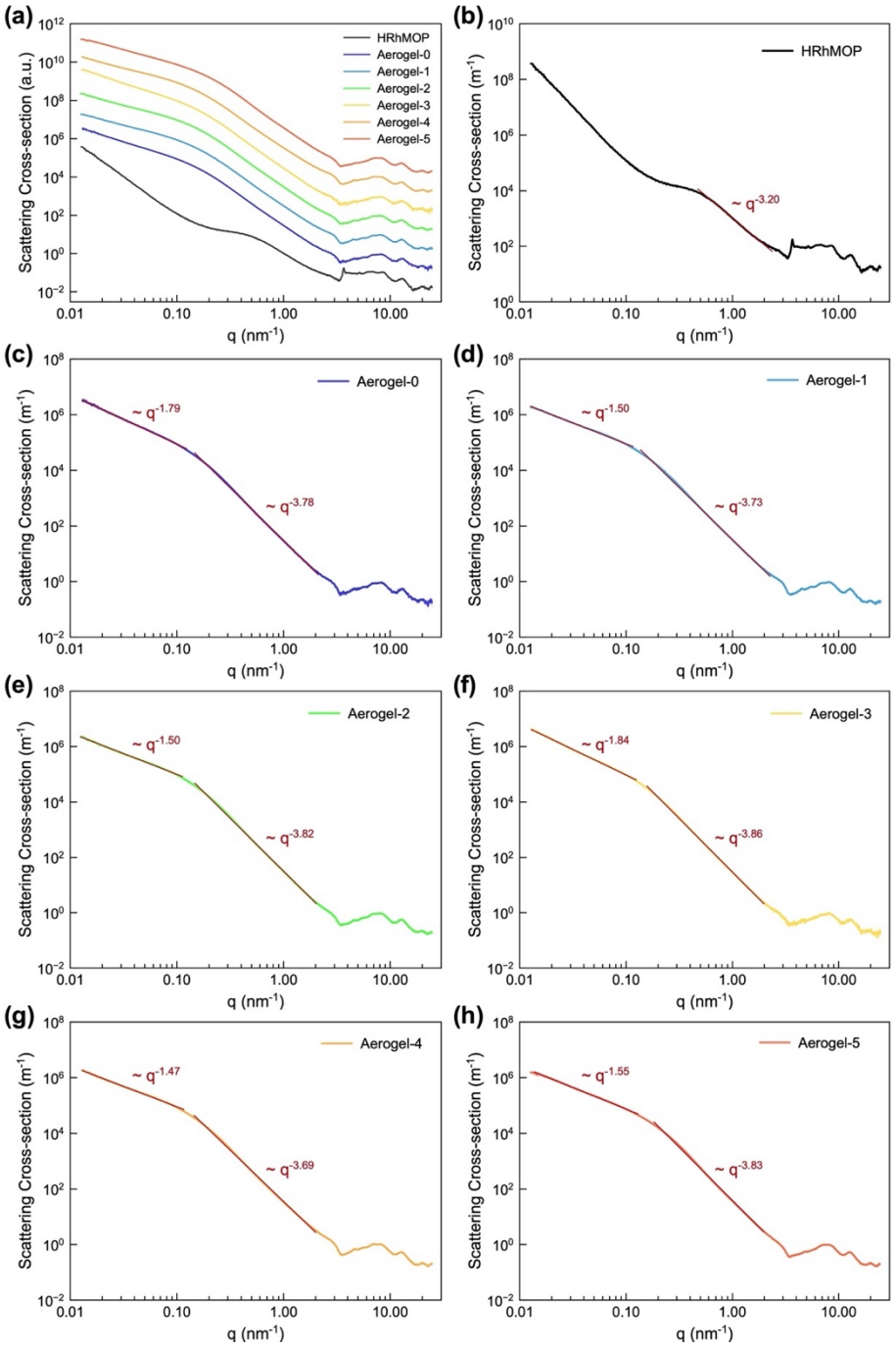

Figure 1-9. (a) SXAX/WAXS curves of **HRhMOP** and **Aerogel-*n*** (the data was stacked for clarity, all data on an absolute intensity scale can be found in Figure 1-14a). Fittings of the SAXS patterns for (b) **HRhMOP**, (c) **Aerogel-0**, (d) **Aerogel-1**, (e) **Aerogel-2**, (f) **Aerogel-3**, (g) **Aerogel-4**, (h) **Aerogel-5** by power-law approximation.

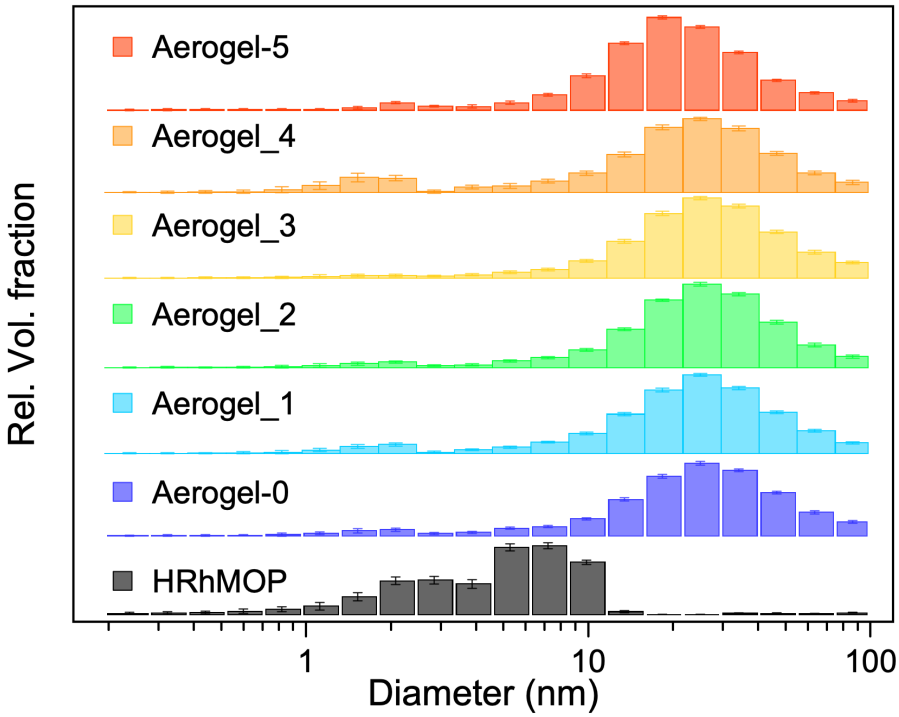

Figure 1-10. Form-free size distributions of **HRhMOP**, **Aerogel-*n*** extracted from SAXS fits from Monte Carlo method.

Besides the power-law approximation, the analysis of the SAXS data by Monte Carlo methods (McSAS) allows for the extraction of form-free size distribution,[62] revealing information of the gel structures at different scales (Figure 1-10). For **Aerogel-*n*** samples, two populations were observed in the corresponding size distribution histograms (the data summarized in Table 3): (1) The small population has a volume-weighted mean diameter of ~ 1.7 nm, in accordance with the size of the neat **HRhMOP** with a mean diameter at 1.9 nm. (2) The larger population, on the other hand, has a mean diameter above 23 nm, which well matches the dimensions of the colloidal particles observed from the SEM images of the gel network (Figure1-7). After aging, the average diameter of the colloidal particles was reduced from 28.4 nm for **Aerogel-0** to 23.6 nm for **Aerogel-5**, implying a densification of these particles (Table 3). Similar to the shrinkage of the gel networks that was attributed to the aging-induced connection of MOPs at the colloidal surfaces, the size reduction in each colloid was explained by the further crosslinking of MOPs inside the colloidal particles (Figure 1-11). Note that MOP crosslinking might not be the only reason for the colloidal densification. Due to the removal of imidazole ligands (**bix** and **diz**), the particles are supposed to possess more free volume, which might be lost during the drying process and result in the reduction in the final particle size. To

further confirm the MOPs crosslinking or rearrangement inside the colloidal particles, porosity of the aged MOP networks was studied.

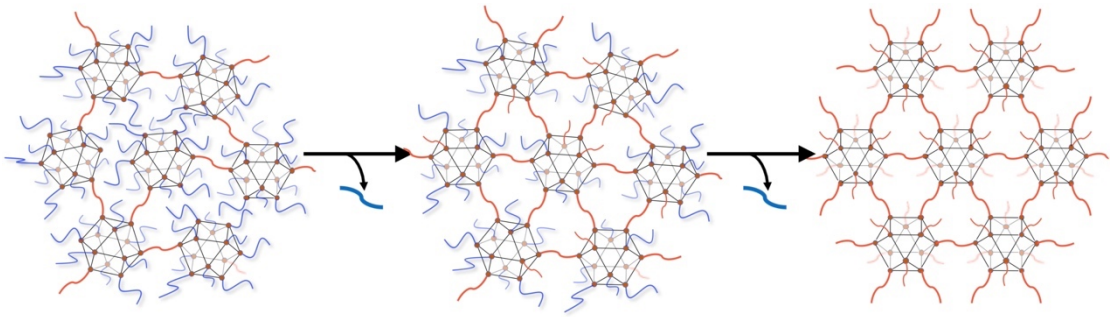

Figure 1-11. Schematic illustration of the molecular scale rearrangement of linked MOPs induced by aging process.

Table 3. Form-free size distribution, power coefficient (slope) and mass fractal dimension of **HRhMOP** and **Aerogel-*n*** obtained from the SAXS fits by Monte Carlo methods and power law approximation, respectively.

Sample	Mean diameter (< 3 nm)	Mean diameter (< 100 nm)	Slope (low-q)	Mass fractal dimension (D_m)	Slope (high-q)
HRhMOP	1.87 ± 0.35 nm	5.95 ± 0.11 nm	-4.0	-	-3.20
Aerogel-0	1.63 ± 0.07 nm	28.40 ± 0.12 nm	-1.79	1.79	-3.78
Aerogel-1	1.62 ± 0.05 nm	26.72 ± 0.13 nm	-1.50	1.50	-3.73
Aerogel-2	1.64 ± 0.07 nm	27.86 ± 0.12 nm	-1.50	1.50	-3.82
Aerogel-3	1.54 ± 0.09 nm	29.36 ± 0.10 nm	-1.84	1.84	-3.86
Aerogel-4	1.57 ± 0.04 nm	25.24 ± 0.16 nm	-1.47	1.47	-3.69
Aerogel-5	1.80 ± 0.09 nm	23.64 ± 0.09 nm	-1.55	1.55	-3.83

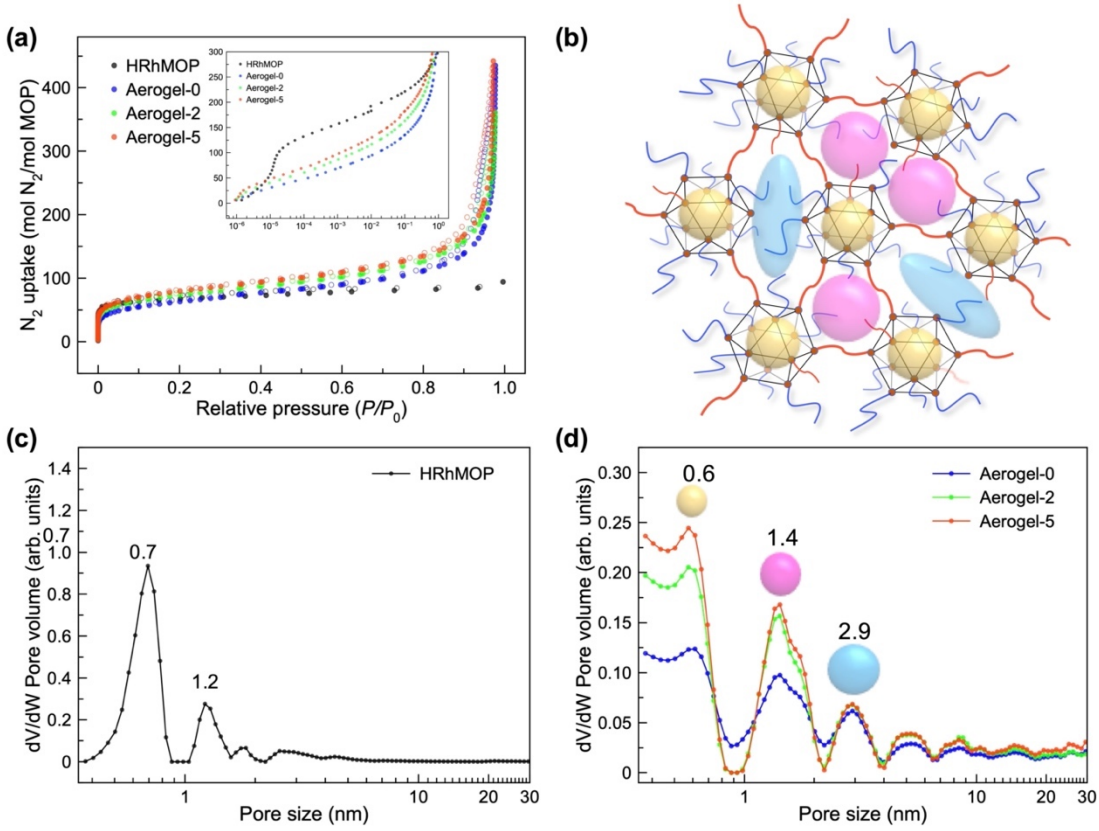

Figure 1-12. (a) N_2 adsorption isotherm at 77 K for **Aerogel-0**, **Aerogel-2**, **Aerogel-5** and **HRhMOP** with adsorption plot in filled circles and desorption plot in unfilled circles. (b) Schematic representation of the porous structure of the linked MOP aerogels after aging. The pore size distribution (PSD) of (c) **HRhMOP** and (d) **Aerogel-*n*** estimated from N_2 isotherm by NLDFT on a slit pore model.

The rearrangement of the linked MOP structure insides the colloids are expected to influence the microporosity of the gels, which was studied by performing N_2 sorption of three dried aerogel samples, **Aerogel-0**, **Aerogel-2** and **Aerogel-5** at 77 K (Figure 1-12a). Compared to the neat **HRhMOP**, all aerogel samples show much higher N_2 capacity especially in the high-pressure region, arising from the macropores and mesopores of the gel network: **HRhMOP** adsorbs 94 moles of N_2 per mole of MOP while **Aerogel-0** adsorbs 427 moles of N_2 per mole of MOP at $P/P_0 \sim 1$.

By repeating the aging cycles, a continuous increase in the Brunauer–Emmett–Teller (BET) surface area was observed from 565 m^2 g^{-1} (**Aerogel-0**) to 758 m^2 g^{-1} (**Aerogel-5**), corresponding to the removal of monodentate ligands that occupied the voids between MOPs (Table 4). In contrast, the total pore volume of the aerogels exhibited a different trend during aging treatment. Compared to **Aerogel-0** with a total pore volume of 1.66 cm^3 g^{-1}, **Aerogel-2** showed a smaller pore volume of 1.42 cm^3 g^{-1}, consistent with the gel shrinkage/densification during the first two aging cycles. Further aging process resulted in an increased volume to 1.77

$cm^3\ g^{-1}$ for **Aerogel-5**, which is attributed to the removal of monodentate ligands and to the rearrangement of linked MOP cages inside each colloidal particle. These results show that the aging process plays an important role in tuning the porosity of the linked MOP system post-synthetically.

Unlike flexible polymers that normally pack densely to block the intrinsic porosity of MOPs,[25] the crosslinking of MOPs with the shorter linker, **bix**, creates the external pores between MOPs, through which the connection of MOP cavities and thus access to their internal cavities is guaranteed by the molecular diffusion (Figure 1-1 and 1-11). This feature not only affords the permanent porosity, but also offers the possibility to control the microporosity of the gel network by rearranging interlinking MOPs. At 77 K, both **HRhMOP** and **Aerogel-*n*** display a sharp uptake of N_2 at low pressure, characteristic of microporous materials (see logarithmic data in the inset of Figure 1-12a). Pore size distribution (PSD) was calculated by using nonlocal density functional theory (NLDFT), as shown in Figure 1-12. The PSD of **HRhMOP** reveals two micropores with size centered at 0.7 nm and 1.2 nm, which are assigned to the intrinsic MOP cavities and the interstitial space between randomly packed MOPs, respectively (Figure 1-12c).[63] In contrast, all **Aerogel-*n*** exhibit a hierarchical porosity of the linked-MOP networks with different pore sizes centered at micro- and mesoporous regions (Figure 1-12d). A micropore is observed with the size centered at ca. 0.6 nm, indicating the preservation of MOP cavities in the amorphous network after gelation and aging. Similar pore size at ~0.66 nm was also observed in the positron annihilation lifetime spectroscopy (PALS) experiments, confirming the intact nature of MOP inside the gel network (Table 5 and Figure 1-13). In addition, two larger pores emerge in the PSD of all aerogel samples with the diameter of 1.4 and 2.9 nm, which can be assigned to the pores between the interlinked MOPs (Figure 1-12b). After aging, the aerogel samples show a clear increase in the volume of micropores with the size at 0.6 and 1.4 nm, indicating the enhancement of gel microporosity by aging process. Note that similar two pore sizes at ~0.50 nm and ~1.36 nm in **Aerogel-*n*** could also be obtained from the peaks of WAXS curves, in which the bigger pore showed a decrease in size from 1.36 nm for **Aerogel-0** to 1.30 nm for **Aerogel-5** (Figure 1-14b and Table 6), suggesting a more crosslinked MOP networks by **bix** as increasing aging degrees.

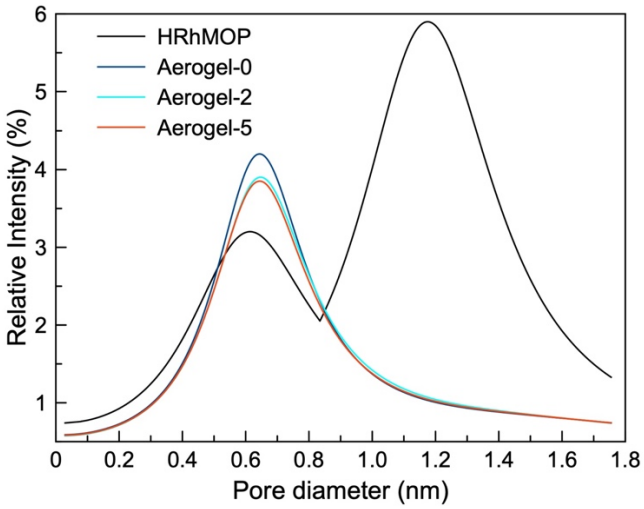

Figure 1-13. Pore size distribution (PSD) derived from the data of positron annihilation lifetime spectroscopy (PALS) of **HRhMOP** and **Aerogel-*n***.

Table 4. Density and pore parameters of HRhMOP, Aerogel-0, Aerogel-2 and Aerogel-5.

Sample	Volume (cm^3)	Weight (mg)	Bulk density[a] (g/cm)	Skeletal density[b] (g/cm^3)	Porosity[c] (%)	BET surface area (m^2/g)	Total pore volume (cm^3/g)
HRhMOP	-	-	1.031	1.17	12.20	875	0.51
Aerogel-0	2.12	22.5	0.0106	2.38±0.20	99.58	565	1.66
Aerogel-2	2.22	23.5	0.0106	2.19±0.13	99.55	677	1.42
Aerogel-5	2.23	25.4	0.0114	2.21±0.11	99.64	758	1.77

Note:

[a]Bulk density was determined by measuring the volume of the **Gel-*n*** and the weight of corresponding **Aerogel-*n***. For **HRhMOP**, it was calculated by the crystal data obtained from SCXRD;

[b] Skeletal density was obtained by helium pycnometry by assuming that there is only negligible difference between DMF gel and aerogel. For **HRhMOP**, it was calculated by crystal data obtained from SCXRD;

[c] Porosity was calculated by $P = 100 \times (1 - \text{bulk density}/\text{skeletal density})$;

[d] BET surface area was obtained from N_2 isotherm measurement;

[e] Total pore volume was determined from N_2 isotherm measurement.

Table 5. Summary of PALS results.

Sample	Lifetime of τ 3 (ns)	Intensity (%)	Average pore size in diameter (nm)
HRhMOP	2.309 ± 0.321;	3.2 ± 0.4;	0.624 ± 0.053;
	8.192 ± 0.721	5.9 ± 0.4	1.198 ± 0.048
Aerogel-0	2.511 ± 0.086	4.2 ± 0.1	0.656 ± 0.013
Aerogel-2	2.522 ± 0.070	3.9 ± 0.1	0.658 ± 0.011
Aerogel-5	2.525 ± 0.070	3.8 ± 0.1	0.658 ± 0.011

Table 6. Pore size of **HRhMOP** and **Aerogel-*n*** estimated by the peaks appearing in WAXS data.

Sample	Peak I				Peak II			
	q_{peak}	FWHM	Area	d-space	q_{peak}	FWHM	Area	d-space
HRhMOP	5.17 nm^{-1}	0.19	3.45	1.22 nm	12.71 nm^{-1}	3.29	133.01	0.49 nm
Aerogel-0	4.63 nm^{-1}	0.06	0.09	1.36 nm	12.93 nm^{-1}	2.65	1.02	0.49 nm
Aerogel-1	4.58 nm^{-1}	0.69	0.13	1.37 nm	12.71 nm^{-1}	3.18	1.27	0.49 nm
Aerogel-2	4.65 nm^{-1}	0.70	0.12	1.35 nm	12.68 nm^{-1}	3.48	1.37	0.50 nm
Aerogel-3	4.61 nm^{-1}	0.32	0.04	1.36 nm	12.64 nm^{-1}	3.92	1.67	0.50 nm
Aerogel-4	4.71 nm^{-1}	0.88	0.23	1.33 nm	12.55 nm^{-1}	3.73	1.41	0.50 nm
Aerogel-5	4.84 nm^{-1}	0.63	0.09	1.30 nm	12.58 nm^{-1}	3.47	1.28	0.50nm

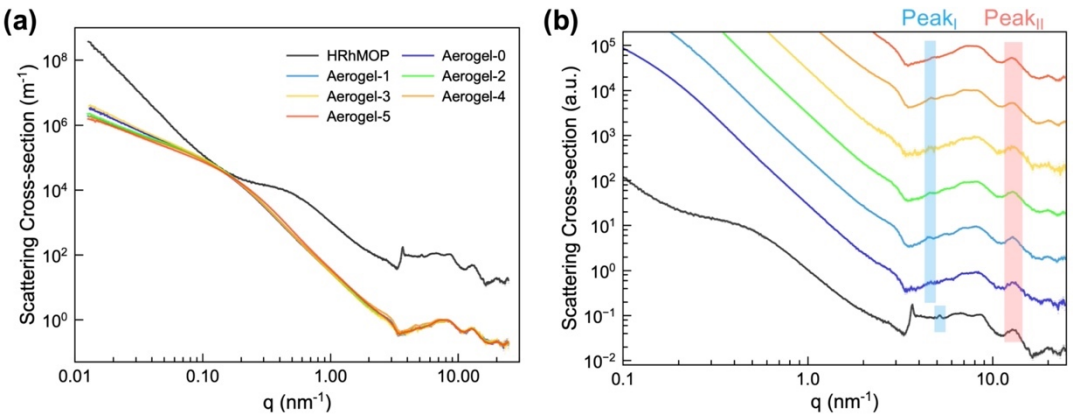

Figure 1-14. (a) Raw data of the SXAX/WAXS curves of **HRhMOP** and **Aerogel-*n***. (b) Zoom in of the WAXS curves of **HRhMOP** and **Aerogel-*n*** (the data was stacked for clarity).

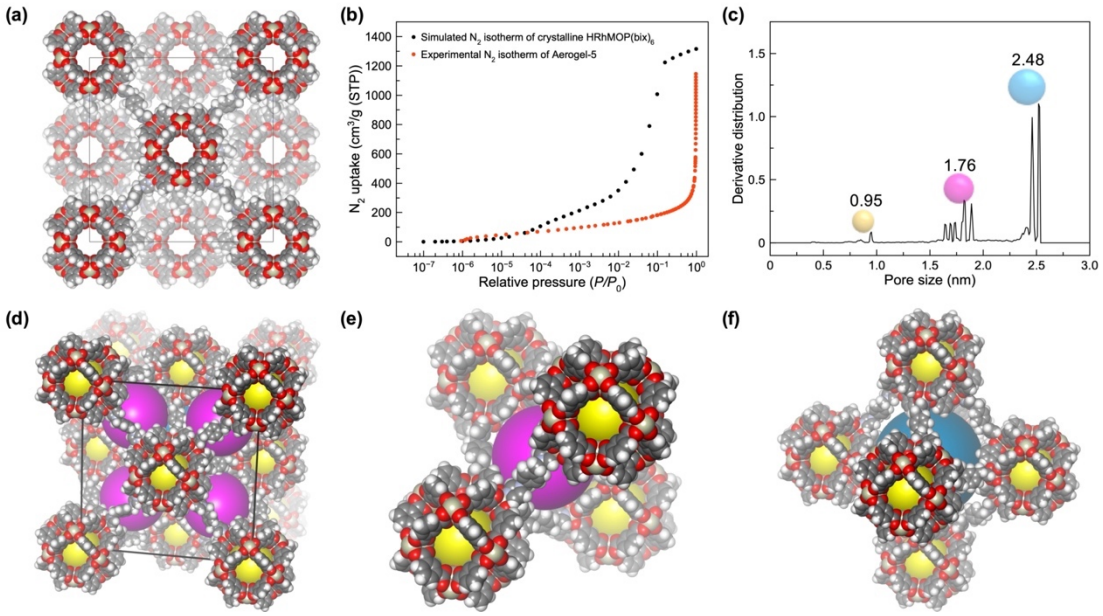

Figure 1-15. (a) Simulated crystalline structure of **HRhMOP(bix)$_6$**, which was minimized by geometry optimization using the LAMMPS software. The elements of C, H, O, N, Rh are drawn in sphere of gray, white, red, light blue and tan, respectively. (b) Simulated N_2 adsorption isotherm at 77 K for the minimized crystalline network of **HRhMOP(bix)$_6$** and (c) the corresponding pore size distribution (PSD). (d-f) Perspective view of the three different pores in the ideal linked MOP networks with f =12 with colors in yellow, pink and blue, respectively.

To correlate the microporosity of aged aerogels with the rearrangement process of interlinking MOPs, an ideal model of the linked MOP network was computed at an extreme condition of f = 12 (Figure 1-15a). With all 12 exohedral Rh sites per MOP bonded as coordinative connections with linker **bix**, a crystalline structure with ***fcu*** topology, named as **HRhMOP(bix)$_6$**, was constructed and its porosity was explored by simulating the corresponding gas adsorption (full details are given in experimental section). **HRhMOP(bix)$_6$** presents a higher gas uptake in the N_2 isotherm than **Aerogel-5**, which can be explained by its much higher ordered microporosity than that of amorphous aerogels (Figure 1-15b). The PSD simulation of the ideal **HRhMOP(bix)$_6$** reveals three populations of pores in the similar size range as the aged aerogels (Figure 1-15c): the smallest pores around 0.95 nm corresponds to MOP cavities, while the other two populations of pores around 1.76 nm and 2.48 nm corresponds to the truncated tetrahedral and octahedral pores which are interconnected through triangular and square windows of adjacent MOPs, respectively (Figure 1-15d-f). This distribution matches well with the PSD obtained experimentally in the aged aerogels, which allows us to propose two reasons to explain the dependency of porosity on aging: (1) the removal of monodentate **bix** or **diz** weakens their blocking effect on MOPs, entailing more

MOP cavities accessible towards gas sorption; (2) as higher f is achieved by continuous aging, MOPs inside each colloidal particle are rearranged by relinkage, “transforming” the initially random MOP aggregates into a more porous network (Figure 1-11). As a result, an enhancement in porosity was observed after aging and the aged samples presented a more distinguishable pore distribution.

Conclusion

In summary, we have demonstrated a strategy to control the structures and properties of the MOP-linked supramolecular gels in multiple length scales. By simply aging the gels, coordination equilibrium is directed into a gel network with higher branch functionality, *f*, leading to the rearrangement of interlinking MOPs and thus microporosity enhancement at the molecular scale. Simultaneously, more colloidal particles are connected with each other at the mesoscale due to the interlinking of MOPs at their surfaces, resulting in the formation of a denser gel network with enhanced mechanical properties at the macroscale. Interestingly, this controlled dissociation and relinkage of linkers during aging process shows the possibility for further exchange with new ligands, allowing for additional modification on the gel network, such as the incorporation of functional groups or the creation of a second network by full use of the coordination chemistry. As a powerful post-synthetic strategy, aging process offer a feasible way to tune the structure of the linked MOP systems, allowing us to control both structures and properties of these amorphous porous soft materials for further application.

Experimental section

Materials

Rhodium acetate was synthesized according to a previously reported procedure.[29] Isophthalic acid (H_2bdc) was purchased from Sigma-Aldrich and used as received. Solvents were purchased from Wako Pure Chemical Industries except those at HPLC grade which were purchased from Fischer Chemicals.

Characterizations

The rheological measurements of the gels were made using a stress-controlled AR-G2 (TA Instruments, New Castle, DE, USA) rheometer. Gel samples after synthesis or aging were pushed out from the syringe (the syringe head was cut) and carefully transferred into a clean glass slide (~ 1 mm in thickness). Then the gel was loaded into the rheometer with the glass slide to perform the rheology tests. The measurements of gels were conducted by frequency sweeping in a compression mode with a 1% strain amplitude that was well inside the linear regime (initial strain is fixed to 1.5%).

The super-critical CO_2 drying process was carried out on SCLEAD-2BD autoclave (KISCO) using super-critical CO_2 at 14 MPa and 50 °C.

Infrared (IR) spectroscopy data were recorded in ATR mode using a Jasco FT/IR-6100 with 1 cm^{-1} resolution and an accumulation of 128 scans. UV-vis was measured in a V-670 spectrophotometer (JASCO).

Scanning Electron Microscopy (SEM) of the microstructures of the aerogel samples were observed using a field-emission scanning electron microscope with a JEOL Model JSM-7001F4 system operating at 10 kV and 5 mA current. The samples were coated with 28 nm Osmium before measurement.

^{1}H NMR spectra were recorded on a Bruker Biospin DRX-600 (600 MHz) spectrometer. For ^{1}H-NMR analysis, 5 mg of aerogel sample was digested in a mixture of DMSO-d_6 (750 µl) and DCl (50 µl). The mixture was then heated at 100 °C overnight to obtain a yellow solution.

N_2 (77 K) gas sorption isotherms of the MOPs and aerogels were recorded on a BELSORP-max volumetric adsorption instrument from BEL Japan Inc. Prior to gas sorption measurement, the samples were activated at 120 °C for 12 h.

Thermogravimetric analyses (TGA) of the MOPs and aerogels were performed in the temperature range from room temperature to 500 ºC at a heating rate of 10 ºC/min with a Rigaku Thermo plus EVO2, under a nitrogen atmosphere.

Time-resolved dynamic light scattering (TRDLS) experiment were performed on a Zetasizer Nano ZS instrument (Malvern Instruments, Malvern, UK). The light source was a HeNe laser working at $\lambda = 633$ nm. The observations were made at the backscattering angle $\theta = 173^{o}$. The time dependence of particle size and the time-averaged scattering intensity during gelation process was evaluated at 80 ºC for 25 min.

The skeletal density of the aerogels was measured by helium pycnometry from Ultrapyc 1200e, Quantachrome Instruments, USA. For the neat HRhMOP, the skeletal density was estimated by the crystal data obtained from SCXRD.

The bulk density of the aerogels was determined by dividing the volume of **Gel-*n*** by the weight of the corresponding aerogel. The volume of **Gel-*n*** after synthesis and aging was calculated from the height and diameter of the wet gel by Vernier caliper (as seen in Figure S4). After super-critical CO_2 drying, the corresponding aerogels were weighted for density calculation. For the neat **HRhMOP**, the bulk density was estimated by the crystal data obtained from SCXRD.

Positron annihilation lifetime spectroscopy (PALS) experiments were conducted on EG&G Ortec Spectrometer. A 1.5 MBq ^{22}NaCl positron source sealed between two sheets of 2.54 μm Mylar was positioned in the center of two Al sample holders. Lifetimes were collected at 298K where a minimum of 5 files of 1 x 10^6 integrated counts was collected over 24h and analyzed using LT v9 software.[64] The data was fitted to 3 lifetimes: the first lifetime, τ1 was attributed to *para*-positronium (*p*-Ps) annihilation and fixed to 0.125 ns. The second lifetime, τ2 due to the free annihilation of the positron with free electrons within the sample, was approximated to 0.4 ns. The final lifetime, τ3, was associated with *ortho*-positronium (*o*-Ps) annihilation and fitted as a discrete lifetime and attributed to the pores within the aerogels. An extra *o*-Ps component was observed for the neat **HRhMOP** sample.

The small-/wide-angle X-ray scattering (SAXS/WAXS) measurements were conducted using the MOUSE (Methodology Optimization for Ultrafine Structure Exploration). X-rays were generated from a microfocus X-ray tube, followed by multilayer optics to parallelize and

monochromatize the X-ray beams to a wavelength of Cu Kα (λ = 0.154). Scattered radiation was detected on an in-vacuum Eiger 1M detector (Dectris, Switzerland), which was placed at multiple distances between 137 - 2507 mm from the sample. All samples were mounted in the sample chamber between two strips of Scotch Magic tape.[65] The resulting data has been processed and scaled to absolute intensity using the DAWN software package in a standardized complete 2D correction pipeline with uncertainty propagation.[66-67] The data was fitted and analyzed using McSAS, a Monte Carlo method to extract form-free size distributions.[68]

Estimation of network branch functionality (*f*) from the gel composition obtained by NMR. Network branch functionality, *f* is the average number of bridges that connect network junctions.[16] In this paper, it is applied to indicate the number of Rh sites per MOP which were used to bridge other MOPs. Based on the gel composition obtained from the ^{1}H NMR analysis of the acid-digested aerogels, the corresponding *f* could be calculated by the following equation:

$$f = 2 \times (12 - n_{bix} - n_{diz})$$

where n_{bix} and n_{diz} is the average number of bix and diz coordinated on MOPs obtained from the ^{1}H NMR experiment. The calculated results are listed in Table 1 and shows that aging process leads to an increase of *f* and thus further crosslinking of MOPs in the linked MOP gels. As shown in Figure 1-16, the structure of the network would be strongly affected by *f*, and the theoretical maximum value of *f* in this system is 12, where all outer Rh sites are used to link with surrounded MOPs.

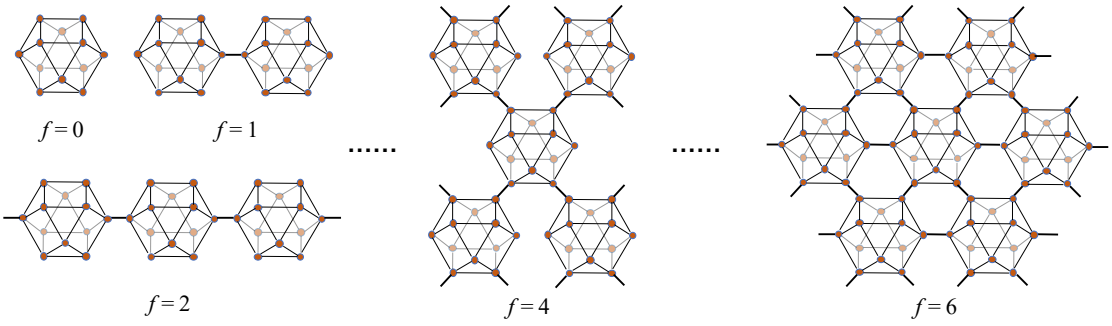

Figure 1-16. Illustrated MOPs interlinking with different network branch functionality, *f*.

Detailed synthesis

Synthesis of precursors

1-dodecyl-1H-imidazole (diz), 1,4-bis(imidazole-1-ylmethyl)benzene (bix) and HRhMOP were synthesized according to our previous reports.[11,30]

Synthesis of HRhMOP(diz)$_{12}$

200 mg of HRhMOP were dispersed in 40 mL of DCM, then 132.5 mg of diz (18 mol. eq.) were added. After sonication for 5 mins, the solution was centrifuged to remove the precipitate. The upper purple solution was collected and evaporated in vacuum. The obtained solid residue was washed twice with EtOH to remove any remaining diz. Finally, the purple solid product was dried under vacuum.

Synthesis of Gel-*n*

In a typical synthesis process, 1 mL DMF solution of HRhMOP(diz)$_{12}$ (2.8 mM) was added to 1 mL DMF solution of bix (33.6 mM, 12 mol. eq.) under vigorous stirring. The resultant transparent purple solution was transferred into the sealed syringe and placed in a preheated oven at 80 °C where it gelated within minutes. The sample was further heated at 80 °C for 8 h for a complete reaction. After the gelation, 5 mL of fresh DMF was added into the gel-holding syringe, which was then heated at 80 °C for 8 h to achieve 1 aging cycles, followed by the removal of the excessive DMF added. The same procedure was repeated in order to obtain gel samples at different aging cycles, and the corresponding gels were named as Gel-*n* where n indicates the number of aging cycles applied.

Synthesis of Aerogel-n

To obtain aerogel samples for further analysis, aged Gel-*n* was soaked with acetone for three days with replacing the fresh acetone each day. Then the solvent-exchanged sample was dried by supercritical CO_2 at 14 MPa and 50 °C for 90 min to obtain Aerogel-*n*. Prior to sorption measurements, the aerogel sample was activated at 120 °C under vacuum for 12 h.

Computational characterization of the porosity in fully linked MOP crystalline network

1. Computational details

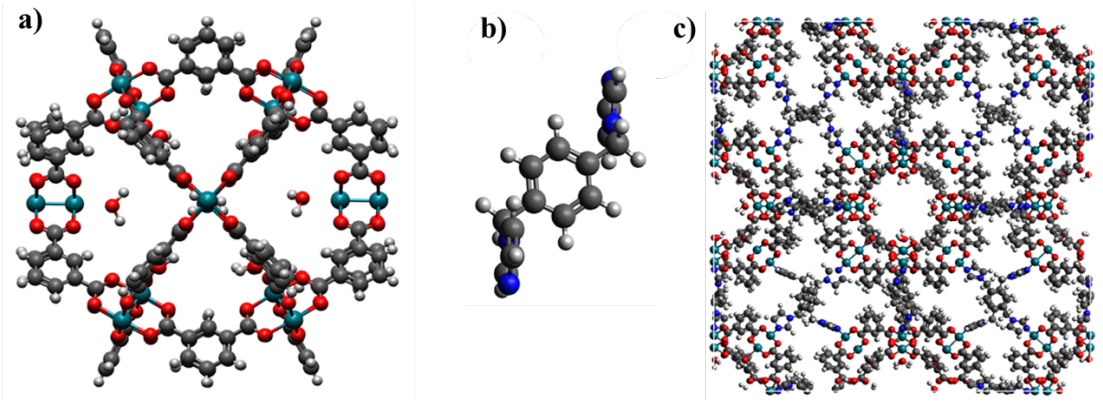

Figure 1-17. Panel (a) shows the 12-connected MOP with Rh as connection point. Water molecules shown inside of the cage are coordinated to Rh. Panel (b) shows the **bix** linker with nitrogen as connection points. Panel (c) shows the resulting crystalline structure with ***fcu*** topology and the 12-connected **HRhMOP** and **bix** as the linker. C = gray, H = white, O = red, N = blue, and Rh = turquoise. Visualized using Avogadro software.[69,70]

Porosity of **HRhMOP** was studied by performing N_2 adsorption simulations at 77K. MOP cages with Rh and bix for the paddlewheel and linker respectively, were mapped onto an ***fcu*** topology using the crystal generator, ToBaCCo 3.0 (https://github.com/tobacco-mofs/tobacco_3.0)[71-74], as shown in Figure 1-17. The resulting crystallographic information files from ToBaCCo 3.0 were used as input for the LAMMPS Interface[75] code by Boyd and coworkers to generate its corresponding input files with universal force field (UFF)[75] parameters for the LAMMPS[76] software. Structures were then minimized twice using LAMMPS, the first one with the unit cell dimensions constant and the second allowed changes in the unit cell dimensions. The minimized structure from LAAMPS is named as **HRhMOP(bix)$_6$**.

Grand canonical Monte Carlo simulations were performed to calculate nitrogen adsorption isotherms at 77K with the RASPA[77] software. Nitrogen uptake simulations were performed for pressures between 0.01 and 99990 Pa. Each run consisted of 20000 initialization cycles followed by 60000 production cycles. All moves including translation, rotation, reinsertion and swap were attempted with equal probability. For the framework, a single cell was employed and considered as rigid during the adsorption simulation. Nonbonded interactions were modeled using a Lennard-Jones potential with a cut off of 12.5 Å. UFF was used for all framework atoms and TraPPE[78] was used for the adsorbed molecules. Adsorbate-adsorbate interactions also included Coulombic interactions.

Helium void fraction and available pore volume were calculated using RASPA. Pore size distribution was calculated using the Zeo++[79-84] software while the surface area was calculated

using RASPA and Zeo++. Density profiles were calculated using RASPA and visualized using the ParaView[85] software.

Helium void fraction was calculated at 298K using its respective Lennard-Jones parameters[85] and using Widom insertions[87,88]. The result was then used to calculate the available pore volume on the structure. Both helium void fraction and available pore volume calculations were run for 10000 cycles. The surface area obtained from RASPA is calculated by using a nitrogen rolling probe and measuring the amount of overlap between framework atoms. This amount is then multiplied by the area of a sphere and the summation over all atoms in the framework gives the surface area.[77] The run consisted of 10000 cycles at 298K, using a surface area probe distance of σ of the nitrogen probe. Surface area was also obtained from Zeo++, where it is calculated by determining the accessibility of pores followed by a Monte Carlo (MC) sampling procedure to integrate the surface area. To determine accessibility and perform MC sampling a probe with radius of 1.2 Å is used in both cases. A total of 2000 MC samples per atom are used. Pore size distribution is calculated in a similar fashion as the surface area, but the MC samples are per unit cell instead of atoms in the framework. A total of 10000 MC samples per unit cell are used. Likewise, probes of radius of 1.2 Å are used for both cases.

Density profiles were calculated for **HRhMOP(bix)$_6$** at 77K and selected pressures: 2.5, 2510, and 15850 Pa. The number of cycles and initialization cycles were 10000 and the restart file from the adsorption simulation was used.

2. Results and discussion

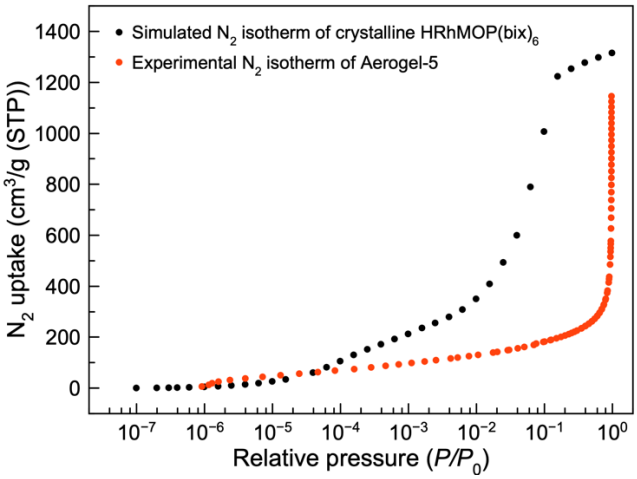

Figure 1-18. N_2 adsorption isotherm at 77K for the minimized **HRhMOP(bix)$_6$** structure

We studied the adsorption of nitrogen in the **HRhMOP(bix)$_6$** structures with the ***fcu*** topology and compared experimental and computational results. First, the helium void fraction

and pore volume were calculated as 0.85 and 2.05 $cm^3\ g^{-1}$, respectively. The values for the pore volume are higher than the ones obtained experimentally with the Aerogels, in which the highest value was 1.77 for **Aerogel-5**, as shown in Table 7. The surface area obtained computationally is significantly different than the ones obtained experimentally for the different aerogel samples. The highest value experimentally obtained was 758.11 $m^2\ g^{-1}$ for **Aerogel-5** and it is around five times smaller than the values obtained from RASPA and Zeo++. Differences on the results between software packages are due to the way that the surface area is calculated. **HRhMOP(bix)$_6$** adsorbs 1315.9 $cm^3\ g^{-1}$, as shown in Figure 1-18, while **Aerogel-0** adsorbs 1075.5 $cm^3\ g^{-1}$.

Table 7. Comparison of experimental and computational surface area and total pore volume.

Structure	Surface Area ($m^2\ g^{-1}$)	Pore Volume ($cm^3\ g^{-1}$)	Adsorption at P/P_0 ~1 ($cm^3\ g^{-1}$)
HRhMOP	665.32	0.3841	248.3
Aerogel-0	564.78	1.6636	1075.5
Aerogel-2	676.51	1.4179	916.7
Aerogel-5	758.11	1.7726	1146.0
HRhMOP(bix)6 R*	3706.38	2.0542	1315.9
HRhMOP(bix)6 Z*	3985.18	1.59	-

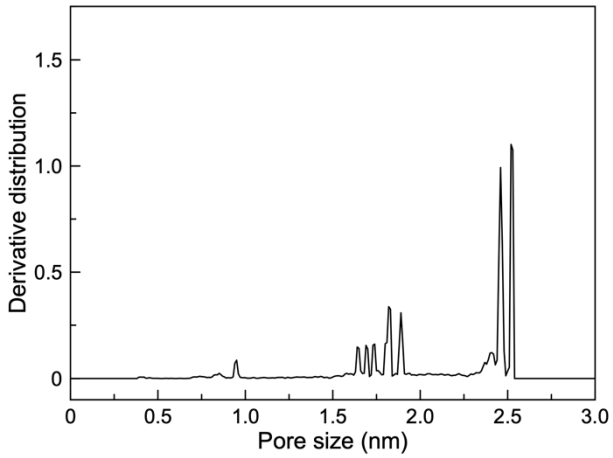

Figure 1-19. Pore size distribution for the **HRhMOP(bix)$_6$** structure calculated by using the Zeo++[78-84] software.

Pore size distribution (PSD) estimated by Zeo++ for **HRhMOP(bix)$_6$** is shown in Figure 1-19. The PSD for **HRhMOP(bix)$_6$** gives a small peak around 0.95 nm corresponding to MOP cavities. Five peaks around 1.64 and 1.89 nm correspond to a distribution of pore sizes between the interlinked MOPs. Similarly, it gives two broad peaks at 2.45 and 2.52 nm corresponding to largest pore on the center of the network.

Density profiles (Figure 1-20) show how the N_2 first starts to occupy the MOP pores at a pressure of 2.5 Pa. At a pressure of 2510 Pa, N_2 occupies the pores between the interlinked MOPs. Lastly, at a pressure of 15850 Pa all the pores are occupied by N_2.

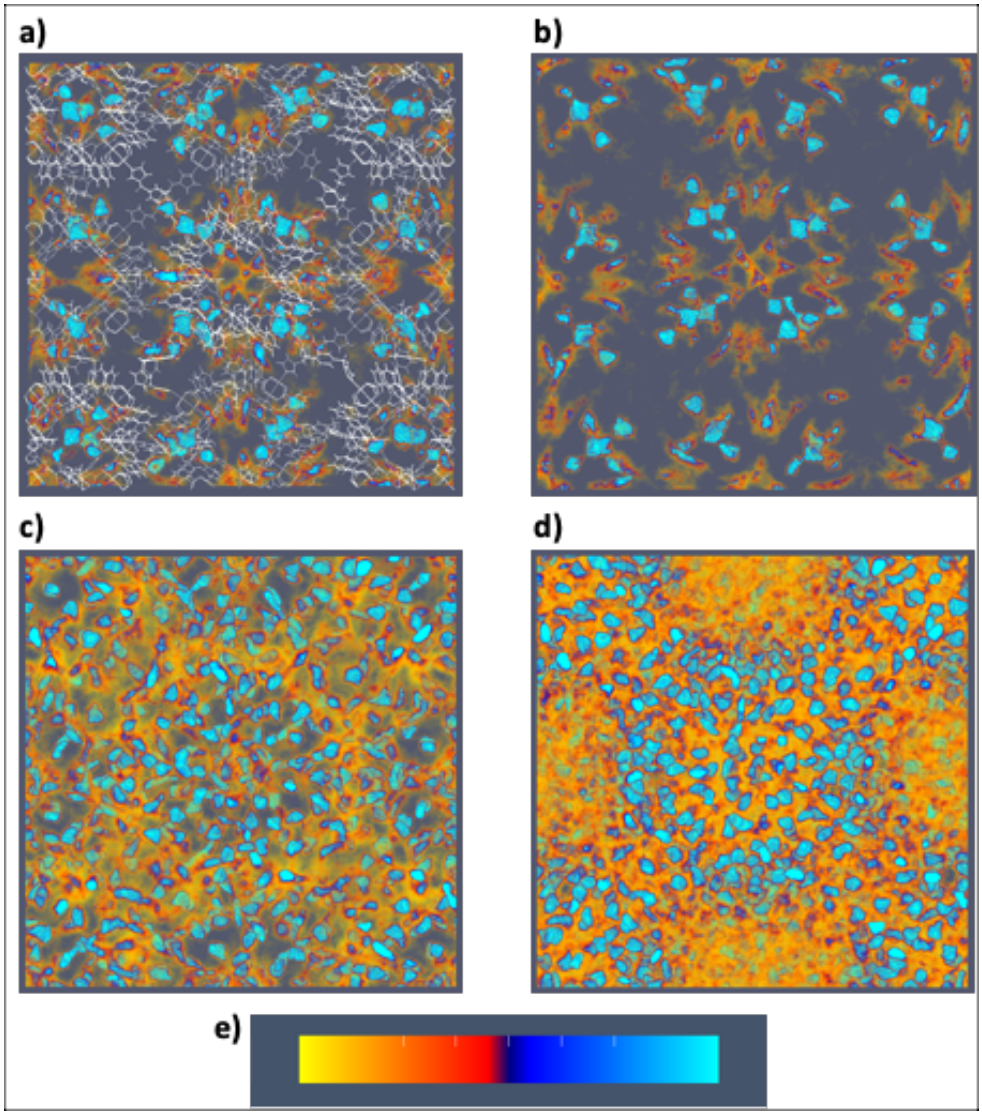

Figure 1-20. (a) Density profile for **HRhMOP(bix)$_6$** with atomic structure at 2.5 Pa of N_2. (b) Low density profile for **HRhMOP(bix)$_6$** at 2.5 Pa of N_2. (c) Medium density profile for **HRhMOP(bix)$_6$** at 2510 Pa of N_2. (d) High density profile for **HRhMOP(bix)$_6$** at 15850 Pa of N_2. (e) The legend of the color profile from the lowest (yellow) to the highest (cyan) N_2 concentration.

Reference

1. Seo, J. S.; Whang, D.; Lee, H.; Jun, S. I.; Oh, J.; Jeon, Y. J.; Kim, K., A homochiral metal–organic porous material for enantioselective separation and catalysis. *Nature* **2000**, *404* (6781), 982-986.

2. Davis, M. E., Ordered porous materials for emerging applications. *Nature* **2002**, *417* (6891), 813-821.

3. Kitagawa, S.; Kitaura, R.; Noro, S.-i., Functional Porous Coordination Polymers. *Angew. Chem. Int. Ed.* **2004**, *43* (18), 2334-2375.

4. Furukawa, H.; Cordova, K. E.; O'Keeffe, M.; Yaghi, O. M., The Chemistry and Applications of Metal-Organic Frameworks. *Science* **2013**, *341* (6149), 1230444.

5. Slater, A. G.; Cooper, A. I., Function-led design of new porous materials. *Science* **2015**, *348* (6238), aaa8075.

6. Bennett, T. D.; Horike, S., Liquid, glass and amorphous solid states of coordination polymers and metal-organic frameworks. *Nat. Rev. Mater.* **2018**, *3* (11), 431-440.

7. Hosono, N.; Kitagawa, S., Modular Design of Porous Soft Materials via Self-Organization of Metal–Organic Cages. *Acc. Chem. Res.* **2018**, *51* (10), 2437-2446.

8. Hou, J.; Sapnik, A. F.; Bennett, T. D., Metal-organic framework gels and monoliths. *Chem Sci.* **2020**, *11* (2), 310-323.

9. Jiang, S.; Jones, J. T.; Hasell, T.; Blythe, C. E.; Adams, D. J.; Trewin, A.; Cooper, A. I., Porous organic molecular solids by dynamic covalent scrambling. *Nat. Commun.* **2011**, *2* (1), 1-7.

10. Das, S.; Heasman, P.; Ben, T.; Qiu, S., Porous organic materials: strategic design and structure-function correlation. *Chem. Rev.* **2017**, *117* (3), 1515-1563.

11. Carné-Sánchez, A.; Craig, G. A.; Larpent, P.; Hirose, T.; Higuchi, M.; Kitagawa, S.; Matsuda, K.; Urayama, K.; Furukawa, S., Self-assembly of metal-organic polyhedra into supramolecular polymers with intrinsic microporosity. *Nat. Commun.* **2018**, *9* (1), 1-8.

12. Dalgarno, S. J.; Power, N. P.; Atwood, J. L., Metallo-supramolecular capsules. Coordination Chemistry Reviews 2008, 252 (8-9), 825-841.

13. Tranchemontagne, D. J.; Ni, Z.; O'Keeffe, M.; Yaghi, O. M., Reticular Chemistry of Metal-Organic Polyhedra. *Angew. Chem. Int. Ed.* **2008**, *47* (28), 5136-5147.

14. Gosselin, A. J.; Rowland, C. A.; Bloch, E. D., Permanently Microporous Metal-Organic Polyhedra. *Chem. Rev.* **2020**, *120* (16), 8987-9014.

15. Foster, J. A.; Parker, R. M.; Belenguer, A. M.; Kishi, N.; Sutton, S.; Abell, C.; Nitschke, J. R., Differentially addressable cavities within metal-organic cage-cross-linked polymeric hydrogels. *J. Am. Chem. Soc.* **2015**, *137* (30), 9722-9729.

16. Zhukhovitskiy, A. V.; Zhong, M.; Keeler, E. G.; Michaelis, V. K.; Sun, J. E.; Hore, M. J.; Pochan, D. J.; Griffin, R. G.; Willard, A. P.; Johnson, J. A., Highly branched and loop-rich gels via formation of metal-organic cages linked by polymers. *Nat. Chem.* **2016**, *8* (1), 33.

17. Yan, X.; Cook, T. R.; Pollock, J. B.; Wei, P.; Zhang, Y.; Yu, Y.; Huang, F.; Stang, P. J., Responsive Supramolecular Polymer Metallogel Constructed by Orthogonal Coordination-Driven Self-Assembly and Host/Guest Interactions. *J. Am. Chem. Soc.* **2014**, *136* (12), 4460-4463.

18. Kawamoto, K.; Grindy, S. C.; Liu, J.; Holten-Andersen, N.; Johnson, J. A., Dual Role for 1,2,4,5-Tetrazines in Polymer Networks: Combining Diels-Alder Reactions and Metal Coordination To Generate Functional Supramolecular Gels. *ACS Macro Lett.* **2015**, *4* (4), 458-461.

19. Nam, D.; Huh, J.; Lee, J.; Kwak, J. H.; Jeong, H. Y.; Choi, K.; Choe, W., Cross-linking Zr-based metal-organic polyhedra via postsynthetic polymerization. *Chem. Sci.* **2017**, *8* (11), 7765-7771.

20. Uchida, J.; Yoshio, M.; Sato, S.; Yokoyama, H.; Fujita, M.; Kato, T., Self-Assembly of Giant Spherical Liquid-Crystalline Complexes and Formation of Nanostructured Dynamic Gels that Exhibit Self-Healing Properties. *Angew. Chem. Int. Ed.* **2017**, *56* (45), 14085-14089.

21. Liu, J.; Duan, W.; Song, J.; Guo, X.; Wang, Z.; Shi, X.; Liang, J.; Wang, J.; Cheng, P.; Chen, Y.; Zaworotko, M. J.; Zhang, Z., Self-Healing Hyper-Cross-Linked Metal-Organic Polyhedra (HCMOPs) Membranes with Antimicrobial Activity and Highly Selective Separation Properties. *J. Am. Chem. Soc.* **2019**, *141* (30), 12064-12070.

22. Andrés, M. A.; Carné-Sánchez, A.; Sánchez-Laínez, J.; Roubeau, O.; Coronas, J.; Maspoch, D.; Gascón, I., Ultrathin Films of Porous Metal-Organic Polyhedra for Gas Separation. *Chem. Eur. J.* **2020**, *26* (1), 143-147.

23. Li, R.-J.; Pezzato, C.; Berton, C.; Severin, K., Light-induced assembly and disassembly of polymers with Pd_nL_{2n}-type network junctions. *Chem. Sci.* **2021**, *12*, 4981-4984.

24. Lal, G.; Derakhshandeh, M.; Akhtar, F.; Spasyuk, D. M.; Lin, J.-B.; Trifkovic, M.; Shimizu, G. K. H., Mechanical Properties of a Metal-Organic Framework formed by Covalent Cross-Linking of Metalp-Organic Polyhedra. *J. Am. Chem. Soc.* **2019**, *141* (2), 1045-1053.

25. Chen, T.-H.; Wang, L.; Trueblood, J. V.; Grassian, V. H.; Cohen, S. M., Poly(isophthalic acid)(ethylene oxide) as a Macromolecular Modulator for Metal-Organic Polyhedra. *J. Am. Chem. Soc.* **2016**, *138* (30), 9646-9654.

26. Shao, L.; Hua, B.; Hu, X.; Stalla, D.; Kelley, S. P.; Atwood, J. L., Construction of Polymeric Metal-Organic Nanocapsule Networks via Supramolecular Coordination-Driven Self-Assembly. *J. Am. Chem. Soc.* **2020**, *142* (16), 7270-7275.

27. Gu, Y.; Alt, E. A.; Wang, H.; Li, X.; Willard, A. P.; Johnson, J. A., Photoswitching topology in polymer networks with metal-organic cages as crosslinks. *Nature* **2018**, *560* (7716), 65-69.

28. Oldenhuis, N. J.; Qin, K. P.; Wang, S.; Ye, H.-Z.; Alt, E. A.; Willard, A. P.; Van Voorhis, T.; Craig, S. L.; Johnson, J. A., Photoswitchable Sol-Gel Transitions and Catalysis Mediated by Polymer Networks with Coumarin-Decorated $Cu_{24}L_{24}$ Metal-Organic Cages as Junctions. *Angew. Chem. Int. Ed.* **2020**, *59* (7), 2784-2792.

29. Furukawa, S.; Horike, N.; Kondo, M.; Hijikata, Y.; Carné-Sánchez, A.; Larpent, P.; Louvain, N.; Diring, S.; Sato, H.; Matsuda, R., Rhodium-organic cuboctahedra as porous solids with strong binding sites. *Inorg. Chem.* **2016**, *55* (21), 10843-10846.

30. Carné-Sánchez, A.; Craig, G. A.; Larpent, P.; Guillerm, V.; Urayama, K.; Maspoch, D.; Furukawa, S., A Coordinative Solubilizer Method to Fabricate Soft Porous Materials from Insoluble Metal-Organic Polyhedra. *Angew. Chem. Int. Ed.* **2019**, *131* (19), 6413-6416.

31. Jeyakkumar, P.; Liang, Y.; Guo, M.; Lu, S.; Xu, D.; Li, X.; Guo, B.; He, G.; Chu, D.; Zhang, M., Emissive Metallacycle-Crosslinked Supramolecular Networks with Tunable Crosslinking Densities for Bacterial Imaging and Killing. *Angew. Chem. Int. Ed.* **2020**, *59*, 15199-15203.

32. McKeown, N. B.; Budd, P. M., Exploitation of Intrinsic Microporosity in Polymer-Based Materials. *Macromolecules* **2010**, *43* (12), 5163-5176.

33. Yin, Z.; Wan, S.; Yang, J.; Kurmoo, M.; Zeng, M.-H., Recent advances in post-synthetic modification of metal-organic frameworks: New types and tandem reactions. *Coord. Chem. Rev.* **2019**, *378*, 500-512.

34. Kalaj, M.; Cohen, S. M., Postsynthetic Modification: An Enabling Technology for the Advancement of Metal-Organic Frameworks. *ACS Cent. Sci.* **2020**, *6* (7), 1046-1057.

35. Wang, Z.; Cohen, S. M., Postsynthetic Covalent Modification of a Neutral Metal-Organic Framework. *J. Am. Chem. Soc.* **2007**, *129* (41), 12368-12369.

36. Burnett, B. J.; Barron, P. M.; Hu, C.; Choe, W., Stepwise Synthesis of Metal-Organic Frameworks: Replacement of Structural Organic Linkers. *J. Am. Chem. Soc.* **2011**, *133* (26), 9984-9987.

37. Tu, B.; Pang, Q.; Wu, D.; Song, Y.; Weng, L.; Li, Q., Ordered Vacancies and Their Chemistry in Metal-Organic Frameworks. *J. Am. Chem. Soc.* **2014**, *136* (41), 14465-14471.

38. Boekhoven, J.; Poolman, J. M.; Maity, C.; Li, F.; van der Mee, L.; Minkenberg, C. B.; Mendes, E.; van Esch, J. H.; Eelkema, R., Catalytic control over supramolecular gel formation. *Nat. Chem.* **2013**, *5* (5), 433-437.

39. Mattia, E.; Otto, S., Supramolecular systems chemistry. *Nat. Nanotechnol.* **2015**, *10* (2), 111-119.

40. Amabilino, D. B.; Smith, D. K.; Steed, J. W., Supramolecular materials. *Chem. Soc. Rev.* **2017**, *46* (9), 2404-2420.

41. Fukui, T.; Kawai, S.; Fujinuma, S.; Matsushita, Y.; Yasuda, T.; Sakurai, T.; Seki, S.; Takeuchi, M.; Sugiyasu, K., Control over differentiation of a metastable supramolecular assembly in one and two dimensions. *Nat. Chem.* **2017**, *9* (5), 493-499.

42. Yagai, S.; Yamauchi, M.; Kobayashi, A.; Karatsu, T.; Kitamura, A.; Ohba, T.; Kikkawa, Y., Control over Hierarchy Levels in the Self-Assembly of Stackable Nanotoroids. *J. Am. Chem. Soc.* **2012**, *134* (44), 18205-18208.

43. Lavrenova, A.; Balkenende, D. W. R.; Sagara, Y.; Schrettl, S.; Simon, Y. C.; Weder, C., Mechano- and Thermoresponsive Photoluminescent Supramolecular Polymer. *J. Am. Chem. Soc.* **2017**, *139* (12), 4302-4305.

44. Adhikari, B.; Aratsu, K.; Davis, J.; Yagai, S., Photoresponsive Circular Supramolecular Polymers: A Topological Trap and Photoinduced Ring-Opening Elongation. *Angew. Chem. Int. Ed.* **2019**, 58 (12), 3764-3768.

45. Wehner, M.; Würthner, F., Supramolecular polymerization through kinetic pathway control and living chain growth. *Nat. Rev. Chem.* **2020**, *4* (1), 38-53.

46. Alemán, J. V.; Chadwick, A. V.; He, J.; Hess, M.; Horie, K.; Jones, R. G.; Kratochvíl, P.; Meisel, I.; Mita, I.; Moad, G.; Penczek, S.; Stepto, R. F. T., Definitions of terms relating to the structure and processing of sols, gels, networks, and inorganic-organic hybrid materials (IUPAC Recommendations 2007). *Pure Appl. Chem.* **2007**, *79* (10), 1801-1829.

47. Draper, E. R.; McDonald, T. O.; Adams, D. J., A low molecular weight hydrogel with unusual gel aging. *Chem. Commun*. **2015**, *51* (30), 6595-6597.

48. Struik, L. C. E., Physical Aging in Amorphous Polymers and Other Materials. Elsevier Scientific Publication Co.: Amsterdam, **1978**.

49. Fuentes-Caparrós, A. M.; de Paula Gómez-Franco, F.; Dietrich, B.; Wilson, C.; Brasnett, C.; Seddon, A.; Adams, D. J., Annealing multicomponent supramolecular gels. *Nanoscale* **2019**, *11* (7), 3275-3280.

50. Aegerter, M. A.; Leventis, N.; Koebel, M. M., *Aerogels Handbook*. Springer New York: **2011**.

51. Levy, D.; Zayat, M., *The Sol-Gel Handbook*, 3 Volume Set: Synthesis, Characterization, and Applications. Wiley: **2015**.

52. Wang, Y.; de Kruijff, R. M.; Lovrak, M.; Guo, X.; Eelkema, R.; van Esch, J. H., Access to Metastable Gel States Using Seeded Self-Assembly of Low-Molecular-Weight Gelators. *Angew. Chem. Int. Ed.* **2019**, *58* (12), 3800-3803.

53. Guterman, T.; Levin, M.; Kolusheva, S.; Levy, D.; Noor, N.; Roichman, Y.; Gazit, E., Real-Time In-Situ Monitoring of a Tunable Pentapeptide Gel-Crystal Transition. *Angew. Chem. Int. Ed.* **2019**, *58* (44), 15869-15875.

54. Panja, S.; Adams, D. J., Stimuli responsive dynamic transformations in supramolecular gels. *Chem. Soc. Rev.* **2021**, *50*, 5165-5200.

55. Legrand, A.; Craig, G. A.; Bonneau, M.; Minami, S.; Urayama, K.; Furukawa, S., Understanding the multiscale self-assembly of metal-organic polyhedra towards functionally graded porous gels. *Chem. Sci.* **2019**, *10* (47), 10833-10842.

56. Lu, P. J.; Zaccarelli, E.; Ciulla, F.; Schofield, A. B.; Sciortino, F.; Weitz, D. A., Gelation of particles with short-range attraction. *Nature* **2008**, *453* (7194), 499-503.

57. Hsiao, L. C.; Newman, R. S.; Glotzer, S. C.; Solomon, M. J., Role of isostaticity and load-bearing microstructure in the elasticity of yielded colloidal gels. *Proc. Natl. Acad. Sci.* **2012**, *109* (40), 16029.

58. Park, J. D.; Ahn, K. H., Structural evolution of colloidal gels at intermediate volume fraction under start-up of shear flow. *Soft Matter* **2013**, *9* (48), 11650-11662.

59. Putra, E. G. R.; Ikram, A.; Bharoto; Santoso, E.; Fang, T. C.; Ibrahim, N.; Mohamed, A. A., Fractal Studies on Titanium-Silica Aerogels using SMARTer. *AIP Conf. Proc.* **2008**, *989* (1), 130-133.

60. Jungblut, S.; Joswig, J.-O.; Eychmüller, A., Diffusion-Limited Cluster Aggregation: Impact of Rotational Diffusion. *J. Phys. Chem. C* **2019**, *123* (1), 950-954.

61. White, C. E.; Olds, D. P.; Hartl, M.; Hjelm, R. P.; Page, K., Evolution of the pore structure during the early stages of the alkali-activation reaction: an in situ small-angle neutron scattering investigation. *J. Appl. Crystallogr.* **2017**, *50* (1), 61-75.

62. Bressler, I.; Pauw, B. R.; Thunemann, A. F., McSAS: software for the retrieval of model parameter distributions from scattering patterns. *J. Appl. Crystallogr.* **2015**, *48* (3), 962-969.

63. Wang, Z.; Craig, G. A.; Legrand, A.; Haase, F.; Minami, S.; Urayama, K.; Furukawa, S., Porous colloidal hydrogels formed by coordination-driven self-assembly of charged metal-organic polyhedra. *Chem. Asian J.* **2021**, *16*, 1092-1100.

64. Kansy, J., Microcomputer program for analysis of positron annihilation lifetime spectra. *Nucl. Instrum. Methods Phys. Res. A: Accel. Spectrom. Detect. Assoc. Equip.* **1996**, *374* (2), 235-244.

65. Smales, G. J.; Pauw, B. R., The MOUSE project: a meticulous approach for obtaining traceable, wide-range X-ray scattering information. *J. Instrum.* **2021**, *16* (06), P06034.

66. Pauw, B. R.; Smith, A. J.; Snow, T.; Terrill, N. J.; Thunemann, A. F., The modular small-angle X-ray scattering data correction sequence. *J. Appl. Crystallogr.* **2017**, *50* (6), 1800-1811.

67. Filik, J.; Ashton, A. W.; Chang, P. C. Y.; Chater, P. A.; Day, S. J.; Drakopoulos, M.; Gerring, M. W.; Hart, M. L.; Magdysyuk, O. V.; Michalik, S.; Smith, A.; Tang, C. C.; Terrill, N. J.; Wharmby, M. T.; Wilhelm, H., Processing two-dimensional X-ray diffraction and small-angle scattering data in DAWN 2. *J. Appl. Crystallogr.* **2017**, *50* (3), 959-966.

68. Zhukhovitskiy, A. V.; Zhong, M.; Keeler, E. G.; Michaelis, V. K.; Sun, J. E. P.; Hore, M. J. A.; Pochan, D. J.; Griffin, R. G.; Willard, A. P.; Johnson, J. A., Highly branched and loop-rich gels via formation of metal-organic cages linked by polymers. *Nat. Chem.* **2016**, *8* (1), 33-41.

69. Avogadro: an open-source molecular builder and visualization tool. Version 1.XX. http://avogadro.cc/.

70. Hanwell, M. D.; Curtis, D. E.; Lonie, D. C.; Vandermeersch, T.; Zurek, E.; Hutchison, G. R., Avogadro: an advanced semantic chemical editor, visualization, and analysis platform. *J. Cheminformatics* **2012**, *4* (1), 17.

71. Gómez-Gualdrón, D. A.; Colón, Y. J.; Zhang, X.; Wang, T. C.; Chen, Y.-S.; Hupp, J. T.; Yildirim, T.; Farha, O. K.; Zhang, J.; Snurr, R. Q., Evaluating topologically diverse metal–organic frameworks for cryo-adsorbed hydrogen storage. *Energy Environ. Sci.* **2016**, *9* (10), 3279-3289.

72. Colón, Y. J.; Gómez-Gualdrón, D. A.; Snurr, R. Q., Topologically Guided, Automated Construction of Metal-Organic Frameworks and Their Evaluation for Energy-Related Applications. *Cryst. Growth Des.* **2017**, *17* (11), 5801-5810.

73. O'Keeffe, M.; Peskov, M. A.; Ramsden, S. J.; Yaghi, O. M., The Reticular Chemistry Structure Resource (RCSR) Database of, and Symbols for, Crystal Nets. *Acc. Chem. Res.* **2008**, *41* (12), 1782-1789.

74. Anderson, R.; Gómez-Gualdrón, D. A., Increasing topological diversity during computational "synthesis" of porous crystals: how and why. *CrystEngComm* **2019**, *21* (10), 1653-1665.

75. Boyd, P. G.; Moosavi, S. M.; Witman, M.; Smit, B., Force-Field Prediction of Materials Properties in Metal-Organic Frameworks. *J. Phys. Chem. Lett.* **2017**, *8* (2), 357-363.

76. Plimpton, S., Fast Parallel Algorithms for Short-Range Molecular Dynamics. *J. Comput. Phys.* **1995**, *117* (1), 1-19.

77. Dubbeldam, D.; Calero, S.; Ellis, D. E.; Snurr, R. Q., RASPA: molecular simulation software for adsorption and diffusion in flexible nanoporous materials. *Mol. Simul.* **2016**, *42* (2), 81-101.

78. Martin, M. G.; Siepmann, J. I., Transferable Potentials for Phase Equilibria. 1. United-Atom Description of n-Alkanes. *J. Phys. Chem. B* **1998**, *102* (14), 2569-2577.

79. Martin, R. L.; Smit, B.; Haranczyk, M., Addressing Challenges of Identifying Geometrically Diverse Sets of Crystalline Porous Materials. *J. Chem. Inf. Model.* **2012**, *52* (2), 308-318.

80. Willems, T. F.; Rycroft, C. H.; Kazi, M.; Meza, J. C.; Haranczyk, M., Algorithms and tools for high-throughput geometry-based analysis of crystalline porous materials. *Microporous Mesoporous Mater.* **2012**, *149* (1), 134-141.

81. Pinheiro, M.; Martin, R. L.; Rycroft, C. H.; Jones, A.; Iglesia, E.; Haranczyk, M., Characterization and comparison of pore landscapes in crystalline porous materials. *J. Mol. Graph. Model.* **2013**, *44*, 208-219.

82. Pinheiro, M.; Martin, R. L.; Rycroft, C. H.; Haranczyk, M., High accuracy geometric analysis of crystalline porous materials. *CrystEngComm* **2013**, *15* (37), 7531-7538.

83. Martin, R. L.; Haranczyk, M., Construction and Characterization of Structure Models of Crystalline Porous Polymers. *Cryst. Growth Des.* **2014**, *14* (5), 2431-2440.

84. Ongari, D.; Boyd, P. G.; Barthel, S.; Witman, M.; Haranczyk, M.; Smit, B., Accurate Characterization of the Pore Volume in Microporous Crystalline Materials. *Langmuir* **2017**, *33* (51), 14529-14538.

85. Ahrens, J.; Geveci, B.; Law, C. In ParaView: An End-User Tool for Large-Data Visualization, *The Visualization Handbook*, **2005**.

86. Talu, O.; Myers, A. L., Molecular simulation of adsorption: Gibbs dividing surface and comparison with experiment. *AIChE J.* **2001**, *47* (5), 1160-1168.

87. Widom, B., Some Topics in the Theory of Fluids. *J. Chem. Phys.* **1963**, *39* (11), 2808-2812.

88. Dullens, R. P. A.; Aarts, D. G. A. L.; Kegel, W. K.; Lekkerkerker, H. N. W., The Widom insertion method and ordering in small hard-sphere systems. *Mol. Phys.* **2005**, *103* (21-23), 3195-3200.

Chapter 2

Porous colloidal hydrogels formed by coordination-driven self-assembly of charged metal-organic polyhedra

Abstract

Introduction of porosity into supramolecular gels endows soft materials with functionalities for molecular encapsulation, release, separation and conversion. Metal-organic polyhedra (MOPs), discrete coordination cages containing an internal cavity, have recently been employed as building blocks to construct polymeric gel networks with potential porosity. However, most of the materials can only be synthesized in organic solvents, and the examples of porous, MOP-based hydrogels are scarce. Here, we demonstrate the fabrication of porous hydrogels based on $[Rh_2(OH\text{-}bdc)_2]_{12}$, a rhodium-based MOP containing hydroxyl groups on its periphery (OH-bdc = 5-hydroxy-1,3-benzenedicarboxylate). By simply deprotonating $[Rh_2(OH\text{-}bdc)_2]_{12}$ with the base NaOH, the supramolecular polymerization between MOPs and organic linkers can be induced in the aqueous solution, leading to the kinetically controllable formation of hydrogels with hierarchical colloidal networks. When heating the deprotonated MOP, $Na_x[Rh_{24}(O\text{-}bdc)_x(OH\text{-}bdc)_{24-x}]$, to induce gelation, the MOP was found to partially decompose, affecting the mechanical property of the resulting gels. By applying a post-synthetic deprotonation strategy, we show that the deprotonation degree of the MOP can be altered after the gel formation without serious decomposition of the MOPs. Gas sorption measurements confirmed the permanent porosity of the corresponding aerogels obtained from these MOP-based hydrogels, showing potentials for applications in gas sorption and catalysis.

Introduction

Supramolecular gels are fascinating soft materials formed by hierarchical self-assembly of low molecular weight gelators (LMWGs).[1] Utilizing noncovalent interaction such as hydrogen bonding, metal-ligand coordination, hydrophobic or electrostatic interactions, well designed LMWGs self-assemble to form supramolecular networks, which show unique properties for applications in separation, drug-delivery, tissue engineering, sensing and optoelectronic devices.[2-4] Among the efforts to tune the gel structures and properties, endowing supramolecular gels with predefined cavities is expected to imbue these soft materials with additional functionalities based on their potential host-guest chemistry.[5-7] In particular, hydrogels formed from the cavity-containing LMWGs are of special interest because they offer great promise in biological and environmental applications such as drug delivery and pollutants

removal, which can make full use of the cavity-based host-guest chemistry.[8-10] Most examples of cavity-containing LMWGs reported so far are limited to traditional organic macrocycles, such as cucurbit[n]urils,[11] cyclodextrins,[12] calix[n]arenes[13] and pillar[n]arenes[14]. Even though these macrocycles provide a well-defined host environment for guest molecules inside hydrogels, chemical synthesis of water-soluble macrocycles with tunable cavity sizes, shapes and surface functionality are still challenging.[15,16]

Coordination-driven self-assembly can be used to prepare cavity-containing molecules with well-defined sizes and shapes.[17-20] Among them, metal-organic cages (MOCs) or metal-organic polyhedra (MOPs), a class of coordination cages with well-defined internal cavities, are potential precursors to incorporate cavities into hydrogels.[21-24] By designing reactive binding sites on the periphery of cages, MOPs have been employed as building blocks to assemble or crosslink with other molecular units into 2D or 3D extended frameworks.[25-30] Specifically, by reacting with polymer linkers, MOPs have been integrated into supramolecular gels with diverse properties, including guest encapsulation, self-healing and stimuli sensitivity.[31-35] Recently, we reported the fabrication of supramolecular gels based on rhodium-based cuboctahedral MOPs, $[Rh_2(C_{12}\text{-bdc})_2]_{12}$ (**C_{12}RhMOP**; C_{12}-bdc = 5-dodecoxybenzene-1,3-dicarboxylate) or $[Rh_2(bdc)_2]_{12}$ (**HRhMOP**; bdc = benzene-1,3-dicarboxylate) with shorter linker, 1,4-bis(imidazol-1-ylmethyl)benzene (**bix**), by controlling the self-assembly pathway.[36-39] Compared to macrocyclic molecules, the size, shape and chemical functionality of MOPs can be easily tuned by ligand design with easily accessible molecules, leading to supramolecular gels with varied host-guest chemistry.[40-42] However, only a few hydrogels assembled from MOPs are reported to date,[43-46] most likely because most reported MOPs are based on copper paddlewheel motifs and thus unstable in aqueous solution. Another hurdle is their poor solubility in polar solvents, further preventing the use of MOPs as gelators in the synthesis of hydrogels.[47-50] To expand the potential of MOPs for further applications a strategy to develop MOP-based hydrogels is essential.

Herein, we report the synthesis of supramolecular hydrogels based on a hydrophilic MOP, $[Rh_2(OH\text{-bdc})_2]_{12}$ (**OHRhMOP**; OH-bdc = 5-hydroxy-1,3-benzenedicarboxylate) with 24 hydroxyl groups (-OH) on its periphery (Figure 1).[51-52] The solubility of **OHRhMOP** and its kinetically trapped molecule, **OHRhMOP(bix)$_{12}$**, in water is greatly increased by partial deprotonation of the MOP to yield the forms **ONaRhMOP** and **ONaRhMOP(bix)$_{12}$**, respectively. Deprotonation enables the synthesis of supramolecular hydrogels despite the poor solubility of **bix** itself in water. We demonstrate that the deprotonation degree, which corresponds to the fraction of deprotonated -OH groups per MOP, plays a key role in the gel formation, the mechanical properties of resulting hydrogels and the partial decomposition of

MOPs. To avoid the decomposition, an alternative route towards the hydrogels was investigated by post-synthetically tuning the deprotonation degree of MOPs within the hydrogels. Gas sorption measurements were performed on the corresponding aerogels to confirm that the cavities of the MOPs are intact inside the gels. Depending on the deprotonation degree of MOPs in the gels, their water sorption behavior can be tuned.

Result and discussion

Our previous studies showed that the key for successful supramolecular polymerization of MOPs is to isolate so-called kinetically trapped molecules with linkers coordinating in a monodentate fashion. In our previous investigations with **C_{12}RhMOP** and **HRhMOP**,[37,38] both trapped molecules were first formed with bix linkers as **RhMOP(bix)$_{12}$**, which were isolated in DMF with good solubility. However, **C_{12}RhMOP**, **HRhMOP** and **bix** are insoluble in water. Therefore, we used the more polar MOP, **OHRhMOP** which has hydroxyl functionalities on its periphery, as a precursor for the polymerization in aqueous solution. We checked the solubility of **OHRhMOP** in water or water/organic mixing solvents and found that **OHRhMOP** displays good solubility in water/acetonitrile (7:5 v/v) mixtures compared to pure water or pure acetonitrile, which does not dissolve the MOPs. This good solubility is most likely attributed to the coordination of acetonitrile molecules (MeCN) to **OHRhMOP** to form **OHRhMOP(MeCN)$_{12}$**, which was confirmed by a color change from green to purple with a shift of maximum absorption peak in UV-visible spectra as discussed later. As **bix** is well dissolved in the same solvent mixture, this water/acetonitrile system ought to be suitable for the isolation of trapped molecules of **OHRhMOP(bix)$_{12}$**.

A solution of 12 equivalent (eq.) of **bix** in water/acetonitrile was added to the solution of **OHRhMOP**, leading to unexpected precipitation. Analysis by ^{1}H NMR experiments confirmed the obtained solid to be the kinetically trapped molecule **OHRhMOP(bix)$_{12}$** (Figure 2-1). This suggests that the solubility of the trapped molecules was not high enough to be isolated in the mixed solution. In order to improve the solubility, the phenolic hydroxyl groups of **OHRhMOP** were deprotonated to yield a salt form of the MOP with sodium ions as **ONaRhMOP** before the addition of **bix**. The solution of **OHRhMOP** was deprotonated to different degrees by the addition of NaOH at different relative concentrations (1, 6, 12 or 24 eq. relative to **OHRhMOP**). Dynamic light scattering (DLS) measurements of these solutions after deprotonation showed a number-weighted size distribution in the range of 1-3 nm, confirming the solubility of these deprotonated MOPs (Figure 2-2a). After concerted addition of 12 mol eq. of bix into the basic solution of **ONaRhMOP**, there is no obvious change in the size distribution, which showed the presence of isolated trapped molecules of an average size of 1-3 nm (Figure 2-2c). Therefore,

it was concluded that deprotonation was effective to solubilize the resulting trapped molecules, **ONaRhMOP(bix)$_{12}$**, in the water/acetonitrile mixture, and their solubility were not affected by the deprotonation degree.

To study the coordination environment of kinetically trapped molecules of **ONaRhMOP(bix)$_{12}$**, the UV-visible spectroscopy was measured before and after the addition of **bix** (Figure 2-2b and d). Due to the coordination of acetonitrile to the MOPs, an absorption maximum of the band (λ_{max}), associated with the π*-σ* transition of the dirhodium paddlewheel moiety, was observed at 559 nm for the solution of **ONaRhMOP** (Figure 2-2b), which can be assigned to the chromophore of rhodium paddlewheel complex with two acetonitrile molecules coordinating on the axial sites (Figure 2-3).[39,53] Note that this shift was independent from the deprotonation degree. After the addition of 12 eq. of **bix** to the **ONaRhMOP** solution with 1 eq. NaOH, the λ_{max} was further shifted to 540 nm (Figure 2-2d). This further blue-shift is explained by the exchange of acetonitrile molecules coordinated to exohedral Rh sites of **ONaRhMOPs** by **bix** due to the higher coordinative affinity of imidazole on **bix**. As **bix** is too big to enter the pores of MOPs, the acetonitrile coordinated to internal Rh inside the MOPs remained without being exchanged by **bix**. This shift was confirmed with the control experiments with rhodium acetate ([$Rh_2(OAc)_4$]); the coordination of 1 eq. monodentate imidazole ligand, 1-dodecyl-1H-imidazole (**diz**), led to the same λ_{max} at 540 nm in acetonitrile (Figure 2-3).

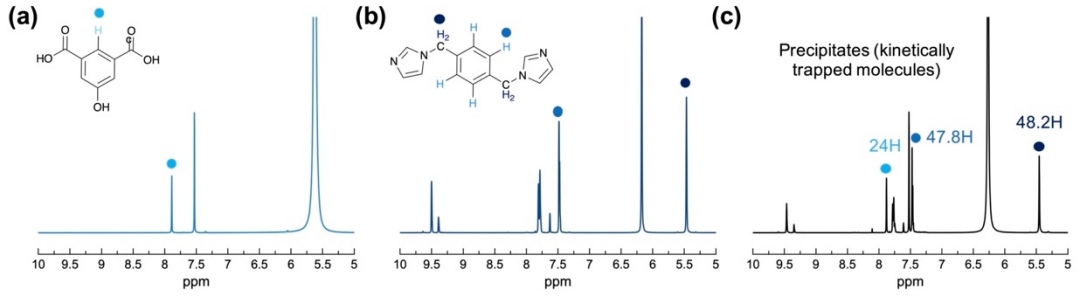

Figure 2-1. (a) ^{1}H NMR spectrum of OH-bdc treated with the same conditions used to digest gel samples. (b) ^{1}H NMR spectrum of **bix** treated with the same conditions used to digest gel samples. (c) ^{1}H NMR spectrum of acid digested solid precipitates obtained by adding 12 eq. **bix** into the solution of **OHRhMOP** without deprotonation. The characteristic proton of OH-bdc and bix used for the calculation of molecular formula was labeled by the light blue and dark blue circles, respectively. The protons of OH-bdc in the precipitates and gel samples were used for the estimation of **MOP**. Based on the integration, the solid precipitates obtained has a composition of **OHRhMOP(bix)$_{12}$**, indicating the formation of trapped molecules.

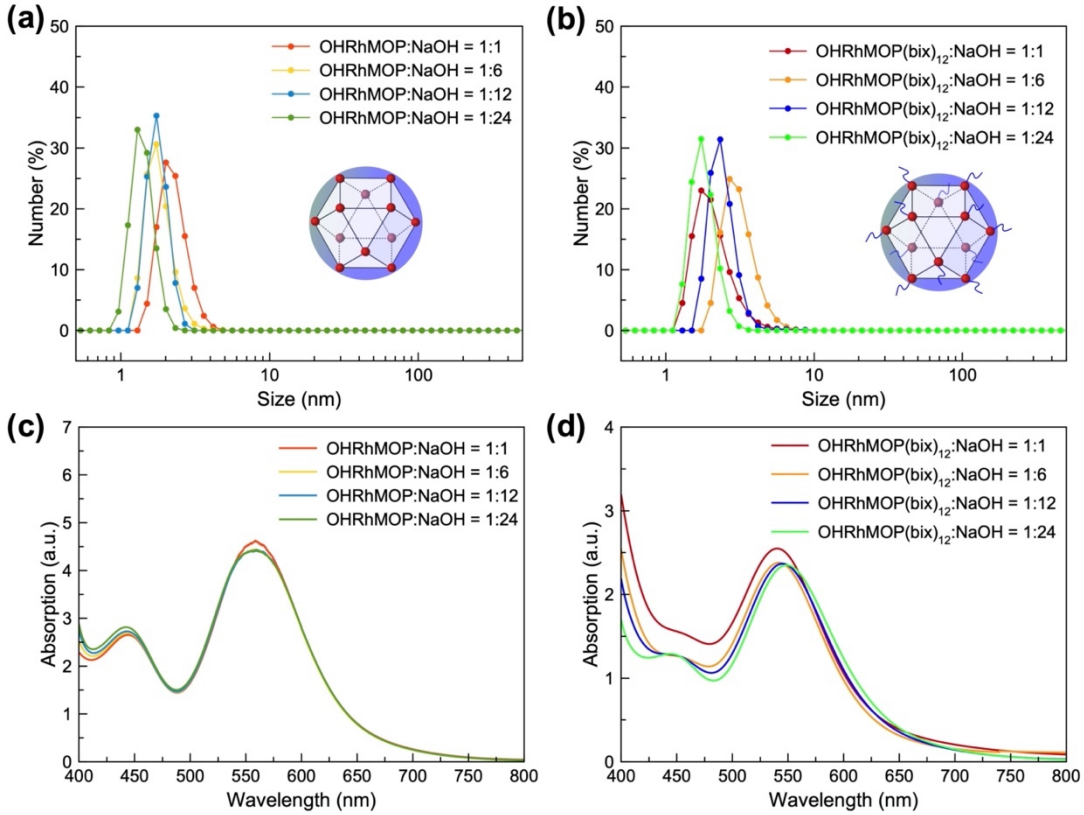

Figure 2-2. DLS measurement of (a) **ONaRhMOP** and (b) **ONaRhMOP(bix)$_{12}$** in the mixing solution at different deprotonation degrees. UV-visible spectra of (a) **ONaRhMOP** and (d) **ONaRhMOP(bix)$_{12}$** in the mixing solution at different deprotonation degrees.

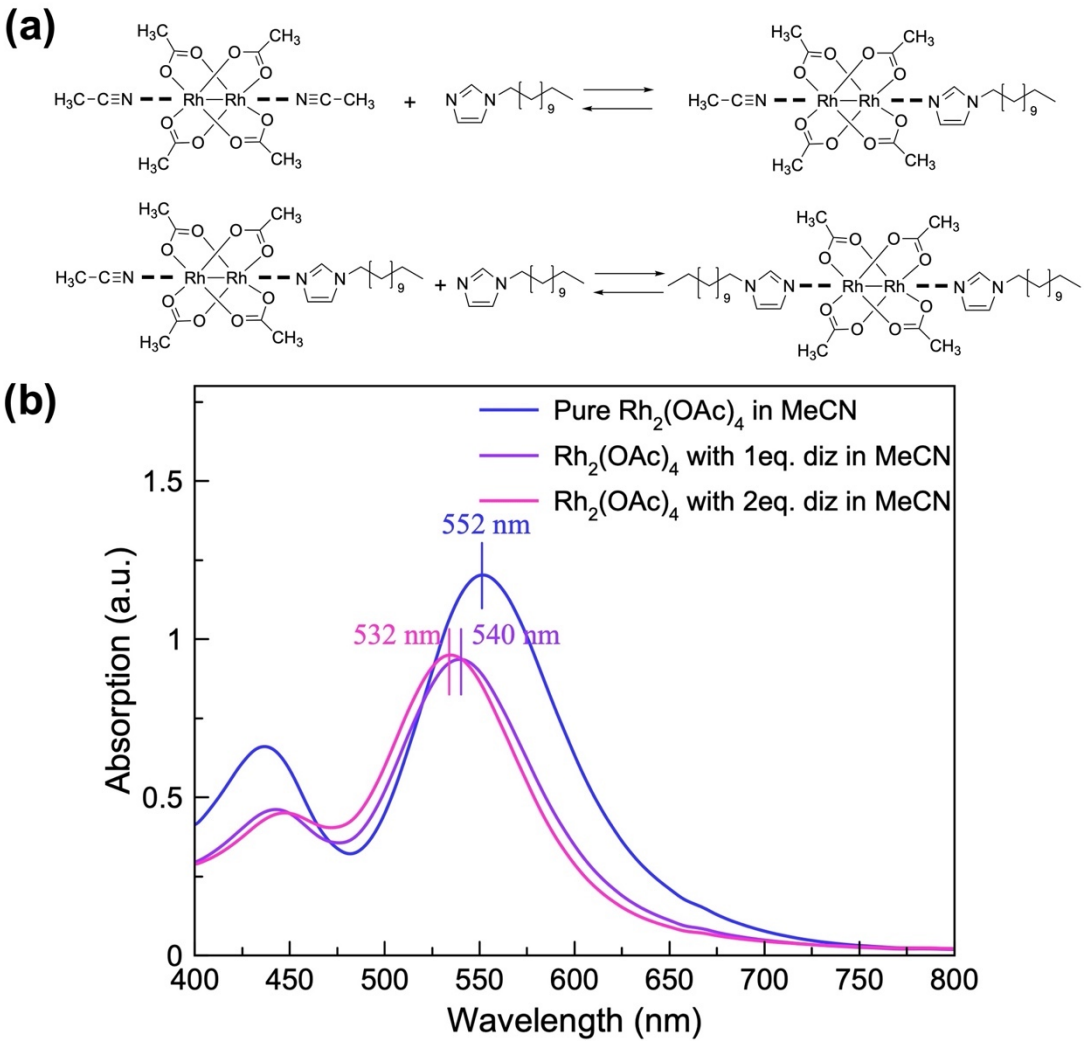

Figure 2-3. (a) Reaction scheme of [$Rh_2(OAc)_4$] with model compound, 1-dodecyl-1H-imidazole (**diz**), in acetonitrile. (b) UV-visible spectroscopy of the solution of [$Rh_2(OAc)_4$] with 0, 1 and 2 mol. eq. of **diz** in acetonitrile.

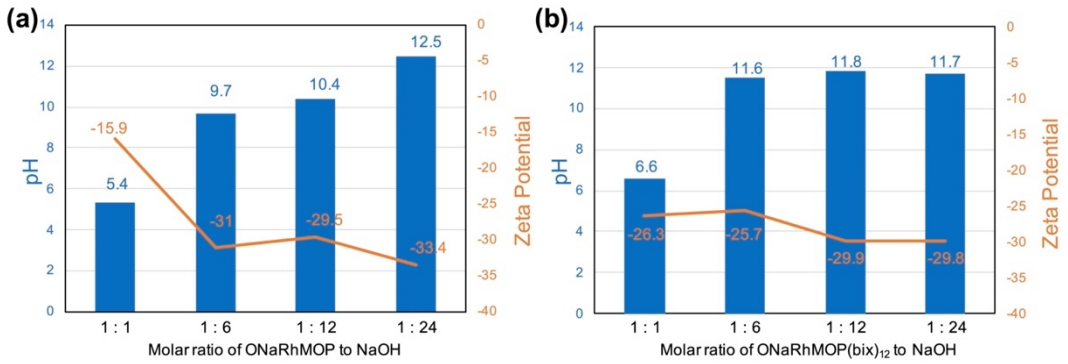

Figure 2-4. pH and zeta potential of the solution of deprotonated (a) **ONaRhMOP** and (b) **ONaRhMOP(bix)$_{12}$** in water/acetonitrile mixture at different NaOH concentration.

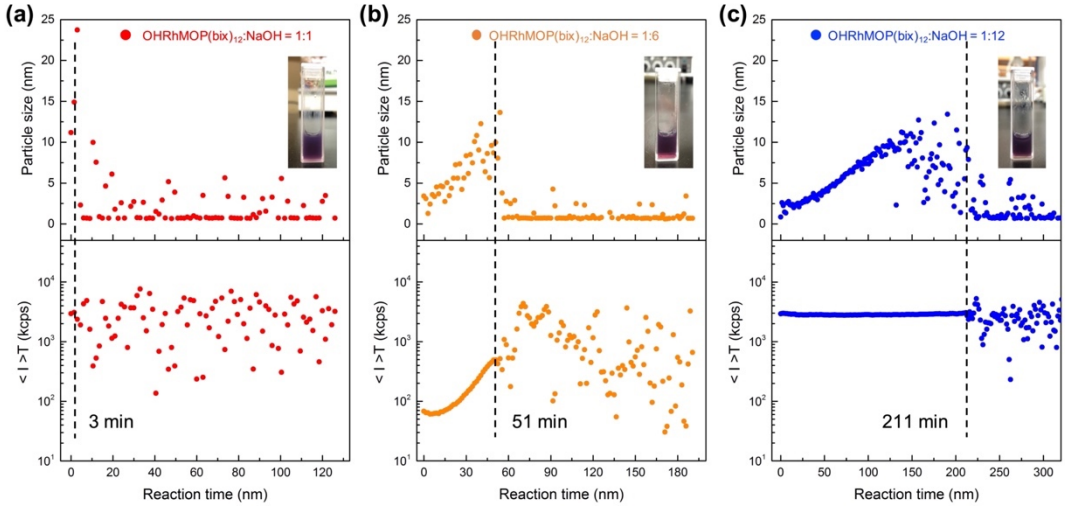

Figure 2-5. Time-resolved dynamic light scattering (DLS) experiments during the supramolecular polymerization of **ONaRhMOP(bix)$_{12}$** at 60ºC at a concentration of 0.93mM, showing the particle size evolution and the time-averaged scattering intensity as a function of time. Systems with different molar equivalent of NaOH relative to MOP were prepared: (a) 1 eq., (b) 6 eq., (c) 12 eq.

To initiate the polymerization between trapped molecules, the solution **ONaRhMOP(bix)$_{12}$** (0.93 mM) was heated at 60 ºC to initiate the removal of the **bix** molecules from the surface of **ONaRhMOP** and to expose the axial exohedral rhodium sites of the MOPs for the subsequent coordination with neighboring trapped **ONaRhMOP(bix)$_n$** molecules. Indeed, transparent gels were successfully obtained for all samples except for the solution with 24 eq. of NaOH. The time-resolved DLS measurements showed the evolution of particle size as a function of time upon heating for the **ONaRhMOP(bix)$_{12}$** solution with 1, 6 and 12 eq. NaOH (Figure 2-5). Once the polymerization begins, the trapped MOP molecules are hierarchically assembled into colloidal particles, leading to a steep increase in particle size. By further forming colloidal networks, the general mobility of the particles is frozen and the diffusion is stopped, rendering reliable measurement of the particle size impossible. To determine the sol-gel transition point, changes in the time-averaged scattering intensity, $\langle I \rangle_T$, were plotted as a function of time, where the time at which random fluctuations appear corresponds to the gelation point.[39] The results show that, as the NaOH concentration increases, the gelation time is markedly delayed from 3 mins to 211 mins. Finally, when the 24 eq. of NaOH was added, no gelation occurs. This delay in gelation can be attributed to the electrostatic repulsion between the deprotonated MOPs. The more -OH groups on the MOPs are deprotonated, the more negatively charged is the resulting **ONaRhMOP**. This negative charge on the MOP molecules is confirmed by zeta-potential measurements (Figure 2-6). As a consequence, these trapped molecules are mutually repelled, thus hindering polymerization or

crosslinking. For the **ONaRhMOP(bix)$_{12}$** deprotonated at the highest concentration of NaOH (24 eq.), this electrostatic repulsion between them is too strong to allow the polymerization to occur.

Based on the DLS results, a series of gels with various deprotonation degrees were synthesized by heating the solution of kinetically trapped **ONaRhMOP(bix)$_{12}$** (see gelation conditions in Table 1). After the gelation, as-synthesized gels within the mixing solvent of water/acetonitrile were washed with fresh water/acetonitrile twice, followed by replacing the mixing solvents with distilled water for three times to yield the final hydrogel samples, named as **Gel$_1$-x** (x indicates the relative molar ratio of NaOH added to MOP). Removal of acetonitrile from these hydrogels was confirmed by ^{1}H NMR analysis of the digested wet gel samples, showing the disappearance of the characteristic peak of acetonitrile at 2.07 ppm (Figure 2-7). Rheological measurements were performed to establish the storage Young's modulus as frequency-independent ($E' \approx 3.8$ kPa and 3.4 kPa for **Gel$_1$-1** and **Gel$_1$-6**, respectively) and one order of magnitude higher than the loss modulus (Figure 2-8a). The sample of **Gel$_1$-12**, however, was too fragile to be self-standing and broke upon handling (Figure 2-6). Therefore, it seems that the deprotonation degree of the MOPs affects not only the gelation kinetics, but also the mechanical properties of the resulting hydrogels, which becomes more fragile at higher deprotonation degree.

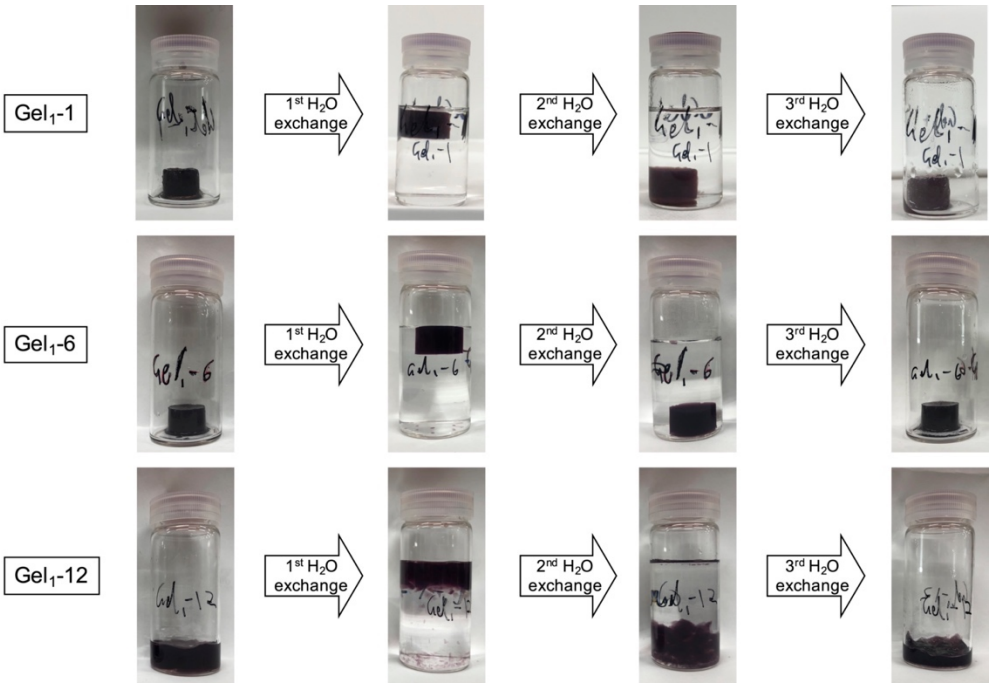

Figure 2-6. Photos of the process of water exchange to prepare **Gel$_1$-x** hydrogels.

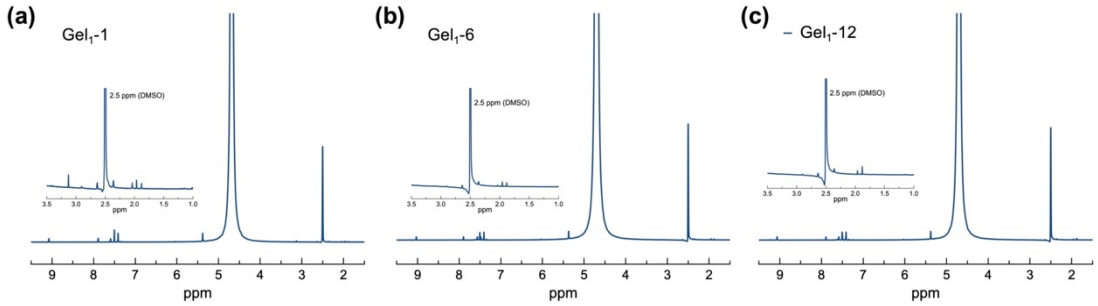

Figure 2-7. ^{1}H NMR spectra of acid-digested wet gels, (a) **Gel$_1$-1**, (b) **Gel$_1$-6**, (c) **Gel$_1$-12** and (d) **Gel$_2$-1** after exchange with fresh water for 3 days. No obvious proton of acetonitrile molecule can be observed in all the gel samples, confirming the complete removal of acetonitrile from the gels.

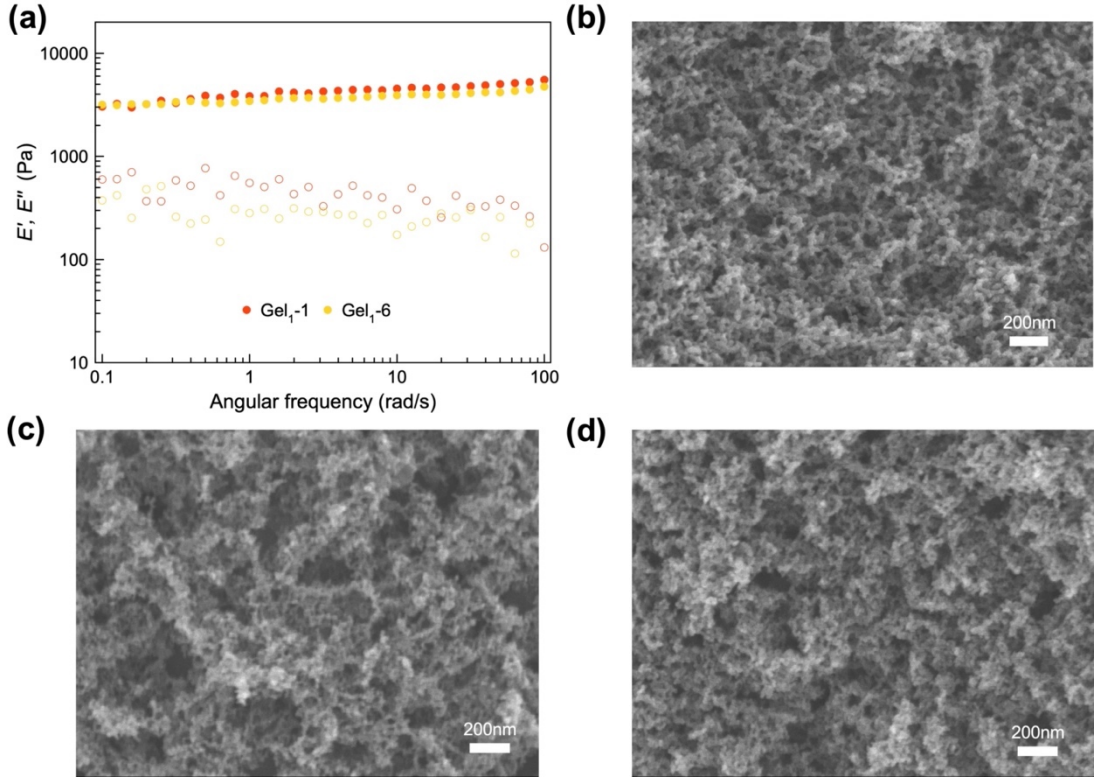

Figure 2-8. (a) Storage Young's modulus (E′) (filled circles) and loss Young's modulus (E") (hollow circles) of **Gel$_1$-1** and **Gel$_1$-6** versus scanning frequency (ω). Representative SEM image of (b) **Aerogel$_1$-1**, (c) **Aerogel$_1$-6** and (d) **Aerogel$_1$-12**.

Similar to the previously reported organogels assembled from **HRhMOP** and **C$_{12}$RhMOP**,[37,38] the characteristic colloidal networks of all **Gel$_1$-x** were revealed by the scanning electron microscopy (SEM) measurements. In the SEM images of their corresponding aerogels, **Aerogel$_1$-x**, which were prepared by replacing water in the gels with acetone for three times and then supercritical CO_2 drying, similar colloidal networks were observed for all samples and the structures were not affected by the deprotonation degree (Figure 2-8). ^{1}H NMR

analysis of the acid-digested aerogels was performed to identify the ratio of **bix**/MOP within the **Gel$_1$-x** samples (Figure 2-9). Contrary to our expectation, the **bix**/MOP ratio was estimated to be higher than 12 for all **Gel$_1$- x** samples, as listed in Table 1; the compositions of **Gel$_1$-1**, **Gel$_1$-6** and **Gel$_1$-12** are $Na_1[Rh_{24}(O\text{-}bdc)_1(OH\text{-}bdc)_{23}](\mathbf{bix})_{13.3}$, $Na_6[Rh_{24}(O\text{-}bdc)_6(OH\text{-}bdc)_{18}](\mathbf{bix})_{14.2}$ and $Na_{12}[Rh_{24}(O\text{-}bdc)_{12}(OH\text{-}bdc)_{12}](\mathbf{bix})_{14.4}$, respectively. Considering that only 12 eq. **bix** was added into the MOP solution for gelation and that the crosslinking of intact cages is only possible with **bix**/MOP ratio lower than 12, the higher **bix**/MOP ratio over 12 can be attributed to the decomposition of **ONaRhMOP**. Despite the good stability of **OHRhMOP** in water, the heating process of the basic solution of isolated **ONaRhMOP(bix)$_{12}$** most likely induced the decomposition of **ONaRhMOP**. Hydrolysis of acetonitrile molecules has been reported when heated in the presence of water and strong base like NaOH, leading to the generation of sodium acetate and ammonia,[54] which might cause the decomposition of MOP. It seems that the dissociated ligands of ONa-bdc were washed away during the washing process, leading to the increase of the **bix**/ONa-bdc ratio and thus the increase of **bix**/MOP ratio when the composition was estimated by ^{1}H NMR (Figure 2-9). Note that **bix**/MOP ratio continuously increased from 13.3 of **Gel$_1$-1** to 14.2 of **Gel$_1$-12** with increasing the NaOH concentration, suggesting a serious decomposition with higher NaOH concentration. To further confirm the MOP decomposition, ^{1}H NMR analysis was performed to detect the free molecules in the supernatants of the washing solvent of water/acetonitrile (Figure 2-10). The characteristic peaks of **bix** and ONa-bdc were observed for all **Gel$_1$-x** samples and the relative ONa-bdc/bix ratio in the supernatant increased from 1.0 for the **Gel$_1$-1** to 2.4 for the **Gel$_1$-12**. Therefore, we can rationalize the increase of **bix**/MOP ratio in gel composition to be the decomposition of a small proportion of the MOP cages by removal of ONa-bdc linkers, which are then washed away in the washing process.

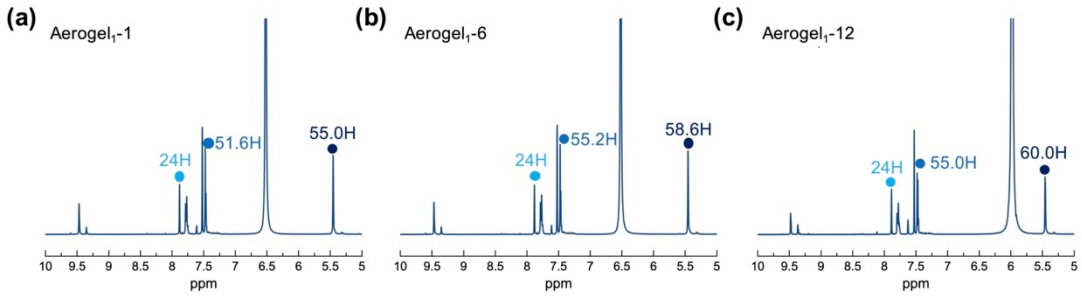

Figure 2-9. ^{1}H NMR spectra of the acid digested aerogel, (a) **Gel$_1$-1**, (b) **Gel$_1$-6** and (c) **Gel$_1$-12**.

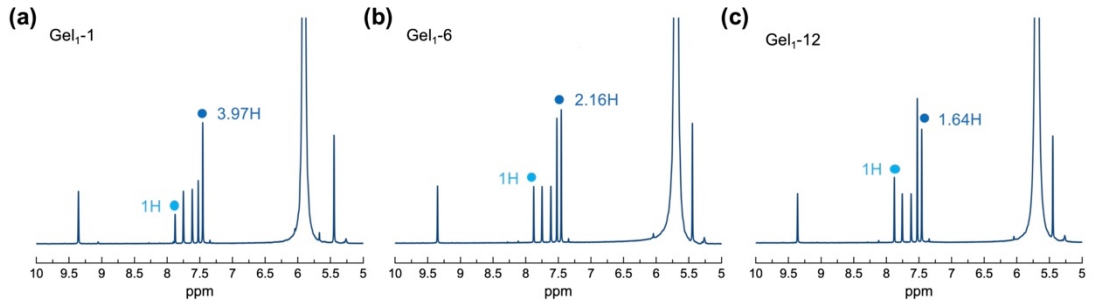

Figure 2-10. ^{1}H NMR spectra of the acid digested residues obtained from the upper washing solvent of (a) **Gel1-1**, (b) **Gel1-6**, (c) **Gel1-12**.

Table 1. Gelation condition and NMR composition of **Gel$_1$-x** and **Gel$_2$-x** samples.

Sample	Mol_{MOP} : Mol_{NaOH}	Gelation condition	**bix**/MOP molar ratio
Gel$_1$-1	1:1	60 ºC for 4h	13.3
Gel$_1$-6	1:6	60 ºC for 8h	14.2
Gel$_1$-12	1:12	60 ºC for 12h	14.4
Gel$_2$-1	1:1	60 ºC for 4h	13.4
Gel$_2$-6	1:6	60 ºC for 4h	13.4
Gel$_2$-12	1:12	60 ºC for 4h	13.4
Gel$_2$-24	1:24	60 ºC for 4h	13.1

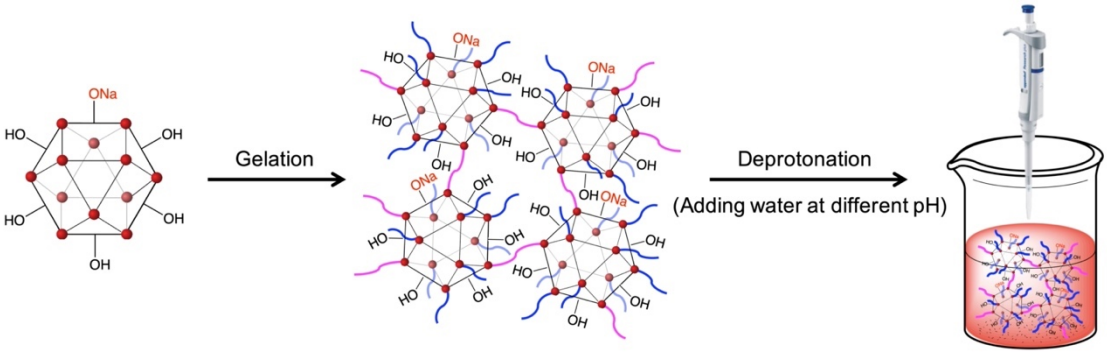

Figure 2-11. Schematic representation of the deprotonation of the hydrogel samples post-synthetically by immersing the as-synthesized gels in water within fix pH. By measuring the change of pH before and after deprotonation, the amount of NaOH consumed for deprotonation can be calculated, as listed in Table S2.

To prepare the MOP hydrogel with a high deprotonation degree but without detrimental MOP decomposition, we applied a post-synthetic deprotonation protocol after the gelation, as shown in Figure 2-11. The concentration of **OHRhMOP** for gelation here was increased from 0.93 mM to 1.4 mM to guarantee the mechanical stability for the deprotonation process (Figure

2-12 and 2-13). To ensure the solubility of the kinetically trapped molecules, only 1 eq. NaOH was added for the initial deprotonation, followed by gelation in the same condition as **Gel$_1$-1**. The obtained gel, named **Gel$_2$-1**, was then soaked for 3 days in water containing different content of NaOH to yield hydrogels named as **Gel$_2$-x** (x indicates the total ratio of NaOH to MOP, x = 1, 6, 12 and 24 here).

Deprotonation of **Gel$_2$-x** samples was evaluated by measuring the pH of the aqueous solution used for the post-synthetic deprotonation before and after immersion of the gel (Figure 2-11). For all samples, the pH of the solution dropped after the deprotonation process, as listed in Table 2. The amount of NaOH consumed during this process increased with increasing the NaOH concentration, and the resulting amount of hydroxyl groups deprotonated in one MOP was calculated to be 6.3, 10.9 and 22.7 for **Gel$_2$-6**, **Gel$_2$-12** and **Gel$_2$-24**, respectively. Note that the -OH groups in MOP are weakly acidic and that deprotonation here is under an equilibrium. Therefore, the calculated amount of consumed NaOH does not directly correspond to the true deprotonation degree. However, this result confirmed that the reaction equilibrium is successfully directed towards the deprotonation of the MOP at higher NaOH concentration. Because the post-synthetic deprotonation was performed at room temperature, the possible hydrolysis of acetonitrile can also be avoided unlike the former strategy where the pre-deprotonated MOP was used for gelation.

Rheology measurements revealed that all **Gel$_2$-x** samples had higher mechanical stiffness than **Gel$_1$-x** (for instance, $E' \approx 5.0$ kPa for **Gel$_2$-1** and $E' \approx 3.8$ kPa for **Gel$_1$-1**) due to the increasing concentration of MOPs used for gel formation (Figure 2-12 and 2-14), corresponding to our previous observation for the concentration-dependent mechanical properties of **C$_{12}$RhMOP** gels.[39] The SEM images of the corresponding aerogels showed the presence of hierarchical colloidal networks, which were not obviously damaged by the post-synthetic deprotonation process (Figure 2-16). Table 1 listed the composition of each **Gel$_2$-x** samples estimated from the ^{1}H NMR measurements of their digested aerogels (Figure 2-15). No obvious change of the **bix**/MOP ratio was observed even after the post-synthetic deprotonation. These results indicate that the post-synthetic method circumvents the serious decomposition of **ONaRhMOP** and maintains the mechanical stiffness of the gels at the high deprotonation degree.

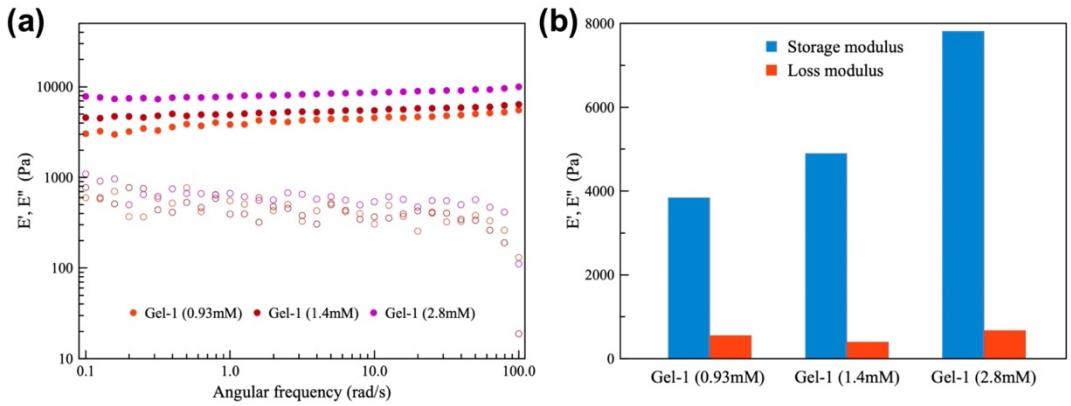

Figure 2-12. Storage Young's modulus (*E′*) (filled circles) and loss Young's modulus (*E″*) (hollow circles) of **Gel-1** at different concentration of MOP versus scanning frequency (ω).

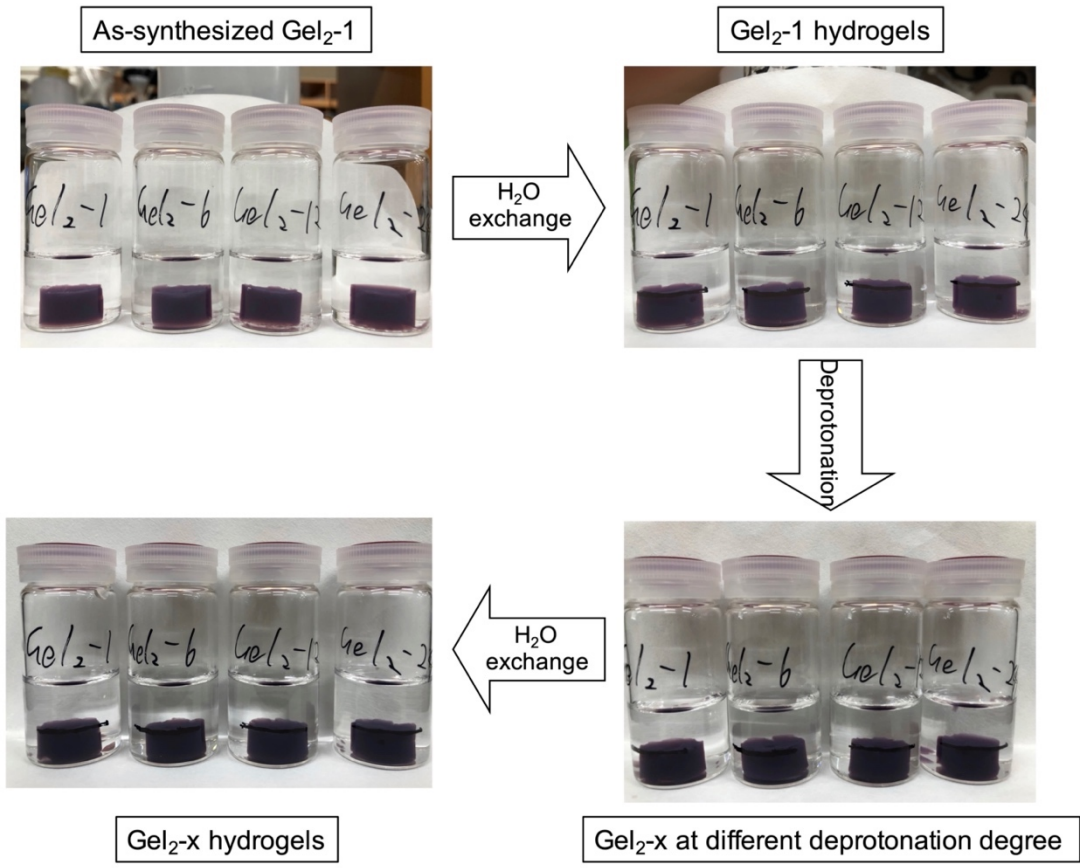

Figure 2-13. Photos of the process of water exchange to prepare **Gel₂-x** hydrogels.

Table 2. pH changes during the post-synthetic deprotonation and the amount of NaOH consumed.

Sample	pH of solution before deprotonation	pH of solution after deprotonation	NaOH consumed during deprotonation (mmol)	Expected amount of NaOH for deprotonation (mmol)
Gel$_2$-6	11.476	8.311	0.01475	0.01400
Gel$_2$-12	11.744	8.811	0.02769	0.03080
Gel$_2$-24	12.085	9.475	0.06080	0.06440

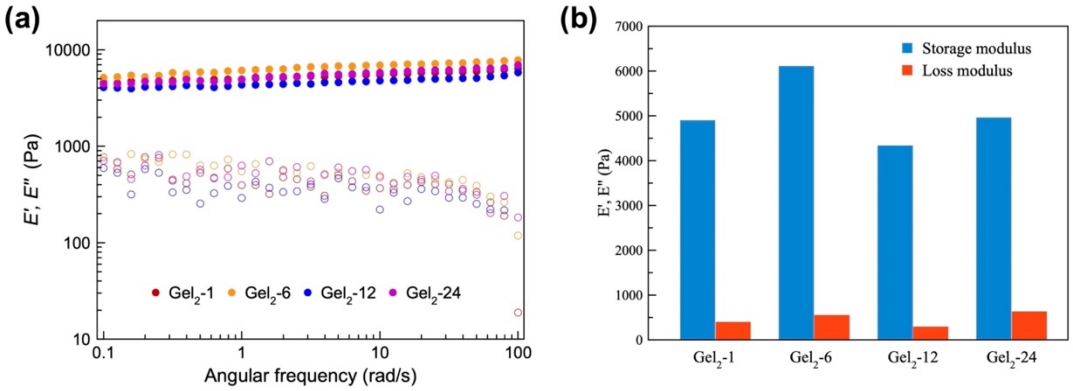

Figure 2-14. (a) Storage Young's modulus (E′) (filled circles) and loss Young's modulus (E") (hollow circles) of **Gel$_2$-1**, **Gel$_2$-6**, **Gel$_2$-12** and **Gel$_2$-24** versus scanning frequency (ω). (b).

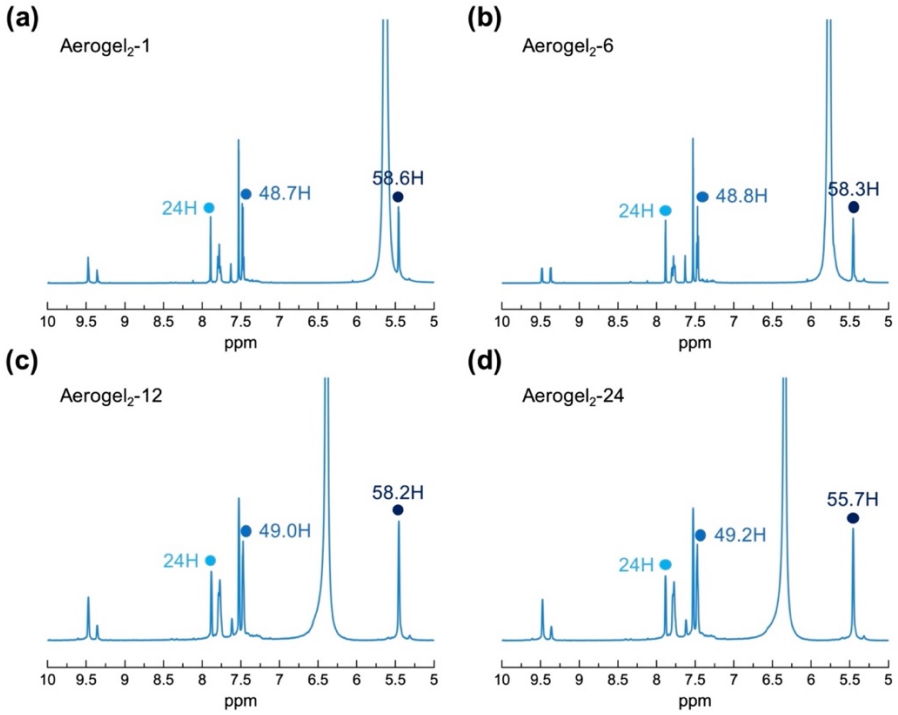

Figure 2-15. ^{1}H NMR spectrum of the acid digested aerogel, (a) **Gel$_2$-1**, (b) **Gel$_2$-6**, (c) **Gel$_2$-12** and (d) **Gel$_2$-24**.

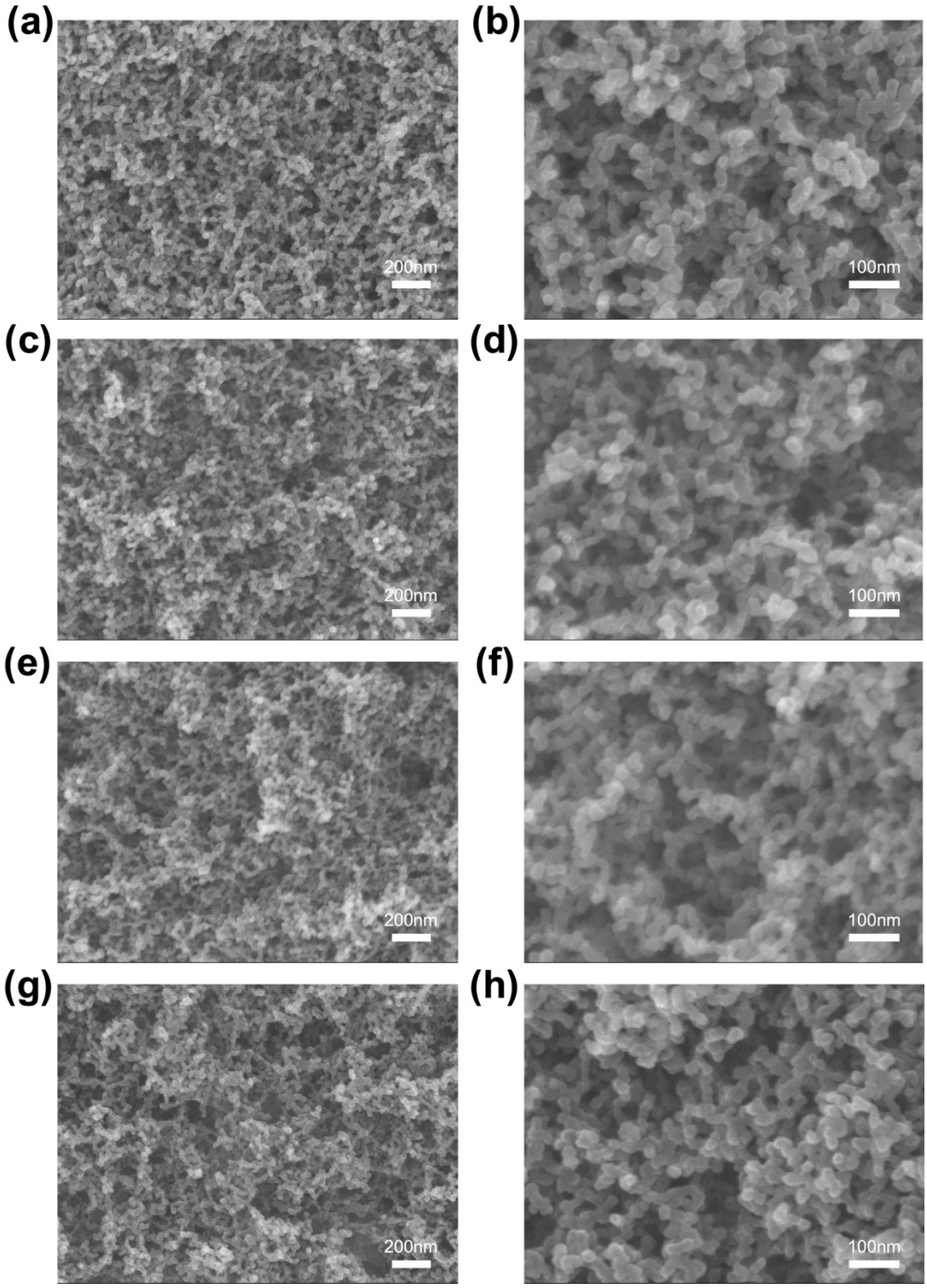

Figure 2-16. SEM images of the aerogels obtained after the Supercritical CO_2 drying of supramolecular gels: (a-b) **Gel$_2$-1**, (c-d) **Gel$_2$-6**, (e-f) **Gel$_2$-12** and (g-h) **Gel$_2$-24**.

In contrast to the polymer linker-based cavity-containing supramolecular gels, the use of shorter linker, **bix,** effectively prevents the MOP cavity to be blocked, which allows to maintain its permanent porosity within the hierarchical gel structures. Thanks to the good chemical stability of rhodium-based MOPs, the aerogels obtained here (**Aerogel$_1$-x** and **Aerogel$_2$-x**) are able to withstand the activation process at 120 ºC under vacuum, allowing us to study their porosity by gas adsorption measurements. Figure 2-17a and d showed the N_2 sorption isotherms of **Aerogel$_1$-x**, **Aerogel$_2$-x** and pure **OHRhMOP** powders. At 77 K, all aerogel samples displayed a sharp uptake of N_2 at the low-pressure region, characteristic of microporous materials. To analyze their microporosity, the pore size distribution (PSD) was calculated by non-local density functional theory (NLDFT). As shown in Figure 2-18, the pore at 0.65 nm observed in **OHRhMOP** was maintained in all the gel samples with the pore size centered at 0.61 nm. This indicates that, even though partial decomposition occurred, most of the MOP cavities were preserved inside the gel networks. In addition, the PSD of all aerogel samples showed the characteristic pore sizes at 1.4 and 2.8 nm, which were most likely attributed to the external pores generated by the linkage of MOPs and **bix** linkers. In the higher-pressure region, all aerogels showed a gradual increase of N_2 uptake, while the pure **OHRhMOP** presented no uptake. At pressures close to $P/P_0 \sim 1.0$, all aerogels showed a steep increase of N_2 adsorption, which should be related to the N_2 condensation on the surface of colloidal networks. CO_2 sorption measurements (195 K) of all aerogel samples were also performed to show a similar sorption behavior, again demonstrating the permanent porosity of the aerogels (Figure 2-17b and 6e). For **Aerogel$_1$-x**, the samples with higher deprotonation degrees seemed to show higher total uptakes of N_2 and CO_2. However, this difference might stem from the serious decomposition of MOPs and thus major change of the molecular composition of aerogels as discussed above. On the other hand, the post-synthetic deprotonation allowed us to circumvent the decomposition of **Aerogel$_2$-x.** As shown in Figure 6d and 6e, the sorption isotherms of this gel series looked almost identical to each other, which indicates that the deprotonation degree exerts negligible influence on the sorption behavior for these gas molecules.

The hydroxyl groups on the MOP surface and their subsequent deprotonation is hydrophilic and prone to affect the sorption behavior of gels, especially for polar guest molecules.[55-57] Figure 2-17c and f show the water vapor sorption isotherms of these aerogels at 298 K. Compared with the pure **OHRhMOP**, all **Aerogel$_1$-x** and **Aerogel$_2$-x** samples showed lower water uptakes in the low-pressure region, indicating the weaker affinity of aerogels for water molecules due to the incorporation of hydrophobic **bix** linkers. In the high-pressure region, greatly increased water uptakes were observed for the aerogels, which can be attributed to the existence of mesopores and macropores inside the aerogels. Notably, the water uptake

behavior of the gels at high-pressure region was obviously influenced by the deprotonation degree and the decomposition. Featuring similar gel structures, **Aerogel$_2$-x** samples show an increased affinity toward water upon increasing the deprotonation degree, as seen in the isotherm of **Aerogel$_2$-24**, which showed a steep water uptake at a lower pressure than the other **Aerogel$_2$-x** samples (x = 1, 6, 12). For the **Aerogel$_1$-x** series, similar to the sorption isotherms of N_2 and CO_2, the affinity of **Aerogel$_1$-x** toward water seems to be affected by the deprotonation and decomposition simultaneously, making it more complicated for further analysis. However, combined with the sorption results of **Aerogel$_2$-x**, it shows that the deprotonation degree does influence the water sorption behavior because of the high polarity of water.

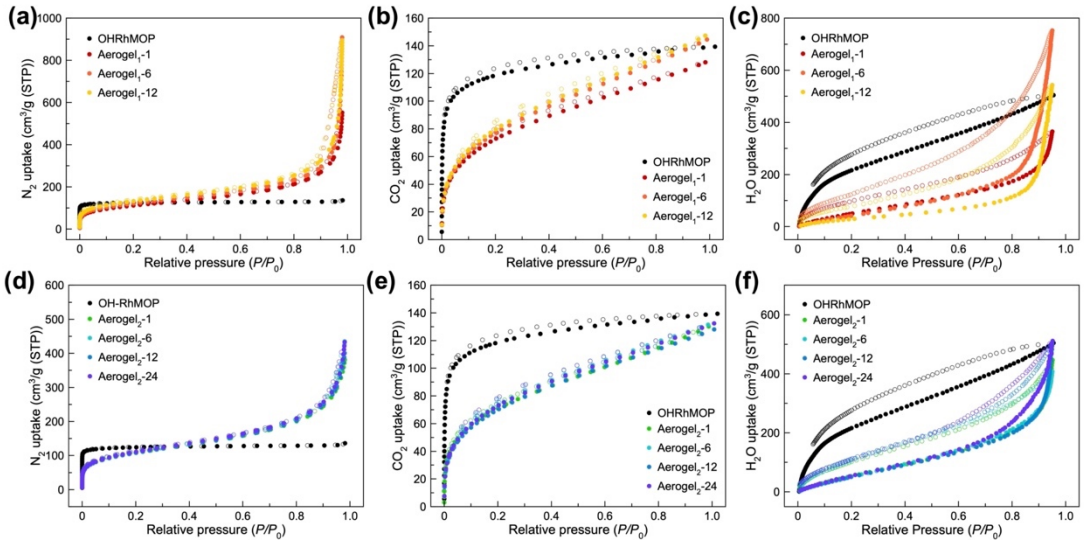

Figure 2-17. N_2 adsorption isotherm at 77 K for (a) **Aerogel$_1$-x** samples and (d) **Aerogel$_2$-x** samples. CO_2 adsorption isotherm at 195 K for (b) **Aerogel$_1$**-x samples and (e) **Aerogel$_2$**-x samples. H_2O vapor isotherm at 298 K for (c) **Aerogel$_1$**-x samples and (f) **Aerogel$_2$**-x samples.

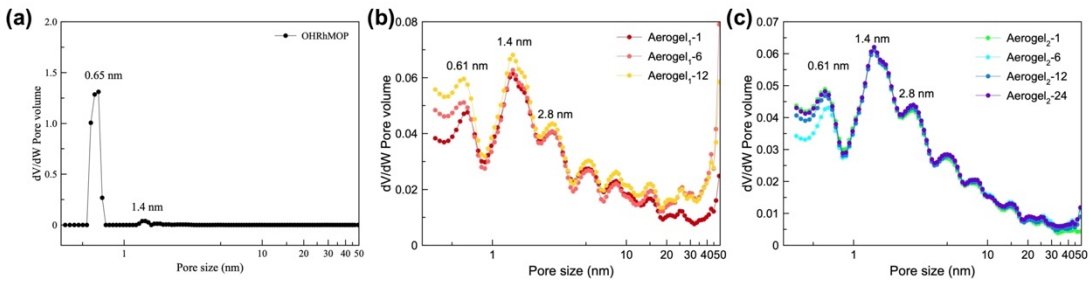

Figure 2-18. The pore size distribution of (a) **OHRhMOP**, (b) **Gel$_1$-x** aerogels and (c) **Gel$_2$-x** aerogels, as estimated by NLDFT from the N_2 gas sorption measurements at 77K.

Conclusion

In conclusion, we have demonstrated two different synthetic routes towards the fabrication of porous hydrogels based on the supramolecular polymerization of **OHRhMOP**. The hydroxyl groups on the periphery of MOPs are able to be deprotonated by the use of base, ensuring their solubility in aqueous solution for the subsequent self-assembly with organic linker, **bix**. Deprotonating the **OHRhMOP** prior to gelation was found to play an important role in the gel formation, in which the gelation kinetics was closely related to the electrostatic repulsion between deprotonated **ONaRhMOP**s. Directly reacting **ONaRhMOP**s with linker **bix** yielded charged gel networks with obvious MOP decomposition, which became more serious when increasing the deprotonation degree. To circumvent the decomposition of MOP, post-synthetic deprotonation was applied after the gel formation, leading to similar hydrogel structures but with a lesser degree of decomposition. The ^{1}H NMR, SEM and rheology measurements performed to compare these two gel systems showed the mechanical properties of the gels were strongly affected by the MOP decomposition. The permanent porosity of their corresponding aerogels was confirmed by the gas sorption measurements, in which MOP deprotonation was found to influence the water sorption behavior. Further study on the decomposition mechanism and structural control of the porous MOP-based hydrogels is ongoing.

Experimental section

Materials

Rhodium acetate[59] and 1,4-bis(imidazol-1-ylmethyl)benzene (**bix**)[37] were synthesized according to a previously reported procedure. 5-hydroxy-1,3-benzenedicarboxylic acid were purchased from Sigma-Aldrich and used as received. Solvents were purchased from Wako Pure Chemical Industries except those at HPLC grade were purchased from Fischer Chemicals.

Characterizations

The rheological measurements of the gels were made using a stress-controlled AR-G2 (TA Instruments, New Castle, DE, USA) rheometer. Gel samples after synthesis were transferred into a clean glass slide (~ 1 mm in thickness). Then the gel was loaded into the rheometer with the glass slide to perform the rheology tests. The measurements of gels were conducted by frequency sweeping in a compression mode with a 1% strain amplitude that was well inside the linear regime (initial strain is fixed to 1.5%).

The super-critical CO_2 drying process was carried out on SCLEAD-2BD autoclave (KISCO) using super-critical CO_2 at 14 MPa and 50 °C.

Scanning Electron Microscopy (SEM) of the microstructures of the aerogel samples were observed using a field-emission scanning electron microscope with a JEOL Model JSM-7001F4 system operating at 10 kV and 5 mA current. The samples were coated with 28 nm Osmium before measurement.

^{1}H NMR spectra were recorded on a Bruker Biospin DRX-600 (600 MHz) spectrometer. For ^{1}H-NMR analysis, 5 mg of aerogel sample was digested in a mixture of DMSO-d_6 (750 µl) and DCl (50 µl). The mixture was then heated at 100 °C overnight to obtain a yellow solution.

N_2 (77 K) and CO_2 (195K) gas sorption isotherms of the MOPs and aerogels were recorded on a BELSORP-mini volumetric adsorption instrument from BEL Japan Inc. Prior to gas sorption measurement, the samples were activated at 120 °C for 12 h.

H_2O vapor (298 K) sorption isotherms of the MOPs and aerogels were recorded on a BELSORP-AQUA2 volumetric adsorption instrument from BEL Japan Inc. Prior to gas sorption measurement, the samples were activated at 120 °C for 12 h.

UV-visible spectroscopy of the MOP solutions were performed in a V-670 spectrophotometer (JASCO).

Time-resolved dynamic light scattering (TRDLS) experiment and zeta potential of the MOP solutions were performed on a Zetasizer Nano ZS instrument (Malvern Instruments, Malvern, UK). The light source was a HeNe laser working at $\lambda = 633$ nm. The observations were made at the backscattering angle $\theta = 173^{o}$. The time dependence of particle size and the time-averaged scattering intensity during gelation process was evaluated at 60 ºC for 4 hours.

Detailed synthesis

Synthesis of precursors

1,4-bis(imidazole-1-ylmethyl)benzene (bix) and OHRhMOP were synthesized according to our previous reports.[37,51]

Synthesis of Gel_1-x series hydrogels

OHRhMOP was dissolved in a mixture of water and acetonitrile (7:5 v/v) to obtain a clear purple solution (1.86 mM). Then pre-prepared solution of NaOH was added at different equivalent relative to **OHRhMOP** for deprotonation (1, 6 and 12 mol. eq., respectively). After sonication, this purple solution was added to the water/acetonitrile solution of **bix** (22.32 mM, 12 mol. eq.) under vigorous stirring. The obtained clear purple solution (0.93 mM MOP) was then placed into a preheated oven at 60 °C to induce gelation. According to the deprotonation degree of **OHRhMOP**, the heating time is set differently depending on the DLS results (4h, 8h and 12h, respectively). After gelation, the gel sample was soaked within fresh water/acetonitrile solution twice to remove the residual chemicals. Then the washed gel was immersed in distilled water for 3 days, replacing the solvent with fresh water each day to remove the acetonitrile to obtain a pure hydrogel based on **OHRhMOP**. The hydrogel obtained here was referred to **Gel_1-1**, **Gel_1-6**, **Gel_1-12** depending on the equivalent of the NaOH added.

Synthesis of Gel_2-x series hydrogels

OHRhMOP was dissolved in a mixture of water and acetonitrile (7:5 v/v) to obtain a clear purple solution (2.80 mM). Then pre-prepared solution of NaOH (1mol. eq. relative to **OHRhMOP**) was added for initial deprotonation. After sonication, this purple solution was added to the water/acetonitrile solution of **bix** (33.6 mM, 12 mol. eq.) under vigorous stirring. The obtained clear purple solution (1.40 mM MOP) was then placed into a preheated oven at 60 °C for 4h towards gelation. After gelation, the gel sample was soaked within fresh

water/acetonitrile solution twice to remove the residual chemicals. Then the washed gel was immersed in distilled water for 3 days, replacing the solvent with fresh water each day to remove acetonitrile to get **Gel_2-1**. For post-synthetic deprotonation, the obtained hydrogel was immersed into the solution of NaOH (5, 11, 23 mol. eq., respectively) and left for two days. After reaction, the hydrogel was washed by fresh water again to get **Gel_2-6**, **Gel_2-12**, **Gel_2-24** depending on the equivalent of the NaOH used.

Synthesis of Gel_1-x and Gel_2-x series aerogels

To obtain aerogel, as-made hydrogel was soaked with acetone for three days, with the acetone replaced each day. Then the solvent-exchanged samples were then dried by supercritical CO_2 at 14 MPa and 40 °C for 90 mins to obtain the aerogel. Prior to sorption measurements, the aerogel sample was activated at 120 °C under vacuum for 12 h.

Reference

1. Steed, J. W., Supramolecular gel chemistry: developments over the last decade. *Chem. Commun.* **2011**, *47* (5), 1379-1383.

2. Sangeetha, N. M.; Maitra, U., Supramolecular gels: Functions and uses. *Chem. Soc. Rev.* **2005**, *34* (10), 821-836.

3. Piepenbrock, M.-O. M.; Lloyd, G. O.; Clarke, N.; Steed, J. W., Metal- and Anion-Binding Supramolecular Gels. *Chem. Rev.* **2010**, *110* (4), 1960-2004.

4. Eelkema, R.; Pich, A., Pros and Cons: Supramolecular or Macromolecular: What Is Best for Functional Hydrogels with Advanced Properties? *Adv. Mater.* **2020**, *32* (20), 1906012.

5. Yan, X.; Cook, T. R.; Pollock, J. B.; Wei, P.; Zhang, Y.; Yu, Y.; Huang, F.; Stang, P. J., Responsive Supramolecular Polymer Metallogel Constructed by Orthogonal Coordination-Driven Self-Assembly and Host/Guest Interactions. *J. Am. Chem. Soc.* **2014**, *136* (12), 4460-4463.

6. Qi, Z.; Schalley, C. A., Exploring Macrocycles in Functional Supramolecular Gels: From Stimuli Responsiveness to Systems Chemistry. *Acc. Chem. Res.* **2014**, 47 (7), 2222-2233.

7. Foster, J. A.; Steed, J. W., Exploiting Cavities in Supramolecular Gels. *Angew. Chem. Int. Ed.* **2010**, *49* (38), 6718-6724.

8. Ji, X.; Wu, R.-T.; Long, L.; Guo, C.; Khashab, N. M.; Huang, F.; Sessler, J. L., Physical Removal of Anions from Aqueous Media by Means of a Macrocycle-Containing Polymeric Network. *J. Am. Chem. Soc.* **2018**, *140* (8), 2777-2780.

9. Mantooth, S. M.; Munoz-Robles, B. G.; Webber, M. J., Dynamic Hydrogels from Host–Guest Supramolecular Interactions. *Macromol. Biosci.* **2019**, *19* (1), 1800281.

10. Ji, X.; Wang, H.; Wang, H.; Zhao, T.; Page, Z. A.; Khashab, N. M.; Sessler, J. L., Removal of Organic Micropollutants from Water by Macrocycle-Containing Covalent Polymer Networks. *Angew. Chem. Int. Ed.* **2020**, *59* (52), 23402-23412.

11. Hwang, I.; Jeon, W. S.; Kim, H. J.; Kim, D.; Kim, H.; Selvapalam, N.; Fujita, N.; Shinkai, S.; Kim, K., Cucurbit[7]uril: A Simple Macrocyclic, pH-Triggered Hydrogelator Exhibiting Guest-Induced Stimuli-Responsive Behavior. *Angew. Chem. Int. Ed.* **2007**, *119* (1-2), 214-217.

12. Deng, W.; Yamaguchi, H.; Takashima, Y.; Harada, A., A Chemical-Responsive Supramolecular Hydrogel from Modified Cyclodextrins. *Angew. Chem. Int. Ed.* **2007**, *46* (27), 5144-5147.

13. Guo, D.-S.; Liu, Y., Calixarene-based supramolecular polymerization in solution. *Chem. Soc. Rev.* **2012**, *41* (18), 5907-5921.

14. Ogoshi, T.; Kakuta, T.; Yamagishi, T.-a., Applications of Pillar[n]arene-Based Supramolecular Assemblies. *Angew. Chem. Int. Ed.* **2019**, *58* (8), 2197-2206.

15. Huang, S.-L.; Jin, G.-X.; Luo, H.-K.; Hor, T. S. A., Engineering Organic Macrocycles and Cages: Versatile Bonding Approaches. *Chem. Asian J.* **2015**, *10* (1), 24-42.

16. Li, B.; Wang, B.; Huang, X.; Dai, L.; Cui, L.; Li, J.; Jia, X.; Li, C., Terphen[n]arenes and Quaterphen[n]arenes (n = 3-6): One-Pot Synthesis, Self-Assembly into Supramolecular Gels, and Iodine Capture. *Angew. Chem. Int. Ed.* **2019**, *58* (12), 3885-3889.

17. Fujita, M.; Tominaga, M.; Hori, A.; Therrien, B., Coordination Assemblies from a Pd(II)-Cornered Square Complex. *Acc. Chem. Res.* **2005**, *38* (4), 369-378.

18. Nitschke, J. R., Construction, Substitution, and Sorting of Metallo-organic Structures via Subcomponent Self-Assembly. *Acc. Chem. Res.* **2007**, *40* (2), 103-112.

19. Chakrabarty, R.; Mukherjee, P. S.; Stang, P. J., Supramolecular Coordination: Self-Assembly of Finite Two- and Three-Dimensional Ensembles. *Chem. Rev.* **2011**, *111* (11), 6810-6918.

20. Sepehrpour, H.; Fu, W.; Sun, Y.; Stang, P. J., Biomedically Relevant Self-Assembled Metallacycles and Metallacages. *J. Am. Chem. Soc.* **2019**, *141* (36), 14005-14020.

21. Tranchemontagne, D. J.; Ni, Z.; O'Keeffe, M.; Yaghi, O. M., Reticular Chemistry of MetalOrganic Polyhedra. *Angew. Chem. Int. Ed.* **2008**, *47* (28), 5136-5147.

22. Hosono, N.; Kitagawa, S., Modular Design of Porous Soft Materials via Self-Organization of Metal-Organic Cages. *Acc. Chem. Res.* **2018**, *51* (10), 2437-2446.

23. Sun, Y.; Chen, C.; Stang, P. J., Soft Materials with Diverse Suprastructures via the Self-Assembly of Metal-Organic Complexes. *Acc. Chem. Res.* **2019**, *52* (3), 802-817.

24. Hu, X.; Feng, S.; Du, J.; Shao, L.; Lang, J.; Zhang, C.; Kelley, S. P.; Lin, J.; Dalgarno, S. J.; Atwood, D. A.; Atwood, J. L., Controlled hierarchical self-assembly of networked coordination nanocapsules via the use of molecular chaperones. *Chem. Sci.* **2020**, *11* (46), 12547-12552.

25. Li, J.-R.; Timmons, D. J.; Zhou, H.-C., Interconversion between Molecular Polyhedra and Metal−Organic Frameworks. *J. Am. Chem. Soc.* **2009**, *131* (18), 6368-6369.

26. Lal, G.; Derakhshandeh, M.; Akhtar, F.; Spasyuk, D. M.; Lin, J.-B.; Trifkovic, M.; Shimizu, G. K. H., Mechanical Properties of a Metal-Organic Framework formed by Covalent Cross-Linking of Metal-Organic Polyhedra. *J. Am. Chem. Soc.* **2019**, *141* (2), 1045-1053.

27. Niu, Z.; Fang, S.; Liu, X.; Ma, J.-G.; Ma, S.; Cheng, P., Coordination-Driven Polymerization of Supramolecular Nanocages. *J. Am. Chem. Soc.* **2015**, *137* (47), 14873-14876.

28. Zhukhovitskiy, A. V.; Zhong, M.; Keeler, E. G.; Michaelis, V. K.; Sun, J. E. P.; Hore, M. J. A.; Pochan, D. J.; Griffin, R. G.; Willard, A. P.; Johnson, J. A., Highly branched and loop-

rich gels via formation of metal–organic cages linked by polymers. *Nat. Chem.* **2016**, *8* (1), 33-41.

29. Lee, J.; Kwak, J. H.; Choe, W., Evolution of form in metal-organic frameworks. *Nat. Commun.* **2017**, *8* (1), 14070.

30. Andrés, M. A.; Carné-Sánchez, A.; Sánchez-Laínez, J.; Roubeau, O.; Coronas, J.; Maspoch, D.; Gascón, I., Ultrathin Films of Porous Metal-Organic Polyhedra for Gas Separation. *Chem. Eur. J.* **2020**, *26* (1), 143-147.

31. Li, L.; Xiang, S.; Cao, S.; Zhang, J.; Ouyang, G.; Chen, L.; Su, C.-Y., A synthetic route to ultralight hierarchically micro/mesoporous Al(III)-carboxylate metal-organic aerogels. *Nat. Commun.* **2013**, 4 (1), 1774.

32. Uchida, J.; Yoshio, M.; Sato, S.; Yokoyama, H.; Fujita, M.; Kato, T., Self-Assembly of Giant Spherical Liquid-Crystalline Complexes and Formation of Nanostructured Dynamic Gels that Exhibit Self-Healing Properties. *Angew. Chem. Int. Ed.* **2017**, *56* (45), 14085-14089.

33. Gu, Y.; Alt, E. A.; Wang, H.; Li, X.; Willard, A. P.; Johnson, J. A., Photoswitching topology in polymer networks with metal-organic cages as crosslinks. *Nature* **2018**, *560* (7716), 65-69.

34. Oldenhuis, N. J.; Qin, K. P.; Wang, S.; Ye, H.-Z.; Alt, E. A.; Willard, A. P.; Van Voorhis, T.; Craig, S. L.; Johnson, J. A., Photoswitchable Sol-Gel Transitions and Catalysis Mediated by Polymer Networks with Coumarin-Decorated Cu24L24 Metal-Organic Cages as Junctions. *Angew. Chem. Int. Ed.* **2020**, *59* (7), 2784-2792.

35. Shao, L.; Hua, B.; Hu, X.; Stalla, D.; Kelley, S. P.; Atwood, J. L., Construction of Polymeric Metal-Organic Nanocapsule Networks via Supramolecular Coordination-Driven Self-Assembly. *J. Am. Chem. Soc.* **2020**, *142* (16), 7270-7275.

36. Furukawa, S.; Horike, N.; Kondo, M.; Hijikata, Y.; Carné-Sánchez, A.; Larpent, P.; Louvain, N.; Diring, S.; Sato, H.; Matsuda, R.; Kawano, R.; Kitagawa, S., Rhodium-Organic Cuboctahedra as Porous Solids with Strong Binding Sites. *Inorg. Chem.* **2016**, *55* (21), 10843-10846.

37. Carné-Sánchez, A.; Craig, G. A.; Larpent, P.; Hirose, T.; Higuchi, M.; Kitagawa, S.; Matsuda, K.; Urayama, K.; Furukawa, S., Self-assembly of metal-organic polyhedra into supramolecular polymers with intrinsic microporosity. *Nat.Commun.* **2018**, *9* (1), 1-8.

38. Carné-Sánchez, A.; Craig, G. A.; Larpent, P.; Guillerm, V.; Urayama, K.; Maspoch, D.; Furukawa, S., A Coordinative Solubilizer Method to Fabricate Soft Porous Materials from Insoluble Metal-Organic Polyhedra. *Angew. Chem. Int. Ed.* **2019**, *58* (19), 6347-6350.

39. Legrand, A.; Craig, G. A.; Bonneau, M.; Minami, S.; Urayama, K.; Furukawa, S., Understanding the multiscale self-assembly of metal-organic polyhedra towards functionally graded porous gels. *Chem. Sci.* **2019**, *10* (47), 10833-10842.

40. Wei, S.-C.; Pan, M.; Fan, Y.-Z.; Liu, H.; Zhang, J.; Su, C.-Y., Creating Coordination-Based Cavities in a Multiresponsive Supramolecular Gel. *Chem. Eur. J.* **2015**, *21* (20), 7418-7427.

41. Ganta, S.; Chand, D. K., Multi-Stimuli-Responsive Metallogel Molded from a Pd_2L_4-Type Coordination Cage: Selective Removal of Anionic Dyes. *Inorg. Chem.* **2018**, *57* (7), 3634-3645.

42. Lu, C.; Zhang, M.; Tang, D.; Yan, X.; Zhang, Z.; Zhou, Z.; Song, B.; Wang, H.; Li, X.; Yin, S.; Sepehrpour, H.; Stang, P. J., Fluorescent Metallacage-Core Supramolecular Polymer Gel Formed by Orthogonal Metal Coordination and Host-Guest Interactions. *J. Am. Chem. Soc.* **2018**, *140* (24), 7674-7680.

43. Foster, J. A.; Parker, R. M.; Belenguer, A. M.; Kishi, N.; Sutton, S.; Abell, C.; Nitschke, J. R., Differentially Addressable Cavities within Metal-Organic Cage-Cross-Linked Polymeric Hydrogels. *J. Am. Chem. Soc.* **2015**, *137* (30), 9722-9729.

44. Howlader, P.; Mukherjee, P. S., Face and edge directed self-assembly of Pd_{12} tetrahedral nano-cages and their self-sorting. *Chem. Sci.* **2016**, *7* (9), 5893-5899.

45. Sutar, P.; Suresh, V. M.; Jayaramulu, K.; Hazra, A.; Maji, T. K., Binder driven self-assembly of metal-organic cubes towards functional hydrogels. *Nat. Commun.* **2018**, *9* (1), 3587.

46. Qin, Y.; Chen, L.-L.; Pu, W.; Liu, P.; Liu, S.-X.; Li, Y.; Liu, X.-L.; Lu, Z.-X.; Zheng, L.-Y.; Cao, Q.-E., A hydrogel directly assembled from a copper metal-organic polyhedron for antimicrobial application. *Chem. Commun.* **2019**, *55* (15), 2206-2209.

47. Liu, G.; Di Yuan, Y.; Wang, J.; Cheng, Y.; Peh, S. B.; Wang, Y.; Qian, Y.; Dong, J.; Yuan, D.; Zhao, D., Process-Tracing Study on the Postassembly Modification of Highly Stable Zirconium Metal-Organic Cages. *J. Am. Chem. Soc.* **2018**, *140* (20), 6231-6234.

48. Mollick, S.; Mukherjee, S.; Kim, D.; Qiao, Z.; Desai, A. V.; Saha, R.; More, Y. D.; Jiang, J.; Lah, M. S.; Ghosh, S. K., Hydrophobic Shielding of Outer Surface: Enhancing the Chemical Stability of Metal-Organic Polyhedra. *Angew. Chem. Int. Ed.* **2019**, *58* (4), 1041-1045.

49. Mollick, S.; Fajal, S.; Mukherjee, S.; Ghosh, S. K., Stabilizing Metal-Organic Polyhedra (MOP): Issues and Strategies. *Chem. Asian J.* **2019**, *14* (18), 3096-3108.

50. Percástegui, E. G.; Ronson, T. K.; Nitschke, J. R., Design and Applications of Water-Soluble Coordination Cages. *Chem. Rev.* **2020**, *120* (24), 13480-13544.

51. Carné-Sánchez, A.; Albalad, J.; Grancha, T.; Imaz, I.; Juanhuix, J.; Larpent, P.; Furukawa, S.; Maspoch, D., Postsynthetic Covalent and Coordination Functionalization of Rhodium(II)-Based Metal-Organic Polyhedra. *J. Am. Chem. Soc.* **2019**, *141* (9), 4094-4102.

52. Grancha, T.; Carné-Sánchez, A.; Hernández-López, L.; Albalad, J.; Imaz, I.; Juanhuix, J.; Maspoch, D., Phase Transfer of Rhodium(II)-Based Metal-Organic Polyhedra Bearing Coordinatively Bound Cargo Enables Molecular Separation. *J. Am. Chem. Soc.* **2019**, *141* (45), 18349-18355.

53. Warzecha, E.; Berto, T. C.; Wilkinson, C. C.; Berry, J. F., Rhodium Rainbow: A Colorful Laboratory Experiment Highlighting Ligand Field Effects of Dirhodium Tetraacetate. *J. Chem. Educ.* **2019**, *96* (3), 571-576.

54. Wang, Z.; Richter, S. M.; Rozema, M. J.; Schellinger, A.; Smith, K.; Napolitano, J. G., Potential Safety Hazards Associated with Using Acetonitrile and a Strong Aqueous Base. *Org. Proc. Res. Dev.* **2017**, *21* (10), 1501-1508.

55. Kong, L.; Zou, R.; Bi, W.; Zhong, R.; Mu, W.; Liu, J.; Han, R. P. S.; Zou, R., Selective adsorption of CO_2/CH_4 and CO_2/N_2 within a charged metal-organic framework. *J. Mater. Chem. A* **2014**, *2* (42), 17771-17778.

56. Stegbauer, L.; Hahn, M. W.; Jentys, A.; Savasci, G.; Ochsenfeld, C.; Lercher, J. A.; Lotsch, B. V., Tunable Water and CO_2 Sorption Properties in Isostructural Azine-Based Covalent Organic Frameworks through Polarity Engineering. *Chem. Mater.* **2015**, *27* (23), 7874-7881.

57. Tan, R.; Wang, A.; Malpass-Evans, R.; Williams, R.; Zhao, E. W.; Liu, T.; Ye, C.; Zhou, X.; Darwich, B. P.; Fan, Z.; Turcani, L.; Jackson, E.; Chen, L.; Chong, S. Y.; Li, T.; Jelfs, K. E.; Cooper, A. I.; Brandon, N. P.; Grey, C. P.; McKeown, N. B.; Song, Q., Hydrophilic microporous membranes for selective ion separation and flow-battery energy storage. *Nat. Mater.* **2020**, *19* (2), 195-202.

58. Furukawa, S.; Horike, N.; Kondo, M.; Hijikata, Y.; Carné-Sánchez, A.; Larpent, P.; Louvain, N.; Diring, S.; Sato, H.; Matsuda, R., Rhodium-organic cuboctahedra as porous solids with strong binding sites. *Inorg. Chem.* **2016**, *55* (21), 10843-10846.

59. Carné-Sánchez, A.; Albalad, J.; Grancha, T.; Imaz, I.; Juanhuix, J.; Larpent, P.; Furukawa, S.; Maspoch, D., Postsynthetic Covalent and Coordination Functionalization of Rhodium (II)-Based Metal–Organic Polyhedra. *J. Am. Chem. Soc.* **2019**, *141* (9), 4094-4102.

Chapter 3

Control of extrinsic porosities in linked metal-organic polyhedra gels by imparting coordination-driven self-assembly with electrostatic repulsion

Abstract

The linkage of metal-organic polyhedra (MOPs) for the synthesis of porous soft materials is one of the promising strategies to combine the processability with permanent porosity. Compared to the defined internal cavity of MOPs, it is still difficult to control the extrinsic porosities generated between crosslinked MOPs because of their random arrangements in the networks. Herein, we report a method to form linked MOP gels with controllable extrinsic porosities by introducing negative charges on the surface of MOPs that facilitates electrostatic repulsion between them. A hydrophilic rhodium-based cuboctahedral MOP (**OHRhMOP**) with 24 hydroxyl groups on its outer periphery can be controllably deprotonated to impart the MOP with tunable electrostatic repulsion in solution. This electrostatic repulsion between MOPs stabilizes the kinetically trapped state, in which a MOP is coordinated with various bisimidazole linkers in a monodentate fashion at a controllable linker/MOP ratio. Heating of the kinetically trapped molecules leads to the formation of gels with similar colloidal networks but different extrinsic porosity. This strategy allows us to design the molecular-level networks and the resulting porosities even in the amorphous state.

Introduction

The development of new porous materials with controllable structures and designable properties is a keystone of modern chemical technology. Metal-organic polyhedra (MOPs), a class of discrete coordination cages with well-defined internal cavities, have emerged as microporous building blocks for the construction of extended porous architectures due to their good solubility and designable outer periphery available for further connection.[1-2] By crosslinking MOPs with ditopic linkers[3-4] or tuning the noncovalent interaction between them (hydrogen bonding,[5-6] electrostatic interaction[7-8] and host-guest interaction,[9-10] for instance), various multidimensional assemblies are synthesized, ranging from crystalline porous solids like metal-organic frameworks (MOFs)[11] to amorphous soft materials such as films[12-13] or gels.[14-16] Considering practical applications, the latter has attracted increasing interests because of their potentials for realizing processable microporous materials.[17-18] For example, MOP-based gels consisting of hierarchical porosities with macro-, meso- and micropores guarantee

the transportation of guest molecules throughout the materials, providing an ideal platform for drug release, catalysis, gas separation and rapid sensing.[19-20] However, in contrast to MOFs with periodically ordered structures that allow for the precise modulation of pore size and shape,[21] it is rather difficult to control these amorphous porous structures. This is because MOP-based amorphous systems possess not only the defined internal cavities but also the irregular extrinsic pores created between randomly arranged or interlinked MOPs. The creation of porous soft materials with high structural controllability and pore designability analogous to MOFs still remains challenging.

By controlling the coordination-driven self-assembly pathway of MOPs, recently we reported the successful fabrication of the linked MOP gels featuring hierarchical porous networks.[22-23] Instead of forming orderly extended frameworks like MOFs, the random crosslinking of MOPs as junctions with bisimidazole links results in the formation of colloids, followed by their further connections to form colloidal gels. In particular, we showed that the post-synthetic aging process induced the reorganization of cross-linked MOP networks inside the colloids, and thus the control of extrinsic porosity.[24] However, so far only limited types of linkers have been successfully installed to form the linked MOP gels. In our previous trials to control their extrinsic porosity using flexible links, only spherical particles were obtained instead of colloidal gels.[18] Considering the importance of linker versatility in the porosity modulation of MOFs,[25-26] this limitation becomes problematic to the expansion of porous soft materials for potential applications.

Besides the linker versatility, the network topology also dictates the structure of extrinsic porosity.[27] One of the straightforward ways to control the topology in linked MOP network is to change the geometry of MOP and linkers.[28-29] Another way is to tune the connectivity on the MOP junctions from full crosslinking to partial linkage to thus control the branched functionality of networks. This method is more characteristic of amorphous networks that offer structural freedom within the material.[30] Although the similar method can be applied to crystalline MOFs, the changing of connectivity on the metal nodes requires the introduction of defects and at the extreme case leads to the collapse of crystalline networks.[31-32] One of the drawbacks to investigate the amorphous network is to determine the exact network structures and to give feedback to the synthetic conditions.[33] Though the extrinsic porosity of linked MOP networks can be designed by the linker versatility and the network topology, the appropriate characterization is essential to correlate the synthesis-structure relationship.

Here we report the formation of linked MOP gels with tunable extrinsic porosity by the charge-assisted coordination-driven self-assembly of a hydrophilic rhodium-based cuboctahedral MOP, $[Rh_2(OH\text{-}bdc)_2]_{12}$ (**OHRhMOP**, OH-bdc = 5-hydroxyl-1,3-

benzenedicarboxylate), with bisimidazole linkers. The presence of 24 hydroxyl (-OH) groups on the MOP periphery can be step-wisely deprotonated in the basic solution to generate controllable native charges on the MOP surface up to the –24 charge. This negative charge provides the electrostatic repulsion between MOPs and competes with their linkage by bisimidazole ligand. By balancing these two interactions, a kinetically trapped state, in which each MOP is coordinated by linkers in a monodentate fashion, can be stabilized after mixing with various types of linkers at a controlled ratio. Heating of the kinetically trapped state leads to the formation of linked MOP gels with controlled network connectivity at the MOP node. The nitrogen sorption measurement and the pore size distribution analysis clearly show the influence of linker type and ratio on the structure of extrinsic porosity between MOPs. This approach based on the synergistic effect of attractive and repulsive interactions between MOPs offers a new opportunity to explore the synthesis-structure relationship within amorphous porous networks.

Results and discussion

The cuboctahedral **OHRhMOP**, composed of 12 rhodium paddlewheel structures and 24 OH-bdc, has a good solubility in polar solvents like alcohols. Once coordinative solvents coordinate to the axial site of **OHRhMOP**, the molecule can be even soluble in water. We previously demonstrated the dissolution of **OHRhMOP** in the mixed solvent of water/acetonitrile and the successful formation of linked MOP gels by crosslinking MOPs with a ditopic linker, 1,4-bis(imidazol-1-ylmethyl)benzene (**bix**).[20] In general, to form linked MOP gels, the prerequisite is to add 12 equivalent (eq.) of linker **bix** to a MOP to form so-called kinetically trapped molecule at the chemical composition of RhMOP(bix)$_{12}$, in which 12 **bix** molecules coordinate in a monodentate fashion to the 12 available axial sites of rhodium paddlewheels existing on the surface of MOP. On the other hand, the stepwise addition of linkers to the MOP solution results in the formation of colloidal particles, named as coordination polymer particles (CPP). To study the effect of MOP charge on the coordination reaction with linkers, titration experiments were performed by stepwise addition of **bix** solution to the MOP solution at different deprotonation degrees, and the corresponding products were monitored by dynamic light scattering (DLS) measurements (Figure 3-1 and 3-2).

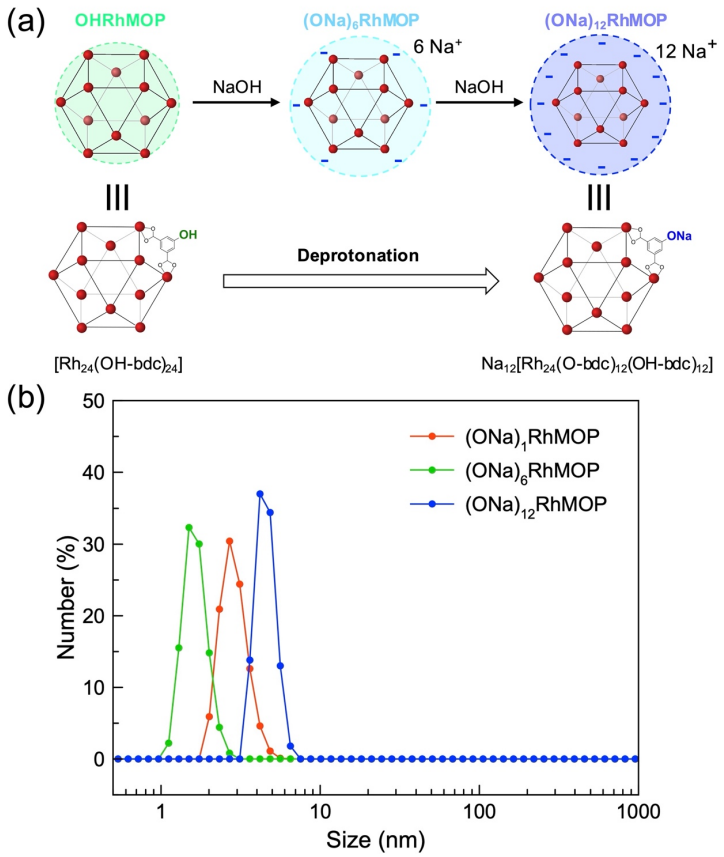

Figure 3-1. (a) Schematical illustration of **OHRhMOP** and its charged form **ONaRhMOP** after deprotonation. (b) DLS measurement of the MOPs at different deprotonation degrees.

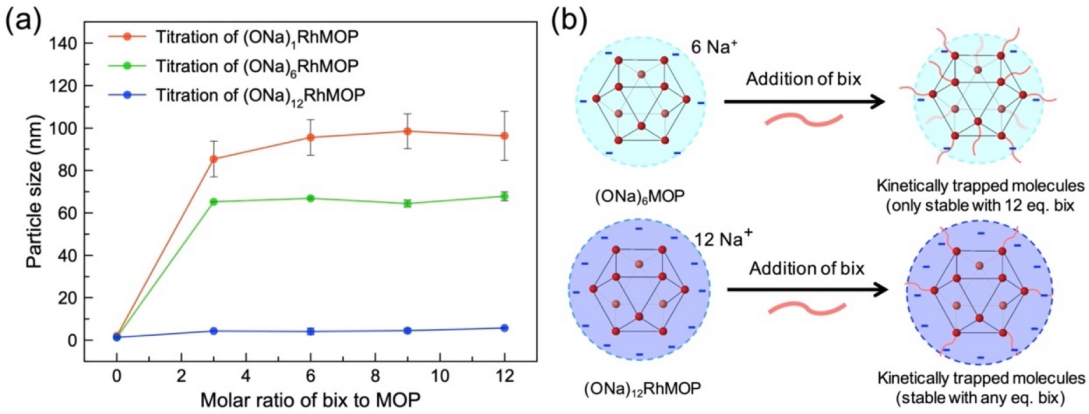

Figure 3-2. (a) DLS-determined size evolution of the assembling products obtained during the titration of differently charged MOPs (0.46 mM) by stepwise addition of **bix**. (b) Schematical showing the difference in the formation of kinetically trapped molecules by using MOPs at different deprotonation degrees.

The hydroxyl groups of **OHRhMOP** were firstly deprotonated in the solution of water/acetonitrile by adding NaOH to obtain its negatively charged form as [Rh_{24}(ONa-bdc)$_n$(OH-bdc)$_{24-n}$], denoted as **(ONa)$_n$RhMOP** where *n* indicates the number of deprotonated -OH groups per MOP. By changing the relative equivalent (eq.) of NaOH to **OHRhMOP** for deprotonation, **(ONa)$_n$RhMOP** with different charges can be obtained with n ranging from 1 to 24, which allows for the control of electrostatic interaction/repulsion between MOPs (Figure 3-1a). The solubility of these deprotonated MOPs in water/acetonitrile was confirmed by DLS measurements showing a number-weighted size distribution around 1-5 nm (Figure 3-1b). During the titration experiments, the stepwise addition of linker **bix** (1 mol. eq. per step) into the solution of **(ONa)$_1$RhMOP** induced obvious growth of its particle size to 85 ± 8 nm at the addition of 3 mol. eq. of **bix** (Figure 3-2a). This size growth suggests the occurrence of coordination reaction and thus the formation of CPPs. For **(ONa)$_6$RhMOP** with a higher charge, a smaller particle size of 65 ± 1 nm was obtained after the addition of 3 mol. eq. of **bix**. Further increasing the deprotonation degree of MOPs to **(ONa)$_{12}$RhMOP** revealed no formation of CPP but a slight size growth to 5.8 ± 0.3 nm upon addition of 12 mol. eq. of **bix**. This slight change can be most likely attributed to the existence of monodentately coordinating **bix** to the axial site of rhodium paddlewheel moieties on the MOPs. The obvious decrease in particle size by increasing deprotonation degrees indicates the influence of MOP charges on their subsequent coordination reactions with the linker. One plausible reason is that the electrostatic repulsion between the negatively charged MOPs dominates their assembling state and suppresses their crosslinking even with the existence of linker **bix** (Figure 3-2b).

To gain deep insights into the coordination environment of the charged **(ONa)$_{12}$RhMOP** with **bix** in the solution, UV-visible spectroscopy of the MOP solution was measured during the stepwise addition of **bix**. As shown in Figure 3-3, the addition of **bix** to the MOP solution induced a continuous shift of the maximum adsorption band (λ_{max}) from 559 nm to 546 nm, which is assigned to the π*-σ* transition of the dirhodium paddlewheel moiety.[34] The similar shift in λ_{max} was also observed in a control experiment with rhodium acetate [$Rh_2(OAc)_4$] in the acetonitrile solution; the replacement of 1 eq. of acetonitrile molecule in the [$Rh_2(OAc)_4$(acetonitrile)$_2$] complex by 1 eq. of monodentate imidazole ligand, 1-dodecyl-1H-imidazole (**diz**), led to a λ_{max} shift from 552 to 540 nm (Figure 2-3). These experiments confirmed the coordination of **bix** to the outer rhodium sites of MOPs during titration. Combined with the DLS data that revealed no CPP formation at any ratio (*m*) of **bix** added, one can hypothesize that only a kinetically trapped molecule, **(ONa)$_{12}$RhMOP(bix)$_m$** can be formed with monodentately coordinating **bix** molecules (Figure 3-2b). Due to the strong electrostatic

repulsion, the resulting MOP molecules become more stable and cannot be crosslinked with each other.

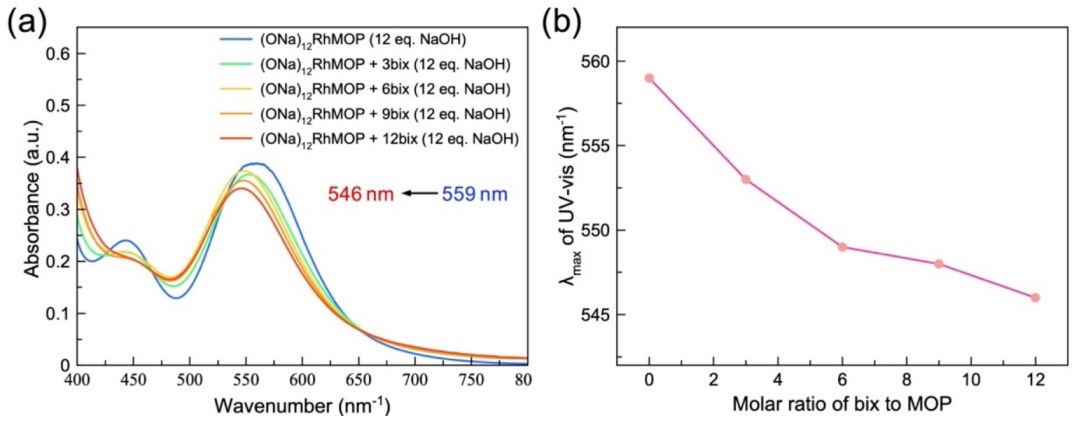

Figure 3-3. (a) UV-visible spectroscopy of the **(ONa)$_{12}$RhMOP** solution with different molar ratios of **bix**. (b) The evolution of the maximum adsorption band (λ_{max}) of MOP solution versus the molar ratio of added **bix**.

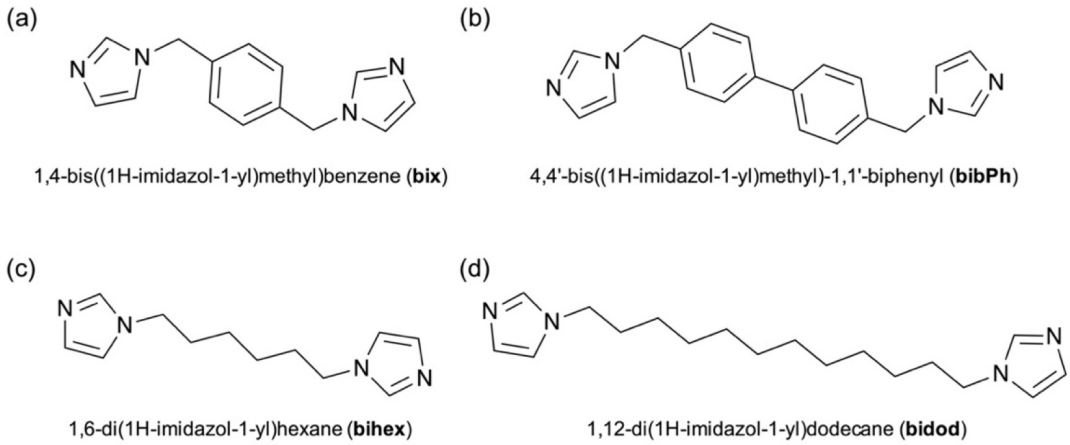

Figure 3-4. The molecular formula of **bix**, **bibPh**, **bihex** and **bidod**.

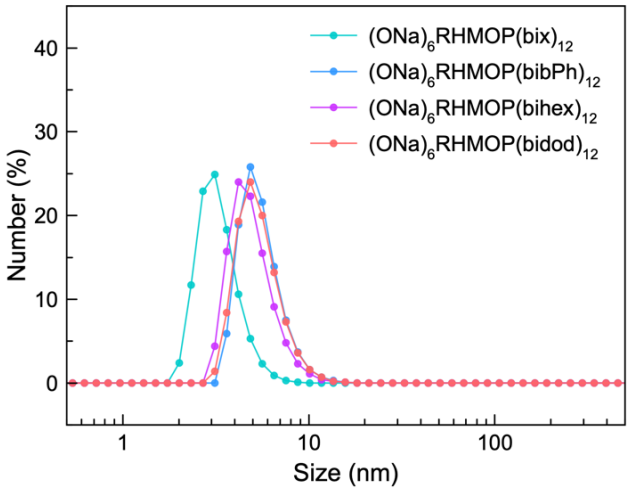

Figure 3-5. DLS measurement of the kinetically trapped molecules formed with different types of linkers.

With the help of stable kinetically trapped molecules, not only **bix** but other bisimidazole linkers can be installed on the surface of negatively charged MOPs. By implementing the further gelation via heating, it is able to form gels by linking these MOPs, which otherwise are not accessible with the use of their neutral counterparts. As a proof-of-concept, four bidentate linkers with different length and flexibility, including **bix**, 4,4'-bis(imidazol-l-ylmethyl)biphenyl (**bibPh**), 1,6-di(1H-imidazol-1-yl)hexane (**bihex**) and 1,12-di(1H-imidazol-1-yl)dodecane (**bidod**), are used here to crosslink MOPs and to synthesize their corresponding gels (see the molecular formula in Figure 3-4). In contrast to the solution of **(ONa)$_1$RhMOP** that immediately gave precipitates after the addition of **bihex** and **bidod**, the addition of 12 mol. eq. of each linker into **(ONa)$_6$RhMOP** solution generated stable kinetically trapped molecules in water/acetonitrile solution as **(ONa)$_6$RhMOP(bix)$_{12}$**, **(ONa)$_6$RhMOP(bihex)$_{12}$**, **(ONa)$_6$RhMOP(bibPh)$_{12}$** or **(ONa)$_6$RhMOP(bidod)$_{12}$**, respectively (Figure 3-5). To investigate the effect of linker type on the coordination reaction, the crosslinking processes of **(ONa)$_6$RhMOP** with different linkers were monitored by time-resolved DLS experiments at 60 ºC, as shown in Figure 3-6 and 3-7. High temperature is required for the gelation to induce the dissociation of monodentately coordinating linkers from the axial site of MOPs to expose accessible metal sites, to which a neighboring kinetically trapped MOP can coordinate. This coordination reaction sequentially happens to crosslink MOPs. As a result of MOP crosslinking, the particle size in DLS continues to grow until the whole system is frozen by colloidal network formation (Figure 3-6 and 3-7). To determine the gelation point, the changes in the time-averaged scattering light intensity ($\langle I \rangle_T$) are plotted versus the reaction time. The gelation point is associated with the time when the $\langle I \rangle_T$ starts fluctuation.[35] Intriguingly, all these four systems showed a similar gelation time of 16-20 mins despite the difference of linkers. This suggests

that the polymerization process is predominantly controlled by the MOP charge instead of linker types.

Four self-standing gels with different linkers (**bix**, **bibPh**, **bihex** and **bidod)** were synthesized by heating the solution of their corresponding kinetically trapped molecules at the same condition (1.4 mM, 60 ºC) (Figure 3-8). The mechanical properties of the resulting gels, referred to **$(ONa)_6$RhMOP-bix**, **$(ONa)_6$RhMOP-bibPh**, **$(ONa)_6$RhMOP-bihex** or **$(ONa)_6$RhMOP-bidod**, respectively, were analyzed by rheometer in a compression mode. As shown in Figure 3-9, all the samples revealed a frequency-independent storage Young's modulus (*E*'), which was one order of magnitude higher than the loss Young's modulus (*E*'). Compared to the gels with more flexible linkers (*E*' ≈ 3.7 and 4.1 kPa for **$(ONa)_6$RhMOP-bihex** and **$(ONa)_6$RhMOP-bidod**, respectively), **$(ONa)_6$RhMOP-bix** and **$(ONa)_6$RhMOP-bibPh** presented higher stiffness with *E*' ≈ 6.0 and 8.0 kPa, respectively. Intriguingly, the relative stiffness of the gels also follows the order of linker length; the longer linkers gave the higher stiffness. Then, the order of stiffness of the resulting gels are as follows; **bibPh**> **bix** > **bidod** > **bihex**. To further investigate the effect of linker types on the gel structures, all the gel samples were successively exchanged with acetone and dried by supercritical CO_2 to obtain their corresponding aerogels for following composition analysis and SEM observation.

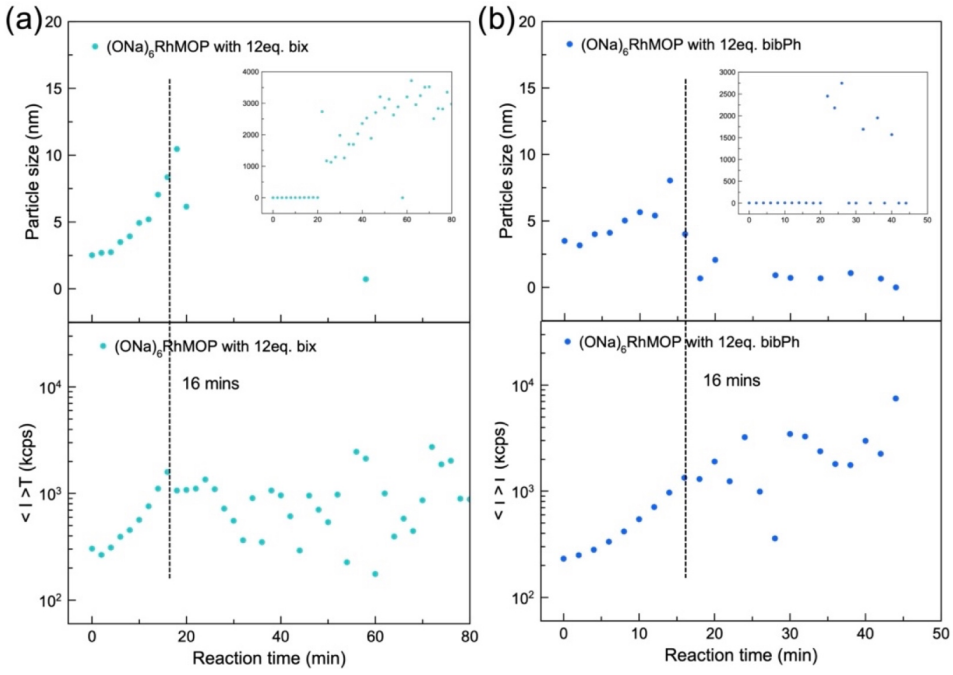

Figure 3-6. Time-resolved dynamic light scattering (DLS) experiments during the supramolecular polymerization of (a) **$(ONa)_6$RhMOP(bix)$_{12}$** and (b) **$(ONa)_6$RhMOP(bibPh)$_{12}$** at 60 ºC.

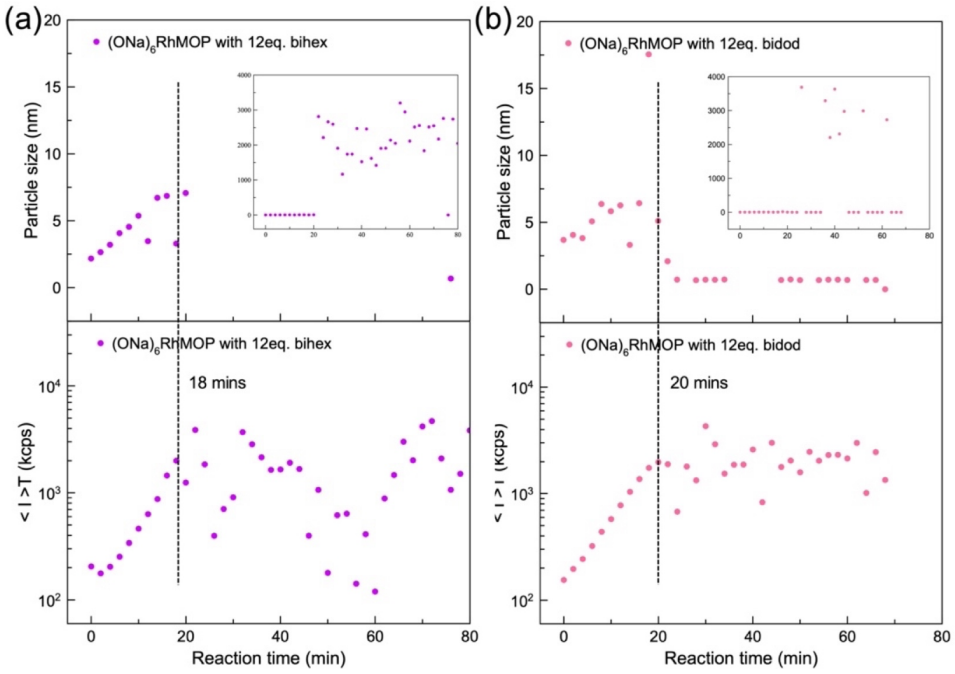

Figure 3-7. Time-resolved dynamic light scattering (DLS) experiments during the supramolecular polymerization of (a) **(ONa)$_6$RhMOP(bihex)$_{12}$** and (b) **(ONa)$_6$RhMOP(bidod)$_{12}$** at 60 ºC.

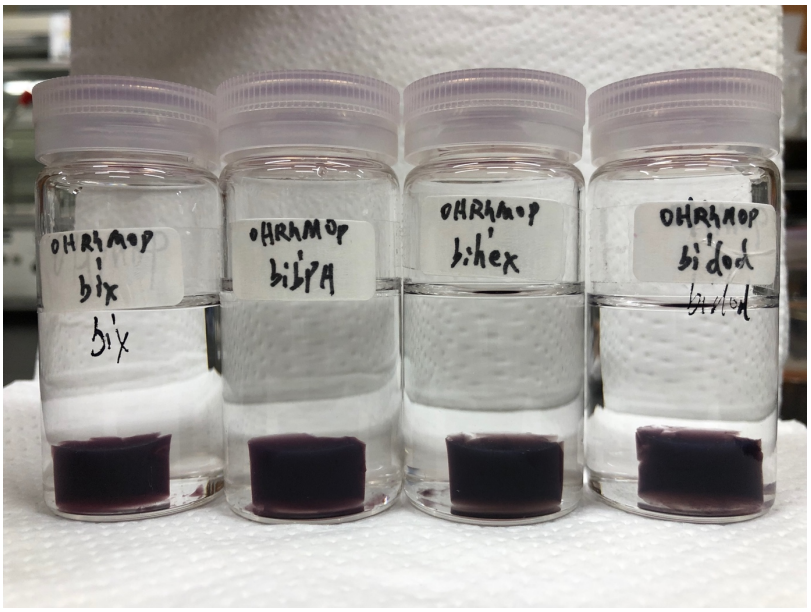

Figure 3-8. Photos of gel samples of (a) **(ONa)$_6$RhMOP-bix**, (b) **(ONa)$_6$RhMOP-bibPh**, (c) **(ONa)$_6$RhMOP-bihex** and (b) **(ONa)$_6$RhMOP-bidod**.

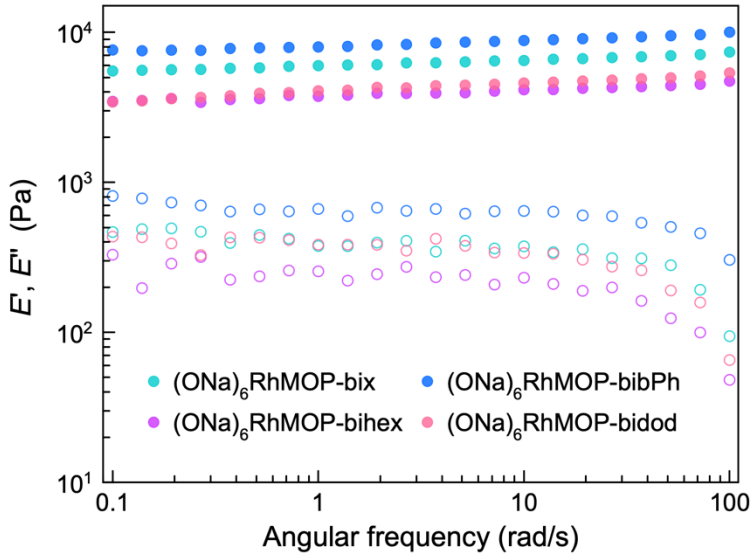

Figure 3-9. Storage Young's modulus (E') (filled circles) and loss Young's modulus (E'') (hollow circles) of gels formed with different linkers versus scanning frequency (ω).

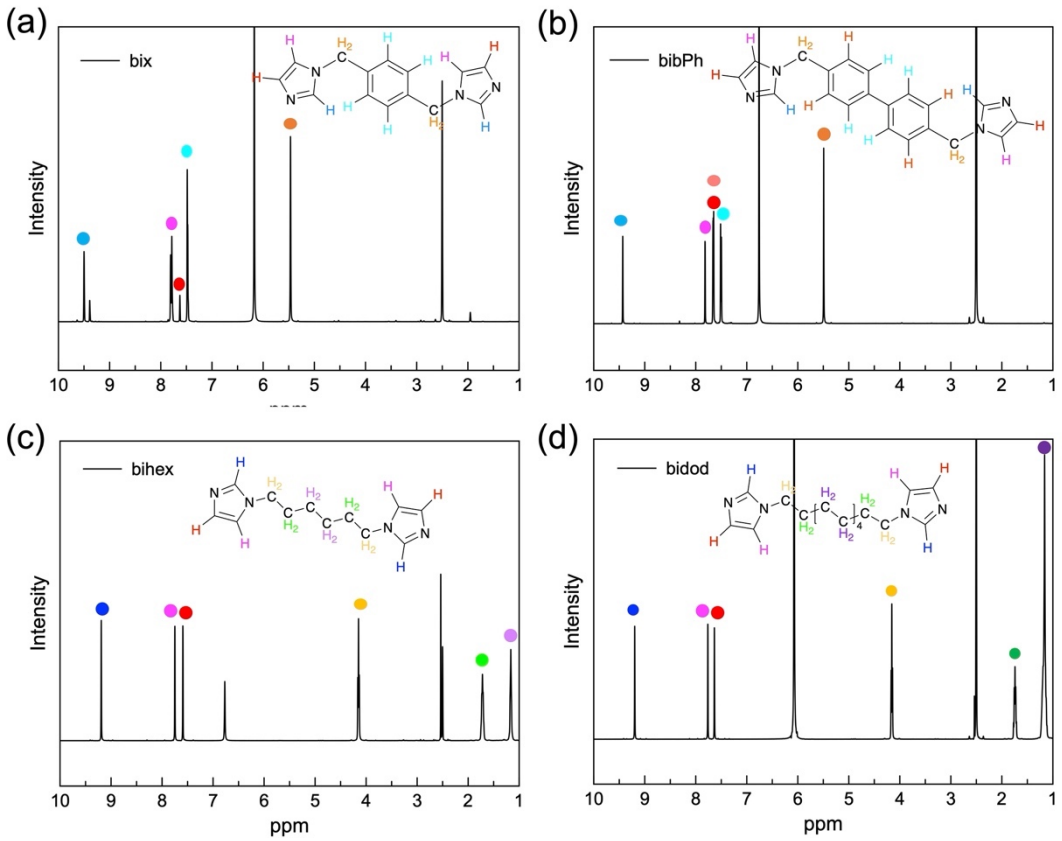

Figure 3-10. ^{1}H NMR spectrum of (a) **bix**, (b) **bibPh**, (c) **bihex** and (d) **bidod** in the same condition of aerogel digestion.

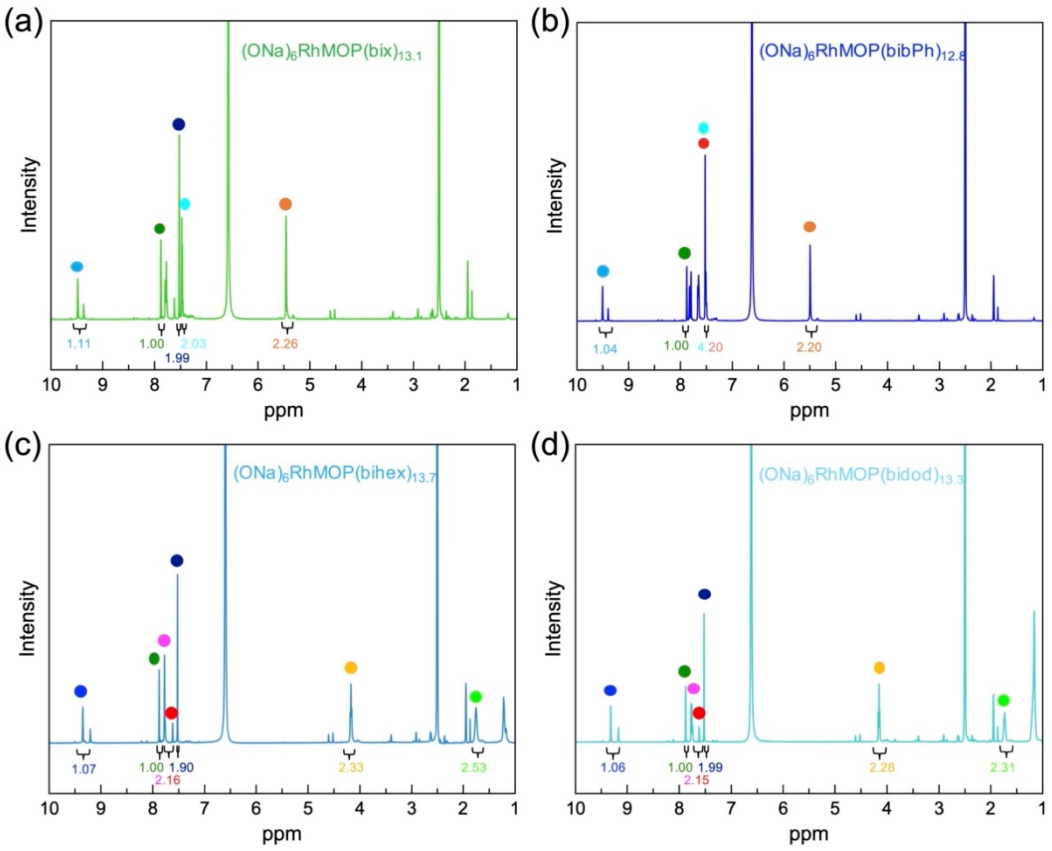

Figure 3-11. ^{1}H NMR spectrum of the digested aerogels obtained from (a) **$(ONa)_6$RhMOP-bix**, (b) **$(ONa)_6$RhMOP-bibPh**, (c) **$(ONa)_6$RhMOP-bihex** and (b) **$(ONa)_6$RhMOP-bidod**.

From ^{1}H NMR experiments of the acid-digested aerogels, the compositions of these four samples were estimated to be $Na_6[Rh_{24}(O\text{-}bdc)_6(OH\text{-}bdc)_{18}](bix)_{13.1}$, $Na_6[Rh_{24}(O\text{-}bdc)_6(OH\text{-}bdc)_{18}](bibPh)_{12.8}$, $Na_6[Rh_{24}(O\text{-}bdc)_6(OH\text{-}bdc)_{18}](bihex)_{13.7}$ and $Na_6[Rh_{24}(O\text{-}bdc)_6(OH\text{-}bdc)_{18}](bidod)_{13.3}$, respectively (Figure 3-10 and 3-11). The slightly higher linker/MOP ratio (≈ 13) than 12 in each aerogel sample was attributed to the partial MOP decomposition induced by heating of basic solution of MOPs as described in our previous paper.[20] The scanning electron microscopy (SEM) images of all the aerogel samples revealed similar characteristic colloidal gel networks consisting of interconnected colloidal nanoparticles with the size of around 20 nm (Figure 3-12). Based on the similar gelation time and the similar gel compositions and structures among these four samples, we conclude that the gelation process is not influenced by linker types but predominantly controlled by the electrostatic interaction between MOPs. As we already determined that the stiffness of gels is more controlled by the mesoscale structure of colloidal networks rather than the molecular-level structure of crosslinked MOPs, we assume that the difference in the gel stiffness can be explained by the flexibility of linkers at the interface between connected colloids.

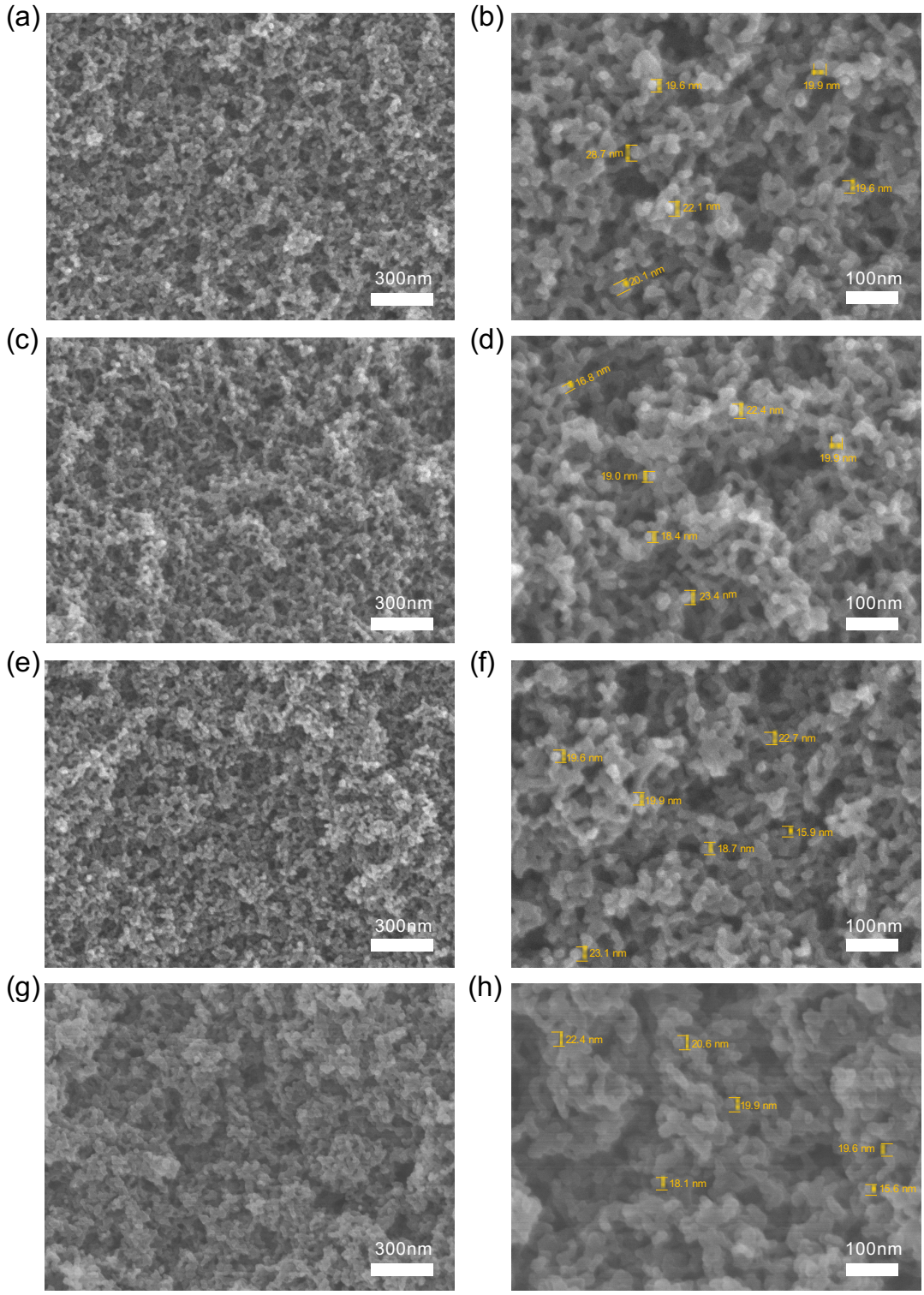

Figure 3-12. SEM images of the aerogels obtained from (a-b) **$(ONa)_6$RhMOP-bix**, (c-d) **$(ONa)_6$RhMOP-bibPh**, (e-f) **$(ONa)_6$RhMOP-bihex** and (g-h) **$(ONa)_6$RhMOP-bidod**.

The crosslinked MOP structures with different linkers inside each colloidal particle would give more impact on their extrinsic microporosity created between crosslinked MOPs. To understand the relationship between the linker type and the extrinsic microporosity, N_2 sorption

measurements of these four aerogels obtained from **$(ONa)_6$RhMOP-bix**, **$(ONa)_6$RhMOP-bibPh**, **$(ONa)_6$RhMOP-bihex** and **$(ONa)_6$RhMOP-bidod** were performed at 77 K. As shown in Figure 3-13a, all the aerogel samples revealed obvious N_2 uptake both at the lower relative pressure corresponding to the characteristics of microporosity and at the higher pressure attributed to the capillary condensation of nitrogen inside meso/macro pores, indicating the hierarchical porosity of the resulting aerogels. Based on the sorption isotherm, the corresponding pore size distribution of each aerogel was calculated by nonlocal density functional theory (NLDFT) (Figure 3-13b) with the slit pore model. For all the samples, a hierarchical pore distribution was observed with the coexistence of multiple pores ranging from nanoscale to mesoscale. Among them, the micropore with the size of ca. 0.6 nm was attributed to the intrinsic MOP cavity (Figure 3-15), which confirmed the preservation of most MOP porosities in the gel networks despite their partial decomposition. Three larger pores with the diameter of 1.4, 2.9 and 5.5 nm were assigned to the extrinsic pores between the crosslinked MOPs, which were clearly observed in the aerogels of **$(ONa)_6$RhMOP-bix**, **$(ONa)_6$RhMOP-bihex**. Due to the linker rigidity of **bix**, **$(ONa)_6$RhMOP-bix** has more defined extrinsic porosity though **bix** and **bihex** has a similar length. On the other hand, $(ONa)_6$RhMOP-bidod showed more broad pores size distribution in the range of 1.4-10 nm. This is more likely attributed to the long and flexible nature of **bidod** that provides more structural freedom to connect MOPs in different ways. The case for **$(ONa)_6$RhMOP-bibPh** with long and rigid linkers, however, looks different from others; only the pore at 1.4 nm can be distinguished while the peaks of pores at 2.9 and 5.5 nm almost disappeared. In addition, CO_2 sorption measurements of all aerogel samples at 196 K were also performed to reveal a linker-related gas capacity (Figure 3-16): at $P/P_0 \sim 1$, the aerogels obtained from **$(ONa)_6$RhMOP-bix**, **$(ONa)_6$RhMOP-bibPh**, **$(ONa)_6$RhMOP-bihex** and **$(ONa)_6$RhMOP-bidod** adsorbs 181, 166, 150 and 143 cm^3 of CO_2 per gram aerogels, which matched the order of **bidod** < **bihex** < **bibPh** < **bix**. Combined with the above N_2 sorption data, it shows that the extrinsic porosity of the linked MOP gels can be changed by the use of different linkers.

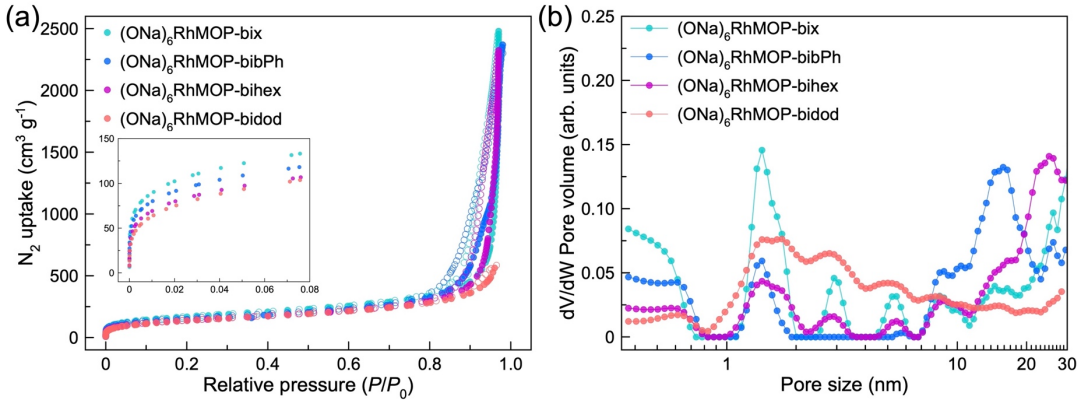

Figure 3-13. (a) N_2 adsorption isotherm at 77 K for aerogels obtained from **(ONa)$_6$RhMOP-bix**, **(ONa)$_6$RhMOP-bibPh**, **(ONa)$_6$RhMOP-bihex** and **(ONa)$_6$RhMOP-bidod**. (b) The corresponding pore size distribution (PSD) estimated from N_2 isotherm by NLDFT on a slit pore model.

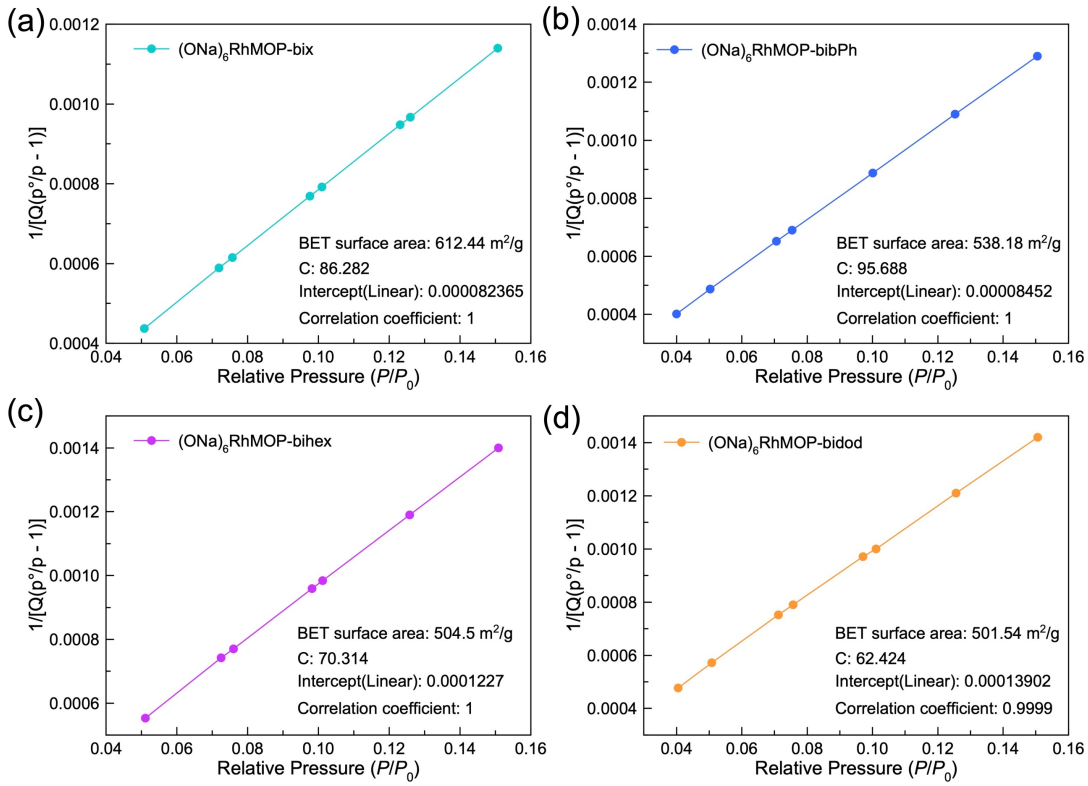

Figure 3-14. Calculation of the BET surface area of the aerogels obtained from (a) **(ONa)$_6$RhMOP-bix**, (b) **(ONa)$_6$RhMOP-bibPh**, (c) **(ONa)$_6$RhMOP-bihex** and (d) **(ONa)$_6$RhMOP-bidod**.

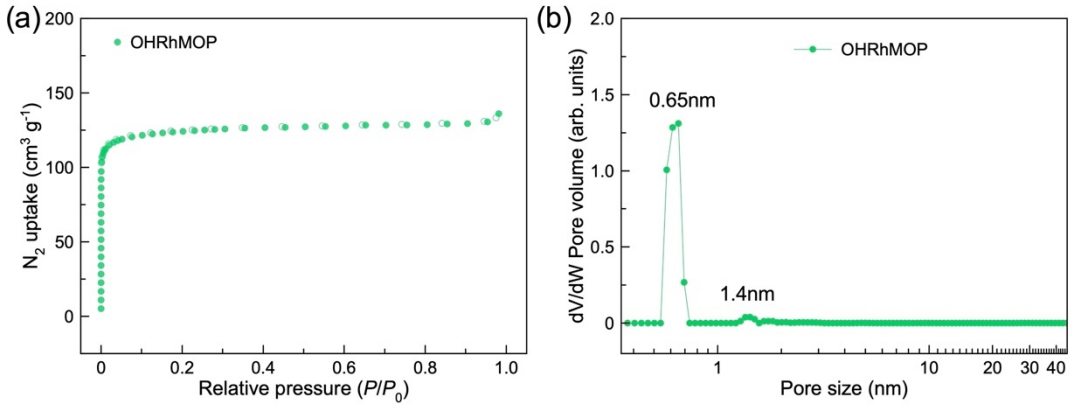

Figure 3-15. (a) N_2 adsorption isotherm at 195 K for **OHRhMOP** and (b) the corresponding PSD plots estimated from N_2 isotherm by NLDFT on a slit pore model.

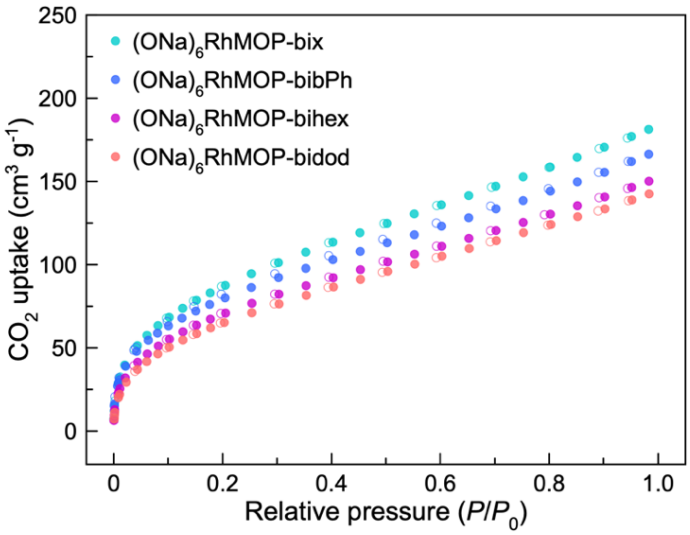

Figure 3-16. ^{1}H NMR spectrum of the digested aerogels obtained from (a) **(ONa)$_6$RhMOP-bix**, (b) **(ONa)$_6$RhMOP-bibPh**, (c) **(ONa)$_6$RhMOP-bihex** and (b) **(ONa)$_6$RhMOP-bidod**.

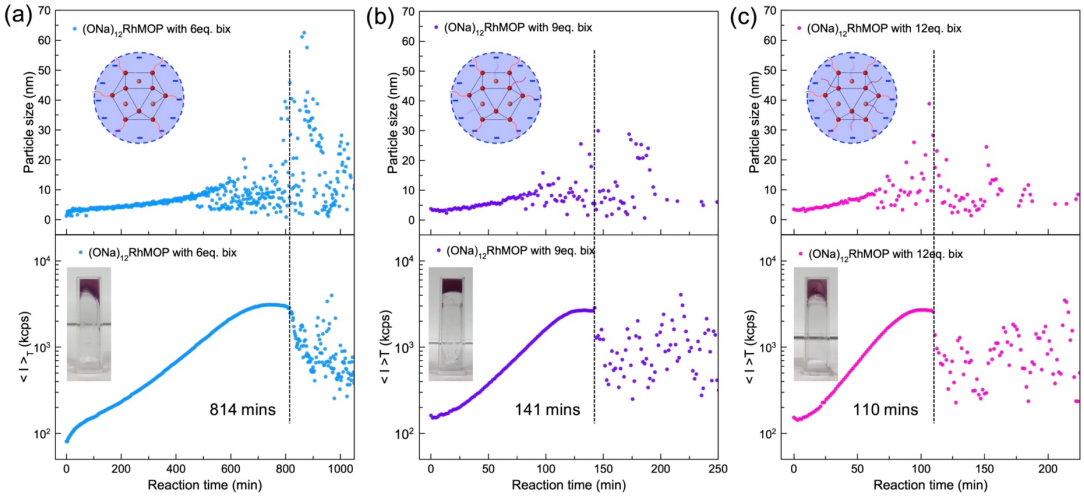

Figure 3-17. Time-resolved dynamic light scattering (DLS) experiments during the supramolecular polymerization of **$(ONa)_{12}$RhMOP** at 60 °C at a concentration of 0.46 mM, showing the particle size evolution and the time-averaged scattering intensity as a function of times. Systems with different molar equivalents of bix added to MOPs were measured: (a) 6 eq. **bix**, (b) 9 eq. **bix** and (c) 6 eq. **bix**.

To obtain gels in the system of **$(ONa)_6$RhMOP**, the full coordination of linkers was required to stabilize the kinetically trapped molecule as **$(ONa)_6$RhMOP(linker)$_{12}$**. This was the requirement for all the crosslinked MOP gels reported so far. However, in the case of **$(ONa)_{12}$RhMOP**, the kinetically trapped molecule can be stabilized with any molar ratio of linker **bix** thanks to the strong electrostatic repulsion between them (Figure 3-2). This stability allows for the control of the crosslinking connectivity of the resulting MOP networks by simply selecting the corresponding linker ratio. To investigate the effect of linker ratio on the polymerization reaction, the crosslinking process of **$(ONa)_{12}$RhMOP** with different ratio of **bix** (6, 9 and 12 mol. eq. relative to MOP, respectively) was monitored by time-resolved DLS experiments at 60 ºC. As shown in Figure 3-17, heating treatment successfully induced the gelation of all solutions but with different gelation times. Determined by the $<I>_T$, the gelation time was found to be strongly influenced by the ratio of **bix**; the gelation time decreased from 814 mins for MOPs with 6 eq. of **bix** to 110 mins for MOPs with 12 eq. of **bix**. This explains that the higher concentration of linker is necessary to induce the crosslinking between highly charged MOPs. The addition of **bix** less than 6 eq. of bix did not lead to the gelation.

The gels of **$(ONa)_{12}$RhMOP(bix)$_6$**, **$(ONa)_{12}$RhMOP(bix)$_9$** and **$(ONa)_{12}$RhMOP(bix)$_{12}$**, were synthesized by adding 6, 9, 12 eq. of **bix** into the solution of **$(ONa)_{12}$RhMOP** and then heating at 60 ºC. The corresponding aerogels were synthesized by washing the gels with acetone for three times and then dried by supercritical CO_2. To estimate the gel composition, ^{1}H NMR experiments of each aerogel sample after acid-digestion were performed (Figure 3-19). For all

these three samples, the molar ratio of bix/MOP was estimated to proportional to the amount of bix added; the compositions of gels from **(ONa)$_{12}$RhMOP(bix)$_6$**, **(ONa)$_{12}$RhMOP(bix)$_9$** and **(ONa)$_{12}$RhMOP(bix)$_{12}$** were $Na_{12}[Rh_{24}(O\text{-}bdc)_{12}(OH\text{-}bdc)_{12}](bix)_{8.7}$, $Na_{12}[Rh_{24}(O\text{-}bdc)_{12}(OH\text{-}bdc)_{12}](bix)_{12.2}$ and $Na_{12}[Rh_{24}(O\text{-}bdc)_{12}(OH\text{-}bdc)_{12}](bix)_{14.9}$, respectively. Considering the relatively high deprotonation degree of MOPs, the reason for this higher **bix**/MOP ratio in gels than it was in the initial kinetically trapped molecules can be attributed to the partial decomposition of MOPs by heating in basic media. Note that the SEM images of these aerogel samples revealed similar colloidal networks despite the difference in their compositions (Figure 3-20). This similar structure suggested the predominant influence of electrostatic interaction on their gelation process. From the rheological measurements (Figure 3-21), the gels exhibited the dependency of mechanical properties on the linker ratio; a lowering the ratio of **bix** decreases the stiffness of gels. Note that the gel sample of **(ONa)$_{12}$RhMOP(bix)$_6$** was too weak to be self-standing (Figure 3-18a). Therefore, a shearing mode was used to measure its mechanical property (Figure 3-18e) to be $E' \approx 0.1$ kPa, which is indeed lower than that of **(ONa)$_{12}$RhMOP(bix)$_9$** and **(ONa)$_{12}$RhMOP(bix)$_{12}$** with $E' \approx 0.9$ and 2.8 kPa, respectively (to compare the modulus obtained from compression and shearing tests, the rheological data was converted as shown in experimental section). This significant change in gel stiffness can be ascribed to the higher crosslinking degree between colloidal particles due to the existence of more available **bix** on their surfaces.

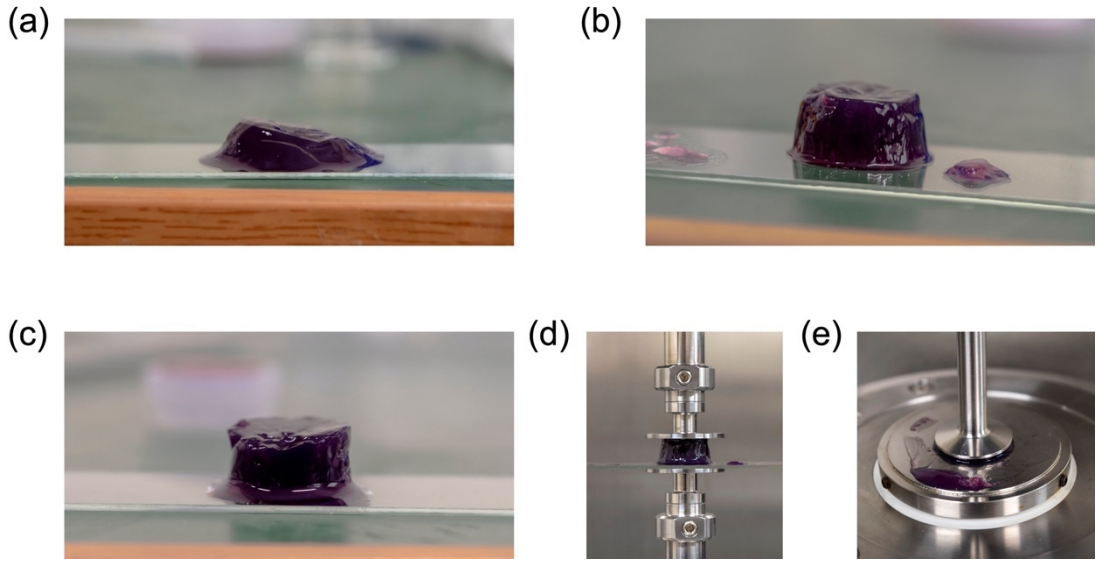

Figure 3-18. Photos of gel samples of (a) **(ONa)$_{12}$RhMOP(bix)$_6$**, (b) **(ONa)$_{12}$RhMOP(bix)$_9$** and (c) **(ONa)$_{12}$RhMOP(bix)$_{12}$**. Photos of the rheological measurement of gel sample under (d) compression mode and (e) shearing mode.

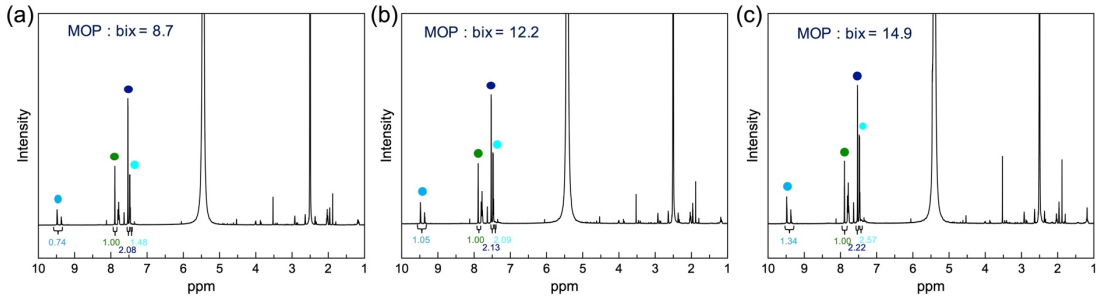

Figure 3-19. ^{1}H NMR spectrum of the digested aerogels obtained from (a) **(ONa)$_{12}$RhMOP(bix)$_{6}$**, (b) **(ONa)$_{12}$RhMOP(bix)$_{9}$** and (b) **(ONa)12RhMOP(bix)$_{12}$**.

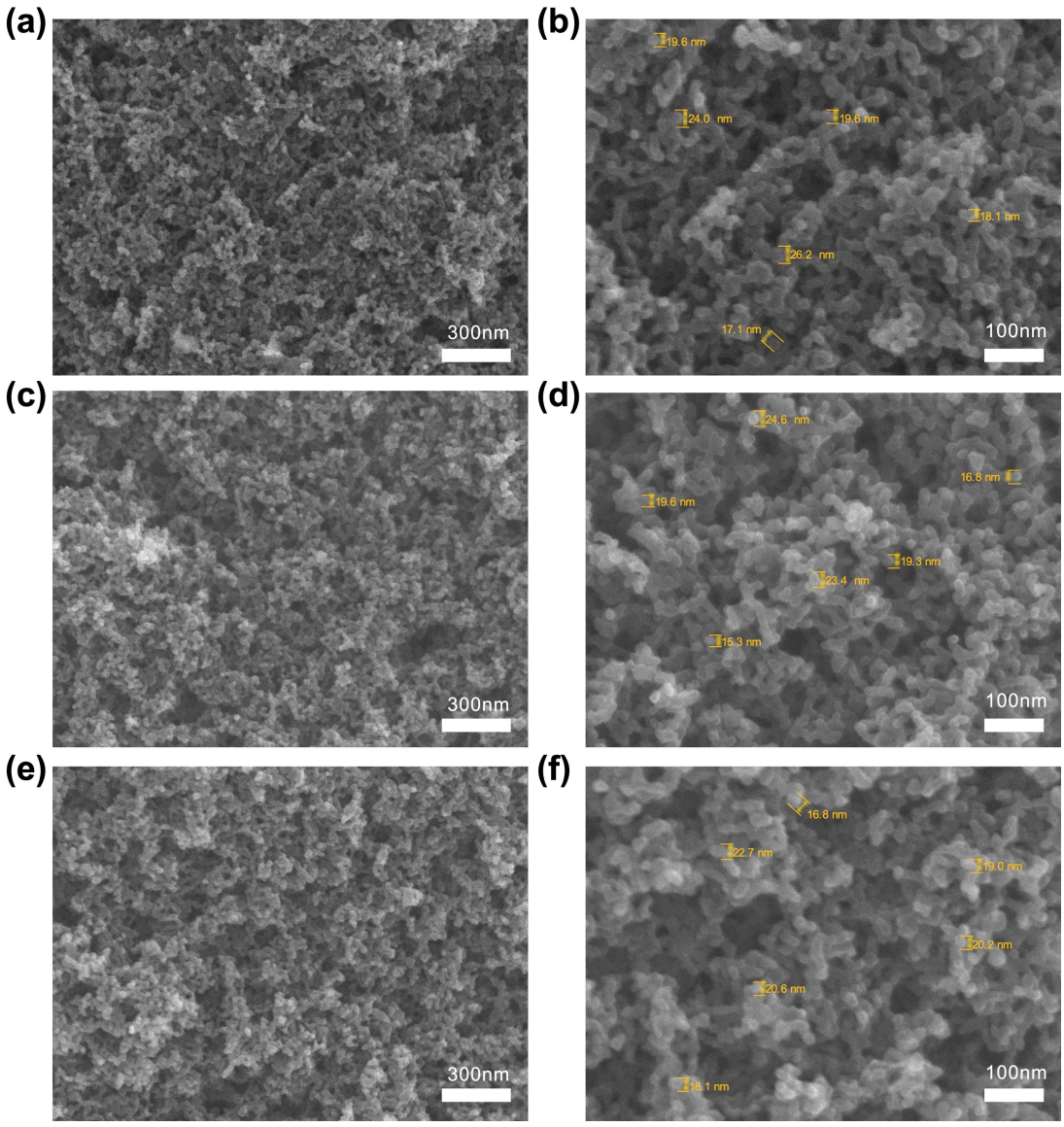

Figure 3-20. SEM images of the aerogel samples obtained from (a-b) **(ONa)$_{12}$RhMOP(bix)$_{6}$**, (c-d) **(ONa)$_{12}$RhMOP(bix)$_{9}$** and (e-f) **(ONa)$_{12}$RhMOP(bix)$_{12}$**.

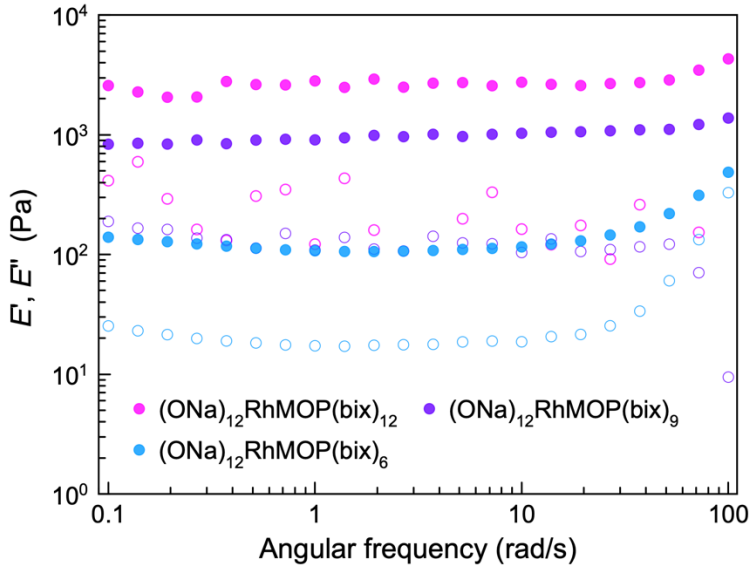

Figure 3-21. Storage Young's modulus (E') (filled circles) and loss Young's modulus (E'') (hollow circles) of gels formed with different **bix** ratio versus scanning frequency (ω). Note that the E' and E'' of **(ONa)$_{12}$RhMOP(bix)$_6$** was estimated from a shearing measurement due to the poor stiffness of this gel which cannot be self-standing

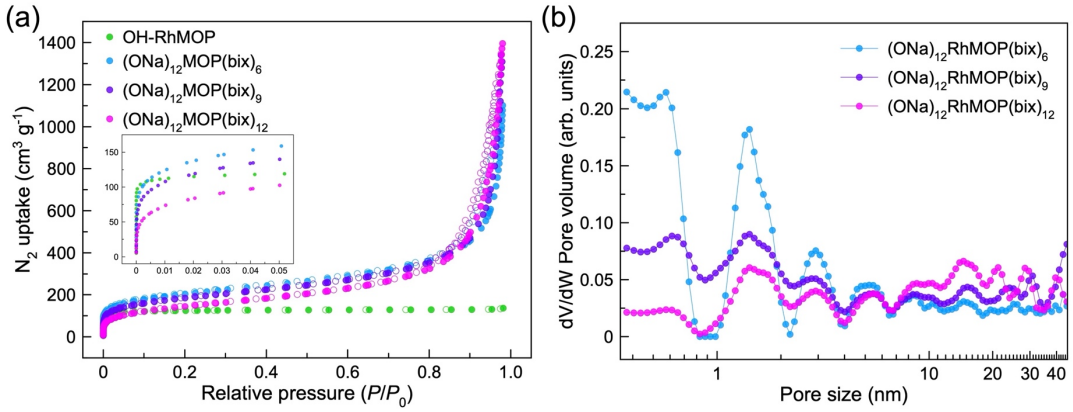

Figure 3-22. (a) N_2 adsorption isotherm at 77 K for aerogels obtained from **(ONa)$_{12}$RhMOP(bix)$_6$**, **(ONa)$_{12}$RhMOP(bix)$_9$** and **(ONa)$_{12}$RhMOP(bix)$_{12}$**. (b) The corresponding pore size distribution (PSD) estimated from N_2 isotherm by NLDFT on a slit pore model.

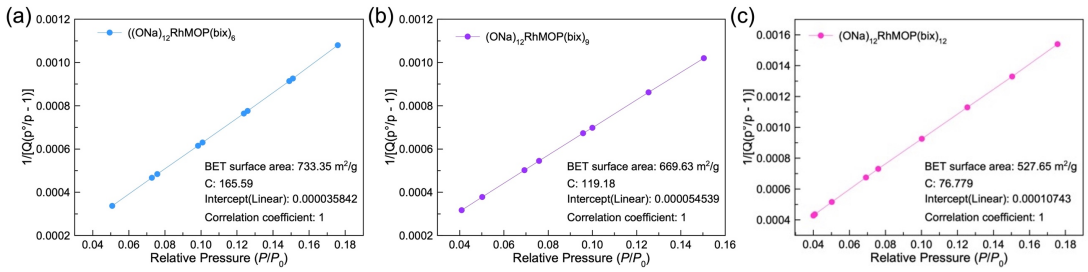

Figure 3-23. CO_2 adsorption isotherm at 195 K for the aerogels obtained from (a) **(ONa)$_{12}$RhMOP(bix)$_6$**, (b) **(ONa)$_{12}$RhMOP(bix)$_9$** and (c) **(ONa)$_{12}$RhMOP(bix)$_{12}$**.

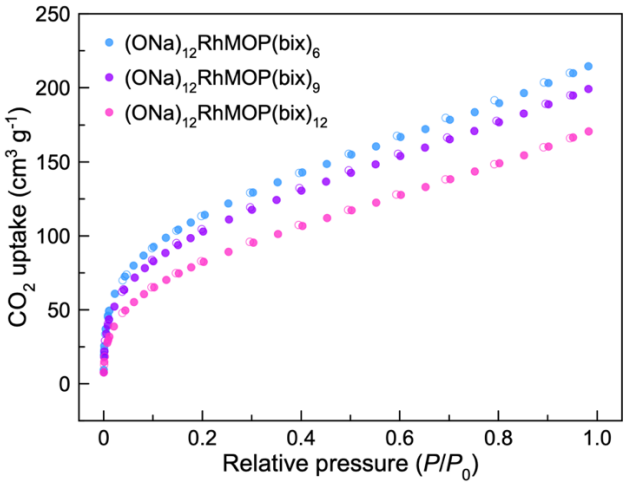

Figure 3-24. CO_2 adsorption isotherm at 195 K for the aerogels obtained from **(ONa)$_{12}$RhMOP(bix)$_6$**, **(ONa)$_{12}$RhMOP(bix)$_9$** and **(ONa)$_{12}$RhMOP(bix)$_{12}$**.

To investigate the effect of linker ratio on the crosslinked MOP structures and thus extrinsic porosity inside each colloidal particle, N_2 sorption experiments of the aerogels obtained from **(ONa)$_{12}$RhMOP(bix)$_6$**, **(ONa)$_{12}$RhMOP(bix)$_9$** and **(ONa)$_{12}$RhMOP(bix)$_{12}$** were performed at 77 K (Figure 3-22). Similar to the sorption properties of aerogels discussed above, a hierarchical porous structure was observed in all samples with high N_2 uptake at both low and high relative pressure regions. This hierarchical porosity can be further confirmed by their corresponding pore size distribution analysis. In the case of the aerogels obtained from **(ONa)$_{12}$RhMOP(bix)$_6$**, micropores of ca. 0.6 nm corresponding to internal MOP cavities and the extrinsic pores between crosslinked MOPs at 1.4 and 2.9 nm are the main contributors for the whole pore volume in the materials. There are less contributions from the larger mesopores. By increasing the **bix** ratio, we see the trend that the relative contribution from MOP cavities (0.6 nm) decreases while the contributions from extrinsic porosities (1.4 and 2.9 nm) and the mesopores (more than 10 nm) increase. This change in the relative pore volume can be

attributed to the further crosslinking of MOPs due to the existence of more available **bix**, leading to higher connectivity at the MOP junctions and thus higher contribution from the extrinsic porosity. As a result, the increasing MOP connectivity inside each colloidal particle contributes to the control of hierarchical porosities in their corresponding aerogels, particularly in the range of extrinsic porosities between crosslinked MOPs and connected colloids. We demonstrated the possibility to design and control the structure and microporosity of soft porous materials even in the amorphous state by the use of the electrostatic repulsion between MOPs.

Conclusion

In summary, we demonstrated a strategy to tune the structures and properties of the linked MOP gels with various types of linkers at a controlled ratio by introducing the electrostatic repulsion between charged MOPs. The outer hydroxyl groups on the MOP periphery were deprotonated by NaOH to generate the controllable negative charge on the MOPs. The electrostatic repulsion between charged MOPs plays a key role in their following coordination reaction with bisimidazole linkers, especially in the formation of stable kinetically trapped molecules. This stability of kinetically trapped molecules allows us to tune their structure or compositions by simply installing different types of linkers onto MOP surfaces at any ratio without a risk of precipitation through MOP crosslinking. Heating of the kinetically trapped molecules with bisimidazole linkers yielded a series of linked MOP gels with controllable connectivity, mechanical properties and hierarchical porosity. Indeed, the formation of stable kinetically trapped MOP with rationally designed linkers allows us to fabricate versatile self-assembling architectures with controllable porosity. We believe that this strategy is not only limited to the synthesis of linked MOP gels but also applicable to the formation of other MOP-based superstructures with increasing complexity and functionality, such as MOP-based MOFs.

Experimental section

Materials

Rhodium acetate,[34] 1,4-bis(imidazol-1-ylmethyl)benzene (**bix**),[18] 4,4'-Bis(imidazol-l-ylmethyl)biphenyl (**bibPh**),[18] 1,6-di(1H-imidazol-1-yl)hexane (**bihex**)[36] and 1,12-di(1H-imidazol-1-yl)dodecane (**bidod**)[37] and **OHRhMOP**[38] were synthesized according to a previously reported procedure. 5-hydroxy-1,3-benzenedicarboxylic acid was purchased from Sigma-Aldrich and used as received. Solvents were purchased from Wako Pure Chemical Industries except those at HPLC grade were purchased from Fischer Chemicals.

Characterizations

The rheological measurements of the gels were made using a stress-controlled AR-G2 (TA Instruments, New Castle, DE, USA) rheometer. Gel samples after synthesis were transferred into a clean glass slide (~ 1 mm in thickness). Then the gel was loaded into the rheometer with the glass slide to perform the rheology tests (Figure 3-18d). The measurements of gels were conducted by frequency sweeping in a compression mode with a 1% strain amplitude that was well inside the linear regime (initial strain is fixed to 1.5%). Note that a shearing mode was used to measure the sample of **$(ONa)_{12}$RhMOP(bix)$_6$** by a Modular Compact Rheometer MCR 502 (Anton Paar, Graz, Austria) (Figure 3-18e). To compare its stiffness with other samples, the storage and loss shear modulus (G' and G'') of **$(ONa)_{12}$RhMOP(bix)$_6$** was converted into the storage and loss Young's modulus (E' and E'') by the following formula for incompressible materials such as gels:

$$E' = G' \times 3$$
$$E'' = G'' \times 3$$

The super-critical CO_2 drying process was carried out on SCLEAD-2BD autoclave (KISCO) using supercritical CO_2 at 14 MPa and 50 °C.

Scanning Electron Microscopy (SEM) of the microstructures of the aerogel samples were observed using a field-emission scanning electron microscope with a JEOL Model JSM-7001F4 system operating at 10 kV and 5 mA current. The samples were coated with 28 nm Osmium before measurement.

^{1}H NMR spectra were recorded on a Bruker Biospin DRX-600 (600 MHz) spectrometer. For ^{1}H-NMR analysis, 5 mg of aerogel sample was digested in a mixture of DMSO-d_6 (750 µl) and DCl (50 µl). The mixture was then heated at 100 °C overnight to obtain a yellow solution.

N_2 (77 K) and CO_2 (195 K) gas sorption isotherms of the MOPs and aerogels were recorded on a BELSORP-max volumetric adsorption instrument from BEL Japan Inc. Prior to gas sorption measurement, the samples were activated at 120 °C for 12 h.

UV-visible spectroscopy of the MOP solutions was performed in a V-670 spectrophotometer (JASCO).

Time-resolved dynamic light scattering (TRDLS) experiments of the MOP solutions were performed on a Zetasizer Nano ZS instrument (Malvern Instruments, Malvern, UK). The light source was a HeNe laser working at λ = 633 nm. The observations were made at the backscattering angle θ = 173º. The time dependence of particle size and the time-averaged scattering intensity during the gelation process was evaluated at 60 ºC.

Detailed synthesis

Synthesis of precursors

bix, **bibPh**, **bidod**, **bihex** and **OHRhMOP** were synthesized according to our previous reports.[18,34,36-38]

Titration of MOP-based assemblies by dropwise addition of bix

OHRhMOP was dissolved in a mixture of water and acetonitrile (7:5 v/v) to obtain a clear purple solution (0.46 mM MOPs). Then a certain amount of NaOH (1, 6 and 12 mol. eq. relative to MOP, respectively) was added for deprotonation at different degrees. After sonication, this purple solution was titrated with 0.6 mL water/acetonitrile solution of 9.2 mM **bix** at a rate of 1 mol. eq. (50 μL) per 5 mins until 12 mol. eq. of **bix** was added. During the titration, the size change of the MOP assemblies was detected in situ by DLS.

Synthesis of gels based on different $(ONa)_{12}$RhMOP/bix ratio

OHRhMOP was dissolved in a mixture of water and acetonitrile (7:5 v/v) to obtain a clear purple solution (2.80 mM MOPs). Then NaOH (12 mol. eq. relative to MOP) was added into the solution for deprotonation. After sonication, 1mL water/acetonitrile solution of **bix** at a certain concentration (16.8, 25.2 and 33.6 mM, respectively) was added to 1 mL purple solution of **$(ONa)_{12}$RhMOP** under vigorous stirring. The obtained clear purple solution (1.40 mM MOP) was then placed into a preheated oven at 60 °C overnight towards gelation. For **$(ONa)_{12}$RhMOP$(bix)_6$** systems, more times (~ 3 days) were needed to get the corresponding gels.

Synthesis of gels based on $(ONa)_6$RhMOP with different linkers

OHRhMOP was dissolved in a mixture of water and acetonitrile (7:5 v/v) to obtain a clear purple solution (2.80 mM). Then NaOH (6 mol. eq. relative to MOP) was added into the solution for deprotonation. After sonication, this purple solution of **$(ONa)_6$RhMOP** was added to the water/acetonitrile solution of linker (**bix**, **bibPh**, **bidod** or **bihex,** 33.6 mM, 12 mol. eq. for each) under vigorous stirring. The obtained clear purple solution (1.40 mM MOP) was then placed into a preheated oven at 60 °C overnight towards gelation. After gelation, the gel sample was soaked within fresh water/acetonitrile solution twice to remove the residual chemicals. Then the washed gel was immersed in distilled water for 3 days, replacing the solvent with fresh water each day to remove acetonitrile to get the resulting hydrogels, which were named as **$(ONa)_6$RhMOP-bix**, **$(ONa)_6$RhMOP-bibPh**, **$(ONa)_6$RhMOP-bihex** and **$(ONa)_6$RhMOP-bidod**.

Synthesis of aerogels from the linked MOP gel samples

To obtain aerogel, as-made hydrogel was soaked with acetone for three days, with the acetone replaced each day. Then the solvent-exchanged samples were then dried by supercritical CO_2 at 14 MPa and 40 °C for 90 mins to obtain the aerogel. Prior to sorption measurements, the aerogel sample was activated at 120 °C under vacuum for 12 h.

Reference

1. Hosono, N.; Kitagawa, S., Modular Design of Porous Soft Materials via Self-Organization of Metal-Organic Cages. *Acc. Chem. Res.* **2018,** *51* (10), 2437-2446.

2. Grancha, T.; Carné-Sánchez, A.; Zarekarizi, F.; Hernández-López, L.; Albalad, J.; Khobotov, A.; Guillerm, V.; Morsali, A.; Juanhuix, J.; Gándara, F.; Imaz, I.; Maspoch, D., Synthesis of Polycarboxylate Rhodium(II) Metal-Organic Polyhedra (MOPs) and their use as Building Blocks for Highly Connected Metal-Organic Frameworks (MOFs). *Angew. Chem. Int. Ed.* **2021,** *60* (11), 5729-5733.

3. Uchida, J.; Yoshio, M.; Sato, S.; Yokoyama, H.; Fujita, M.; Kato, T., Self-Assembly of Giant Spherical Liquid-Crystalline Complexes and Formation of Nanostructured Dynamic Gels that Exhibit Self-Healing Properties. *Angew. Chem. Int. Ed.* **2017,** *56* (45), 14085-14089.

4. Lal, G.; Derakhshandeh, M.; Akhtar, F.; Spasyuk, D. M.; Lin, J.-B.; Trifkovic, M.; Shimizu, G. K. H., Mechanical Properties of a Metal-Organic Framework formed by Covalent Cross-Linking of Metal-Organic Polyhedra. *J. Am. Chem. Soc.* **2019,** *141* (2), 1045-1053.

5. Sutar, P.; Suresh, V. M.; Jayaramulu, K.; Hazra, A.; Maji, T. K., Binder driven self-assembly of metal-organic cubes towards functional hydrogels. *Nat. Commun.* **2018,** *9* (1), 3587.

6. Qin, Y.; Chen, L.-L.; Pu, W.; Liu, P.; Liu, S.-X.; Li, Y.; Liu, X.-L.; Lu, Z.-X.; Zheng, L.-Y.; Cao, Q.-E., A hydrogel directly assembled from a copper metal-organic polyhedron for antimicrobial application. *Chem. Commun.* **2019,** *55* (15), 2206-2209.

7. Gosselin, A. J.; Decker, G. E.; Antonio, A. M.; Lorzing, G. R.; Yap, G. P. A.; Bloch, E. D., A Charged Coordination Cage-Based Porous Salt. *J. Am. Chem. Soc.* **2020,** *142* (21), 9594-9598.

8. Le Ouay, B.; Yoshino, H.; Sasaki, K.; Ohtsubo, Y.; Ohtani, R.; Ohba, M., Crystalline assembly of metal-organic polyhedra driven by ionic interactions with polyoxometalates. *Chem. Commun.* **2021,** *57* (42), 5187-5190.

9. Wei, S.-C.; Pan, M.; Fan, Y.-Z.; Liu, H.; Zhang, J.; Su, C.-Y., Creating Coordination-Based Cavities in a Multiresponsive Supramolecular Gel. *Chem. Eur. J.* **2015,** *21* (20), 7418-7427.

10. Nitta, N.; Takatsuka, M.; Kihara, S.-i.; Hirao, T.; Haino, T., Self-Healing Supramolecular Materials Constructed by Copolymerization via Molecular Recognition of Cavitand-Based Coordination Capsules. *Angew. Chem. Int. Ed.* **2020,** *59* (38), 16690-16697.

11. Lee, J.; Kwak, J. H.; Choe, W., Evolution of form in metal-organic frameworks. *Nat. Commun.* **2017,** *8* (1), 14070.

12. Xie, X.-Y.; Wu, F.; Liu, X.; Tao, W.-Q.; Jiang, Y.; Liu, X.-Q.; Sun, L.-B., Photopolymerization of metal-organic polyhedra: an efficient approach to improve the hydrostability, dispersity, and processability. *Chem. Commun.* **2019,** *55* (44), 6177-6180.
13. Yin, J.-F.; Zheng, Z.; Yang, J.; Liu, Y.; Cai, L.; Guo, Q.-Y.; Li, M.; Li, X.; Sun, T. L.; Liu, G. X.; Huang, C.; Cheng, S. Z. D.; Russell, T. P.; Yin, P., Unexpected Elasticity in Assemblies of Glassy Supra-Nanoparticle Clusters. *Angew. Chem. Int. Ed.* **2021,** *60* (9), 4894-4900.
14. Gu, Y.; Alt, E. A.; Wang, H.; Li, X.; Willard, A. P.; Johnson, J. A., Photoswitching topology in polymer networks with metal-organic cages as crosslinks. *Nature* **2018,** *560* (7716), 65-69.
15. Shao, L.; Hua, B.; Hu, X.; Stalla, D.; Kelley, S. P.; Atwood, J. L., Construction of Polymeric Metal-Organic Nanocapsule Networks via Supramolecular Coordination-Driven Self-Assembly. *J. Am. Chem. Soc.* **2020,** *142* (16), 7270-7275.
16. Sutar, P.; Maji, T. K., Recent advances in coordination-driven polymeric gel materials: design and applications. *Dalton Trans.* **2020,** *49* (23), 7658-7672.
17. Foster, J. A.; Steed, J. W., Exploiting Cavities in Supramolecular Gels. *Angew. Chem. Int. Ed.* **2010,** *49* (38), 6718-6724.
18. Carné-Sánchez, A.; Craig, G. A.; Larpent, P.; Hirose, T.; Higuchi, M.; Kitagawa, S.; Matsuda, K.; Urayama, K.; Furukawa, S., Self-assembly of metal-organic polyhedra into supramolecular polymers with intrinsic microporosity. *Nat. Commun.* **2018,** *9* (1), 2506.
19. Foster, J. A.; Parker, R. M.; Belenguer, A. M.; Kishi, N.; Sutton, S.; Abell, C.; Nitschke, J. R., Differentially Addressable Cavities within Metal-Organic Cage-Cross-Linked Polymeric Hydrogels. *J. Am. Chem. Soc.* **2015,** *137* (30), 9722-9729.
20. Wang, Z.; Craig, G. A.; Legrand, A.; Haase, F.; Minami, S.; Urayama, K.; Furukawa, S., Porous Colloidal Hydrogels Formed by Coordination-Driven Self-Assembly of Charged Metal-Organic Polyhedra. *Chem. Asian J.* **2021,** *16* (9), 1092-1100.
21. Yaghi, O. M.; O'Keeffe, M.; Ockwig, N. W.; Chae, H. K.; Eddaoudi, M.; Kim, J., Reticular synthesis and the design of new materials. *Nature* **2003,** *423* (6941), 705-714.
22. Carné-Sánchez, A.; Craig, G. A.; Larpent, P.; Guillerm, V.; Urayama, K.; Maspoch, D.; Furukawa, S., A Coordinative Solubilizer Method to Fabricate Soft Porous Materials from Insoluble Metal–Organic Polyhedra. *Angew. Chem. Int. Ed.* **2019,** *58* (19), 6347-6350.
23. Legrand, A.; Liu, L.-H.; Royla, P.; Aoyama, T.; Craig, G. A.; Carné-Sánchez, A.; Urayama, K.; Weigand, J. J.; Lin, C.-H.; Furukawa, S., Spatiotemporal Control of Supramolecular Polymerization and Gelation of Metal-Organic Polyhedra. *J. Am. Chem. Soc.* **2021,** *143* (9), 3562-3570.
24. Wang, Z.; Villa Santos, C.; Legrand, A.; Haase, F.; Hara, Y.; Kanamori, K.; Aoyama, T.; Urayama, K.; Doherty, C. M.; Smales, G. J.; Pauw, B. R.; Colón, Y. J.; Furukawa, S., Multiscale

structural control of linked metal-organic polyhedra gel by aging-induced linkage-reorganization. *Chem. Sci.* **2021,** *12* (38), 12556-12563.

25. Kitagawa, S.; Kitaura, R.; Noro, S.-i., Functional Porous Coordination Polymers. *Angew. Chem. Int. Ed.* **2004,** *43* (18), 2334-2375.

26. Horike, S.; Shimomura, S.; Kitagawa, S., Soft porous crystals. *Nat. Chem.* **2009,** *1* (9), 695-704.

27. Gu, Y.; Zhao, J.; Johnson, J. A., Polymer Networks: From Plastics and Gels to Porous Frameworks. *Angew. Chem. Int. Ed.* **2020,** *59* (13), 5022-5049.

28. Zhukhovitskiy, A. V.; Zhong, M.; Keeler, E. G.; Michaelis, V. K.; Sun, J. E. P.; Hore, M. J. A.; Pochan, D. J.; Griffin, R. G.; Willard, A. P.; Johnson, J. A., Highly branched and loop-rich gels via formation of metal-organic cages linked by polymers. *Nat. Chem.* **2016,** *8* (1), 33-41.

29. Sun, Y.; Chen, C.; Stang, P. J., Soft Materials with Diverse Suprastructures via the Self-Assembly of Metal-Organic Complexes. *Acc. Chem. Res.* **2019,** *52* (3), 802-817.

30. Jangizehi, A.; Schmid, F.; Besenius, P.; Kremer, K.; Seiffert, S., Defects and defect engineering in Soft Matter. *Soft Matter* **2020,** *16* (48), 10809-10859.

31. Dissegna, S.; Epp, K.; Heinz, W. R.; Kieslich, G.; Fischer, R. A., Defective Metal-Organic Frameworks. *Adv. Mater.* **2018,** *30* (37), 1704501.

32. Wu, H.; Chua, Y. S.; Krungleviciute, V.; Tyagi, M.; Chen, P.; Yildirim, T.; Zhou, W., Unusual and Highly Tunable Missing-Linker Defects in Zirconium Metal-Organic Framework UiO-66 and Their Important Effects on Gas Adsorption. *J. Am. Chem. Soc.* **2013,** *135* (28), 10525-10532.

33. Jeyakkumar, P.; Liang, Y.; Guo, M.; Lu, S.; Xu, D.; Li, X.; Guo, B.; He, G.; Chu, D.; Zhang, M., Emissive Metallacycle-Crosslinked Supramolecular Networks with Tunable Crosslinking Densities for Bacterial Imaging and Killing. *Angew. Chem. Int. Ed.* **2020,** *59* (35), 15199-15203.

34. Furukawa, S.; Horike, N.; Kondo, M.; Hijikata, Y.; Carné-Sánchez, A.; Larpent, P.; Louvain, N.; Diring, S.; Sato, H.; Matsuda, R.; Kawano, R.; Kitagawa, S., Rhodium-Organic Cuboctahedra as Porous Solids with Strong Binding Sites. *Inorg. Chem.* **2016,** *55* (21), 10843-10846.

35. Legrand, A.; Craig, G. A.; Bonneau, M.; Minami, S.; Urayama, K.; Furukawa, S., Understanding the multiscale self-assembly of metal-organic polyhedra towards functionally graded porous gels. *Chem. Sci.* **2019,** *10* (47), 10833-10842.

36. Qi, Y.; Luo, F.; Che, Y.; Zheng, J., Hydrothermal Synthesis of Metal-Organic Frameworks Based on Aromatic Polycarboxylate and Flexible Bis(imidazole) Ligands. *Cryst.l Growth Des.* **2008,** *8* (2), 606-611.

37. Xu, J.-F.; Chen, Y.-Z.; Wu, L.-Z.; Tung, C.-H.; Yang, Q.-Z., Dynamic Covalent Bond Based on Reversible Photo [4 + 4] Cycloaddition of Anthracene for Construction of Double-Dynamic Polymers. *Org. Lett.* **2013,** *15* (24), 6148-6151.

38. Carné-Sánchez, A.; Albalad, J.; Grancha, T.; Imaz, I.; Juanhuix, J.; Larpent, P.; Furukawa, S.; Maspoch, D., Postsynthetic Covalent and Coordination Functionalization of Rhodium(II)-Based Metal-Organic Polyhedra. *J. Am. Chem. Soc.* **2019,** *141* (9), 4094-4102.

Chapter 4

Fabrication of linked metal-organic polyhedra gels with permanent porosities by simple liquid exchange

Abstract

One viable way towards porous, amorphous materials is to fabricate gels based on the supramolecular assembly of porous metal-organic polyhedra (MOPs). To show permanent porosity in such amorphous soft material requires the complete removal of solvents trapped inside the gels to yield the corresponding aerogels, which gives rise to irreversible structural collapse during the drying process and thus change in their performances. Here, we report the first porous wet gel with permanent porosity by simply exchanging the solvent matrix of supramolecular gels made from the linked MOPs. All DMF solvent molecules trapped inside the gel networks and the MOP cavities are removed by solvent exchange with bulkier liquids, which in turn cannot enter the pore of MOP due to their larger molecular size. This strategy endows the linked MOP gels with available porosity without any structural damage. Greatly enhanced CO_2 gas capacity of gels is observed by introducing bulk solvent molecules such as the ionic liquid, 1-butyl-3-methylimidazolium tetrafluoroborate, which also exerts positive influences on the final performance of gels like mechanical properties and low volatility. A large library of functional liquids is shown available in this strategy to fabricate porous gels and to tailor their properties at the same time, demonstrating potentials for their application in a wider field like gas adsorption or separation, electrics and catalysis.

Introduction

Microporous materials have shown superiority in practical applications of gas storage and separation due to their high surface area to capture gas molecules.[1] Inevitably, when thinking about porous materials, we would normally refer to solid sorbents due to their structural rigidity and robustness.[2] These sorbents can be crystalline materials like metal-organic frameworks (MOFs), which rely on the coordinative connection of metal nodes and organic linkers to form extending periodical networks with well-defined and permanent porosity.[3] Or they can be amorphous ones such as the polymer of intrinsic porosity (PIM), of which the internal pores are coming from the arrangement of their rigid polymer chains.[4] In contrast, conventional liquid materials with fluidity are accepted as nonporous or merely having ill-defined and transient "pores" which are generated by the random thermal motion of the liquid molecules.[5,6] From the perspective of industrial use, liquid sorbents possessed unique advantages over their solid

counterparts for gas capture due to their fluid nature and efficiency in heat transfer, allowing them to be easily handled during the sorption process.[7] In fact, CO_2 scrubbing using liquid adsorbents has long been an industrially mature technology compared to solid porous materials.[8] However, the lack of intrinsic porosity in the liquids results in a low gas capacity and an undesired absorptive process, in which a large amount of energy is required to regenerate the liquid absorbent.[9] These drawbacks have largely restricted their further application.

Recent work has shown that persistent cavities can be engineered into liquids to endow the so-called porous liquids with intrinsic permanent porosity.[10] By combining the properties of liquids and porous solids, porous liquids may show promising applications in sorption systems requiring shape- and size-selective behavior, or flowing systems for loading and delivering gaseous guests.[11] Initially proposed by James and co-authors, three different types of porous liquids are recognized: (1) Type I are neat molecular liquids containing internal cavities. (2) Type II are solutions of porous molecules dissolved in solvents that are bulkier enough to be sterically hindered from the pores. (3) Type III are suspensions of porous particles dispersed in the sterically hindered solvents.[12] Compared to type I porous liquid that requires hosts modification to lower down its melting point to endow fluidity,[13,14] type II and III porous liquids are more feasible for synthesis by rational design of porous host species and bulk solvents.[15] For instance, porous organic cages (POCs),[16,17] metal-organic polyhedra (MOPs)[18] and metal-organic frameworks (MOFs)[19-21] have been successfully dissolved or dispersed in the bulkier solvents like crown ether[16] and ionic liquids[19] to endow the resulting liquids with permanent porosity. Despite these achievements, they still have some disadvantages concerning the gas sorption process. All the intrinsic pores inside the porous liquids are isolated from each other and are mainly surrounded by the bulkier liquid molecules. When sorption happens, the gas molecules cannot be captured by these pores directly, instead they need to diffuse through the liquid molecules until the pores are encountered. Even though the gas molecules are captured by the pores, the transfer of them between different internal cavities would be slow due to the existence of surrounding liquids. As a result, the sorption process in the liquid state is slower than other solid systems, which is undesirable for practical use.

To tackle this issue, one possible way can be the controlled formation of connected porous structures inside the liquids, allowing for the construction of channels for fast gas diffusion. In terms of this concept, gel materials, which are well known for their ability to combine the advantages of both liquids and solids, stand out as the ideal candidates. Macroscopically, gels consist of three-dimensional (3D) solid networks that span a large volume of solvents and entrap it through the surface-tension effect.[22] By introducing permanent cavities into the gel systems, there is a high chance to afford a hierarchical porous network with connected channels

for gas sorption. Recently, we reported the fabrication of linked MOP gels with hierarchical porous networks by coordinatively crosslinking cuboctahedral MOPs, $[Rh_2(bdc)_2]_{12}$ (**HRhMOP**; bdc = benzene-1,3-dicarboxylate), with bidentate linkers, **bix** (1,4-bis(imidazol-1-ylmethyl)benzene).[23] However, to access the internal pores of MOPs, the linked MOP gels must be transformed into aerogels via the drying process, leading to a complete property loss of wet gels. As a result, there is a trade-off between the preservation of the gel properties and the access of porosity within it.

Here, we demonstrate a liquid-exchange strategy to prepare the linked MOP gels with accessible porosity even in the wet state. Instead of removing the common volatile solvents inside the gels, the replacement of them by selected sterically hindered liquids yields the porous wet gels while preventing the occupancy of gel inner pores by the liquid molecules. As a proof-of-concept, a type of ionic liquid (**IL**), 1-butyl-3-methylimidazolium tetrafluoroborate ($[BMIM]^+[BF_4]^-$), was chosen as the exchanging liquid due to its bulkier molecular size than MOP cavities as well as its high thermal stability allowing for further activation process (Figure 1). The existence of robust MOP networks inside the gels guaranteed the successful exchange process without major shape change or collapse. Compared to the neat **IL**, the resulting **IL**-based MOP gels showed greatly increased gas sorption capacity, indicating for the first time the accessible porosities inside the wet gels. Various liquids with different molecular structures were also used here for the liquid exchange and their corresponding gels were compared to show the versatility of this strategy. Combined with simulation and sorption measurements, we demonstrate the fabrication of new gel-state porous soft materials beyond the porous solids and porous liquids.

Results and discussion

Similar to the creation of porous liquids, the prerequisite in preparing a porous gel is to introduce the permanent porosity into the gel systems. Here we chose **HRhMOP** as the porous building blocks because the thermal stability of these MOPs allows their internal cavities to be maintained during the harsh activation process. And the short rigid bidentate ligand **bix** was selected as the linker to afford a tougher MOP network that can withstand the liquid exchange without gel collapse. Typically, the linked MOP gels are synthesized through the previously reported coordinative solubilizer method.[23] By reversibly attaching a coordinatively monodentate ligand, **diz** (1-dodecyl-1H-imidazole), to the exohedral Rh sites of **HRhMOP**, the solubility of MOPs in DMF was greatly increased. Then these monodentate ligands were replaced with **bix** in DMF through ligand-exchange reaction, leading to the formation of kinetically trapped molecules **HRhMOP(bix)$_{10}$(diz)$_{12}$** with **bix** coordinating in a monodentate

fashion. Heating the solution of the kinetically trapped molecules at 80 °C induced the crosslinking of MOPs into colloidal gels by the dissociation of excessive imidazole ligands to expose the free metal sites on MOP for subsequent coordination with neighboring MOPs.[24] As the result of crosslinking, the linked MOP gels were formed with hierarchical porous networks featuring multiple pores over different length scale, including intrinsic cavities of MOP cages, micro-and mesopores between interlinking MOPs and macropores of the colloidal gel network. Ideally, both the macropores and mesopores are occupied by the liquids, while the micropores and MOP cavities can be accessible by using sterically hindering liquid molecules, thus offering the perfect porous channels for molecules to diffuse despite the existence of surrounding liquid solvents (see Figure 1).

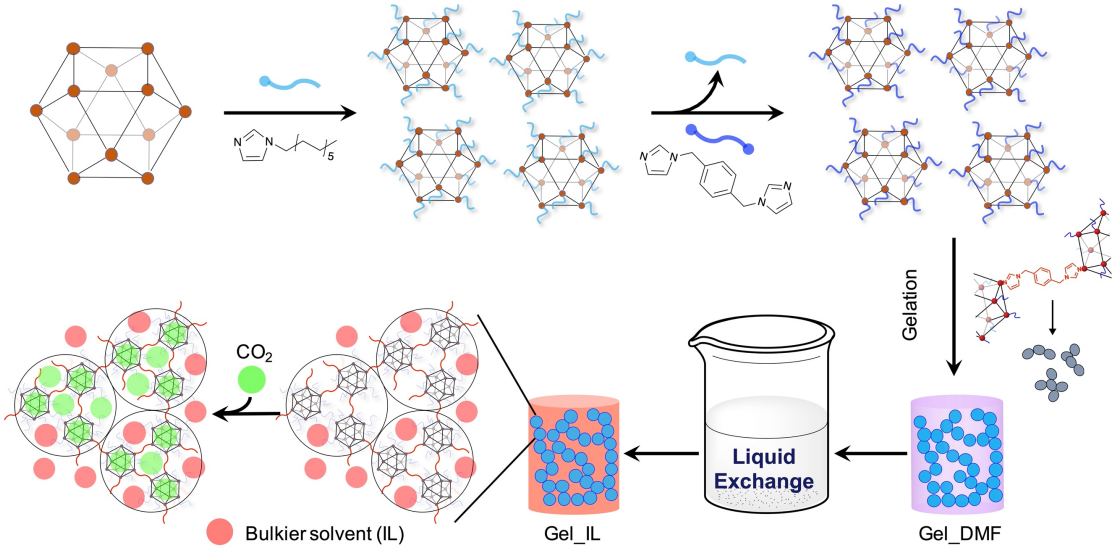

Figure 4-1. Schematic illustration of the preparation of porous linked MOP gel by liquid exchange.

Rather than directly drying the as-synthesized MOP gels in DMF (**Gel_DMF**) to obtain aerogels, the gel sample was immersed into **IL**, $[BMIM]^+[BF_4]^-$, to exchange with DMF solvents inside the gel. Due to the different densities between DMF and **IL**, **Gel_DMF** initially floated at the top of the exchanging **IL** solvents, as shown in Figure 4-2. After replacing the exchanging solvents repeatedly for 3 times, the resulting gel sank to the bottom of the vial, being as an initial indication that DMF had been replaced by $[BMIM]^+[BF_4]^-$ to swell the gel. The solvent exchange process was also monitored by measuring the ^{1}H NMR spectra of the upper exchanging solution at each exchange cycle. As shown in Figure 4-3, a successive decrease of DMF concentration in the exchanging solution was observed throughout the whole exchange process. After 3 exchange cycles, the characteristic proton peaks of DMF disappeared, suggesting a complete replacement of DMF by $[BMIM]^+[BF_4]^-$ in the resulting gel, which was named as **Gel_IL**. Compared to initial **Gel_DMF**, **Gel_IL** displayed highly increased stability at high temperature; thermogravimetric analysis (TGA) revealed that **Gel_IL** has almost zero

volatility at room temperature and only starts to lose weight up to 300 °C (Figure 4-4). This improvement can be attributed to the higher thermal stability of $[BMIM]^+[BF_4]^-$ than volatile DMF, which further confirms the successful preparation of **Gel_IL** by the simple liquid exchange method.

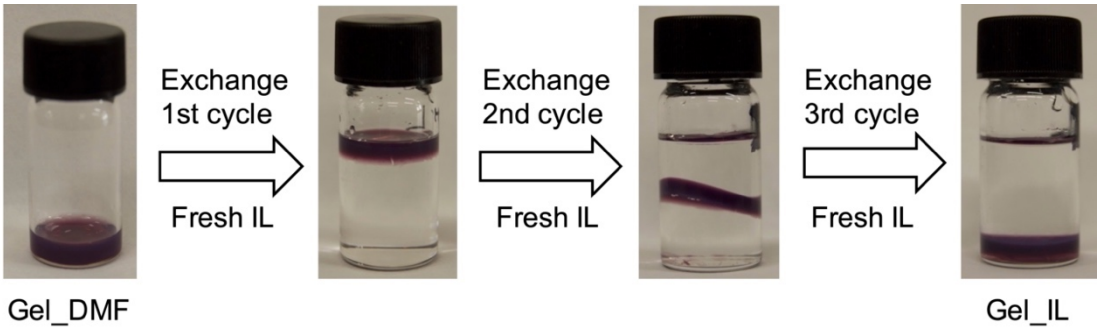

Figure 4-2. Pictures of the linked MOP gel undergoing liquid exchange from **Gel_DMF** to **Gel_IL**.

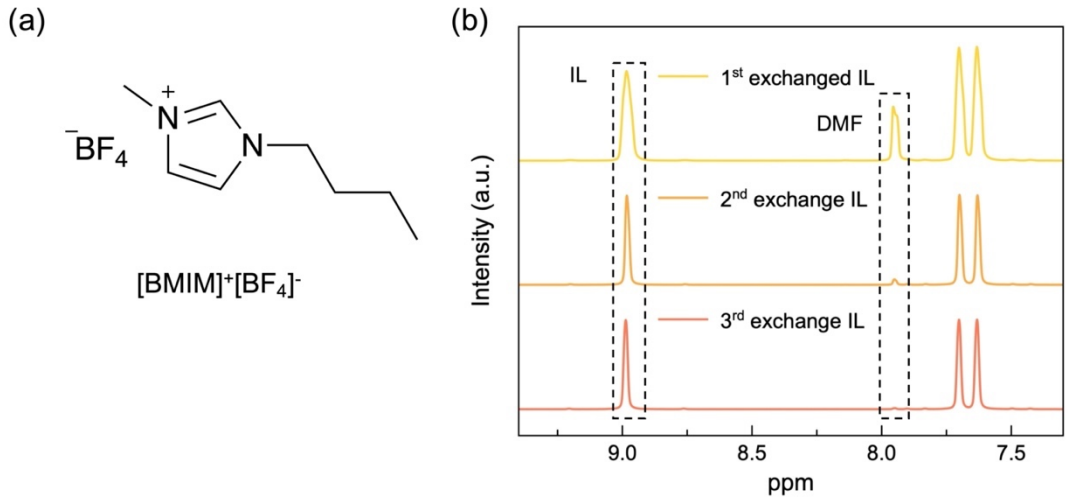

Figure 4-3. (a) The molecular formula of the ionic liquid $[BMIM]^+[BF_4]^-$. (b) ^1H NMR spectra of the upper solvent (**IL**) after each cycle of liquid exchange.

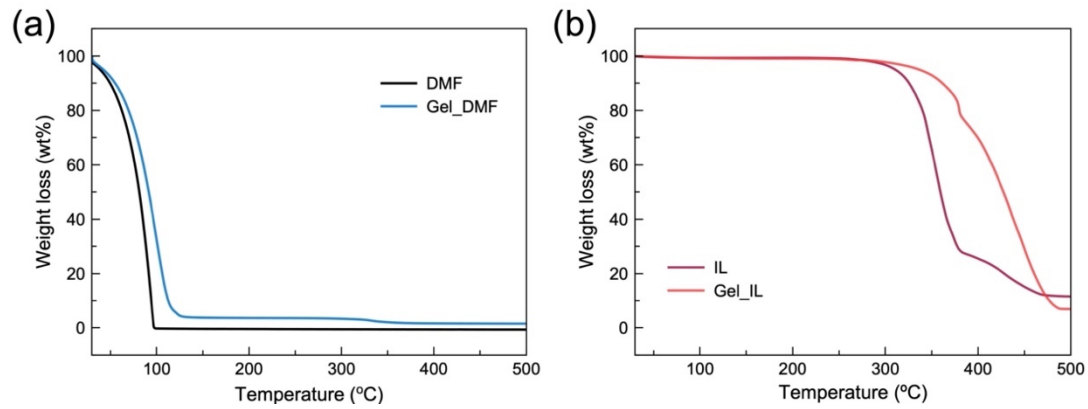

Figure 4-4. TGA plots for (a) DMF and **Gel_DMF**, (b) **IL** and **Gel_IL**.

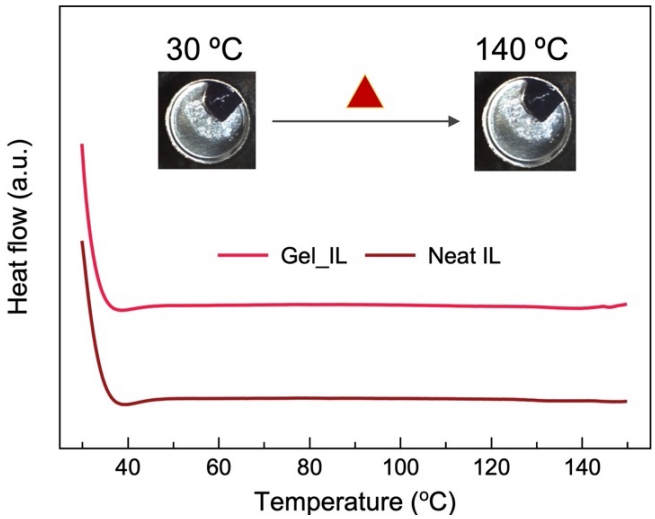

Figure 4-5. DSC plots of the pure **IL** and **Gel_IL** from 30 °C to 140 °C (inset: the pictures of **Gel_IL** during the DSC measurement at 30 °C and 140 °C).

This liquid exchange method was able to change the organic solvent trapped inside the gel phase smoothly without changing the appearance of the resulting gels (Figure 4-2). Even upon heating **Gel_IL**, there is no obvious change in the gel samples, and the featureless differential scanning calorimetry (DSC) trace measured over the range of 30 °C to 140 °C further confirms their thermal stability without decomposition or detrimental reaction between MOPs and **IL** (Figure 4-5). The liquid exchange process also leaves the underlying MOP networks unaltered. From the scanning electron microscopy (SEM) images of the corresponding aerogels obtained by exchanging with fresh acetone and then supercritical CO_2 drying, **Gel_IL** consisted of the same characteristic colloidal network as observed in **Gel_DMF** (Figure 4-6). Based on the ^{1}H NMR analysis of the acid-digested aerogels, the composition of **Gel_IL** was estimated to be **HRhMOP(bix)$_{8.0}$(diz)$_{0.9}$**, which was approximately the same as that of **Gel_DMF** (**HRhMOP(bix)$_{8.1}$(diz)$_{0.7}$**) (Figure 4-7). Therefore, neither the composition nor the structure of the linked MOP gel was changed despite the incorporation of the bulkier liquid, **IL** ($[BMIM]^+[BF_4]^-$), indicating the intact conservation of the linked MOP gel during the solvent exchange.

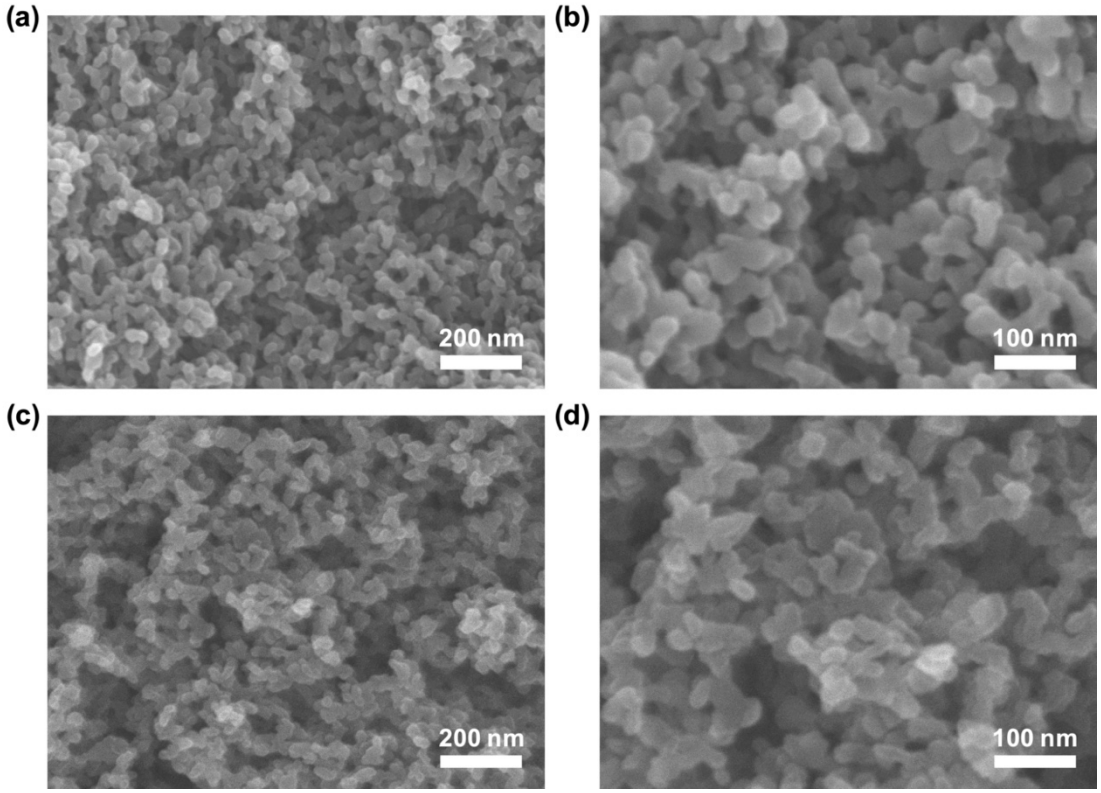

Figure 4-6. SEM images of the aerogels obtained from (a-b) **Gel_DMF**, (c-d) **Gel_IL**.

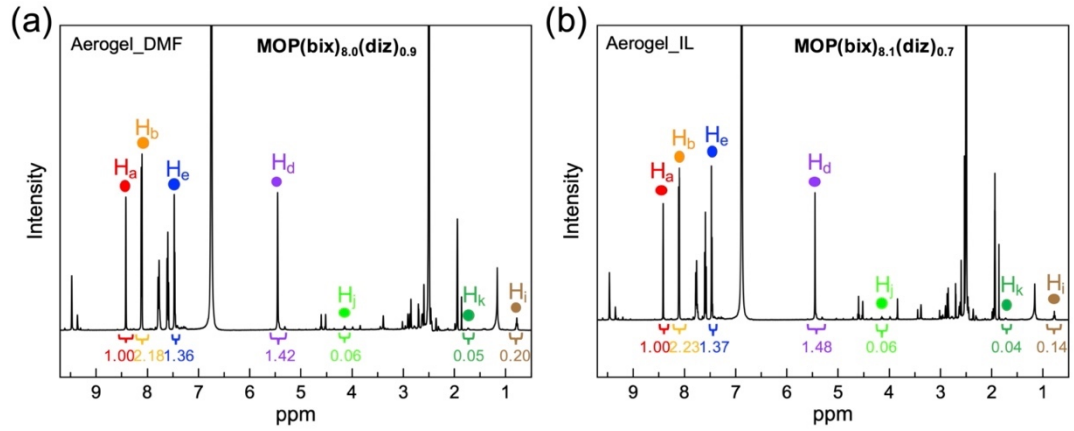

Figure 4-7. ^{1}H NMR spectrum of the acid-digested aerogels obtained from (d) **Gel_DMF**, (e) **Gel_IL**. The distinctive protons H_a, H_b and H_c for **HRhMOP**, H_i, H_j, H_k and H_o for **diz** were used to calculate the molecular formula of the resulting aerogels from each gel sample for integration. As labeled in the figure, several protons were used for each compound and their integrations were averaged for accuracy. Following this methodology, the compositions of each aerogel sample were estimated to be **HRhMOP(bix)$_{8.0}$(diz)$_{0.9}$** for **Gel_DMF**, **HRhMOP(bix)$_{8.1}$(diz)$_{0.7}$** for **Gel_IL**, respectively.

Whether a material is a gel or not is confirmed by its viscoelastic response in dynamic rheology, wherein storage Young's modulus (E') and loss Young's modulus (E'') of samples are measured against frequency (ω, rad s^{-1}). Both **Gel_DMF** and **Gel_IL** showed gel-like behavior with a frequency-independent E' that was one order of magnitude higher than E'' (Figure 4-8b). It is worth noting that after the liquid exchange, **Gel_IL** became tougher with E' = ~ 17.0 kPa, which was an increase of one order of magnitude in comparison to the as-synthesized **Gel_DMF** (E' = 3.9 kPa). Considering the intact structure and composition of linked MOP networks inside the gels, this enhancement in gel stiffness might be related to the high viscosity of the exchanged $[BMIM]^+[BF_4]^-$ trapped within the gels (Figure 4-9). Although the viscosity of DMF was too low to be exactly determined by the viscometer, the viscosity of $[BMIM]^+[BF_4]^-$ was measured to be approximately 62 mPa·s and much higher than that of DMF, which was supposed to improve the resistance of gels to deformation under force.

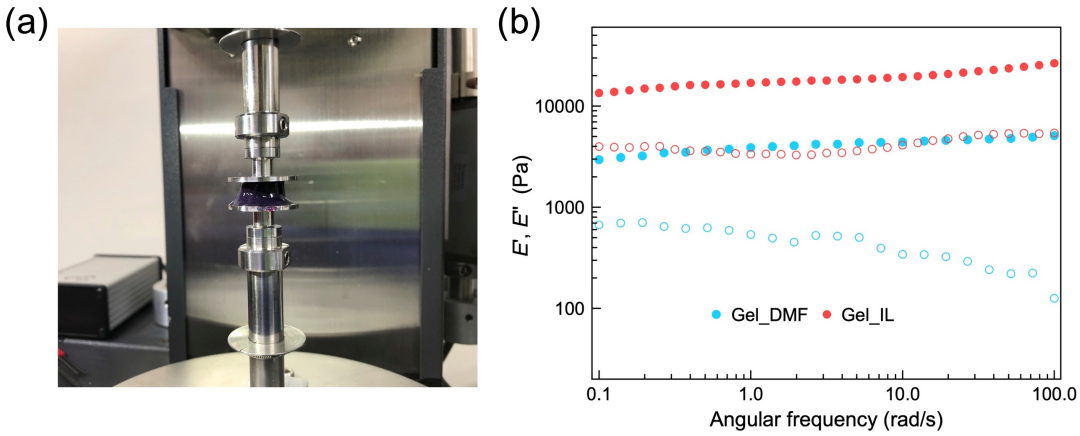

Figure 4-8. (a) The photo of the rheological measurement of the gel sample. (b) Storage Young's modulus (E') (filled circles) and loss Young's modulus (E'') (hollow circles) of **Gel_DMF** and **Gel_IL** versus scanning frequency (ω).

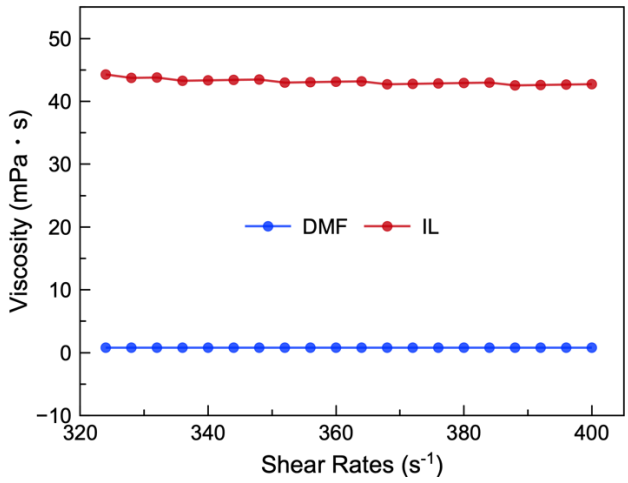

Figure 4-9. The viscosity curve of liquid DMF and **IL**.

The above results show that liquid exchange is an efficient method to replace the solvent media of the linked MOP gel with desired liquids without affecting the inner MOP network. Furthermore, the incorporation of the ionic liquid has endowed the resulting gel with higher thermal stability and enhanced mechanical properties, making them more promising for practical use like gas capture. However, one drawback of this gel system is its low concentration of MOP network (solid aerogel part) out of the liquid media. From the ^{1}H NMR analysis of **Gel_IL** by acid digestion, the ratio between the MOP network and $[BMIM]^{+}[BF_4]^{-}$ can be calculated to reveal only 1.8 wt% of MOP network within the wet gel with most of the gel volume contributed by the liquid $[BMIM]^{+}[BF_4]^{-}$ molecules (Figure 4-11). To introduce higher porosities to the gels for the sake of sorption, it is necessary to find ways to control or increase the loading of MOP network inside the gels.

The first trial was made by increasing the concentration of **HRhMOP** used during gel formation, which was performed currently from an initial solution of 1.4 mM MOP. However, this synthesis of concentrated MOP gels failed due to the uncontrollable gelation which was too fast to be handled. As increasing the MOP content, the amount of the kinetically trapped molecules formed in the solution was concomitantly increased, leading to an accelerated dissociation and crosslinking reaction followed by fast precipitation of MOP aggregates before gel formation. To avoid the precipitation at high MOP concentration, an alternative post-synthetic way was applied in combination with the liquid exchange strategy, in which a mixing solution of $[BMIM]^{+}[BF_4]^{-}$ and acetone was used instead of the neat **IL**. The low boiling point of acetone allows it to be easily removed from the resulting exchanged gels upon heating, leading to the decreasing volume of liquids and thus the increasing loading of MOP networks inside the gels (Figure 4-10). By tuning the volume ratio of acetone to $[BMIM]^{+}[BF_4]^{-}$ (0/1, 5/1,

10/1 and 15/1 in v/v, respectively), **Gel_IL (n wt%)** were obtained with different loadings of MOP network, where *n* indicates the weight percentage of the linked MOP network as estimated by ^{1}H NMR analysis of the acid-digested gel samples (Figure 4-11). Note that the rheological measurements revealed a greatly increased gel stiffness with the increasing loading of MOP network (Figure 4-12). Compared to the initial **Gel_IL (1.8wt%)** with *E*' = ~ 17.0 kPa, **Gel_IL (10.2wt%)** presents a more solid-like mechanical behavior with *E*' = ~ 570.2 kPa. This mechanical evolution can be attributed to the evaporation-induced dense packing of the inner colloidal MOP network, which was supported from both the gel shrinkage during acetone removal (Figure 4-10) and SEM images of the corresponding aerogels (Figure 4-13). This wide tunable rheological range of **Gel_IL** series is believed to be very promising for practical applications.

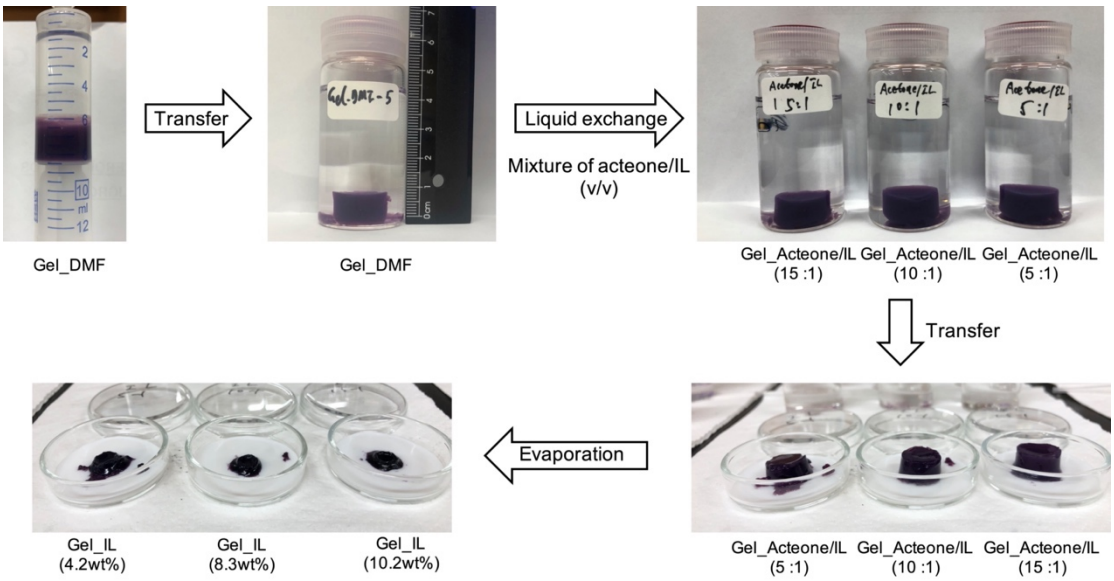

Figure 4-10. The typical process used to prepare **Gel_IL** with higher concentrations of MOP networks.

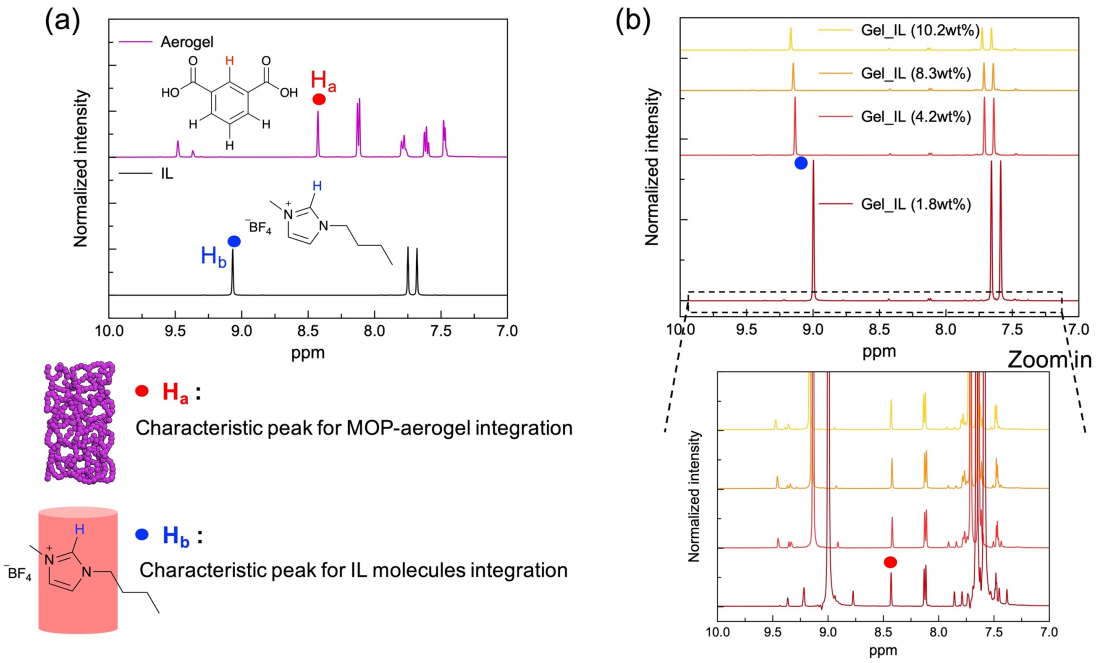

Figure 4-11. (a) ^{1}H NMR spectrum of MOP aerogel and IL molecules. (a) ^{1}H NMR spectrum of the digested aerogel samples obtained from **Gel_IL** at different concentrations of MOP networks.

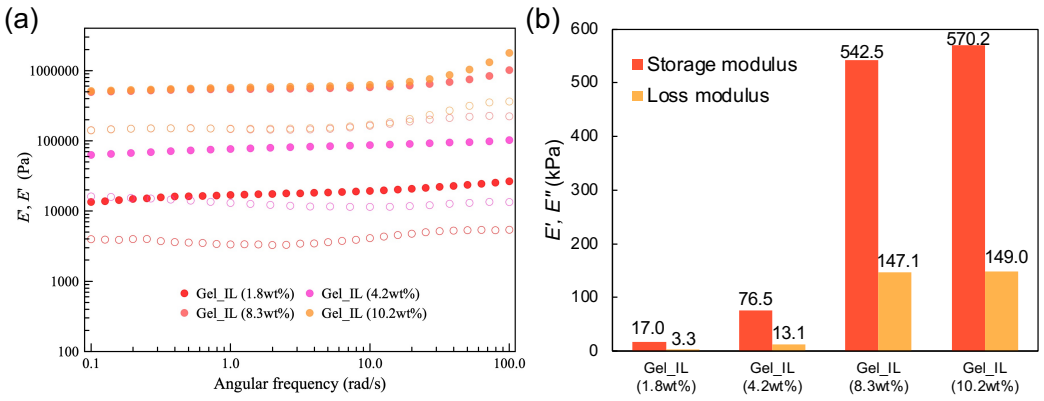

Figure 4-12. (a) Storage Young's modulus (*E*') (filled circles) and loss Young's modulus (*E*'') (hollow circles) of **Gel_IL** with different concentrations of MOP networks. (b) Mechanical stiffness (E' and E'' at 1 rad/s) of **Gel_IL** with different concentrations of MOP networks.

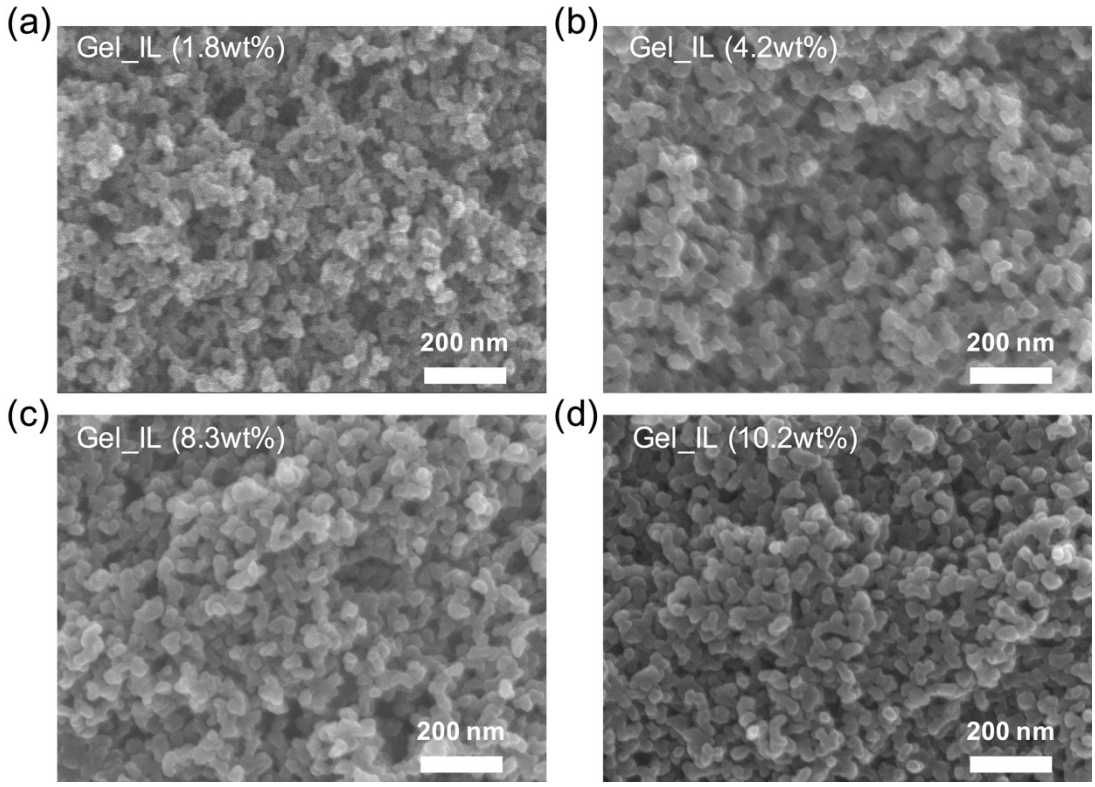

Figure 4-13. SEM images of the aerogels obtained from **Gel_IL** with different concentrations of MOP networks.

The aim of this liquid exchange strategy was to create the linked MOP gel with permanent microporosity which is accessible even at the wet state. The ionic liquids, **IL** ($[BMIM]^+[BF_4]^-$), were used as bulky solvent molecules to expel themselves from the cavities of MOPs so that their intrinsic porosity can be easily accessed without the need to remove these solvents. To investigate the effect of $[BMIM]^+[BF_4]^-$ on the porosity of the resulting gels, CO_2 sorption measurements of **Gel_IL** at 303K were performed and the isotherms were compared with the neat **IL** (Figure 4-14a). Thanks to their good thermal stability, all **Gel_IL** samples were heated at 120 °C in vacuum overnight for activation without detrimental gel collapse. Only the DMF or acetone molecules that remained inside the MOP cavities were supposed to be removed during the activation, guaranteeing the accessible pores for gas capture (Figure 4-1). As shown in the isotherm of Figure 4-14a, the existence of accessible pores affords all the **Gel_IL** with greatly increased CO_2 capacity compared to the neat **IL**. At $P/P_0 \sim 1$, **Gel_IL (1.8wt%)** adsorbed 0.97 cm^3 CO_2 per gram sample, which was three times more than the uptake of neat **IL** (0.32 cm^3 g^{-1}). Further increasing the concentration of MOP networks led to a higher gas uptake of 1.32 cm^3 g^{-1} and 1.40 cm^3 g^{-1} for **Gel_IL (4.2wt%)** and **Gel_IL (8.3wt%)**, respectively, confirming that these accessible additional pores are coming from the inner MOP

networks. For **Gel_IL (10.2wt%)**, the gel with the highest loading of MOP network, a slightly decreased amount of CO_2 uptake (1.26 cm^3 g^{-1}) was observed. This slight decrease in gas capacity can be explained by the significant change of solvent viscosity or mobility in the highly concentrated gel. Different from the neat liquids, the mobility of the solvent molecules trapped in the gels is greatly affected by the gel structures. Increasing the content of MOP network resulted in a much denser packing of the solid colloidal network with not only decreased volume of liquids ($[BMIM]^+[BF_4]^-$) but also decreased size and volume of macropores spanning the gels (see SEM images of the corresponding aerogels in Figure 4-13). From the macroscopic view, the gel became more "solid-like" with greatly improved mechanical stiffness, as confirmed by the above rheological measurements (Figure 4-12). From the molecular scale, the molecular motion of $[BMIM]^+[BF_4]^-$ molecules became more restricted within the densified gel network, leading to lower free volumes than its neat state for the following solution and diffusion of gas molecules (Figure 4-15). Considering that the CO_2 uptake within the gel would follow the solution-diffusion model, the decreased solubility of gas molecules in the solvent phase (**IL**) would suppress the CO_2 sorption of the linked MOP phase and thus inhibit the overall sorption process. As a result, the CO_2 capacity of the corresponding **Gel_IL** at the high loadings of MOP network was slightly decreased (Figure 4-14a).

Positron annihilation lifetime spectroscopy (PALS) experiments were performed to further investigate the porosity of **Gel_IL**. As a widely applied technique in liquid sorbents, PALS allows us to detect the voids within materials even at the liquid state. Exposure of the gel samples to a positron source such as ^{22}Na leads to the formation of ortho-positronium (o-Ps), which is a parallel spin complex between e^+ and e^-. The lifetime of o-Ps can be correlated to the average pore diameter of the materials by a well-established model, in which a larger pore corresponds to slower decay rates and thus longer lifetime. Therefore, by collecting the lifetime of o-Ps, information of the accessible porosities within the gel samples can be obtained, allowing us to estimate the corresponding pore size distribution (PSD) plot as shown in Figure 4-14c (see detailed lifetime and pore size data in Table 1). The o-Ps lifetime of 2.75 ± 0.04 ns measured for neat **IL** corresponds to an average void diameter of 0.69 ± 0.01 nm, which is attributed to the transient pores formed by random movement of the liquid molecules. The o-Ps lifetime of 2.53 ± 0.07 ns measured for the linked MOP aerogel corresponds to an average pore diameter of 0.66 ± 0.01 nm, which matches well with the size of MOP internal cavities. After combining these two components into the wet gels, **Gel_IL** gave a lifetime of around 2.7 ns with the average pore size (~0.68 nm) in between the MOP network (solid phase) and liquid $[BMIM]^+[BF_4]^-$ (solvent phase). Note that only one peak can be observed from the PSD plot of all **Gel_IL** samples and it is very difficult to distinguish whether this pore size is contributed

by both of these two components or not. As increasing the concentration of MOP network, there was no obvious change in the average pore diameter of the wet gel samples. However, a decreasing trend in the intensity of the pores can be noticed from 10.4% of **Gel_IL (1.8wt%)** to 4.7% of **Gel_IL (10.2wt%)**, which might be explained by the decreased mobility of $[BMIM]^+[BF_4]^-$ molecules inside the highly concentrated gels. As discussed above, further increasing the loading of MOP network has yielded a more "solid-like" gel with greatly increasing **IL** viscosity within the gel. With the increase of $[BMIM]^+[BF_4]^-$ viscosity, its molecular movement was supposed to be highly restricted with lower free volume, leading to decreased number of transient voids and thus less contribution to the overall gel porosities. As a result, the intensity of the pores of **Gel_IL** in the PSD curves was decreased with increasing content of MOP network, which is also consistent with the above sorption data for the decreasing CO_2 capacity of gels at higher loading of MOP network.

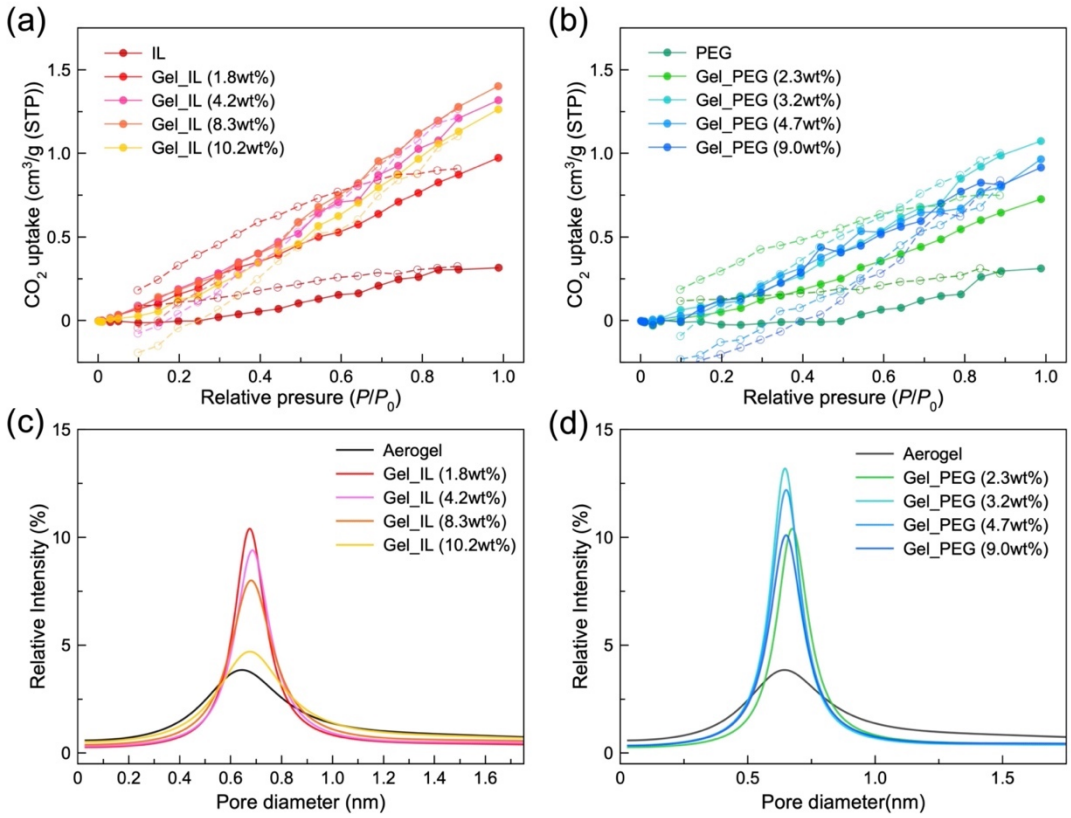

Figure 4-14. CO_2 adsorption isotherm at 303K for (a) **Gel_IL** and (b) **Gel_PEG** with different concentration of MOP networks. PALS-derived pore size distribution (PSD) plot of (a) **Gel_IL** and (b) **Gel_PEG** with different concentration of MOP networks

Table 1. PALS results of **Gel_IL** series.

Sample	Lifetime of τ 3 (ns)	Intensity (%)	Average pore size in diameter (nm)
IL	2.751 ± 0.040	10.2 ± 0.1	0.692 ± 0.006
Gel_IL (1.8wt%)	2.629 ± 0.032	10.4 ± 0.1	0.674 ± 0.005
Gel_IL (4.2wt%)	2.727 ± 0.034	9.4 ± 0.1	0.689 ± 0.005
Gel_IL (8.3wt%)	2.692 ± 0.031	8.0 ± 0.1	0.683 ± 0.004
Gel_IL (10.2wt%)	2.702 ± 0.050	4.7 ± 0.1	0.685 ± 0.007
Aerogel	2.525 ± 0.070	3.8 ± 0.1	0.658 ± 0.011

Table 2. PALS results of **Gel_PEG** series.

Sample	Lifetime of τ 3 (ns)	Intensity (%)	Average pore size in diameter (nm)
PEG	2.534 ± 0.004	18.4 ± 0.1	0.660 ± 0.001
Gel_PEG (2.3wt%)	2.435 ± 0.014	16.6 ± 0.1	0.644 ± 0.002
Gel_ PEG (3.2wt%)	2.460 ± 0.021	13.2 ± 0.1	0.648 ± 0.003
Gel_ PEG (4.7wt%)	2.493 ± 0.021	12.2 ± 0.1	0.654 ± 0.003
Gel_IL (9.0wt%)	2.480 ± 0.027	10.1 ± 0.1	0.652 ± 0.004
Aerogel	2.525 ± 0.070	3.8 ± 0.1	0.658 ± 0.011

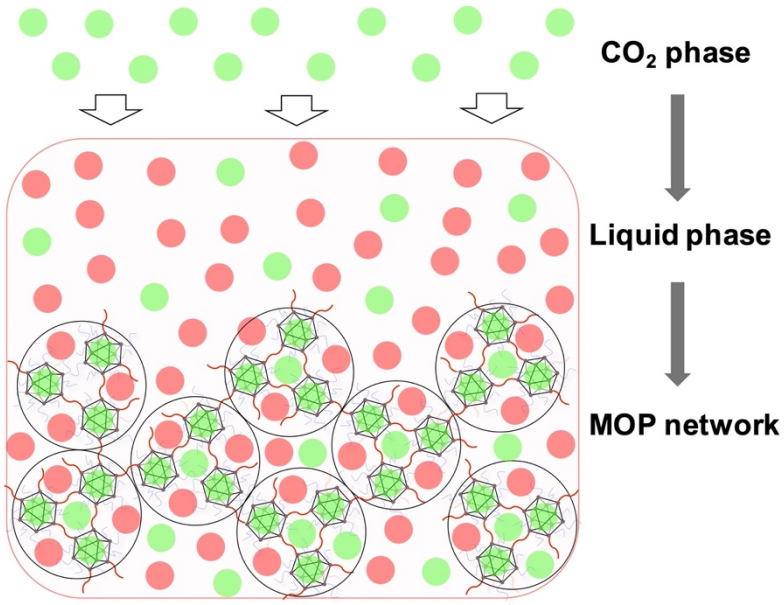

Figure 4-15. Schematic illustration of the diffusion path of CO_2 gas molecules within the wet gel samples.

The CO_2 sorption and PALS measurements have confirmed the permanent porosity to be accessible in the wet gels of **Gel_IL** thanks to the bulkier molecular structure of **IL** than the MOP aperture. To gain a deep insight into the microscopic scenario of MOPs with **IL** inside the gels, molecular dynamics (MD) simulations were performed by building a computational model of **HRhMOP**/**IL** composite with a MOP surrounded by $[BMIM]^+[BF_4]^-$ molecules (Figure 4-16 and 4-17, see detailed information in Supporting Information). For comparison, another composite model of **HRhMOP**/**PEG** was also construed by replacing $[BMIM]^+[BF_4]^-$ with polyethylene glycol 400 (**PEG**), which is a linear liquid molecule with an average molecular weight of 400 (Figure 4-18). Figure 4-16a shows the atomic densities of **IL** and **PEG** as a function of the radial distance from the centre of mass (COM) of **HRhMOP** collected from their simulation models, respectively. Unlike the **PEG** molecules that mainly penetrate and occupy the MOP cavities, **IL** shows less accessibility to the pores of MOPs although a certain amount of $[BMIM]^+$, which is the cationic part of **IL**, has been found inside the cages. Interestingly, their ionic counterparts $[BF_4]^-$ rarely enter the pore window and never enter the MOP pore, suggesting a preferred orientation of $[BMIM]^+$ with its hydrocarbon tail entering the MOP pore and its positively charged methylimidazolium heading outside the pore window. As such, $[BF_4]^-$ is expected to remain outside the pore, in close interaction with the positively charged methylimidazolium head (Figure 4-16f). This unique orientation of $[BMIM]^+[BF_4]^-$ molecules allows for the maximum preservation of MOP cavities for potential gas molecules, as also can be seen in the porosity map of **HRhMOP**/**IL** (Figure 4-17c). A central red pore with a size around 6 Å can be found in the MOP cage at the centre of the simulation box for **HRhMOP**/**IL**, indicating the accessible porosity which is in turn absent in the case of **HRhMOP**/**PEG** (Figure 4-17b and c). Experimental CO_2 sorption and PALS measurements of **Gel_PEG** at different loadings of MOP network have been performed and compared with **Gel_IL** (Figure 4-14b and d). Coincident with the simulation results, the introduction of MOP networks into **PEG** resulted in only limited enhancement in CO_2 capacity due to the penetration of linear **PEG** chains.

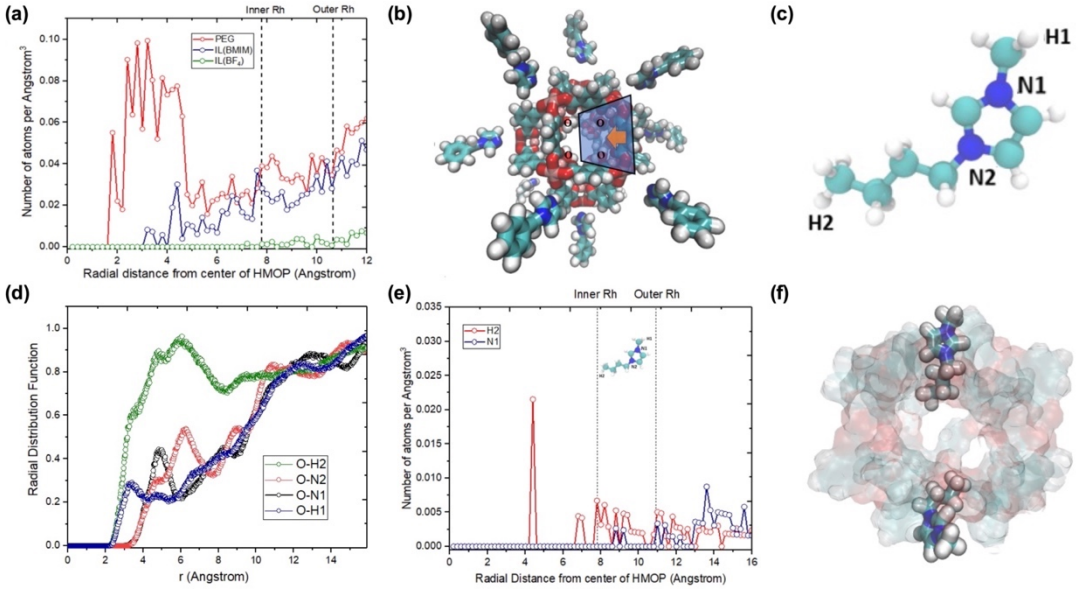

Figure 4-16. (a) Atomic density as a function of the distance from the centre of mass of the **HRhMOP** for **PEG** (red), $[BMIM]^+$ (blue) and $[BF_4]^-$ (green). (b) Scheme of the 1-benzylimidazole capped **HRhMOP**, showcasing its truncated cone-shaped window. Color code: O (red), H (white), C (cyan), Rh (pink). (c) Scheme of $[BMIM]^+$. Colour code: N (blue). (d) Radial distribution functions between $O_{HRhMOP\text{-}water}$, and the $[BMIM]^+$ sites. (e) Atomic density as a function of the distance from the centre of mass of the **HRhMOP** for the head (blue) and tail (red) of $[BMIM]^+$. (f) Snapshot from **HRhMOP**/**IL** simulations (at 38.2 ns) that captures two $[BMIM]^+$ cations in their typical orientation, with the head outside the pore and the tail inside the pore. For clarity purposes, all other **IL** molecules were removed and the MOP was represented as a transparent colored surface without the capping 1-benzilimidazole molecules.

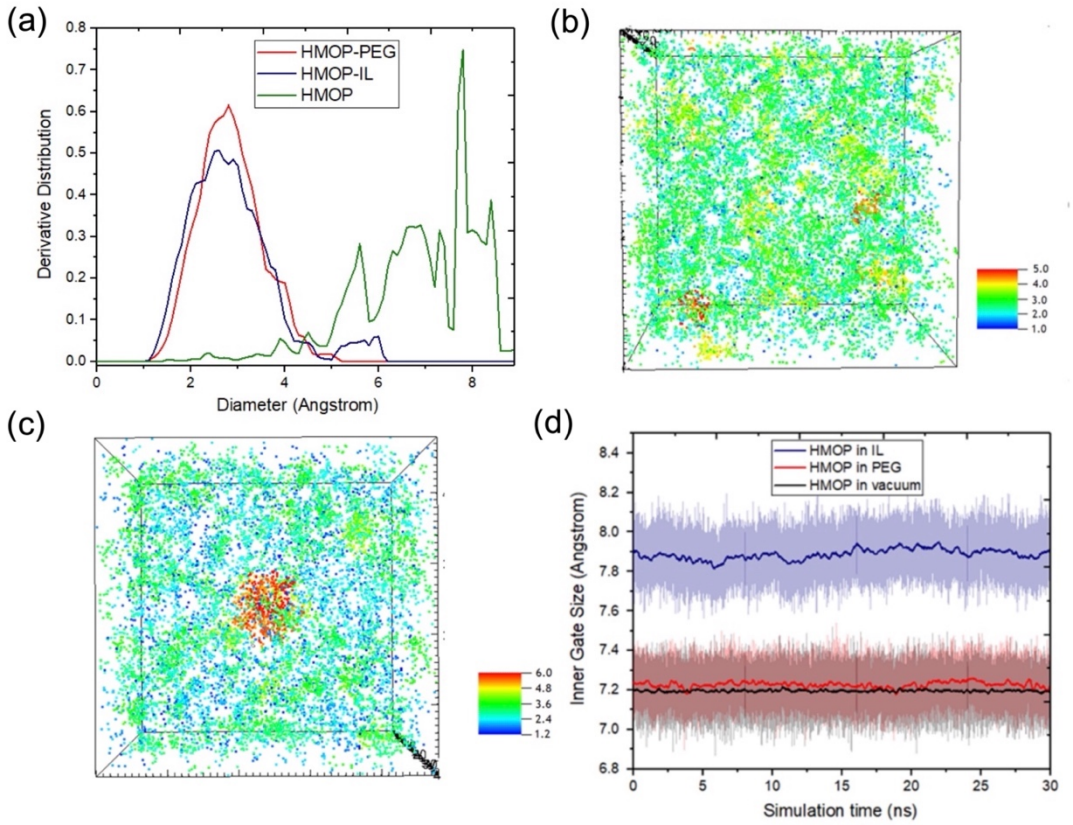

Figure 4-17. (a) Pore size distribution for **PEG/HRhMOP** (red), **IL/HRhMOP** (blue) and **HRhMOP** (green). (b) and (c) porosity maps highlighting the pore sizes for the **PEG/HRhMOP** and the **IL/HRhMOP** composite models respectively. (d) Inner Gate's size as a function of time.

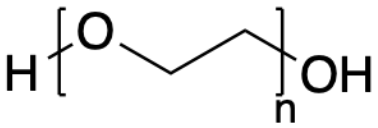

Figure 4-18. Molecular formula of **PEG**

The above experimental and simulated results suggest that the molecular structure of solvent plays an important role in the porosity of their corresponding wet gels. In fact, a large library of liquid molecules can be introduced into these gel systems by the simple liquid exchange strategy. Except for **IL** and **PEG**, another four molecular liquids, including 15-crown-ether (**CE**), 1-butylpyridinium bis(trifluoromethanesulfonyl)imide ($[Bpy]^+[NTf_2]^-$), hydroxy-terminated poly(dimethylsiloxane **(PDMS-OH**) and poly(dimethylsiloxane-co-methylphenylsiloxane) (**PDMS-Ph**), were incorporated into the linked MOP gels to demonstrate the versatility. All the resulting MOP gels, referred as **Gel_CE**, **Gel_**[**Bpy**][**NTf_2**], **Gel_PDMS-OH** and **Gel_PDMS-Ph**, displayed higher CO_2 uptake at 303 K compared to their neat liquid molecules, indicating the existence of accessible porosities in each wet gel sample (Figure 4-19). This versatility of solvents makes this strategy very attractive because it allows us to impart new functionalities to the resulting porous gel materials by the rational choice of suitable liquid media. For example, the introduction of the ionic liquid ($[BMIM]^+[BF_4]^-$) here has endowed the resulting MOP gels with high ionic conductivity, as shown in Figure 4-20. The ionic conductivity of **Gel_IL(1.8wt%)** at 80 ºC was measured to be 18.8 mS cm^{-1}, which is even higher than the pure **IL** (17.6 mS cm^{-1}) (Figure 4-20a). As increasing the concentration of MOP network, the conductivity of the MOP gels continued to decrease from 14.8 mS cm^{-1} for **Gel_IL(4.2wt%)** to 14.8 mS cm^{-1} for **Gel_IL(8.3wt%)** to 8.9 mS cm^{-1} for **Gel_IL(10.2wt%)**, respectively. This decreased gel conductivity at increasing loading of MOP networks can be explained by the decreased mobility of conductive $[BMIM]^+[BF_4]^-$ molecules, which was consistent with the sorption behavior of **Gel_IL** samples as discussed above.

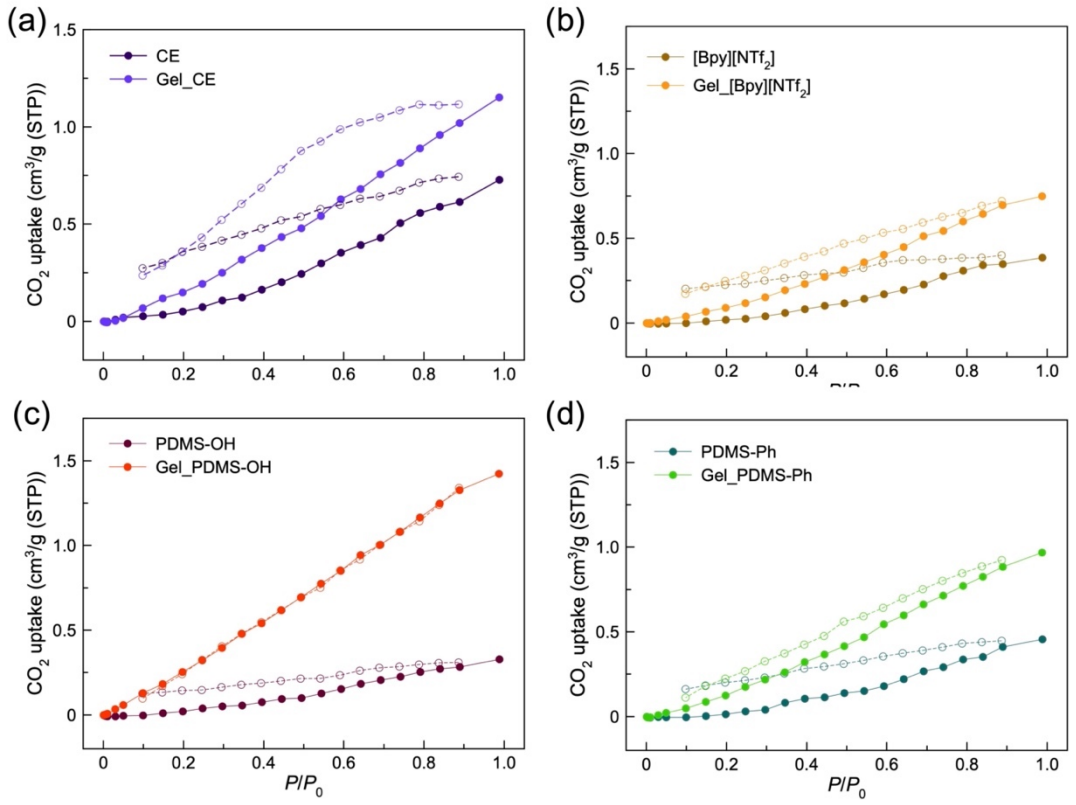

Figure 4-19. CO_2 sorption measurement at 303 K of (a) **Gel_CE**, (b) **Gel_[Bpy][NTf₂]**, (c) **Gel_PDMS-OH** and (d) **Gel_PDMS-Ph** obtained by direct liquid exchange strategy.

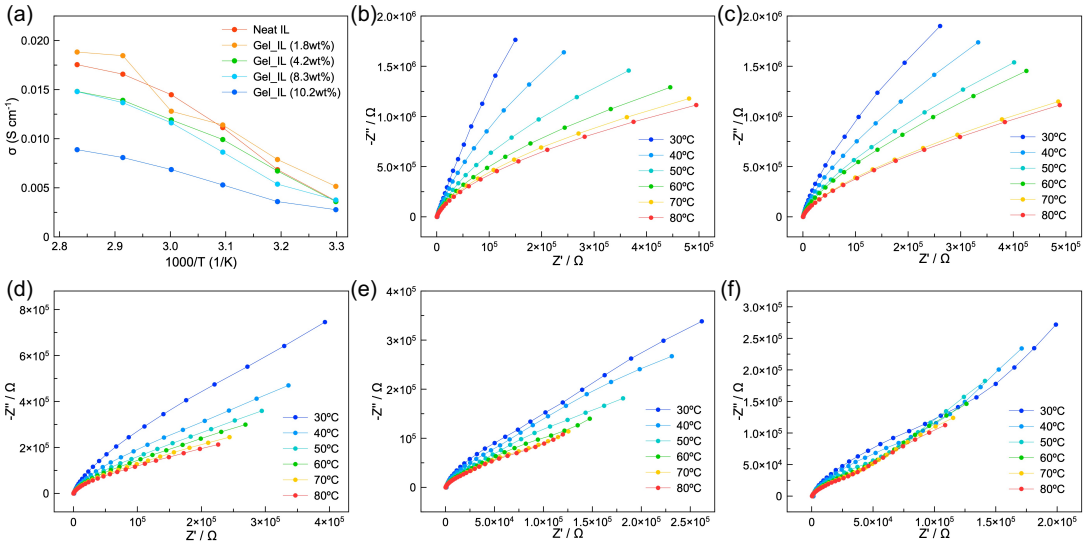

Figure 4-20. (a) Ion conductivity of neat **IL** and **Gel_IL** series as a function of temperature under N_2 atmosphere. (b) Nyquist plots of (b) **IL**, (c) **Gel_IL(1.8wt%)**, (d) **Gel_IL(4.2wt%)**, (e) **Gel_IL(8.3wt%)** and (f) **Gel_IL(10.2wt%)** from 1 Hz to 0.1 Hz measured at 30-80 ºC N_2 atmosphere.

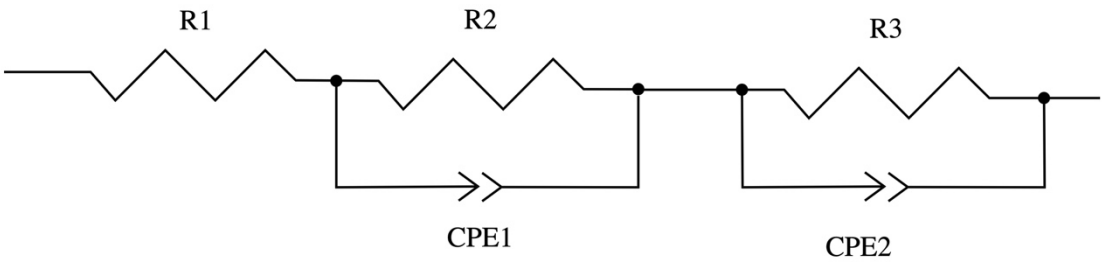

Figure 4-21. Equivalent circuit used for the fitting of impedance measurements. R1, R2, R3, CPE1 and CPE2 represent the resistance and constant phase element, respectively.

Conclusion

In summary, we demonstrated a liquid-exchange strategy to obtain linked MOP gel with permanent porosity. Since the performance of the gel was determined by both the MOP network and solvent that was trapped inside the gel, the ability to incorporate the inner solvents featuring different structures and properties allows us to modify the gel in a more controllable way. As the target solvent, an ionic liquid (**IL**) was selected here to completely replace the DMF solvents in both the MOP cavities and gel networks by simply immersing the as-synthesized MOP gel in **IL** solvents. Due to the molecular size of the exchanged **IL** that is too big to enter the MOP pore, the cavity of MOP remained almost fully empty and thus acted as accessible pores for the gas adsorption even in the form of wet gels. In addition to the permanent porosity, the introduction of **IL** as solvents endowed the resulting MOP gel with zero volatility, high thermal stability and significantly enhanced mechanical properties. This strategy opens the door to synthesize porous gels featuring unique advantages in comparison with either porous solids or porous liquids. Different from porous liquids especially type II or III, there is no need for bulky solvents to dissolve or disperse the porous components (porous cages, for instance) in the porous gels. And the nature of the gel allows us to process it into different shapes, which cannot be achieved by common porous solids with crystalline structures. Except for **IL**, five different liquid molecules including **PEG**, $[Bpy]^+[NTf_2]^-$, **PDMS-OH**, **PDMS-Ph** and **CE** were also used here as liquid media of the MOP gels to show the versatility of this strategy. By combining linked MOP gels with various functional solvents, porous soft materials with interesting properties are expected to be created with potentials in different applications, such as gas adsorption or separation, or catalysis. For instance, the use of **IL** as solvent imparted the resulting porous MOP gel with high ionic conductivity, showing potential for its potential use as gel electrolyte.

Experimental section

Materials

Rhodium acetate was synthesized according to a previously reported procedure.[25] Isophthalic acid (H_2bdc), 1-butylpyridinium bis(trifluoromethanesulfonyl)imide ($[Bpy]^+[NTf_2]^-$), hydroxy-terminated poly(dimethylsiloxane **(PDMS-OH**) and poly(dimethylsiloxane-co-methylphenylsiloxane) (**PDMS-Ph**) were purchased from Sigma-Aldrich and used as received. 1-Butyl-3-methylimidazolium tetrafluoroborate ($[BMIM]^+[BF_4]^-$), Polyethylene glycol 400 (**PEG**) and 15-crown-5-ether (**CE**) were purchased from Tokyo Chemical Industry (TCI). Solvents were purchased from Wako Pure Chemical Industries except those at HPLC grade which were purchased from Fischer Chemicals.

Characterizations

The rheological measurements of the gels were made using a stress-controlled AR-G2 (TA Instruments, New Castle, DE, USA) rheometer. Gel samples after synthesis were transferred into a clean glass slide (~ 1 mm in thickness). Then the gel was loaded into the rheometer with the glass slide to perform the rheology tests. The measurements of gels were conducted by frequency sweeping in a compression mode with a 1% strain amplitude that was well inside the linear regime (initial strain is fixed to 1.5%).

The super-critical CO_2 drying process was carried out on SCLEAD-2BD autoclave (KISCO) using supercritical CO_2 at 14 MPa and 50 °C.

Thermogravimetric analyses (TGA) were performed in the temperature range from room temperature to 500 ºC at a heating rate of 10 ºC/min with a Rigaku Thermo plus EVO2, under a nitrogen atmosphere.

Differential scanning calorimetry (DSC) was carried out in the temperature range from 30 ºC to 150 ºC at a heating rate of 10 ºC/min using Hitachi DSC 7020, under a nitrogen atmosphere.

Scanning Electron Microscopy (SEM) of the microstructures of the aerogel samples were observed using a field-emission scanning electron microscope with a JEOL Model JSM-7001F4 system operating at 10 kV and 5 mA current. The samples were coated with 28 nm Osmium before measurement.

^{1}H NMR spectra were recorded on a Bruker Biospin DRX-600 (600 MHz) spectrometer. For composition analysis, 5 mg of aerogel sample was digested in a mixture of DMSO-d_6 (750 μl) and DCl (50 μl). The mixture was then heated at 100 °C overnight to obtain a yellow solution. To determine the concentration of the MOP network in the exchanged solvents, 30 mg of wet gel sample was used for digestion in the same condition as above.

CO_2 (303 K) gas sorption isotherms of the MOPs and aerogels were recorded on a BELSORP-max volumetric adsorption instrument from BEL Japan Inc. Prior to gas sorption measurement, the samples were activated at 120 °C for 12 h except for the sample of **Gel_CE** which were activated at 80 °C.

Positron annihilation lifetime spectroscopy (PALS) experiments were conducted on EG&G Ortec Spectrometer. A 1.5 MBq ^{22}NaCl positron source sealed between two sheets of 2.54 μm Mylar was positioned in the center of two Al sample holders. Lifetimes were collected at 298K where a minimum of 5 files of 1 x 10^6 integrated counts was collected over 24h and analyzed using LT v9 software.[26] The data was fitted to 3 lifetimes: the first lifetime, τ1 was attributed to *para*-positronium (*p*-Ps) annihilation and fixed to 0.125 ns. The second lifetime, τ2 due to the free annihilation of the positron with free electrons within the sample, was approximated to 0.4 ns. The final lifetime, τ3, was associated with *ortho*-positronium (*o*-Ps) annihilation and fitted as a discrete lifetime and attributed to the pores within the wet gel samples. An extra *o*-Ps component was observed for the neat **HRhMOP** sample.

Conductivity measurements were performed using a BioLogic VSP-300 with an EC Frontier sample cell (SB1A, ϕ = 5 mm, d = 5 mm). Impedance data of the neat IL and gel samples was collected over the frequency range from 0.1 Hz to 1.0 MHz with an input voltage amplitude of 30 mV in the temperature range from 30 ºC to 80 ºC under N_2 atmosphere. Impedance signals of all samples were obtained as Nyquist plots and the impedance data sets were fitted by equivalent circuit simulation to obtain the resistance values using ZView software. The proton conductivity was calculated by the equation of $\sigma = L / (Z \times A)$, where L is the length between the electrodes (cm), A is the electrode area (cm^2) and Z is the impedance (Ω).

Detailed synthesis

Synthesis of precursors

1-dodecyl-1H-imidazole (**diz**), 1,4-bis(imidazole-1-ylmethyl)benzene (**bix**) and **HRhMOP** were synthesized according to our previous reports.[27]

Synthesis of HRhMOP(diz)$_{12}$

200 mg of **HRhMOP** were dispersed in 40 mL of DCM, then 132.5 mg of **diz** (18 mol. eq.) were added. After sonication for 5 mins, the solution was centrifuged to remove the precipitate. The upper purple solution was collected and evaporated in vacuum. The obtained solid residue was washed twice with EtOH to remove any remaining **diz**. Finally, the purple solid product was dried under vacuum.

Synthesis of Gel_DMF

In a typical synthesis process, 1mL DMF solution of **HRhMOP(diz)$_{12}$** (2.8 mM) was added to 1 mL DMF solution of **bix** (33.6 mM, 12 mol. eq.) under vigorous stirring. The resultant transparent purple solution (1.4 mM) was transferred into the sealed syringe, followed by heating at 80 °C for 8 h. After the gelation, the fresh gel was transferred into the vial with excessive fresh DMF and was then heated at 80 °C for 8 h for aging. The same aging procedure was repeated 3 times to obtain gel samples with increased porosity, and the corresponding gel was named as **Gel_DMF**.

Synthesis of Gel_IL by liquid exchange.

The liquid exchange was applied to obtain **Gel_IL**. For the common method, as-made **Gel_DMF** was immersed in the $[BMIM]^+[BF_4]^-$ for three days, replacing the fresh $[BMIM]^+[BF_4]^-$ each day. After the DMF in the gel was removed completely, **Gel_IL** was made.

Synthesis of Gel_IL with different concentrations of MOP networks

The concentrated **Gel_IL** was prepared by an evaporation method. Typically, as-made **Gel_DMF** was immersed in acetone for three days, replacing the fresh acetone each day. After the DMF in the gel was removed, the exchanged gel was immersed in a mixing solution of acetone and $[BMIM]^+[BF_4]^-$ at a certain volume ratio (0:1, 5:1, 10:1and 15:1, respectively). This exchange process was repeated for another three days, then the resulted gels were left in oven at 50 °C to slowly remove the acetone. Finally, the gels were dried in vacuum at 80 °C to obtain **Gel_IL** with the MOP network at different concentrations.

Synthesis of Gel_PEG by liquid exchange.

The same procedure as for **Gel_IL** was used, in which **PEG** instead of $[BMIM]^+[BF_4]^-$ was used.

Synthesis of Gel_CE by liquid exchange.

The same procedure as for **Gel_IL** was used, in which **CE** instead of $[BMIM]^+[BF_4]^-$ was used.

Synthesis of Gel_PDMS-Ph by liquid exchange.

The same procedure as for **Gel_IL** was used, in which **PDMS-Ph** instead of $[BMIM]^+[BF_4]^-$ was used.

Synthesis of Gel_PDMS-OH by liquid exchange.

The same procedure as for **Gel_IL** was used, in which **PDMS-OH** instead of $[BMIM]^+[BF_4]^-$ was used.

Synthesis of Gel_$[Bpy]^+[NTf_2]^-$ by liquid exchange.

The same procedure as for **Gel_IL** was used, in which $[Bpy]^+[NTf_2]^-$ instead of $[BMIM]^+[BF_4]^-$ was used.

Synthesis of MOP aerogel from the wet gel samples

To obtain aerogel samples for further analysis, the wet gel sample was soaked with acetone for three days with replacing the fresh acetone each day. Then the solvent-exchanged sample was dried by supercritical CO_2 at 14 MPa and 50 °C for 90 min to obtain the corresponding aerogels.

Computational Study of the IL/HMOP and PEG/HMOP composites accessible porosity

1. Materials and Methods

In order to build a representative atomistic model of the **IL/HRhMOP** and **PEG/HRhMOP** composites, a non-periodic **HRhMOP** spherical particle was first built. This model was generated by cutting the periodic **HRhMOP** structure from Carné-Sánchez, Albalad et al.[28] Rh atoms at the paddle-wheel nodes of the resulting **HRhMOP** spherical particle were under-coordinated at both axial positions. Water molecules were incorporated to saturate the inner axial positions, while 1-benzilimidazole moieties were added on its outer surface so as to mimic the aromatic chains that hold together the **HRhMOP** cages in the interlinked three-dimensional **HRhMOP** network. Universal Force Field (UFF)[29] parameters were assigned to describe both bonded and non-bonded interactions of the **HRhMOP** and the coordinated water molecules by using the OBGMX[30] suite. Force field parameters for 1-benzylimidazole moieties were assigned by using a topology generator[31] for small organic molecules. These parameters were adopted from Merck Molecular Force Field (MMFF) to model small organic molecules which

were tested for some drug design-related applications.[32,33] This force field was also used previously for modeling drug-polymer[34], drug-graphene[35] and drug-protein[36] systems as well as the dissolution of crystals of small organic molecules[37]. The distance between Rh and N(1-benzylimidazole) was fixed to 2.4 Å by using the geometric information given for tertPy-HRhMOP system[28] which exhibits a similar Rh-N coordination. To consider the intrinsic strain that exists in the interlinked three-dimensional **HRhMOP** network, unphysical fluctuations of 1-benzylimidazole moieties need to be prevented. To this end, the angles between the centre of mass (COM) of **HRhMOP** polyhedra, N atom of each 1-benzylimidazole moiety coordinated to Rh and its COM, were restrained to 180˚ by a harmonic potential, with a k value of 150 kJ mol^{-1} consistent with previous DFT calculations performed by Fristsch et al.[38] and the experimental study of Pruchnick et al.[39] Charges were obtained by density functional theory (DFT) calculations using the RESP module of CP2K[40] software at the PBE[41] level of theory considering DZVP-MOLOPT basis sets[42] combined with GTH pseudopotentials[42] for all atoms. All non-bonded parameters of the **HRhMOP** model are summarised in Table 3.

Two systems were further prepared starting from this **HRhMOP** structure to model **IL**/**HRhMOP** and **PEG**/**HRhMOP** composites, where **PEG** stands for poly(ethylene glycol) and **IL** for 1-butyl-3-methylimidazolium tetrafluoroborate ($[BMIM]^+[BF_4]^-$). Initially, 50 Å length cubic simulation boxes with an **HRhMOP** particle at their center were filled with **IL** and **PEG** monomers by means of Grand Canonical Monte Carlo simulations (GCMC) at 50 bar and room temperature using the sorption module of Materials Studio software package. [36] These simulations provided an estimated number of **IL** molecules (303) and **PEG** monomers (724) for each system.

To model the **IL**/**HRhMOP** composite, $[BMIM]^+$ and $[BF_4]^-$ molecules were randomly located outside the **HRhMOP** particles by using the *gmx insert-molecules* subroutine of the Gromacs simulation package.[43] This insertion subroutine locates selected molecules into selected regions of the simulation box taking into account atomic radii as defined in Gromacs[43] (vdwradii.dat) database. **IL** molecules were modeled according to AMBER[44] force field-based parameters by Andrade et al[45]. This force field was chosen because of its reasonable prediction of bulk density of the **IL** (1.18 ± 0.05 g/cm^3 in good agreement with different experimentally measured values such as 1.19 ± 0.01[46], 1.1979 ± 0.0005[47], 1.19878 ± 0.0011[48], 1.20089 ± 0.015[49], 1.21 ± 0.01[50], 1.26 ± 0.01[51]). This **IL**/**HRhMOP** system was first minimized using a steepest descent algorithm for 20000 steps, after which a 5 ns-long NPT (P = 1 bar, T = 300 K) equilibration run was performed. The temperature was kept constant by a Nose-Hoover algorithm and pressure by the isotropic Parinello-Rahman barostat algorithm, with 1 ps and 10

ps as coupling constants respectively. These simulations were run with Gromacs-5.1.2[43] patched with plumed-2.1.2[52] plug-in as MD engine.

For the **PEG**/**HRhMOP** composite, the GCMC- calculated number of **PEG** monomers were first loaded to a 50 x 50 x 50 A^3 simulation box containing a 15 Å radius dummy atom at its centre. Force field parameters for **PEG** monomers were taken from DREIDING[53] while charges were considered as in our previous study[54]. DREIDING force field was previously used to model **PEG**[55] as well as PAM and PANIPAAm polymers[56] and was shown to capture some important polymeric properties such radius of gyration, density in water solvation, solvent accessible surface area and shape anisotropy in water with reasonable accuracy. Subsequently, *in silico* polymerization was performed using the *Polymatic*[57] code with LAMMPS[58] as MD engine, and a polydisperse **PEG** model was obtained. **PEG** chains were selected to match the experimentally measured average of ~ 10 monomers, eliminating chains that were too short or too long. The dummy atom at the centre of the simulation box was removed and the **HRhMOP** particle model was inserted in its place, followed by 21 MD polymer relaxation simulations.[59,60] This series of 21 MD simulations consisted of 7 cycles of 3 simulations, in the NVT_{max}, NVT_{min} and NPT ensembles respectively, with T_{max} (600 K), T_{min} (300 K), and increasing P in the first 3 cycles up to P_{max} (50000 bar) followed by a decrease to 1 bar in the last 4 cycles. This scheme was successfully applied to equilibrate many polymers, [54,57,59-61]and was shown to lead to polymer densities in good agreement with the experiment, provided the T_{min}, T_{max} and P_{max} parameters are carefully tuned. To test this approach for our **PEG** model, we performed a set of simulations for bulk **PEG** and implemented the 21 steps. In the final relaxation step, we calculated the simulated polymer density of **PEG** as 1.012 ± 0.003 g/cm^3, where the value is an average over 10 ns of an NPT simulation trajectory and the error is taken as the standard deviation. Experimental studies have reported a large range of **PEG** density values, typically ranging from 1.121 cm^3/g[62] to 1.21 cm^3/g[63] and with values as low as 1.02 cm^3/g[64] at room temperature. We think that the underestimation of the simulated density is due to the fact that the polymer chains are only ~ 10 monomers long in this study, while they are much longer in the experimental studies cited before. This is not a problem in the context of our work, since a higher density would only accentuate the results we obtain. Both the bulk **PEG** and **HRhMOP**/**PEG** composite simulations were performed with Gromacs-5.1.2[43] patched with plumed-2.1.2[52] plug-in as MD engine.

50 ns long production runs in the NVT (T= 300 K) ensemble were then performed starting from both equilibrated composites, with T kept constant by using the Nose-Hoover thermostat algorithm with a 1 ps coupling constant. The time step was set to 1 fs and three-dimensional periodic boundary conditions were applied. Rh atoms were tethered to their initial positions to

prevent the HMOP from drifting along with the simulation box. Particle Mesh Ewald method was employed to account for long range electrostatic interactions. The cutoff for the LJ interactions and the real part of the Ewald sum was set to 13 Å. Lorenz-Berthelot mixing rules were used to compute the parameters for unlike LJ sites.[65] These runs were analyzed using the Zeo++[66] (REF) and the *VisIt* [67] programs.

2. Results and Discussion

Figure 4-16a shows the atomic densities of **IL**, **PEG** and **HRhMOP** as a function of the radial distance from the COM of the **HRhMOP** for the last 10 ns of the MD simulations. The pore window, which can be described as a truncated cone with the largest circular end on the outside (outer gate) and the smallest circular end on the inside (inner gate) is also included as a reference in Figure 4-16b. Both **PEG** and $[BMIM]^+$ access the porosity of the **HRhMOP**, although the effect is by far more marked for **PEG**, which features 2- to 4-fold higher atomic density than the **IL** do inside the pore. Interestingly, $[BF_4]^-$ rarely enters the window and never enters the pore. This suggests that $[BMIM]^+$ enters the pore oriented in such a way that its positively charged methylimidazolium head stays in the window, while only its hydrocarbon tail enters the pore. As such, $[BF_4]^-$ is expected also to remain outside the pore, in close interaction with the positively charged methylimidazolium head.

In order to confirm this, we plotted site-site radial distribution functions (RDF) between the O of the water molecule coordinated to Rh atoms and different **IL** sites (see Figures 4-16c and d). Radial distribution functions are essentially the probability distribution of finding a site of type β (atoms at $[BMIM]^+$ labeled in Figure 4-16c) at a distance r of a site of type α ($O_{HRhMOP\text{-}water}$). This probability distribution is normalized to the bulk density of these sites. As such, it tends to 1 at long distances in fluid-like systems. Only the RDF of $O_{HRhMOP\text{-}water}$ - $H2_{[BMIM]+}$, where H2 is hydrogen in the hydrocarbon tail, is found to have a bulk-like density (~1 intensity values) close to the $O_{HRhMOP\text{-}water}$ atoms, at a distance of ~5 Å. $H1_{[BMIM]+}$, $N1_{[BMIM]+}$ and $N2_{[BMIM]+}$, atoms that constitute part of the methylimidazolium head, increase in density the farther they are from the water molecules, outside of the **HRhMOP**. This implies that these sites do not interact with the water molecules, and thus, supporting the idea that $[BMIM]^+$ is typically oriented with its tail entering the pore and its head outside the pore window. Additional support to this conclusion can be found when breaking the atomic density of the **IL** into the head and tail compositions (Figure 4-16e) as well as in a radial distribution function showing a strong interaction between $[BMIM]^+$'s head and benzilimidazole moieties (Figure 4-22). A snapshot showcasing two **IL** molecules in this orientation is presented in Figure 4-16f.

Figure 4-16a also shows that **PEG** enters deeper into the pore than $[BMIM]^+$ does, with non-zero atomic density values starting at 1.6 Å versus 3 Å for the IL cation. We have analysed the effect of this on the free volume available in each composite by computing the pore size distribution,[64] as shown in Figure 4-17a. The empty **HRhMOP**, represented in green, exhibits pores with diameters up to 8 Å. Adding both **PEG** and **IL** reduced the free volume in both cases, however, a peak between 5 and 6 Å diameter, present for the **IL** composite (blue line) is absent for the **PEG** one (red line). These results are consistent with what was found in Figure 4-16a.

To support this point, we further compared the free volume and accessible N_2 surface area in IL-loaded, PEG-loaded and empty **HRhMOP** cages. The latter was found to have 0.386 cm^3 g^{-1} pore volume and 927.5 m^2 g^{-1} N_2 accessible surface area, in good agreement with the experimental data.[25] For the composites, the **HRhMOP** pore volume was found to be 0.05 cm^3 g^{-1} and 0.318 cm^3 g^{-1} for **PEG**- and **IL**-based composites. Furthermore, we built porosity maps indicating the pore sizes by color to assess pore accessibility, these are shown in Figures 4-17b (**PEG**/**HRhMOP**) and Figures 4-17c (**IL**/**HRhMOP**). Red is associated with the larger pores, while blue corresponds to the smallest ones. A central red pore is found in the centre of the simulation box for the **IL**/**HRhMOP** case, but is absent in the **PEG**/**HRhMOP** case. This pore corresponds to the additional PSD peak at ~ 6 Å diameter in Figure 4-17a. This implies that part of the porosity of the **HRhMOP** is preserved when it is immersed in **IL**, while it is not the case for the **PEG**-based composite. Moreover, the **HRhMOP** pore in **IL**/**HRhMOP** composite is not only available but also accessible by potential guest gas molecules, because it is surrounded by a yellow layer, coinciding with ~ 5 Å diameter pores, and there are several green paths that get close to it (~ 4 Å diameter).

We also analyzed the possible collective motions involved in the pore accessibility. To this end, we measured the inner gate size (as the distance between the O atoms of two opposite water molecules along the diameter of the inner circle of the pore window) as a function of the simulation time (Figure 4-17d) for the pristine **HRhMOP** and its composites. While the inner gate of the **PEG**/**HRhMOP** composite remains the same dimension as that of the pristine **HRhMOP**, it is significantly expanded in the **IL**/**HRhMOP** composite case by ~ 0.7 Å due to the bulkiness of the head of $[BMIM]^+$. This scenario supports further accessibility of the pores for potential guest molecules in the **IL**-based composites.

3. Conclusion

Our simulations provide a microscopic scenario compatible with the experimentally observed difference between **PEG**/**HRhMOP** and **IL**/**HRhMOP** in terms of their adsorption properties. **PEG** enters the **HRhMOP** and completely fills its porosity, without modifying the size of the

pore windows. **IL**'s hydrocarbon tails enter the pore but do not completely fill it, while their charged heads interact with the pore window, increasing the window diameter and thus enhancing pore accessibility. This explains the higher uptake capacity for **IL**/**HRhMOP** composites than for their **PEG**/**HRhMOP** counterparts.

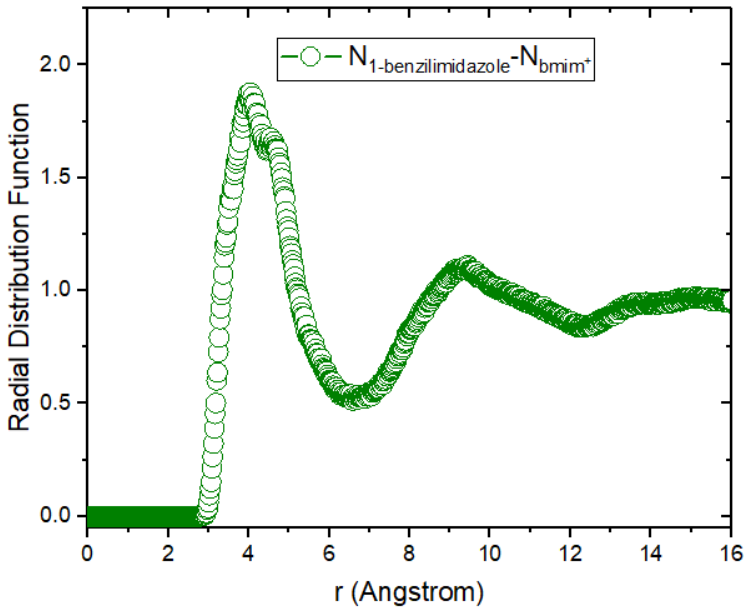

Figure 4-22. Radial distribution function of tethered N atom of 1-benzilimidazole and N atom in $[BMIM]^+$ structure (N1 in Figure 1d).

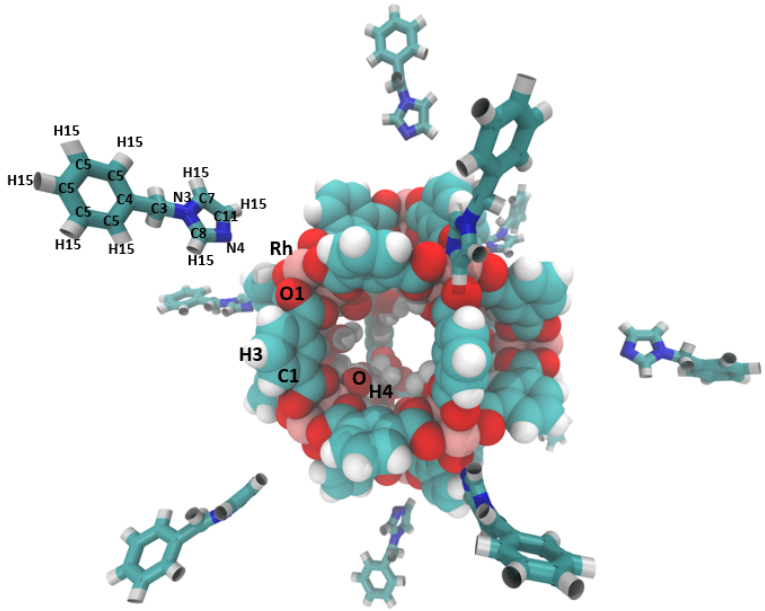

Table 3. LJ parameters and charges for **HRhMOP** polyhedra and 1-Benzylimidazole. Color code for figure: Oxygen: Red, Hydrogen: White, Carbon: Cyan, Rhodium: Pink, Nitrogen: Blue.

Sample	Sigma (Å)	Epsilon (kJ mol^{-1})	Charge (e)
O1	3.11800	0.251200	-0.255476
H3	2.57100	0.184200	-0.007305
C1	3.43100	0.439600	0.071092
H4	2.57100	0.184200	0.164477
Rh	2.60900	0.221900	0.475236
O	3.11800	0.251200	-0.328954
N3	3.06469	0.376560	0.047600
N4	3.29632	0.836800	-0.565300
C4	3.55005	0.292880	-0.143500
C5	3.55005	0.292880	-0.150000
C7	3.63487	0.209200	-0.301600
C8	3.63487	0.209200	0.036500
C11	3.63487	0.209200	0.077200
C3	3.87541	0.230120	0.399100
H13	2.35197	0.092048	0.000000
H15	2.35197	0.092048	0.150000

Reference

1. Das, S.; Heasman, P.; Ben, T.; Qiu, S., Porous organic materials: strategic design and structure-function correlation. *Chem. Rev.* **2017**, *117* (3), 1515-1563.

2. Slater, A. G.; Cooper, A. I., Function-led design of new porous materials. *Science* **2015**, *348* (6238), aaa8075.

3. Kitagawa, S.; Kitaura, R.; Noro, S.-i., Functional Porous Coordination Polymers. *Angew. Chem. Int. Ed.* **2004**, *43* (18), 2334-2375.

4. McKeown, N. B.; Budd, P. M., Polymers of intrinsic microporosity (PIMs): organic materials for membrane separations, heterogeneous catalysis and hydrogen storage. *Chem. Soc. Rev.* **2006**, *35* (8), 675-683.

5. Shan, W.; Fulvio, P. F.; Kong, L.; Schott, J. A.; Do-Thanh, C.-L.; Tian, T.; Hu, X.; Mahurin, S. M.; Xing, H.; Dai, S., New Class of Type III Porous Liquids: A Promising Platform for Rational Adjustment of Gas Sorption Behavior. *ACS Appl. Mater. Interfaces* **2018**, *10* (1), 32-36.

6. James, S. L., The Dam Bursts for Porous Liquids. *Adv. Mater.* **2016**, *28* (27), 5712-5716.

7. Liu, H.; Liu, B.; Lin, L.-C.; Chen, G.; Wu, Y.; Wang, J.; Gao, X.; Lv, Y.; Pan, Y.; Zhang, X.; Zhang, X.; Yang, L.; Sun, C.; Smit, B.; Wang, W., A hybrid absorption–adsorption method to efficiently capture carbon. *Nat. Commun.* **2014**, *5* (1), 5147.

8. He, S.; Chen, L.; Cui, J.; Yuan, B.; Wang, H.; Wang, F.; Yu, Y.; Lee, Y.; Li, T., General Way To Construct Micro- and Mesoporous Metal-Organic Framework-Based Porous Liquids. *J. Am. Chem. Soc.* **2019**, *141* (50), 19708-19714.

9. Bavykina, A.; Cadiau, A.; Gascon, J., Porous liquids based on porous cages, metal-organic frameworks and metal-organic polyhedra. *Coord. Chem. Rev.* **2019**, *386*, 85-95.

10. Jie, K.; Zhou, Y.; Ryan, H. P.; Dai, S.; Nitschke, J. R., Engineering Permanent Porosity into Liquids. *Adv. Mater.* **2021**, *33* (18), 2005745.

11. Jie, K.; Onishi, N.; Schott, J. A.; Popovs, I.; Jiang, D.-e.; Mahurin, S.; Dai, S., Transforming Porous Organic Cages into Porous Ionic Liquids via a Supramolecular Complexation Strategy. *Angew. Chem. Int. Ed.* **2020**, *59* (6), 2268-2272.

12. O'Reilly, N.; Giri, N.; James, S. L., Porous Liquids. *Chem. Eur. J.* **2007**, *13* (11), 3020-3025.

13. Zhang, J.; Chai, S.-H.; Qiao, Z.-A.; Mahurin, S. M.; Chen, J.; Fang, Y.; Wan, S.; Nelson, K.; Zhang, P.; Dai, S., Porous Liquids: A Promising Class of Media for Gas Separation. *Angew. Chem. Int. Ed.* **2015**, *54* (3), 932-936.

14. Ma, L.; Haynes, C. J. E.; Grommet, A. B.; Walczak, A.; Parkins, C. C.; Doherty, C. M.; Longley, L.; Tron, A.; Stefankiewicz, A. R.; Bennett, T. D.; Nitschke, J. R., Coordination cages as permanently porous ionic liquids. *Nat. Chem.* **2020**, *12* (3), 270-275.

15. Bennett, T. D.; Coudert, F.-X.; James, S. L.; Cooper, A. I., The changing state of porous materials. *Nat. Mater*. **2021**, *20*, 1179-1187.

16. Giri, N.; Del Pópolo, M. G.; Melaugh, G.; Greenaway, R. L.; Rätzke, K.; Koschine, T.; Pison, L.; Gomes, M. F. C.; Cooper, A. I.; James, S. L., Liquids with permanent porosity. *Nature* **2015**, *527* (7577), 216-220.

17. Egleston, B. D.; Luzyanin, K. V.; Brand, M. C.; Clowes, R.; Briggs, M. E.; Greenaway, R. L.; Cooper, A. I., Controlling Gas Selectivity in Molecular Porous Liquids by Tuning the Cage Window Size. *Angew. Chem. Int. Ed.* **2020**, *59* (19), 7362-7366.

18. Deng, Z.; Ying, W.; Gong, K.; Zeng, Y.-J.; Yan, Y.; Peng, X., Facilitate Gas Transport through Metal-Organic Polyhedra Constructed Porous Liquid Membrane. *Small* **2020**, *16* (11), 1907016.

19. Costa Gomes, M.; Pison, L.; Červinka, C.; Padua, A., Porous Ionic Liquids or Liquid Metal-Organic Frameworks? *Angew. Chem. Int. Ed.* **2018**, *57* (37), 11909-11912.

20. Knebel, A.; Bavykina, A.; Datta, S. J.; Sundermann, L.; Garzon-Tovar, L.; Lebedev, Y.; Durini, S.; Ahmad, R.; Kozlov, S. M.; Shterk, G.; Karunakaran, M.; Carja, I. D.; Simic, D.; Weilert, I.; Klüppel, M.; Giese, U.; Cavallo, L.; Rueping, M.; Eddaoudi, M.; Caro, J.; Gascon, J., Solution processable metal-organic frameworks for mixed matrix membranes using porous liquids. *Nat. Mater.* **2020**, *19* (12), 1346-1353.

21. Cahir, J.; Tsang, M. Y.; Lai, B.; Hughes, D.; Alam, M. A.; Jacquemin, J.; Rooney, D.; James, S. L., Type 3 porous liquids based on non-ionic liquid phases - a broad and tailorable platform of selective, fluid gas sorbents. *Chem. Sci.* **2020**, *11* (8), 2077-2084.

22. Foster, J. A.; Steed, J. W., Exploiting Cavities in Supramolecular Gels. *Angew. Chem. Int. Ed.* **2010**, *49* (38), 6718-6724.

23. Carné-Sánchez, A.; Craig, G. A.; Larpent, P.; Guillerm, V.; Urayama, K.; Maspoch, D.; Furukawa, S., A Coordinative Solubilizer Method to Fabricate Soft Porous Materials from Insoluble Metal-Organic Polyhedra. *Angew. Chem. Int. Ed.* **2019**, *131* (19), 6413-6416.

24. Legrand, A.; Craig, G. A.; Bonneau, M.; Minami, S.; Urayama, K.; Furukawa, S., Understanding the multiscale self-assembly of metal-organic polyhedra towards functionally graded porous gels. *Chem. Sci.* **2019**, *10* (47), 10833-10842.

25. Furukawa, S.; Horike, N.; Kondo, M.; Hijikata, Y.; Carné-Sánchez, A.; Larpent, P.; Louvain, N.; Diring, S.; Sato, H.; Matsuda, R., Rhodium-organic cuboctahedra as porous solids with strong binding sites. *Inorg. Chem.* **2016**, *55* (21), 10843-10846.

26. Kansy, J., Microcomputer program for analysis of positron annihilation lifetime spectra. *Nucl. Instrum. Methods Phys. Res. A: Accel. Spectrom. Detect. Assoc. Equip.* **1996**, *374* (2), 235-244.

27. Carné-Sánchez, A.; Craig, G. A.; Larpent, P.; Hirose, T.; Higuchi, M.; Kitagawa, S.; Matsuda, K.; Urayama, K.; Furukawa, S., Self-assembly of metal-organic polyhedra into supramolecular polymers with intrinsic microporosity. *Nat. Commun.* **2018**, *9* (1), 1-8.

28. Carné-Sánchez, A.; Albalad, J.; Grancha, T.; Imaz, I.; Juanhuix, J.; Larpent, P.; Furukawa, S.; Maspoch, D., Postsynthetic Covalent and Coordination Functionalization of Rhodium (II)-Based Metal-Organic Polyhedra. *J. Am. Chem. Soc.* **2019**, *141* (9), 4094-4102.

29. Rappé, A. K.; Casewit, C. J.; Colwell, K.; Goddard III, W. A.; Skiff, W. M., a full periodic table force field for molecular mechanics and molecular dynamics simulations. *J. Am. Chem. Soc.* **1992**, *114* (25), 10024-10035.

30. Garberoglio, G., OBGMX: A web-based generator of GROMACS topologies for molecular and periodic systems using the universal force field. *J. Comput. Chem.* **2012**, *33* (27), 2204-2208.

31. Zoete, V.; Cuendet, M. A.; Grosdidier, A.; Michielin, O., SwissParam: a fast force field generation tool for small organic molecules. *J. Comput. Chem*. **2011**, *32* (11), 2359-2368.

32. Saddala, M. S.; Adi, P. J., Discovery of small molecules through pharmacophore modeling, docking and molecular dynamics simulation against Plasmodium vivax Vivapain-3 (VP-3). *Heliyon* **2018**, *4* (5), e00612.

33. Gao, Y.; Olsen, K. W., Drug–polymer Interactions at Water-Crystal Interfaces and Implications for Crystallization Inhibition: Molecular Dynamics Simulations of Amphiphilic Block Copolymer Interactions with Tolazamide Crystals. *J. Pharm. Sci.* **2015**, *104* (7), 2132-2141.

34. Hasanzade, Z.; Raissi, H., Investigation of graphene-based nanomaterial as nanocarrier for adsorption of paclitaxel anticancer drug: a molecular dynamics simulation study. *J. Mol. Model* **2017**, *23* (2), 36.

35. Caulfield, T.; Medina-Franco, J. L., Molecular dynamics simulations of human DNA methyltransferase 3B with selective inhibitor nanaomycin A. *J. Struct. Biol.* **2011**, *176* (2), 185-191.

36. Greiner, M.; Elts, E.; Schneider, J.; Reuter, K.; Briesen, H., Dissolution study of active pharmaceutical ingredients using molecular dynamics simulations with classical force fields. *J. Cryst. Growth* **2014**, *405*, 122-130.

37. Fritsch, N.; Wick, C. R.; Waidmann, T.; Dral, P. O.; Tucher, J.; Heinemann, F. W.; Shubina, T. E.; Clark, T.; Burzlaff, N., Multiply bonded metal (II) acetate (rhodium, ruthenium,

and molybdenum) complexes with the trans-1, 2-bis (N-methylimidazol-2-yl) ethylene ligand. *Inorg. Chem.* **2014**, *53* (23), 12305-12314.

38. Pruchnik, F. P.; Robert, F.; Jeannin, Y.; Jeannin, S., New Rhodium (II) Complexes with 2, 2 ‘: 6 ‘, 2 ‘‘-Terpyridine. *Inorg. Chem.* **1996**, *35* (14), 4261-4263.

39. Hutter, J.; Iannuzzi, M.; Schiffmann, F.; VandeVondele, J., cp2k: atomistic simulations of condensed matter systems. *Wiley Interdiscip. Rev. Comput. Mol. Sci.* 2014, *4* (1), 15-25.

40. Perdew, J. P.; Burke, K.; Ernzerhof, M., Generalized gradient approximation made simple. *Phys. Rev. Lett.* **1996**, *77* (18), 3865.

41. VandeVondele, J.; Hutter, J., Gaussian basis sets for accurate calculations on molecular systems in gas and condensed phases. *J. Chem. Phys.* **2007**, *127* (11), 114105.

42. Goedecker, S.; Teter, M.; Hutter, J., Separable dual-space Gaussian pseudopotentials. *Phys. Rev.* **1996**, *54* (3), 1703.

43. Van Der Spoel, D.; Lindahl, E.; Hess, B.; Groenhof, G.; Mark, A. E.; Berendsen, H. J., GROMACS: fast, flexible, and free. *J. Comput. Chem*. **2005**, *26* (16), 1701-1718.

44. Cornell, W. D.; Cieplak, P.; Bayly, C. I.; Gould, I. R.; Merz, K. M.; Ferguson, D. M.; Spellmeyer, D. C.; Fox, T.; Caldwell, J. W.; Kollman, P. *A.,* A second generation force field for the simulation of proteins, nucleic acids, and organic molecules. *J. Am. Chem. Soc.* **1995**, *117* (19), 5179-5197.

45. de Andrade, J.; Böes, E. S.; Stassen, H., Computational study of room temperature molten salts composed by 1-alkyl-3-methylimidazolium cations force-field proposal and validation. *J. Phys. Chem. B* **2002**, *106* (51), 13344-13351.

46. Zhang, S.; Sun, N.; He, X.; Lu, X.; Zhang, X., Physical properties of ionic liquids: database and evaluation. *J. Phys. Chem. Ref. Data* **2006**, *35* (4), 1475-1517.

47. Pandit, S. A.; Rather, M. A.; Bhat, S. A.; Rather, G. M.; Bhat, M. A., Influence of the anion on the equilibrium and transport properties of 1-butyl-3-methylimidazolium based room temperature ionic liquids. *J. Solut. Chem.* **2016**, *45* (12), 1641-1658.

48. Rao, S. G.; Mohan, T. M.; Krishna, T. V.; Raju, K.; Rao, B. S., Excess thermodynamic properties of ionic liquid 1-butyl-3-methylimidazolium tetrafluoroborate and N-octyl-2-pyrrolidone from T=(298.15 to 323.15) K at atmospheric pressure. *J. Chem. Thermodyn.* **2015**, *89*, 286-295.

49. Ciocirlan, O.; Croitoru, O.; Iulian, O., Density and refractive index of binary mixtures of two 1-alkyl-3-methylimidazolium ionic liquids with 1, 4-dioxane and ethylene glycol. *J. Chem. Eng. Data* **2014**, *59* (4), 1165-1174.

50. Nishida, T.; Tashiro, Y.; Yamamoto, M., Physical and electrochemical properties of 1-alkyl-3-methylimidazolium tetrafluoroborate for electrolyte. *J. Fluor. Chem.* **2003**, *120* (2), 135-141.

51. Branco, L. C.; Rosa, J. N.; Moura Ramos, J. J.; Afonso, C. A., Preparation and characterization of new room temperature ionic liquids. *Chem. Eur. J.* **2002**, *8* (16), 3671-3677.

52. Tribello, G. A.; Bonomi, M.; Branduardi, D.; Camilloni, C.; Bussi, G., PLUMED 2: New feathers for an old bird. *Comput. Phys. Commun.* **2014**, *185* (2), 604-613.

53. Mayo, S. L.; Olafson, B. D.; Goddard, W. A., DREIDING: a generic force field for molecular simulations. *J. Phys. Chem.* **1990**, *94* (26), 8897-8909.

54. Semino, R.; Moreton, J. C.; Ramsahye, N. A.; Cohen, S. M.; Maurin, G., Understanding the origins of metal-organic framework/polymer compatibility. *Chem. Sci,* **2018**, *9* (2), 315-324.

55. Shin, H.; Pascal, T. A.; Goddard III, W. A.; Kim, H., Scaled effective solvent method for predicting the equilibrium ensemble of structures with analysis of thermodynamic properties of amorphous polyethylene glycol-water mixtures. *J. Phys. Chem. B* **2013**, *117* (3), 916-927.

56. Rukmani, S. J.; Kupgan, G.; Anstine, D. M.; Colina, C. M., A molecular dynamics study of water-soluble polymers: analysis of force fields from atomistic simulations. *Mol. Simul.* **2019**, *45* (4-5), 310-321.

57. Abbott, L. J.; Hart, K. E.; Colina, C. M., Polymatic: a generalized simulated polymerization algorithm for amorphous polymers. *Theor. Chem. Acc.* **2013**, *132* (3), 1334.

58. Plimpton, S., Fast parallel algorithms for short-range molecular dynamics; Sandia National Labs., Albuquerque, NM (United States): **1993**.

59. Larsen, G. S.; Lin, P.; Hart, K. E.; Colina, C. M., Molecular simulations of PIM-1-like polymers of intrinsic microporosity. *Macromolecules* **2011**, *44* (17), 6944-6951.

60. Semino, R.; Ramsahye, N. A.; Ghoufi, A.; Maurin, G., Microscopic model of the metal-organic framework/polymer interface: a first step toward understanding the compatibility in mixed matrix membranes. *ACS. Appl. Mater. Interfaces* **2016**, *8* (1), 809-819.

61. Larsen, G. S.; Hart, K. E.; Colina, C. M., Predictive simulations of the structural and adsorptive properties for PIM-1 variations. *Mol. Simul.* **2014**, *40* (7-9), 599-609.

62. Zhang, K.; Yang, J.; Yu, X.; Zhang, J.; Wei, X., Densities and viscosities for binary mixtures of poly (ethylene glycol) 400+ dimethyl sulfoxide and poly (ethylene glycol) 600+ water at different temperatures. *J. Chem. Eng. Data* **2011**, *56* (7), 3083-3088.

63. Rubinson, K. A.; Meuse, C. W., Deep hydration: Poly (ethylene glycol) Mw 2000-8000 Da probed by vibrational spectrometry and small-angle neutron scattering and assignment of ΔG° to individual water layers. *Polymer* **2013**, *54* (2), 709-723.

64. Thiyagarajan, P.; Chaiko, D.; Hjelm Jr, R., A neutron scattering study of poly (ethylene glycol) in electrolyte solutions. *Macromolecules* **1995**, *28* (23), 7730-7736.

65. Allen, M. P.; Tildesley, D. J., Computer simulation of liquids. Oxford university press: 2017.

66. Willems, T. F.; Rycroft, C. H.; Kazi, M.; Meza, J. C.; Haranczyk, M., Algorithms and tools for high-throughput geometry-based analysis of crystalline porous materials. *Microporous Mesoporous Mater* **2012**, *149* (1), 134-141.

67. Childs, H., VisIt: an end-user tool for visualizing and analyzing very large data. **2012**.

Chapter 5

Direct formation of hierarchical hybrid membranes (HHMs) with hierarchical porous MOP networks by sol-gel process

Abstract

The hybridization of crystalline porous materials with organic polymers has been proposed as a promising strategy to fabricate porous soft membranes with both tunable porosity for gas sorption/separation and good processability for practical handling. However, the high requirement on the dispersity/compatibility of the porous fillers in/with the polymer matrix has greatly limited the performances of the resulting composites, so-called mixed matrix membranes (MMMs), to be further improved. Here, we demonstrate the synthesis of hierarchical hybrid membranes (HHMs) by in situ forming a hierarchical porous network of linked metal-organic polyhedra (MOPs) as the secondary continuous phase in polyurethane (PU) as the polymer matrix. In contrast to the inevitable aggregation of nanofillers inside MMMs, the construction of the linked MOP network in PU allows these porous cages to be permanently fixed within HHMs without the need to improve their dispersibility. Furthermore, the connection of the porous MOPs across the polymer matrix significantly improved the molecular diffusion throughout the materials, endowing the resulting HHMs with greatly enhanced gas selectivity and permeability.

Introduction

Microporous materials have attracted much attention due to their high potentials for various applications in fields ranging from gas sorption and separation[1], molecular storage and catalysis[2] to sensors and electronics[3]. So far, a large library of microporous materials has been created and developed,[4] which can be classified into mainly two categories depending on the long-range order of their structures. Among them, one is the porous crystalline material which possesses an extending network with high surface area and well-defined stable porosity, like metal-organic frameworks (MOFs)[5] or covalent-organic frameworks (COFs)[6]. Although the regular porous structures endow them with ease in structural adjustment and property control, their low processability as the compensation of crystallinity limits their development in practical application. To tackle the limitation in processability, another type of microporous materials with amorphous structures has been developed, such as the polymers of intrinsic microporosity (PIM) whose intrinsic porosity comes from the arrangement of their rigid polymer chains.[7] Despite their good solubility and processability, it's still challenging to

precisely control their pore size and to stabilize their porosity from physical aging. To harness better performances, one alternative solution is to create hybrid porous materials, so-called mixed matrix membranes (MMMs), by blending microporous materials as nanofillers and organic polymers as the processable matrix. This hybridization is believed to allow for the combination of advantages from both of them, such as the controllable porosity from nanofillers and processability from polymers.[8-9] Initially this has been through the addition of zeolites, silicas or activated carbons, but recently the focus has shifted towards the utilization of MOFs due to their versatile structures and tunable pore attributes in favor of high permeability and selectivity of the resulting MMMs.[10-13] However, as in all other hybrid systems, the limited dispersibility of MOFs within polymers still remained challenging to restrict the improvement of the membrane performances. Except for their tendency to aggregate during synthesis, the surface functional groups, aspect ratio, particle morphologies and crystal sizes of MOFs also play an important role to determine the final performances of the composite membranes. All these factors make it complicated to further investigate the integration of MOFs with polymer matrix.[14]

Metal-organic polyhedra (MOP) is a class of discrete cage-like molecules with permanent internal cavities.[15-16] Considered as the subunits (or supramolecular building blocks) of MOFs, MOPs not only inherit the feature of MOFs such as well-defined geometry, tunable pore size and designable functionality, but also retain their molecular identities with good solubility in a wide variety of solvents. All these unique advantages make MOP an ideal candidate to integrate with polymer as the porous nanofiller to synthesize composite materials.[17-18] However, so far only a few MOP-based composite membranes have been reported. In most cases, additional modifications of MOPs were required to improve the compatibility of MOPs with their corresponding polymer matrix.[19-22] Except for the costly synthetic efforts, the introduction of functional polymer chains on MOP surfaces would block the accessibility of MOP cavities to external gas molecules, thus compensating for the benefits of incorporated MOPs as nanofillers in composite membranes for applications like gas separation.[23] Therefore, it is necessary to develop a new strategy to not only guarantee the dispersibility of MOPs within polymer matrix without additional modifications but also retain the microporosity of MOPs for gas molecular diffusion and separation.

Here we address the issues of dispersibility and porosity preservation in the MOPs-based composite membranes by introducing a new concept, hierarchical hybrid membranes (HHMs). Instead of dispersing functionalized MOPs or crosslinking MOPs with polymer chains that may block their cavities, a hierarchical porous MOP network was formed in situ by coordinatively crosslinking a rhodium-based MOP (**HRhMOP**) with a bisimidazole linker within the polymer

polyurethane (PU). The resulting HHMs consisted of interpenetrated double networks, in which the continuous polymer phase contributed to the mechanical properties of the films while the linked MOP network guaranteed the interconnection of micropores for the molecular diffusion throughout the whole system. The aggregation issue of MOPs during film synthesis was avoided by fixing or crosslinking them into the porous network as a secondary phase, which also exerted a synergistic effect with the PU matrix to obtain the resulting HHMs with greatly enhanced mechanical strength and gas separation performances. Considering the possibility of forming the linked porous networks from versatile MOPs or MOFs, this new generation of hybrid porous membranes offers an alternative strategy to overcome the limitation of current MOP- or MOF-based MMMs.

Results and discussion

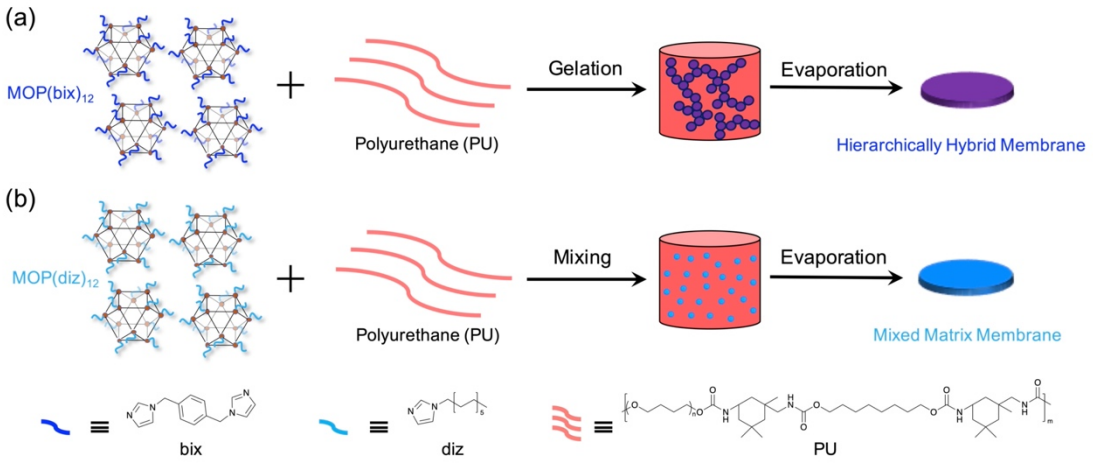

Figure 5-1. The schematic illustration of the synthetical process of (a) **HHM-*n*** and (b) **MMM-*n***.

The rhodium-based cuboctahedral MOPs, $[Rh_2(bdc)_{12}]_{12}$ (**HRhMOP**; bdc = (1,4-bis(imidazole-1-ylmethyl)benzene), are attractive candidates for integration with polymers because the high thermal and chemical stability of the MOPs allows their internal cavities to be preserved during the composite synthesis.[24] Furthermore, the exposed axial sites of rhodium paddlewheels existing on the surface of MOPs are highly labile to be coordinated with organic linkers, making them ideal starting precursors to construct interconnected porous networks within the polymer matrix.[25] In our previous study, we reported the fabrication of the linked MOP gels by coordinatively crosslinking **HRhMOP** with a bidentate linker, **bix** (1,4-bis(imidazole-1-ylmethyl)benzene) in the solvent of DMF.[26] As discussed in chapter 1, the resulting MOP gels consist of hierarchical porous structures with multiple pores at size over multiple length scales. Taking this hierarchical porosity into account, the linked MOP network is expected to afford

optimal gas molecular diffusion for separation applications if it can be incorporated into polymers to form HHMs.

The composite membranes HHMs were synthesized through a slightly modified coordinative solubilizer method, which has been reported in our previous work to synthesize the linked MOP gels based on **HRhMOP**.[26] Firstly, **HRhMOP** is coordinatively attached by a monodentate ligand, **diz** (1-dodecyl-1H-imidazole), to increase the solubility of the resulting **HRhMOP(diz)$_{12}$** in DMF. Addition of 12 equivalence (eq.) of linker **bix** into the MOP solution induces a ligand-exchange reaction, in which the attached **diz** on MOPs is replaced by **bix**. This replacement of ligands leads to the formation of kinetically trapped molecules, **HRhMOP(bix)$_{10}$(diz)$_2$** with bix coordinating in a monodentate fashion. Heating the solution of kinetically trapped molecules triggers the dissociation of **bix** and **diz** from the MOP surfaces, exposing the accessible axial rhodium sites which can be subsequently coordinated by neighboring kinetically trapped MOPs. This coordination reaction sequentially happens to crosslink MOPs until the network formation. Instead of forming the gel in DMF, here an elastic polymer polyurethane (PU) was introduced into the solution of kinetically trapped molecules, followed by heating treatment in the PTFE Petri-dishes without sealing. During the evaporation of the DMF solvent, a linked MOP network was formed in situ within PU, leading to the formation of the composite membranes as **HHM-*n*** (n indicates the weight percentage of **HRhMOP(diz)$_{12}$** related to PU) (Figure 5-1a). As the control experiment, the corresponding mixed matrix membranes as **MMM-*n*** were also synthesized by simply dispersing **HRhMOP(diz)$_{12}$** in PU without the addition of **bix** for crosslinking, as shown in Figure 5-1b.

To confirm the crosslinking reaction between MOPs and linkers in the presence of polymer, the PU-containing DMF solution of kinetically trapped molecules was firstly heated at 80 ºC in a sealed vial. As shown in Figure 5-2a, a composite gel was formed as expected, which indicates the occurrence of MOP polymerization through crosslinking with **bix**. The gel was then washed thrice with DMF and thrice with acetone, followed by supercritical CO_2 ($SCCO_2$) drying to obtain the corresponding aerogel (Figure 5-2a). The scanning electron microscope (SEM) images of this aerogel revealed a characteristic colloidal network, which is similar to the structure of the pure linked MOP gels as we reported previously without the addition of polymer (Figure 5-2b and 2c). This unchanged structure strongly suggests that the crosslinking between MOPs and **bix** is not influenced by the existence of polymer PU. Therefore, it is viable to synthesize the composite membranes **HHM-*n*** with interlinked MOP network by the simultaneous polymerization of MOPs and evaporation of DMF solvents as designed (Figure 5-1a).

After the synthesis of **HHM-*n*** and their corresponding control samples (**MMM-*n***) at different MOP loadings, these two different composite films were measured by SEM to reveal a completely different morphology between **HHM-*n*** and **MMM-*n***. As shown in Figure 5-3, **HHM-*n*** samples presented a homogeneous surface similar to the pristine PU. As increasing the MOP concentration, no aggregation can be observed and only the surface of **HHM-*n*** became rougher. Although the image contrast is not clear enough, there seems to be a colloidal network formed underneath the surface of **HHM-*n***. This can be further confirmed by the SEM cross-section images of **HHM-*n***, which showed the existence of a colloidal network within the composite samples (Figure 5-4). In particular, the colloidal particles, which were formed by interlinked MOPs and embedded within the PU matrix without any voids at their interfaces, can be clearly distinguished on the cross-section of **HHM-30**. This morphology indicates the successful formation and distribution of the linked MOP network within PU. For the films of **MMM-*n***, in contrast, both the surface and cross-sectional SEM images displayed a phase-separated morphology with the occurrence of numerous spherical aggregates (Figure 5-5 and 5-6). Intriguingly, the size of these spherical aggregates was proportional to the loading of MOP fillers, implying that the phase separation was induced by the MOPs added. SEM-EDX mapping of the surface of **MMM-30** confirmed the concentrated aggregation of MOPs within the spherical aggregates, which is in contrast to the homogeneous distribution of the linked MOP network inside the films of **HHM-30** (reflected by Rh elements in Figure 5-7). In fact, the polymer PU used here was synthesized in the form of block copolymer, which consists of the hard and soft segments at the same polymer chains (Figure 5-1). Therefore, it is possible to change the morphology of PU through the introduction of nanofillers.[13, 27] For samples of **MMM-n** incorporating isolated **HRhMOP(diz)$_{12}$**, the soft dodecyl chains on the peripheries of MOPs are supposed to exert a stronger interaction with the soft segments of PU chains. This interaction can significantly promote the phase separation between the hard and soft domains. However, this phase separation is inhibited when the MOPs are crosslinked with linker **bix** to form the colloidal network as a secondary phase within **HHM-*n***, affording a well-distributed hierarchical hybrid system which can also be confirmed by optical microscopy (Figure 5-8).

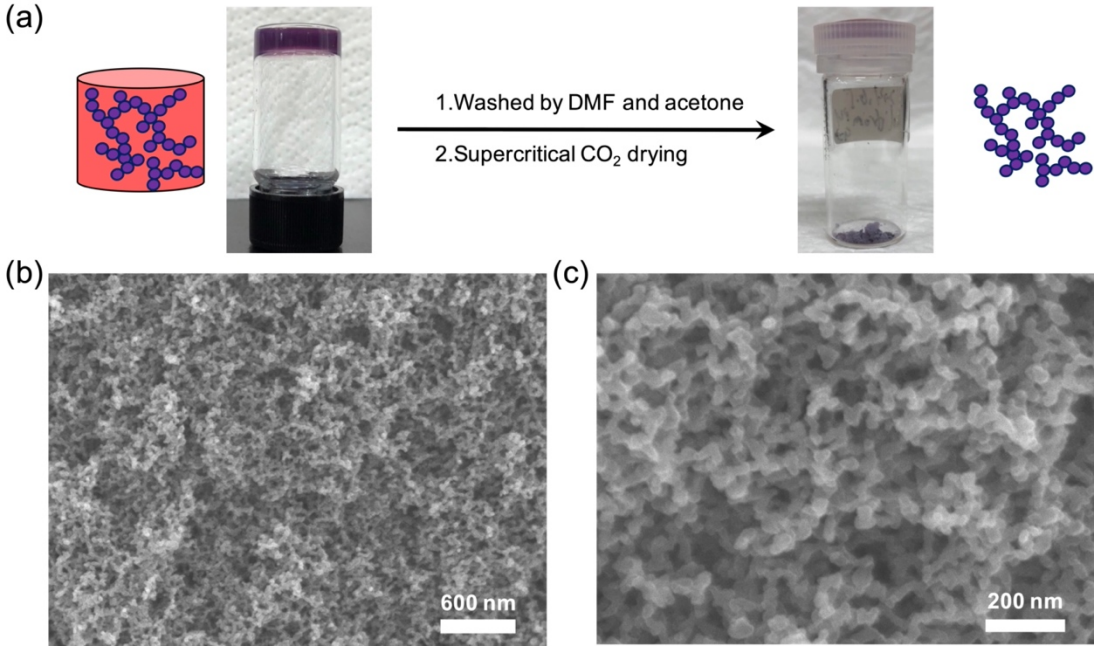

Figure 5-2. (a) Formation of PU-containing gel based on MOPs and its aerogel dried by supercritical CO_2 drying after the exchange with DMF and acetone. (b-c) The SEM images of the corresponding aerogel sample.

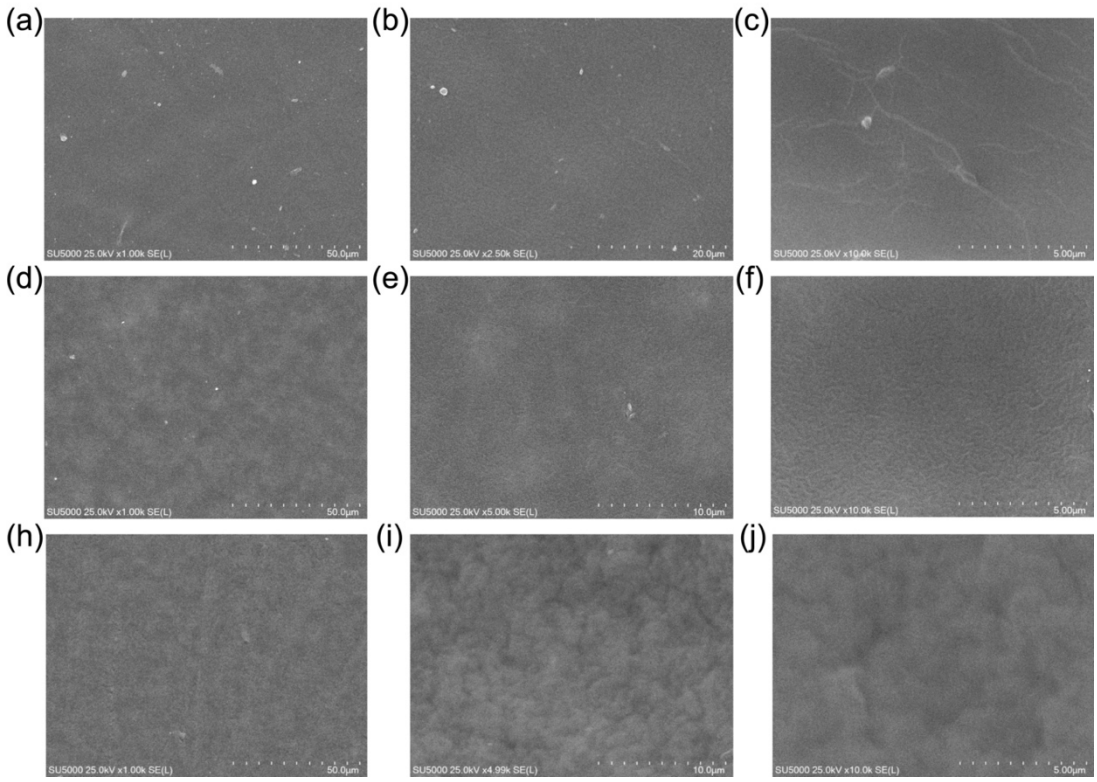

Figure 5-3. Surface SEM images of (a-c) pristine PU, (d-f) **HHM-10** and (h-j) **HHM-30**.

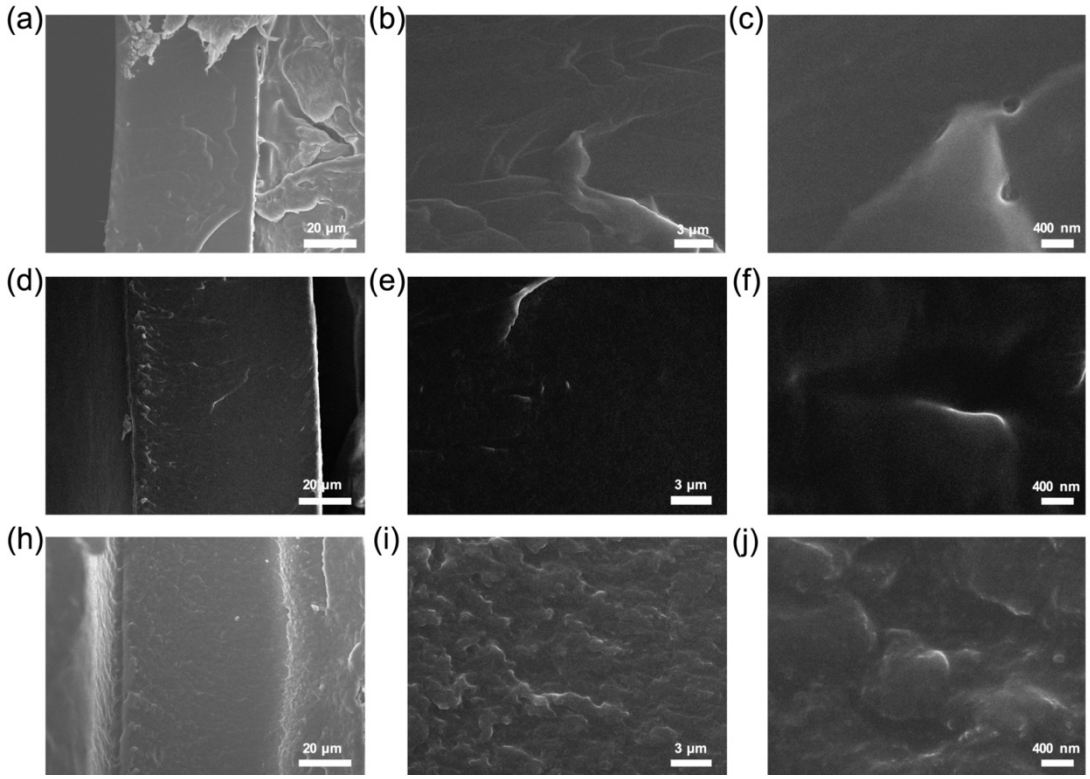

Figure 5-4. Cross-sectional SEM images of (a-c) pristine PU, (d-f) **HHM-10** and (h-j) **HHM-30**.

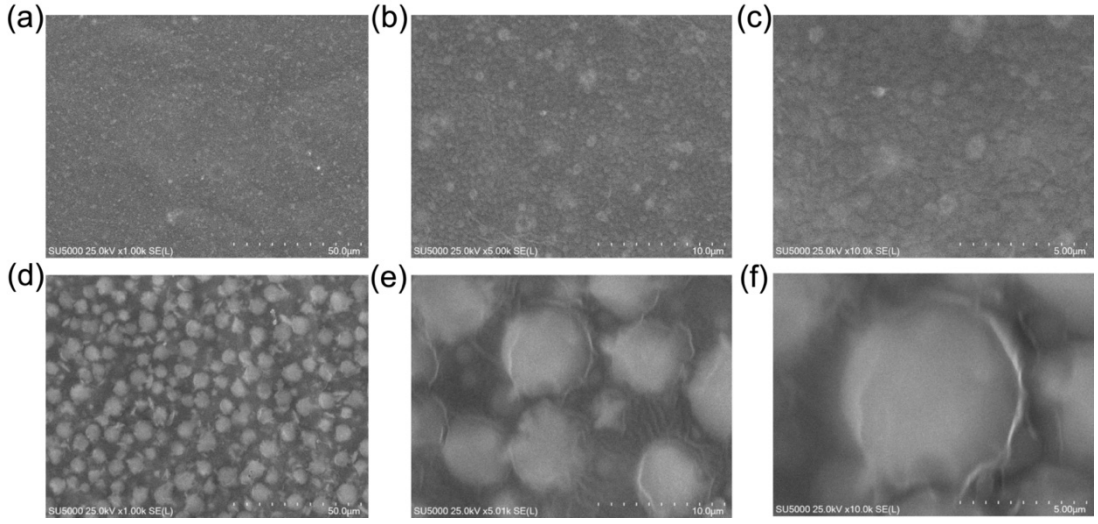

Figure 5-5. Surface SEM images of (a-c) **MMM-10** and (d-f) **MMM-30**.

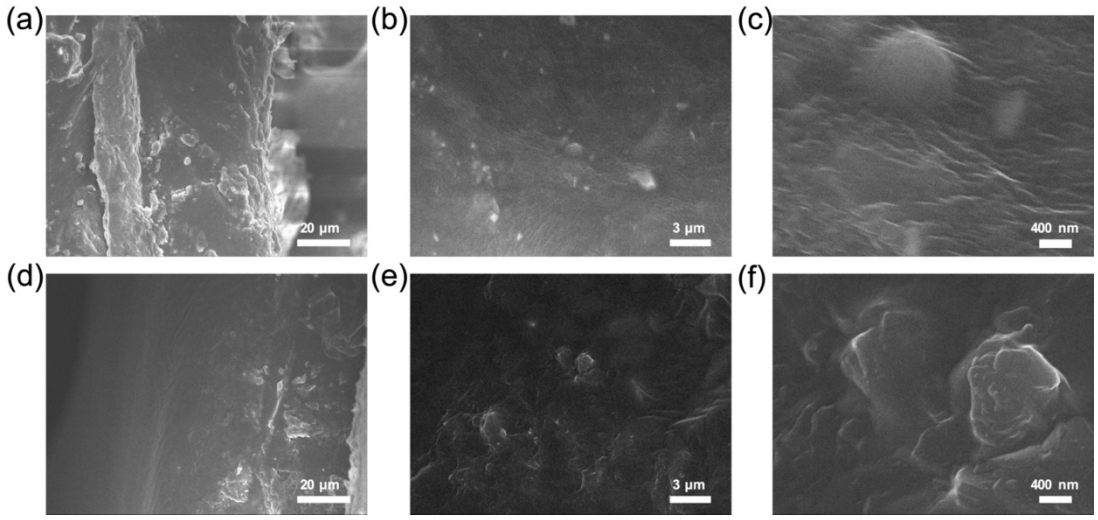

Figure 5-6. Cross-sectional SEM images of (a-c) **MMM-10** and (d-f) **MMM-30**.

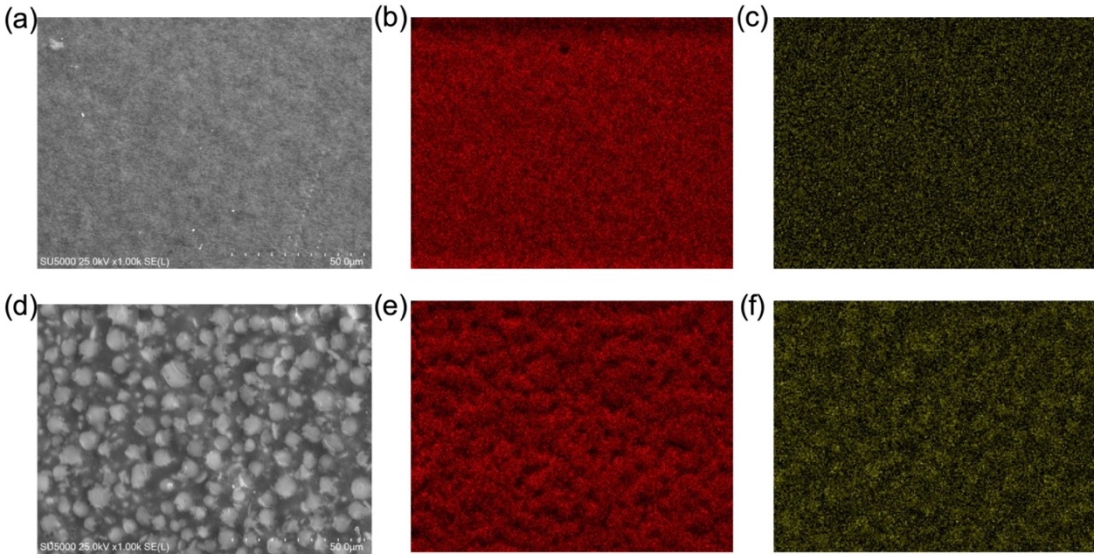

Figure 5-7. Surface SEM-EDX images of (a-c) **HHM-30** and (d-f) **MMM-30** with C element in red and Rh element in yellow.

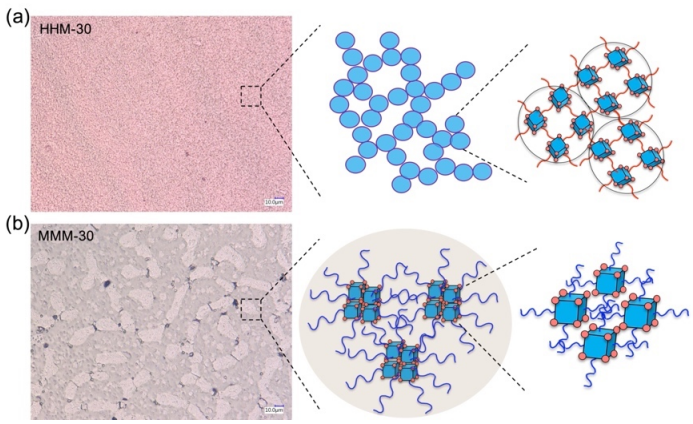

Figure 5-8. Optical microscopy of (a) **HHM-30** and (c) **MMM-30**.

The difference in the morphologies has endowed the corresponding membrane samples with different mechanical properties (Figure 5-9). The addition of isolated MOPs into **MMM-*n*** greatly undermined the film-forming stability of the resulting film samples, among which **MMM-20** and **MMM-30** became too weak to be peeled off from the Petri dishes (Figure 5-9i and 5-9j). Note that the film samples of **MMM-*n*** were further observed to "melt" and lose all the membrane properties after storage for a month, suggesting a low stability (Figure 5-10). In contrast, **HHM-*n*** showed a significant enhancement of mechanical properties due to the incorporation of the MOP-based secondary network. Tensile test of these membranes revealed that as increasing the MOP loadings the toughness of **HHM-*n*** continued to increase with the films breaking at a decreased elongation (Figure 5-11a). Dynamic mechanical analysis (DMA) of **HHM-*n*** in a tensile mode was performed to show the enhancement of membrane toughness with the continuously increasing storage Young's modulus (*E*') from 1.7 MPa of PU to 14.4 MPa of **HHM-20** (Figure 5-11b). Intriguingly, there is a big jump of *E*' between **HHM-5** and **HHM-10**, which can be explained by the formation of a more complete MOP network across the composites at higher MOP loadings. Although a slightly reduced modulus was observed for **HHM-30** with *E*' = 11.2 MPa, all the samples of **HHM-*n*** showed better mechanical properties than the pristine PU polymer.

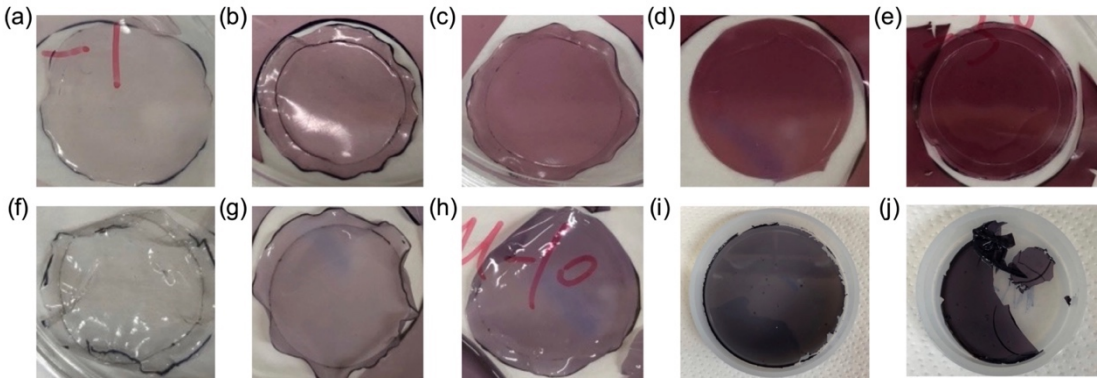

Figure 5-9. Photos of the membrane samples of (a) **HHM-*n*** and (b) **MMM-*n***.

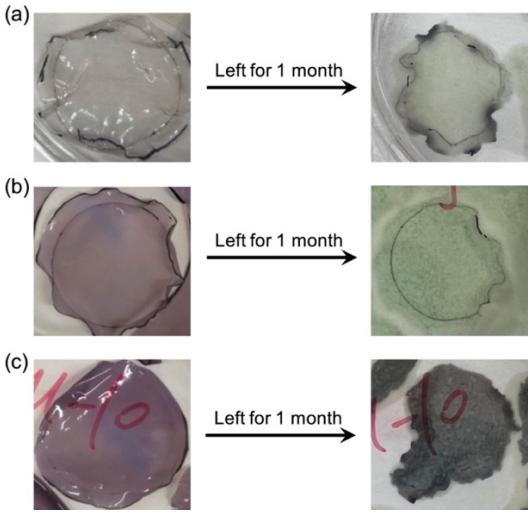

Figure 5-10. Photos of (a) **MMM-1**, (b) **MMM-5** and (c) **MMM-10** before and after leaving for 1 month.

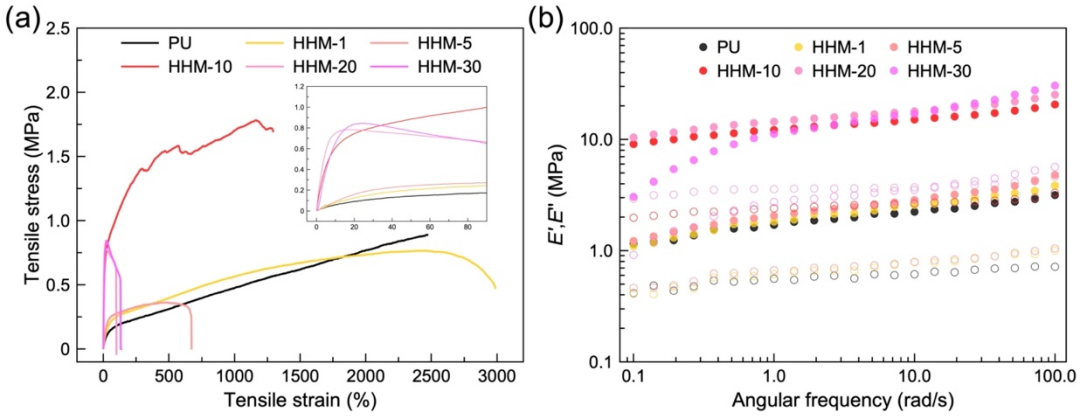

Figure 5-11. (a) Stress-strain curves of **HHM-*n*** membranes from tensile tests. (b) Storage Young's modulus (*E*') (filled circles) and loss Young's modulus (*E*'') (hollow circles) of **HHM-*n*** membranes from dynamic mechanical analysis (DMA) tests.

The structural change or phase separation in **HHM-*n*** and **MMM-*n*** were explored with the help of differential scanning calorimetry (DSC) and infrared (IR) spectra. The thermal glass transition temperature (T_g) of the soft segments of PU was observed at ~57 ºC for all the membrane samples without obvious shifts,[13, 27] indicating that the presence of either MOP or linked MOP network has not changed the chain packing of these soft segments (Figure 5-12). However, the slope of T_g for **MMM-*n*** decreased with the incorporation of MOPs especially at high MOP concentration, while the change of T_g slope in **HHM-*n*** was not obvious. This change in **MMM-*n*** indicates a stronger interference of the soft segment chains by the MOP nanofillers, which might be associated with phase separation. IR spectra of both membranes reveal the characteristic peaks of MOPs at 1612 cm^{-1} and 733 cm^{-1} with the increasing intensity along with the MOP loadings, confirming the preservation of MOPs no matter they were dispersed in

MMM-*n* or crosslinked within **HHM-*n*** (Figure 5-13). Furthermore, two characteristic peaks of PU were observed on the composite films at 1718 cm^{-1} and 1633 cm^{-1}, which corresponds to the free carbonyl group (C=O) and its hydrogen-bonded form with -NH- group in the PU chains, respectively. By comparing the relative intensity of these two peaks, the effect of MOPs on the strength of hydrogen bonding, which reflects the formation of hard domains through the hard segments in PUs, can be analyzed (Figure 5-13 inset). In the IR spectra of **MMM-*n***, the related intensity of peak at 1633 cm^{-1} greatly decreased as increasing the loadings of MOPs, indicating the suppression of hydrogen bonding and thus less interaction between the hard segments. Combined with the SEM and DSC data, it can be speculated that the interaction between MOPs and the soft segments of PUs facilitated the formation of soft domains while disturbing the hydrogen bonding formation between hard segments. As a result, adverse phase separation was obtained with the suppressed formation of hard domains, leading to the deterioration of the mechanical properties of **MMM-*n***. In contrast, the IR spectra of **HHM-*n*** revealed no obvious change of intensity in these two peaks, indicating the orthogonal formation of the linked MOP network within PUs during the membrane preparation. Due to the existence of the secondary MOP network, the resulting composite films were obtained with greatly enhanced mechanical properties as discussed before (Figure 5-11). The thermogravimetric analysis (TGA) of all the membranes was performed to show an increasing char yield with increasing MOP contents, confirming the incorporation of MOP nanofillers or the linked MOP network (Figure 5-14). At high MOP loadings, an accelerated initial degradation between 200 ºC and 300 ºC was observed in both composite films compared to the pristine PU. In particular, **MMM-*n*** showed a lower initial degradation temperature than **HHM-*n*** and PU (Figure 5-14a). This difference can be explained by the greatly decreased amount of hydrogen bonding within **MMM-*n*** due to the interference of the MOP nanofillers, endowing the resulting membranes with lower thermal stability. On the other hand, the introduction of the linked MOP network exerted less influence on the structure of **HHM-*n***, which was more thermally stable up to 250 ºC (Figure 5-14a).

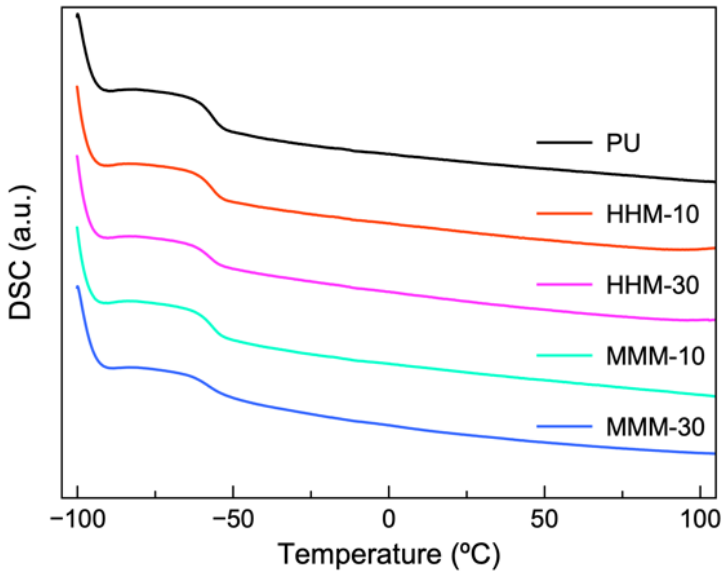

Figure 5-12. DSC plot of (a) **HHM-*n*** and (b) **MMM-*n***.

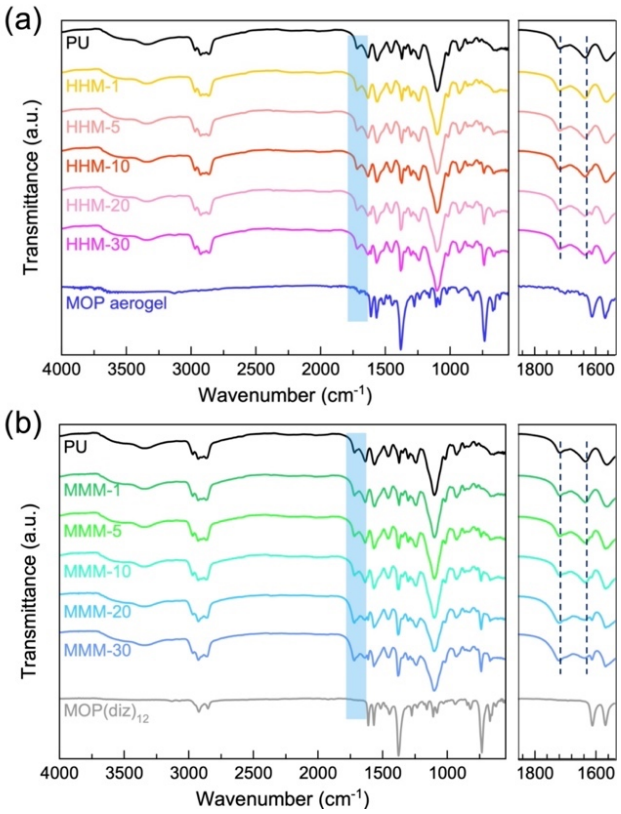

Figure 5-13. IR spectra of (a) **HHM-*n*** and (b) **MMM-*n***.

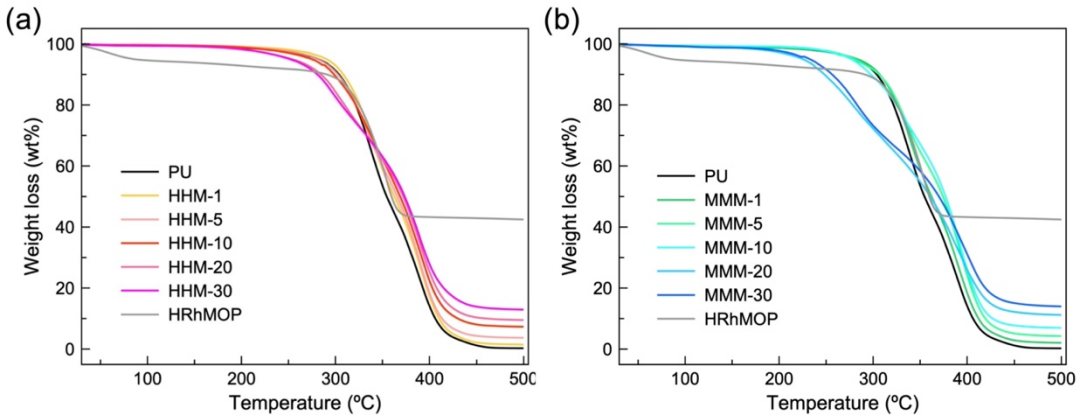

Figure 5-14. TGA plot of (a) **HHM-*n*** and (b) **MMM-*n***.

To further confirm the construction of linked MOP network within the composite membranes as the secondary continuous phase, leakage tests of **HHM-*n*** and **MMM-*n*** were performed by immersing the film samples in the solvent of DMF for three days (Figure 5-15a). Both **MMM-*n*** and the pristine PU were completely dissolved by DMF to obtain the transparent solution, while the pink films of **HHM-*n*** were retained without being dissolved by DMF. Considering the good solubility of PU in DMF, the remaining film in the solution of **HHM-*n*** can only be ascribed to the linked MOP network which was insoluble in any solvent due to the MOP crosslinking. After the leakage test, the corresponding upper solution of **MMM-*n*** was measured by UV-visible spectroscopy to reveal the characteristic peak of **diz**-coordinating **HRhMOP** (Figure 5-15b). The intensity of this peak was observed to continuously increase with increasing MOP concentration, which indicated the preservation of MOPs inside the composites and their dissolution from films into DMF. For the samples of **HHM-*n***, however, no characteristic peak of MOP can be observed in the upper DMF solution, implying zero leakage of MOPs from films into DMF. This result also indicates that all the MOPs in **HHM-*n*** were consumed in the crosslinking reaction through linkers **bix** to form the network as expected. Encouraged by the successful formation of linked MOP network within PU, the sample of **HHM-30** was further washed by DMF for three times to remove PU polymers, followed by solvent exchange thrice with acetone and then $SCCO_2$ drying to obtain the corresponding aerogel (Figure 5-16a). SEM images of the aerogel sample revealed a characteristic colloidal network similar to our previously reported linked MOP gel structure, further confirming the existence of the well-constructed MOP network within the composites (Figure 5-16b and 5-16c).

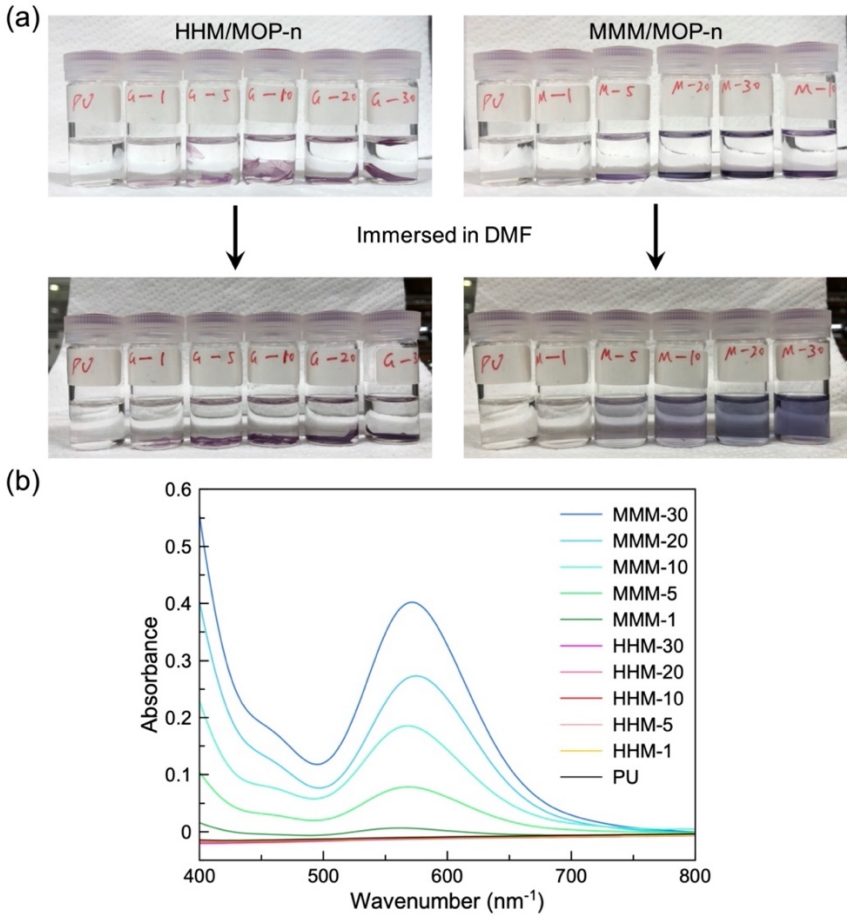

Figure 5-15. (a) Leakage tests of **HHM-*n*** **MMM-*n*** in DMF. (b) UV-visible spectroscopy of the upper solution of the mixture of film samples with DMF after leakage test.

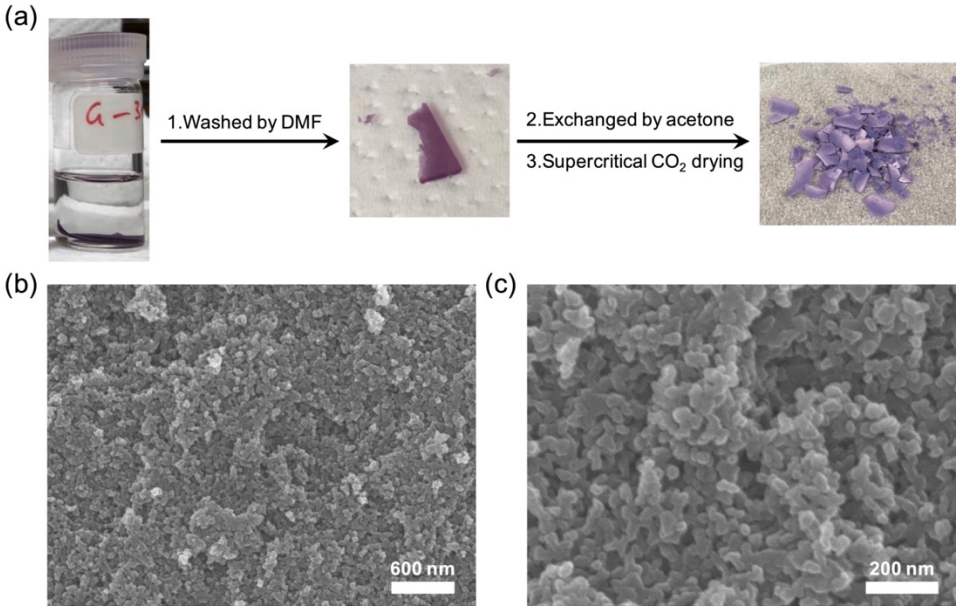

Figure 5-16. (a) Photos of the **HHM-30** sample after washing process with DMF and the resulting aerogel sample after the $SCCO_2$ drying process. (b) SEM images of the aerogel sample obtained from **HHM-30**.

Different from the common MMM composites incorporating porous nanofillers which were either individually dispersed or amorphously grafted onto the main backbones of polymer matrix, the construction of linked MOP network within HHM afforded the composites with hierarchical porosity by connecting the internal cavities of MOPs and the nano-and mesopores between interlinked MOPs. This interconnected porosity is expected to guarantee the diffusion of certain gas molecules throughout the whole composite materials, thus facilitating the separation of gas molecules through the affinity of rhodium sites while improving the gas permeability within the connected porous channel at the same time. To verify this hypothesis, samples of **HHM-*n*** at different MOP loadings were tested against the permeability of CO_2, N_2, H_2, O_2 and CH_4 at 25 ºC, respectively (Figure 5-17). Due to the bad film-forming stability of **MMM-*n*** at high MOP concentrations, only samples of **MMM-1**, **MMM-5** and **MMM-10** were measured to reveal a negligibly improved gas permeability compared to the pristine PU membrane. In contrast, significantly increased permeability of all types of gases was observed in all samples of **HHM-*n*** as increasing the MOP loadings. In particular, the permeability of CO_2 and CH_4 in **HHM-20** increased to be 128.6 and 8.8 barrier, corresponding to about 164% and 73% improvements over the pristine PU sample. The highest permeability of N_2, H_2 and O_2 was achieved for **HHM-10** to be 3.9, 23.3 and 8.5 barrier, which was around 77%, 120% and 89% higher than the pure PU, respectively. Similarly, only the membranes of **HHM-*n*** demonstrated greatly enhanced gas selectivity as increasing the MOP concentration (Figure 5-18). Compared to the pristine PU, the selectivity of CO_2/N_2, CO_2/CH_4, H_2/N_2, H_2/CH_4 and O_2/N_2 for **HHM-30** was increased by 56%, 49%, 58%, 48% and 50%, respectively. Combined with the improved gas permeability, the superiority of the composite HHM membrane with in situ formed porous MOP network in gas separation was confirmed (Figure 5-19). Although the separation performance of **HHM-*n*** was still not so astonishing in the Robeson 2008 upper bound (Figure 5-20), here we demonstrate the importance of morphology or existing form of MOPs as porous fillers in the gas separation behavior of composite systems.

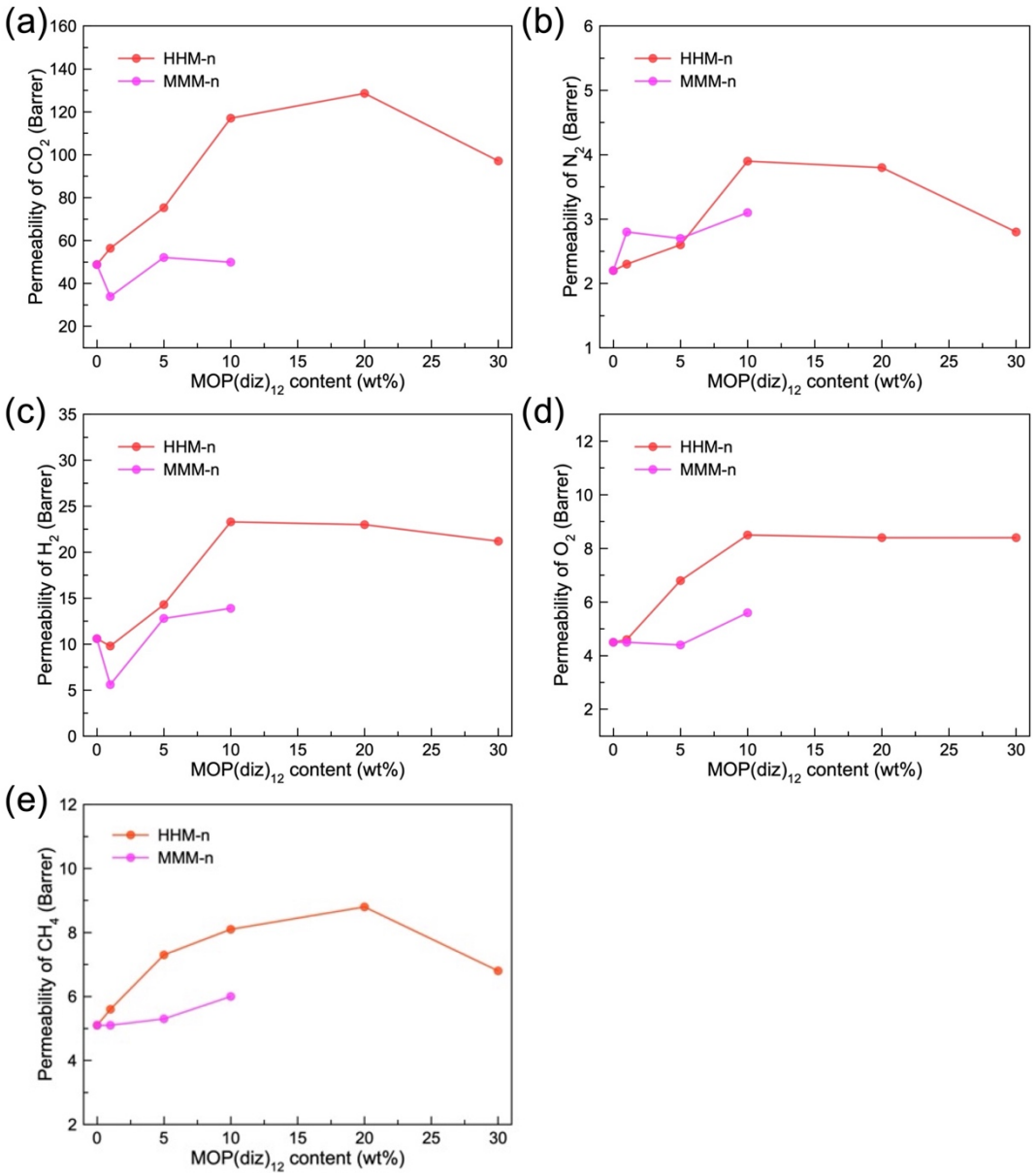

Figure 5-17. (a) CO_2, (b) N_2, (c) H_2, (d) O_2 and (e) CH_4 gas permeability of **HHM-*n*** and **MMM-*n*** at different MOP loadings.

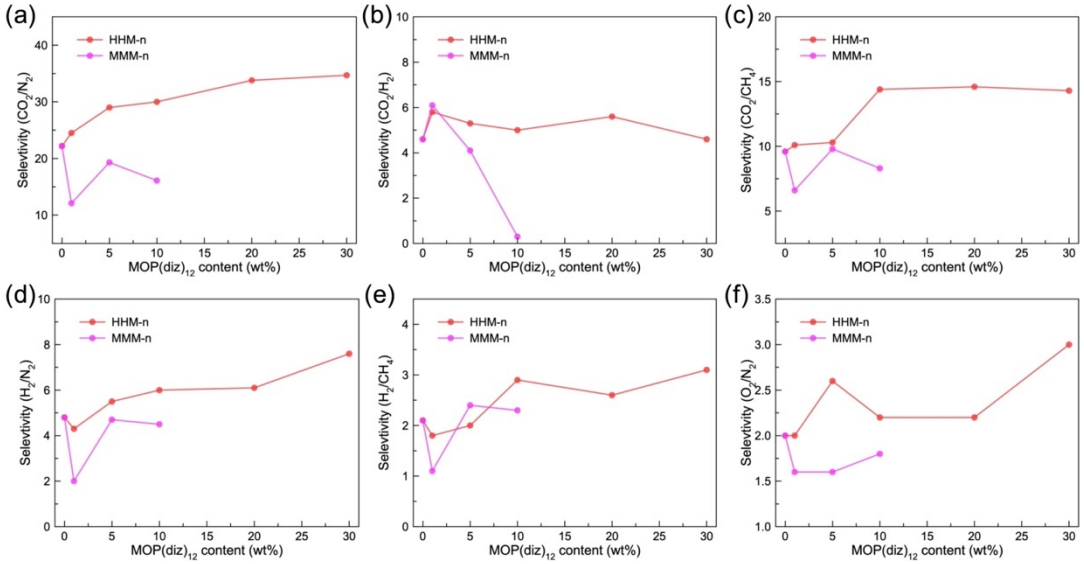

Figure 5-18. Gas selectivity between (a) CO_2/N_2, (b) CO_2/H_2, (c) CO_2/CH_4, (d) H_2/N_2 (e) H_2/CH_4 and (f) O_2/N_2 of **HHM-*n*** and **MMM-*n*** at different MOP loadings.

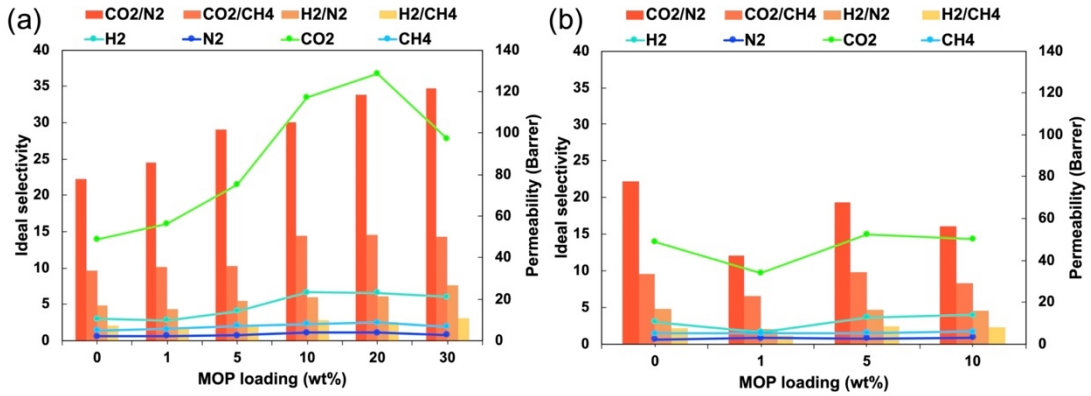

Figure 5-19. Gas separation performance of (a) **HHM-*n*** and (b) **MMM-*n*** at different MOP loadings.

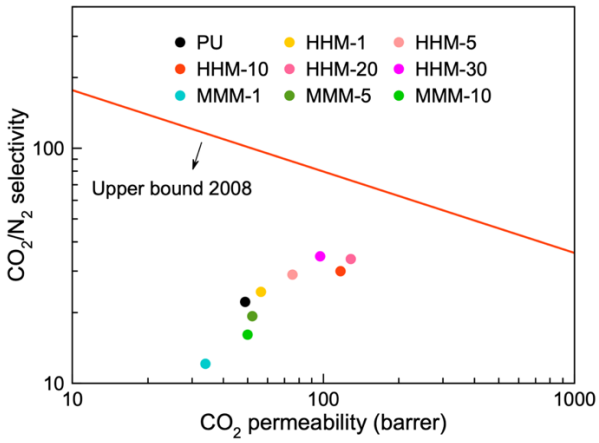

Figure 5-20. Comparison of the gas separation performance of (a) **HHM-*n*** and (b) **MMM-*n*** with the Robeson 2008 upper bound.

Conclusion

In summary, a series of hierarchical hybrid membranes (**HHM-*n***) was fabricated by using polymer polyurethane (PU) as the matrix and hierarchical porous MOP network as the secondary continuous phase. Different from the common MMM composites where the porous nanofillers were simply dispersed or covalently grafted onto the backbone of the polymer chains, in situ supramolecular crosslinking of MOPs with organic linkers was induced within PU during the membrane synthesis, allowing for the construction of linked MOP network which not only fixed the MOPs within PU without aggregation but also guaranteed the molecular diffusion throughout the material through its interconnected porosities. Both mechanical properties and gas separation performances of **HHM-*n*** were significantly improved due to the incorporation of linked MOP network, the presence of which was confirmed by the SEM images and leakage tests. In addition, mixed matrix membranes (**MMM-*n***) were also synthesized as control samples by simply dispersing isolated MOPs into PUs. In contrast to **HHM-*n*** with unchanged polymer morphology and homogenous MOP distribution, **MMM-*n*** revealed an adverse phase separation with deteriorated film-forming stability and unimproved gas separation properties. This difference in the performances of their corresponding membranes strongly demonstrates the influence of morphology or existing forms of MOPs as porous fillers on the final properties of the hybrid systems. In fact, except for the MOPs used here, a large library of porous candidates like MOFs or COFs is available to construct their corresponding porous networks inside the composite materials, showing potentials to further improve their performances not only in gas separation but also in other applications such as pollutants extraction and electrolytes.

Experimental section

Materials

Rhodium acetate, 1-dodecyl-1H-imidazole (**diz**), and 1,4-bis(imidazol-1-ylmethyl)benzene (**bix**) were synthesized according to a previously reported procedure.[25] 5-hydroxy-1,3-benzenedicarboxylic acid were purchased from Sigma-Aldrich and used as received. Solvents were purchased from Wako Pure Chemical Industries except those at HPLC grade were purchased from Fischer Chemicals. Poly(tetramethylene glycol) (PTMG, Mw: 2000 g/mol) was purchased from Sigma-Aldrich and dried under vacuum overnight at 80°C to remove any residual water. Octanediol chain extender and dibutyltindilaurate (DBTDL) as a catalyst were provided from Sigma-Aldrich and dried over 4 Å molecular sieves. Isophorone diisocyanate (IPDI), dehydrated dimethylacetamide (DMAc), dimethylformamide (DMF) were purchased from Wako Pure Chemical Industries and used as received.

Characterizations

The rheological measurements of the membrane samples were made using a stress-controlled AR-G2 (TA Instruments, New Castle, DE, USA) rheometer. Dynamic mechanical analysis (DMA) measurements of the membranes were conducted by frequency sweeping in a tensile mode with a 0.5% strain amplitude that was well inside the linear regime (initial strain is fixed to 0.3%). The tensile tests of the membranes were performed by stretching the samples in a strain rate of $\varepsilon = 1.5\ min^{-1}$.

The super-critical CO_2 drying process was carried out on SCLEAD-2BD autoclave (KISCO) using supercritical CO_2 at 14 MPa and 50 °C.

Thermogravimetric analyses (TGA) were performed in the temperature range from room temperature to 500 ºC at a heating rate of 10 ºC/min with a Rigaku Thermo plus EVO2, under a nitrogen atmosphere.

Differential scanning calorimetry (DSC) was carried out in the temperature range from 30 ºC to 150 ºC at a heating rate of 10 ºC/min using Hitachi DSC 7020, under a nitrogen atmosphere.

Scanning Electron Microscopy (SEM) of cross-sectional morphologies of the membranes were observed using a field-emission scanning electron microscope with a JEOL Model JSM-7001F4 system operating at 10 kV and 5 mA current. The surface morphologies of the

membrane samples were observed using a scanning electron micro- scope (FESEM, Hitachi S-4800) and energy dispersive X-ray (EDX, Hitachi SU-6600) techniques. The samples were coated with 14 nm Osmium before measurement.

Fourier transform infrared (FTIR) spectra of the MOPs and the membrane samples were conducted on a Jasco FT/IR-6100 in the range of 4000-500 cm^{-1} with a resolution of 4 cm^{-1} and 128 scans.

Pure gas permeability of the membranes was measured using the constant volume–variable pressure method at room temperature. All membranes were individually tested for CO_2 capture (CO_2, CH_4, N_2, O_2 and H_2). The diffusivity and solubility coefficients of each sample were calculated by the time-lag (θ) method. For each sample, three membranes were tested, and the average permeability coefficients were reported. The details for measurement are as follow:

The gas permeability of all membranes was measured using a constant volume-variable pressure method. The permeation gas cell comprises a stainless steel holder with an effective area of 2 cm^3 (Millipore XX4502500) equipped with gas and vacuum lines.[29] The changes in pressure and temperature are recorded by an absolute pressure sensor (Keller PAA33X). Gas transport in the polyurethane membranes is explained by the solution-diffusion mechanism, where the gas permeability is the product of gas diffusivity (D) and gas solubility (S) coefficients: $P_i = D_i \times S_i$. The gas permeation coefficient is calculated from the equation below:

$$P = J_i \frac{l}{\Delta p} = 10^{10} \frac{273.15}{76} \frac{V}{AT} \left(\frac{dp}{dt}\right) \frac{l}{\Delta p}$$

where J_i is the gas flux, l is the membrane thickness, and Δp is the pressure drop between the feed and permeate side of the membrane. Besides, (dp/dt) is the pressure difference rate in the steady-state gas transmission through the membrane. V, A, and T represent the permeate volume, the effective area of the membrane, and measurement temperature, respectively. The gas permeability unit is $mol.m.m^{-2}.s^{-1}.Pa^{-1}$ or barrer = $10^{-10} cm^3(STP)cm\ cm^{-2}s^{-1}cmHg^{-1}$.

The ideal selectivity of the membrane $\alpha_{i/j}$ is calculated by the ratio of permeability coefficients of two individual gases i and j, which also can be written as the product of the diffusivity and solubility coefficients:

$$\alpha_{i/j} = \frac{P_i}{P_j} = \frac{D_i S_i}{D_j j}$$

The diffusivity coefficient of each gas can be calculated from the time-lag method:

$$\mathrm{D}_i = \frac{l^2}{6\theta}$$

Linear extrapolation of the slope from the steady-state region of p vs. t curve and compute the x-axis intercept gives θ.

Detailed synthesis

Synthesis of precursors

1-dodecyl-1H-imidazole (**diz**), 1,4-bis(imidazole-1-ylmethyl)benzene (**bix**) and **HRhMOP** were synthesized according to our previous reports.[23]

Synthesis of polyurethane (PU)

The PU was synthesized by a two-step bulk polymerization method. First, PTMG was reacted with an excess IPDI (PTMG : IPDI = 1 : 3 molar ratio) under nitrogen atmosphere at 75 ºC, followed by the addition of 0.1 mL DBTDL to obtain a macro diisocyanate pre-polymer. After 2 h, an exact amount of the chain extender octanediol was added for equimolar adjustment of the NCO:OH ratio. The synthesized polyurethane was washed and precipitated in methanol: water (50:50 wt%) to remove any unreacted monomers or low molecular weight polymers. Samples were dried at 70 ºC under vacuum before use. The molar ratio of PTMG: IPDI: chain extender was 1:3:2.

Synthesis of HRhMOP(diz)$_{12}$

200 mg of **HRhMOP** were dispersed in 40 mL of DCM, then 132.5 mg of **diz** (18 mol. eq.) were added. After sonication for 5 mins, the solution was centrifuged to remove the precipitate. The upper purple solution was collected and evaporated in vacuum. The obtained solid residue was washed twice with EtOH to remove any remaining **diz**. Finally, the purple solid product was dried under vacuum.

Synthesis of HHM-n

The PU membrane and its composites with linked MOP networks at different loadings were prepared in DMF by using the solution casting method. In a typical synthesis process, **HRhMOP(diz)$_{12}$** and **bix** (12 mol. eq. related to MOPs) were separately dissolved in the DMF solution of PU (3wt%), respectively. Then the solution of MOPs was added into the solution of **bix** under vigorous stirring. The resultant transparent purple solution was transferred into the Teflon Petri-dish and heated at 80 ºC overnight. After the evaporation of DMF solvent upon heating, the films were obtained and removed from the Petri-dishes, followed by drying under vacuum at 80 ºC overnight. The resulting composite films were named as **HHM-n** where n indicates the weight percentage of **HRhMOP(diz)$_{12}$** related to the PU matrix.

Synthesis of MMM-n

The PU membrane and its composites with isolated MOPs at different loadings were prepared in DMF by using the solution casting method. In a typical synthesis process, **HRhMOP(diz)$_{12}$** was dissolved in the DMF solution of PU (3wt%). Then the resultant transparent pink solution was transferred into the Teflon Petri-dish and heated at 80 ºC overnight. After the evaporation of DMF solvent upon heating, the films were obtained and removed from the Petri-dishes, followed by drying under vacuum at 80 ºC overnight. The resulting composite films were named as **MMM-n** where n indicates the weight fraction of **HRhMOP(diz)$_{12}$** related to the PU matrix.

Reference

1. Krause, S.; Hosono, N.; Kitagawa, S., Chemistry of Soft Porous Crystals: Structural Dynamics and Gas Adsorption Properties. *Angew. Chem. Int. Ed.* **2020**, *59* (36), 15325-15341.

2. Liu, J.; Chen, L.; Cui, H.; Zhang, J.; Zhang, L.; Su, C.-Y., Applications of metal-organic frameworks in heterogeneous supramolecular catalysis. *Chem. Soc. Rev.* **2014**, *43* (16), 6011-6061.

3. Yao, M.-S.; Li, W.-H.; Xu, G., Metal-organic frameworks and their derivatives for electrically-transduced gas sensors. *Coord. Chem. Rev.* **2021**, *426*, 213479.

4. Slater, A. G.; Cooper, A. I., Function-led design of new porous materials. *Science,* **2015**, *348* (6238), aaa8075.

5. Furukawa, H.; Cordova, K. E.; O'Keeffe, M.; Yaghi, O. M., The Chemistry and Applications of Metal-Organic Frameworks. *Science,* **2013**, 341 (6149), 1230444.

6. Lohse, M. S.; Bein, T., Covalent Organic Frameworks: Structures, Synthesis, and Applications. *Adv. Funct. Mater.* **2018**, *28* (33), 1705553.

7. McKeown, N. B.; Budd, P. M., Polymers of intrinsic microporosity (PIMs): organic materials for membrane separations, heterogeneous catalysis and hydrogen storage. *Chem. Soc. Rev.* **2006**, *35* (8), 675-683.

8. Pastore, V. J.; Cook, T. R., Coordination-Driven Self-Assembly in Polymer–Inorganic Hybrid Materials. *Chem. Mater.* **2020**, *32* (9), 3680-3700.

9. Jin, F.; Liu, J.; Chen, Y.; Zhang, Z., Tethering Flexible Polymers to Crystalline Porous Materials: A Win-Win Hybridization Approach. *Angew. Chem. Int. Ed.* **2021**, *60* (26), 14222-14235.

10. Rodenas, T.; Luz, I.; Prieto, G.; Seoane, B.; Miro, H.; Corma, A.; Kapteijn, F.; Llabrés i Xamena, F. X.; Gascon, J., Metal-organic framework nanosheets in polymer composite materials for gas separation. *Nat. Mater.* **2015**, *14* (1), 48-55.

11. Ghalei, B.; Sakurai, K.; Kinoshita, Y.; Wakimoto, K.; Isfahani, Ali P.; Song, Q.; Doitomi, K.; Furukawa, S.; Hirao, H.; Kusuda, H.; Kitagawa, S.; Sivaniah, E., Enhanced selectivity in mixed matrix membranes for CO_2 capture through efficient dispersion of amine-functionalized MOF nanoparticles. *Nat. Energy,* **2017**, *2* (7), 17086.

12. Liu, G.; Chernikova, V.; Liu, Y.; Zhang, K.; Belmabkhout, Y.; Shekhah, O.; Zhang, C.; Yi, S.; Eddaoudi, M.; Koros, W. J., Mixed matrix formulations with MOF molecular sieving for key energy-intensive separations. *Nat. Mater.* **2018**, *17* (3), 283-289.

13. Pournaghshband Isfahani, A.; Sadeghi, M.; Nilouyal, S.; Huang, G.; Muchtar, A.; Ito, M. M.; Yamaguchi, D.; Sivaniah, E.; Ghalei, B., Tuning the morphology of segmented block

copolymers with Zr-MOF nanoparticles for durable and efficient hydrocarbon separation membranes. *J. Mater. Chem. A*. **2020**, *8* (18), 9382-9391.

14. Dechnik, J.; Gascon, J.; Doonan, C. J.; Janiak, C.; Sumby, C. J., Mixed-Matrix Membranes. *Angew. Chem. Int. Ed.* **2017**, *56* (32), 9292-9310.

15. Hosono, N.; Kitagawa, S., Modular Design of Porous Soft Materials via Self-Organization of Metal-Organic Cages. *Acc. Chem. Res.* **2018**, *51* (10), 2437-2446.

16. Gosselin, A. J.; Rowland, C. A.; Bloch, E. D., Permanently Microporous Metal-Organic Polyhedra. *Chem. Rev.* **2020**, *120* (16), 8987-9014.

17. Liu, X.; Wang, X.; Bavykina, A. V.; Chu, L.; Shan, M.; Sabetghadam, A.; Miro, H.; Kapteijn, F.; Gascon, J., Molecular-Scale Hybrid Membranes Derived from Metal-Organic Polyhedra for Gas Separation. *ACS Appl. Mater. Interfaces.* **2018**, *10* (25), 21381-21389.

18. Liu, Y.; Cai, L.; Ma, L.; Li, M.; Yang, J.; Chen, K.; Yin, P., Modulating Polymer Dynamics via Supramolecular Interaction with Ultrasmall Nanocages for Recyclable Gas Separation Membranes with Intrinsic Microporosity. *Nano Lett.* **2021**, *21* (21), 9021-9029.

19. Liu, J.; Duan, W.; Song, J.; Guo, X.; Wang, Z.; Shi, X.; Liang, J.; Wang, J.; Cheng, P.; Chen, Y.; Zaworotko, M. J.; Zhang, Z., Self-Healing Hyper-Cross-Linked Metal-Organic Polyhedra (HCMOPs) Membranes with Antimicrobial Activity and Highly Selective Separation Properties. *J. Am. Chem. Soc.* **2019**, *141* (30), 12064-12070.

20. Xie, X.-Y.; Wu, F.; Liu, X.; Tao, W.-Q.; Jiang, Y.; Liu, X.-Q.; Sun, L.-B., Photopolymerization of metal-organic polyhedra: an efficient approach to improve the hydrostability, dispersity, and processability. *Chem. Commun*. **2019**, *55* (44), 6177-6180.

21. Taggart, G. A.; Antonio, A. M.; Lorzing, G. R.; Yap, G. P. A.; Bloch, E. D., Tuning the Porosity, Solubility, and Gas-Storage Properties of Cuboctahedral Coordination Cages via Amide or Ester Functionalization. *ACS Appl. Mater. Interfaces.* **2020**, *12* (22), 24913-24919.

22. Yang, Z.; Liu, G.; Yuan, Y. D.; Peh, S. B.; Ying, Y.; Fan, W.; Yu, X.; Yang, H.; Wu, Z.; Zhao, D., Homoporous hybrid membranes containing metal-organic cages for gas separation. *J. Membr. Sci.* **2021**, *636*, 119564.

23. Chen, T.-H.; Wang, L.; Trueblood, J. V.; Grassian, V. H.; Cohen, S. M., Poly(isophthalic acid)(ethylene oxide) as a Macromolecular Modulator for Metal-Organic Polyhedra. *J. Am. Chem. Soc.* **2016**, *138* (30), 9646-9654.

24. Furukawa, S.; Horike, N.; Kondo, M.; Hijikata, Y.; Carné-Sánchez, A.; Larpent, P.; Louvain, N.; Diring, S.; Sato, H.; Matsuda, R.; Kawano, R.; Kitagawa, S., Rhodium-Organic Cuboctahedra as Porous Solids with Strong Binding Sites. *Inorg. Chem.* **2016**, *55* (21), 10843-10846.

25. Carné-Sánchez, A.; Craig, G. A.; Larpent, P.; Hirose, T.; Higuchi, M.; Kitagawa, S.;

Matsuda, K.; Urayama, K.; Furukawa, S., Self-assembly of metal-organic polyhedra into supramolecular polymers with intrinsic microporosity. *Nat. Commun.* **2018**, *9* (1), 2506.

26. Carné-Sánchez, A.; Craig, G. A.; Larpent, P.; Guillerm, V.; Urayama, K.; Maspoch, D.; Furukawa, S., A Coordinative Solubilizer Method to Fabricate Soft Porous Materials from Insoluble Metal-Organic Polyhedra. *Angew. Chem. Int. Ed.* **2019**, *58* (19), 6347-6350.

27. Isfahani, A. P.; Sadeghi, M.; Wakimoto, K.; Gibbons, A. H.; Bagheri, R.; Sivaniah, E.; Ghalei, B., Enhancement of CO_2 capture by polyethylene glycol-based polyurethane membranes. *J. Membr. Sci.* **2017**, *542*, 143-149.

28. Robeson, L. M., The upper bound revisited. *J. Membr. Sci.* **2008**, *320* (1), 390-400.

29. Isfahani, A. P.; Ghalei, B.; Wakimoto, K.; Bagheri, R.; Sivaniah, E.; Sadeghi, M., Plasticization resistant crosslinked polyurethane gas separation membranes. *J. Mater. Che. A.* **2016,** *4* (44), 17431-17439.

Lists of publications

General introduction

Directional asymmetry over multiple length scales in reticular porous materials

Alexandre Legrand, **Zaoming Wang**, Javier Troyano, Shuhei Furukawa

Chem. Sci., **2021**, *12*, 18-33.

Chapter 1

Multiscale structural control of linked metal-organic polyhedra gel by aging-induced linkage-reorganization

Zaoming Wang, Christian Villa Santos, Alexandre Legrand, Frederik Haase, Yosuke Hara, Kazuyoshi Kanamori, Takuma Aoyama, Kenji Urayama, Cara M. Doherty, Glen J. Smales, Brian R. Pauw, Yamil J. Colon, Shuhei Furukawa

Chem. Sci., **2021**, *12*, 12556-12563.

Chapter 2

Porous Colloidal Hydrogels Formed by Coordination-Driven Self-Assembly of Charged Metal-Organic Polyhedra

Zaoming Wang, Gavin A. Craig, Alexandre Legrand, Frederik Haase, Saori Minami, Kenji Urayama, Shuhei Furukawa

Chem. Asian J., **2021**, *16*, 1092-1100.

Chapter 3

Control of extrinsic porosities in linked metal-organic polyhedra gels by imparting coordination-driven self-assembly with electrostatic repulsion

Zaoming Wang, Takuma Aoyama, Eli Sanchez-Gonzales, Tomoko Inose, Kenji Urayama, Shuhei Furukawa

Posted on Chemrxiv Preprint. 10.26434/chemrxiv-2022-8gbb1

Chapter 4

Fabrication of linked metal-organic polyhedra gels with permanent porosities by simple liquid exchange

Zaoming Wang, Gavin A. Craig, Frederik Haase, Aydin Ozcan, Guillaume Maurin, Takuma Aoyama, Mingshui Yao, Kenji Urayama, Rocio Semino, Cara M. Doherty, Keiji Horio, Masakazu Higuchi, Satoshi Horike, Susumu Kitagawa, Shuhei Furukawa

In preparation.

Chapter 5

Direct formation of hierarchical hybrid membranes (HHMs) with hierarchical porous MOP networks by sol-gel process

Zaoming Wang, Ali Pournaghshband Isfahani, Guoji Huang, Takuma Aoyama, Kenji Urayama, Behnam Ghalei, Easan Sivaniah, Shuhei Furukawa

In preparation.

Other publications

[1] A comparative study of honeycomb-like 2D π-conjugated metal–organic framework chemiresistors: conductivity and channels

Mingshui Yao, Ping Wang, Yifan Gu, Tomoyuki Koganezawa, Hirotaka Ashitani, Yoshiki Kubota, **Zaoming Wang**, Zeyu Fan, Ken-ichi Otake, Susumu Kitagawa

Dalton Trans., **2021**, *50*, 13236-13245.

[2] Controlled sequential assembly of metal-organic polyhedra into colloidal gels with high chemical complexity

Min Ying Tsang, Shun Tokuda, Po-Chun Han, **Zaoming Wang**, Alexandre Legrand, Marina Kawano, Masahiko Tsujimoto, Yuki Ikeno, Kenji Urayama, Kevin C.-W. Wu, Shuhei Furukawa

Submitted to Small Structures. In revision.

[3] Porous Organic Polymer Gels as a Synthetic Hybridization Platform for De- signing Versatile Molecular Separators

Yan Su, **Zaoming Wang** Alexandre Legrand, Takuma Aoyama, Weitao Wang, Ken-ichi Otake, Kenji Urayama, Susumu Kitagawa, Shuhei Furukawa, Cheng Gu

Submitted to J. Am. Chem. Soc. In revision. († equal contribution)